Liquid-Jet Photoemission Studies of the Interface between Metal-Oxide Nanoparticles and Aqueous Solution

Im Fachbereich Physik der Freien Universität Berlin

eingereichte Dissertation

zur Erlangung des akademischen Grades

eines Doktors der Naturwissenschaften (Dr. rer. nat.)

vorgelegt von

Hebatallah Ali

Berlin

2019

Gutachter:

1. Prof. Dr. Gerard J. M. Meijer
   Department of Molecular Physics, Fritz-Haber-Institut der Max-Planck-Gesellschaft, Berlin, Germany.

2. Prof. Dr. John C. Hemminger
   Department of Chemistry, University of California, Irvine, California, USA.

3. Prof. Dr. Wolfgang Kuch
   Institute of experimental physics, Freie Universität Berlin, Berlin, Germany.

4. Prof. Dr. Richard J. Saykally
   Department of Chemistry, University of California, Berkeley, California, USA.

Defense date: 23rd of January 2020.

This Thesis was written under the supervision of Prof. Dr. Gerard J. M. Meijer and Dr. Bernd Winter at the Molecular Physics department- Fritz Haber Institute of the Max Planck Society.

During this course, I was granted a PhD scholarship from the Egyptian Ministry of Higher Education and Ain Shams University, Cairo, Egypt.

Abstract

This thesis reports on the electronic structure of water adsorption on transition metal oxide (TMO) nanoparticle (NP) surfaces using liquid jet photoelectron spectroscopy. My focus is to determine the nature of water adsorption (associative/dissociative) on TMO surfaces from NPs fully immersed in liquid water. Probing the electronic structure of this solid — liquid interface is crucial for a variety of scientific and technological fields, such as material science, corrosion, electrochemistry, and photocatalytic water splitting. Especially the latter is receiving ample interest due to the current environmental pollution and energy shortage problems. In this context, I have studied the molecular species forming at the NP — water interface for the arguably most efficient photocatalytic systems: hematite iron oxide (α-Fe_2O_3) and anatase titanium dioxide (TiO_2). Using soft X-ray photoelectron spectroscopy (PES) from liquid microjets, I have detected valence and core-level photoelectrons, as well as Auger electrons, from liquid water, NP – water interface, and the interior of the aqueous-phase NPs. Such methods are shown to be highly sensitive to the adsorbed interfacial species on the NP surfaces.

In the α-Fe_2O_3 NP aqueous solution, water has been found to be dissociatively adsorbed on the surface, proven by the water-dissociation product hydroxide, detected by resonant and non-resonant photoelectron spectroscopy (PES), as well as partial-electron-yield X-ray absorption spectroscopy (PEY-XAS) at the oxygen K-edge. The iron L_3-edge PEY-XAS measurements have proven to be sensitive to the chemical environment of the Fe^{3+} ions at the NP surface. By comparing the pre-edge peak intensities of local versus non-local autoionization signals, the ultrafast charge-transfer time from interfacial Fe^{3+} into the aqueous environment can be estimated.

The TiO_2 NP — water interface study has revealed that the nature of water interaction with a defect-free TiO_2 surface depends on the surrounding chemical environment. Water has been found to be molecularly adsorbed at the surface in an acidic environment and dissociatively adsorbed at a pH above neutral (slightly basic, pH 7.8). This is inferred from resonant and non-resonant PES and PEY-XA spectra at the O K-edge, taken from the adsorbed oxygen interfacial species. Based on these findings, combined with the previously reported ambient pressure photoelectron spectroscopic results of similar systems at neutral pH, I have proposed a TiO_2—water interaction mechanism which depends on the aqueous solution pH and hence on the proton mobility in these environments. This mechanism solves a long-standing question about the nature of water adsorption on TiO_2 surfaces.

Furthermore, soft X-ray photoelectron spectroscopy (XPS) and PEY-XAS were carried out at the nitrogen K-edge for TiO_2 NPs dispersed in 0.3 M NH_4OH aqueous solution (pH 7.8) to identify the composition and thickness of the so-called Stern layer surrounding the TiO_2 NPs. It was found to be composed of NH_4^+ ions, with an approximately 0.35 nm thickness. Also, I observed a significant amount of OH^- molecules created upon water dissociation on the TiO_2 surface and subsequently trapped around the Stern layer, forming a diffuse layer, by comparing the XP spectra of hydroxide signals from the NP aqueous solution with the reference samples (0.5 M NH_4OH and 5 M NaOH solutions). Complementary information is obtained from the bulk sensitive photon-emission spectroscopic study (photon yield detection) at the oxygen K-edge which allows to quantify the total amount of OH^- in the TiO_2 aqueous solution to be 0.6 M. Such a large OH^- concentration can only be explained when taking a source of OH^- generation into account, which is water dissociation at the TiO_2 NP surface. I also provide experimental evidence that almost all OH^- ions in the TiO_2 NP aqueous solution coordinate with three water molecules, forming a tetrahedral hydration configuration, and constitute > 0.44-nm-thick diffuse layers around TiO_2 NPs. This diffuse layer, together with the NH_4^+ Stern layer, form a > 0.8-nm-thick electric double layer (EDL) around the dispersed TiO_2 NPs. Lastly, I proposed two models of charged-ion distributions in the EDL around TiO_2 NPs, where the proton is either anchored at the TiO_2 surface or quickly diffusing away into the bulk solution. Both models are preventing the unwanted H^+ — OH^- recombination, although the second model is more realistic as the efficient H^+ dynamics provides continuous freeing surface sites for further water dissociation.

Zusammenfassung

Diese Arbeit berichtet über die Aufklärung und Erforschung der elektronischen Struktur der Wasser-Grenzschicht an Übergangsmetalloxid (TMO) Nanopartikel (NP) Oberflächen unter Verwendung der Flüssigstrahl-Photoelektronen Spektroskopie. Mein Fokus liegt auf der Bestimmung der Art (assoziativ/dissoziativ) der Wasseradsorption an TMO-Oberflächen aus vollständig eingetauchten Nanopartikeln in flüssigem Wasser. Die Erforschung der elektronischen Struktur dieser Fest-Flüssig-Grenzfläche ist entscheidend für eine Vielzahl von wissenschaftlichen und technologischen Bereichen in der Materialwissenschaft, bei der Korrosion, in der Elektrochemie und bei der photokatalytischen Wasserspaltung. Vor allem Letzteres stößt aufgrund der aktuellen Umweltverschmutzung und Energieknappheit auf großes Interesse. In diesem Zusammenhang habe ich die Bildung molekularer Spezies an der NP-Wasser-Schnittstelle für die effizientesten photokatalytischen Systeme untersucht: Hämatit-Eisenoxid (α-Fe_2O_3) und Anatase-Titandioxid (TiO_2). Mit Hilfe der Photoelektronen Spektroskopie (PES) im weichen Röntgenbereich an einem Mikroflüssigkeitsstrahl habe ich Valenz- und Rumpf-Niveau-Photoelektronen sowie Auger-Elektronen von flüssigem Wasser, aus der Nanopartikel-Wasser-Grenzfläche und aus dem Inneren der Nanopartikel in der wässrigen Phase erfasst. Solche Verfahren erwiesen sich als sehr empfindlich gegenüber Änderungen in der Zusammensetzung der Spezien an der NP-Oberfläche.

Für die Grenzfläche zwischen den α-Fe_2O_3 Nanopartikeln und Wasser wurde festgestellt, dass Wasser an der Oberfläche dissoziativ adsorbiert wird. Dies wurde aus den Hydroxyl-Signalen geschlossen, die mit Hilfe der resonanten, nicht-resonanten und den sogenannten partiellen Elektronen-Ausbeute-Röntgenabsorptionsspektren (PEY-XA) an der Sauerstoff K-Kante gewonnen wurden. Entsprechend haben sich die Eisen L_3-Kanten PEY-XAS-Messungen als empfindlich gegenüber der chemischen Umgebung der Fe^{3+}-Ionen an der NP-Oberfläche erwiesen. Durch den Vergleich des Anteils der vor der Kante liegenden Peak-Intensitäten an lokalen und nicht-lokalen Autoionisationssignalen wird eine sehr schnelle Ladungsübertragungszeit von ~ 1fs von den Fe^{3+}-Ionen in der Grenzfläche in die wässrige Umgebung abgeschätzt.

Die TiO_2-Nanopartikel-Wassergrenzflächenstudie hat gezeigt, dass die Art der Wasserwechselwirkung mit einer defektfreien TiO_2-Oberfläche von der chemischen Umgebung abhängt. Es wurde festgestellt, dass im sauren pH-Bereich Wasser molekular an der Oberfläche adsorbiert und im neutralen bis leicht-basischem pH-Bereich (pH 7,8) dissoziativ adsorbiert wird. Dies konnte anhand von Signalen der adsorbierten Sauerstoff-Grenzflächenspezies, die von resonanten, nicht-resonanten und den PEY-XA-Spektren an der O-K-Kante gewonnen wurden, geschlossen werden. Basierend auf diesen Erkenntnissen und aus den zuvor berichteten Photoelektronen-spektroskopischen Ergebnissen eines ähnlichen Systems bei neutralem pH-Wert schlage ich einen TiO_2-Wasser-Interaktionsmechanismus vor, der von dem pH-Wert der wässrigen Lösung und damit von der Protonenmobilität in diesen Umgebungen abhängt. Dieses Modell beantwortet eine seit langem bestehende Frage nach der Art der Wasseraufnahme auf der TiO_2-Oberfläche. Darüber hinaus wurden Photoelektronenspektroskopie-Messungen im weichen Röntgenbereich und PEY-XAS Messungen an der Stickstoff-K-Kante für TiO_2-Nanopartikel durchgeführt, die in einer 0,3 M NH_4OH-Wasserlösung (bei pH 7,8) dispergiert sind, um die Zusammensetzung und Dicke der so genannten Stern-Schicht, die die TiO_2-Nanopartikel umgibt, zu identifizieren. Es wurde festgestellt, dass die Stern-Schicht aus NH_4^+-Ionen besteht und einer Dicke von etwa 0,35 nm hat. Außerdem beobachtete ich eine signifikante Menge an OH^- Molekülen, die bei der Wasserdissoziation auf der TiO_2-Oberfläche entstanden sind und anschließend ausserhalb der Stern-Schicht sich ansammeln und eine diffuse Schicht bilden. Dies wurde anhand von Vergleichen der Hydroxidsignalen in den Photoelektronen-Spektren aus der Nanopartikel-Wasserlösung mit den Referenzproben (0,5 M NH_4OH- und 5 M NaOH-Lösungen) ermittelt. Weitere Erkenntnisse wurden aus den bulk-sensitiven Röntgenemissionsspektroskopischen Studien (durch Photonenausbeutedetektion) an der Sauerstoff-K-Kante gewonnen, die es ermöglichte, die Gesamtmenge an OH^- in der wässrigen TiO_2-Lösung auf 0,6 M zu quantifizieren. Eine solch große OH^- Konzentration kann nur unter Berücksichtigung einer Quelle der OH^- Erzeugung erklärt werden – diese kann nur die Wasserdissoziation an der TiO_2-Nanopartikel-Oberfläche sein. Ich stelle auch experimentelle Beweise zur Verfügung, dass fast alle OH^- Ionen in der wässrigen TiO_2 Nanopartikel-Lösung mit drei Wassermolekülen tetraedisch koordinieren, die damit eine ca. > 0,44 nm dicke diffuse Schicht um die TiO_2 Nanopartikel bilden. Diese diffuse Schicht bildet zusammen mit der NH_4^+ Stern-Schicht eine > 0,8 nm dicke elektrische Doppelschicht (EDL) um die dispergierten TiO_2 Nanopartikel. Schließlich habe ich zwei Modelle der Verteilung geladener Ionen in der EDL um den TiO_2 Nanopartikeln herum vorgeschlagen, bei denen das Proton entweder an der TiO_2-Oberfläche verankert ist oder schnell in den Bulk diffundiert. Beide Modelle verhindern die unerwünschte H^+ - OH^- Rekombination, obwohl das zweite Modell realistischer ist, da die effiziente H^+ Dynamik eine kontinuierliche Freisetzung von Oberflächenstellen für die weitere Wasserdissoziation ermöglicht.

List of Abbreviations

AP-PES	Ambient Pressure Photoelectron Spectroscopy
Aq	Aqueous
Aq. sol.	Aqueous solution
BE	Binding Energy
CPMD	Car-Parrinello Molecular Dynamics
CCD	Charged Coupled Device
DFT	Density Functional Theory
DPU	Differential Pumping Unit
EAL	Effective Attenuation Length
EDL	Electric Double Layer
ETMD	Electron Transfer Medicated Decay
E_g	Energy gap
FEP	Fluorinated Ethylene Propylene
Fs	Femtosecond
HER	H_2 Evolution Reaction
HOMO	Highest Occupied Molecular Orbital
HPLC	High-Performance Liquid Chromatography
IC	Interaction Chamber
ICD	Intermolecular Coulombic Decay
IMFP	Inelastic Mean Free Path
KE	Kinetic Energy
LUMO	Lowest Unoccupied Molecular Orbital
MCP	Micro-Channel Plate
MD	Molecular Dynamics
ML	Monolayer
NP	Nanoparticle
OER	O_2 Evolution Reaction
$P^{C}EY$	Partial Electron Yield spectrum integrated over the relaxation channels involving solely core orbitals
PES	Photoelectron Spectroscopy

PEC	Photoelectrochemical Cells
PEEK	Poly-Ether Ether Ketone
PEY-XA	Partial Electron Yield X-ray Absorption
PFY-XA	Partial Fluorescence Yield X-ray Absorption
$P^{V}EY$	Partial Electron Yield spectrum integrated over the relaxation channels involving solely valence orbitals
PZC	Point of Zero Charge
RIXS	Resonant Inelastic X-ray Scattering
RPES	Resonant Photoemission Spectrum
SEM	Scanning Electron Microscopy
TEY	Total Electron Yield
TMO	Transition Metal Oxide
vdW	van der Waals
VLS	Variable Line Spacing
XA	X-Ray Absorption
XANES	X-Ray Absorption Near-Edge Structure
XMCD	X-Ray Magnetic Circular Dichroism
XRD	X-Ray Diffraction

Contents

Chapter 1
Introduction and Motivation

The energy crisis, global warming, and environmental pollution are the most crucial problems facing humankind.[1] The fact that our societies are based on fossil fuel is feeding those problems. Also, the continuous increase in human population, the expansion of the global economy and fast development of industrial society have required a commensurate increase in energy sources to fulfill the needs of the rapidly changing world civilization. Here, fossil fuels represent the consumable energy source most heavily relied on.[2] They cannot continue to play this role for long, as it fails to fulfill the increasingly sophisticated needs of our worldwide civilization. Fossil fuels are essentially the product of a natural hyper-slow carbon cycle[3] that took millions of years. This makes it quantitatively limited, and it will be consumed at a certain point in the future. On the other side, fossil fuel consumption is accompanied by the emission of so-called "greenhouse gases" such as carbon dioxide, sulfur and nitrogen oxides. These greenhouse gases are the main causes of environmental pollution, climate change and global warming.[4]

Hence, an alternative energy source is urgently needed. However, it is also important to maintain the beneficial factors of using fossil fuels such as their high energy density, ease of transportation and convenience in energy release.[5] This high energy density actually comes from the sunlight which implies that another conversion method of this energy into chemical potential would be the best candidate for clean and renewable energy in the future. Sunlight is an extremely high-energy source: Half an hour of sunshine on Earth provides sufficient energy to cover all user needs worldwide for a full year.[6-7] Accordingly, research is dedicated to developing effective strategies for conversion and harvesting the solar energy as well as storing it via solar cells, photovoltaic cells and H_2 fuel generation.[5] The latter is the technology most-expected to replace fossil fuel due to its unique advantages i.e. (i) its high energy density of 120-142 kJ/kg, (ii) the fact that it is extracted by splitting liquid water molecules (the most abundant molecule on Earth) and (iii) its combustion product $(H_2O)_{g,}$ an environment-friendly gas.

The natural biological water splitting process is photosynthesis where the solar energy is absorbed by plants and converted to split the water molecules, producing H_2 and so-called biological O_2 molecules. This natural photosynthesis has inspired scientists for long time. In 1971 Fujishima and Honda[8] showed that water can decompose at the titanium dioxide surface under applied voltage (photoelectrochemical (PEC) conditions), which has widely become known as artificial photosynthesis[8]:

$2H^+ + 2e^- \rightarrow H_2(g)$	(HER: H_2 evolution reaction)	Eq. (1.1)
$2H_2O \rightarrow O_2 + 4H^+ + 4e^-$	(OER: O_2 evolution reaction)	Eq. (1.2)
Overall: $2H_2O \rightarrow O_2 + 2H_2$	(light condition) $\Delta E^0 = -1.23\ V$	Eq. (1.3)

This equation is thermodynamically unfavorable, and an amount of 1.23 eV energy is needed for water splitting to occur. This is where solar energy comes into play in photoelectrochemical cells as an energy conversion tool.

A photoelectrochemical cell (PEC) is composed of two electrodes (cathode and photoanode) and an electrolyte solution, as shown in Figure 1-1 (A). The photoanode is a semi-conductor which is also called working electrode. It is responsible for absorbing solar energy and converting it into electron-hole pairs. Electrons are transmitted into the conduction band while positive holes are in the valence band, separated by the energy gap (E_g) (see Figure 1-1 (B)). These electrons and holes are spatially separated by the band bending at semiconductor surfaces. Electrons are transported into the metal counter electrode (cathode) via an external connector. These electrons reduce H^+ to H_2 at the counter electrode surface while the holes created in the anode valence band move to the surface and oxidize water to O_2.[5, 9-10] The energy diagram of the process is shown in Figure 1-1 (B).

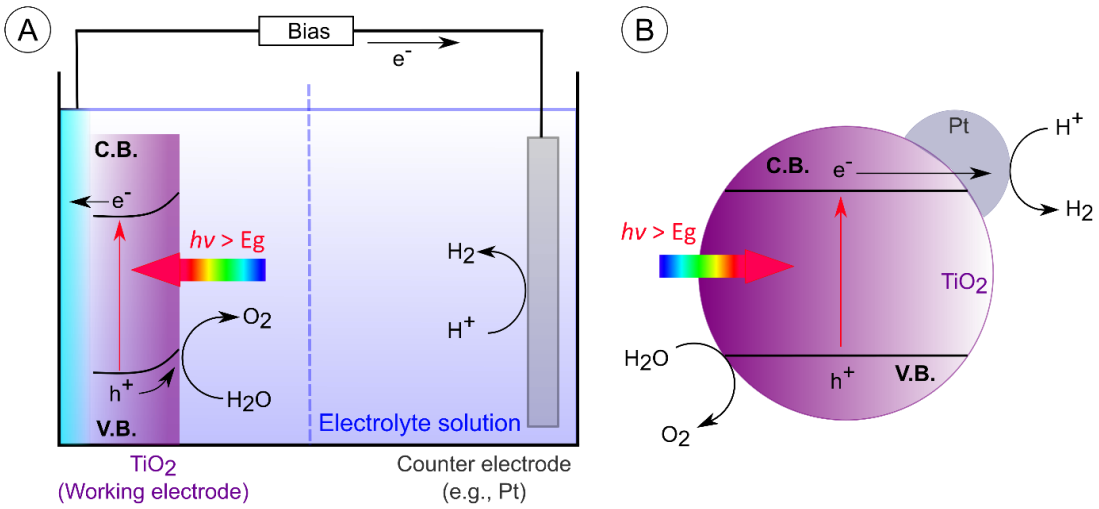

Figure 1- 1

(A) Illustration of a photoelectrochemical cell that consists of a semiconducting photoanode and a metal cathode. (B) Corresponding energy diagram. This Figure is adopted and modified from reference [9].

There are continuous efforts towards enhancing the water-splitting efficiency, finding novel catalyzer and increasing the reaction kinetics on the surfaces of both the photoanode and the cathode to match the rates of charge generation and separation.[5] However, some considerations should be taken into account when choosing semiconductor materials as photoanode for an efficient solar water splitting:

(i) **Potential requirement:** From the water splitting energetics, equation (1.3), it follows that the band gap of the photoanode material should exceed 1.23 eV. Nonetheless, other energy losses in the PEC are happening during operation (e.g. the overpotential loss at the electrodes and the ionic loss in the electrolyte), and they should be considered. An actual cell requires a potential difference between the two halves of the reactions of at least 1.6 V.[5]

(ii) **Band structure:** The energy positions of band-edges of the conduction and valence band (and not only the bandgap, i.e. the energy difference between them) need to be carefully taken into consideration as they affect the reduction and oxidation reactions of water. Also, these band-edge positions are affected by the adsorbed aqueous molecular species (OH^-, H^+, H_2O) on the electrode surface[11]. Such information on the band-edge positions as well as the nature of the water adsorption (associative/ dissociative) on the surface, are most directly revealed from photoelectron (PE) spectroscopic measurements for which ultra-high vacuum is needed. Meanwhile, it is challenging to perform PE measurements from solid surfaces in contact with an aqueous environment (due to the vapor pressure equilibrium of the liquid water in vacuum, detailed in Section 3.3). I address this lack of electronic structure information of the liquid—solid interface which is the central aspect of this study. Also, I review the pervious technical efforts to overcome this apparent incongruity of measuring PE (in ultra-high vacuum) from solid surface in contact with liquid water. Finally, I explain my approach to enhance our capability to collect electrons emitted from solid surfaces covered by bulk aqueous solution.

(iii) **High crystallization and surface area:** Both the oxidation and reduction reactions happen at the electrode surfaces. For efficiency enhancement of these reactions, a highly crystalline surface area is obviously favorable as it provides better charge transport and higher surface activities for both the OER and the HER.[5] Significant efforts have been dedicated to design and study the efficiency of PEC equipped with nanoparticle (NP) coated electrodes[12-13] as their structures offer a larger surface area.

(iv) **Stability:** The electrode materials are desired to have long lifetimes as well as high stability in both acidic and basic solutions to avoid degradation[14] which would reduce the efficiency of the solar water splitting.

(v) **Low-cost material**: For an economically competitive technology, the cost is a big issue. The selected material should be highly abundant in the Earth's crust and its exploitation should be relatively cheap.

Within the context of these requirements, the transition-metal oxides (TMO) are the very fitting candidates. Surprisingly, our knowledge about their electronic structure interactions with liquid water is relatively poor. Only with a molecular-level understanding of the water adsorption nature (molecularly or dissociatively) on the different transition metal oxide surfaces, it would be possible to develop efficient and competitive photoelectrochemical cells for water splitting. This is the main motivation of this thesis, which addresses two main aspects: (i) Demonstrate the applicability of PES for measuring the electronic structure of the transition metal oxide in contact with bulk water (mimicking the PEC conditions). (ii) Characterize the nature of water interaction with the hematite iron oxide (Fe_2O_3) and with the anatase titanium dioxide (TiO_2); The choice of these two TMOs is elaborated next.

The following brief overview of the technical methodologies that have been applied, including the one I used in this study, is meant to place my work into the context of existing studies:

(i) There is a large number of single-crystal solid surface studies in ultra-high vacuum condition. The solid surfaces are exposed to liquid water for hours/days before transferring them into the ultra-high vacuum chamber where the measurements take place.[15-17] Scientists using this ex-situ methodology were relying on the solid surface being able to "remember" having been exposed to water and ultra-fines traces of the aqueous adsorbed species remaining bonded on the surface. Although useful, this method does not represent solids in contact with the liquid water.

(ii) The interactions of well-defined TMO surfaces with few water molecules were studied under ultra-high vacuum condition. In this method, the H_2O molecules are introduced into the vacuum chamber as gas through a leak valve.[18] This method enabled formation of water "bilayer" at the TMO surfaces.[19-21] Although the bilayer gives an indication of the water adsorption nature, it is still dealing with single to few adsorbed water molecules.

(iii) The so-called "fast-frozen technique" examines TMO—water interaction by freezing water layers on top of a single crystal surface.[22-26] It is very likely that freezing the liquid is reflected in the measured photoelectron spectra, especially that aqueous ion dynamics and reactivities are reduced.

(iv) With the continuous development of the photoelectron spectroscopic technique, the so-called ambient pressure measurements became possible. This refers to photoelectrons measured from solid surfaces covered by few water layers stabilized by relative

humidity.[27-29] These are yet model systems, barely representing the solid surface in contact with bulk water.

(v) In addition, liquid cells are used to collect photoelectron signals across an ultra-thin graphene membrane (the cell window).[30-31] Both the membrane interaction with the water molecules and its effect of strongly attenuating the photoelectron signal due to the small inelastic mean free path of the emitted electron (as discussed in Section 2.4) need to be carefully taken into account.

(vi) The liquid-microjet technique which I use in my studies, allows the introduction of a laminar water surface of (5-50) μm diameter into the measurement chamber, while maintaining the vacuum conditions for the detection of photoelectrons from the liquid (described in detail in Section 3.3). This enables the detection of the electronic structure of liquid water by coupling the liquid jet technique to photoelectron spectroscopy using a suitable light source.[32-33] In this study, I use synchrotron-radiation-based soft X-ray electron spectroscopy from a liquid microjet to characterize the electronic structure of the transition metal oxides—water interface for nanoparticles (NP) dispersed in aqueous solutions. These nanoparticles represent the solid surface interacting with bulk liquid water. This approach not only allows the study of the TMO—water interfaces, it also enables the desirable variation of pH. The results are presented in this thesis (Chapters 5, 6 and 7) for two selected transition metal oxides. It is important to mention that the stability of the TMO nanoparticles in liquid water is not trivial. NPs tend to reduce their surface energy by aggregation which leads to precipitation and sedimentation. Only by adding stabilizer ions into the solution, these ions would be adsorbed at the NPs surface. This charges the NP surfaces, and NPs repel each other and can thus be stabilized in solutions without aggregation. On the other side the stabilizer ions would prevent water molecules from interacting with the NP surface. To overcome this problem specific procedures have been applied for each sample in order to reduce the number of stabilizer ions relative to the NP available surface sites. These free NP surface sites can interact with the surrounding water molecules. Details of the procedure adopted for each sample are presented in the Section "Methods and Materials" in the corresponding Chapters 5, 6 and 7.

In this thesis, hematite iron oxide (α-Fe_2O_3) and anatase titanium dioxide (TiO_2) interacting with liquid water (in aqueous solution) are studied with a main focus on characterizing the associative/dissociative nature of water adsorption. The choice of these systems is based on the aforementioned requirements for selecting water splitting material. Hematite iron oxide has a band gap of 2.2 eV while the band gap of anatase TiO_2 is 3.2 eV. Accordingly, both materials absorb a significant amount of the solar spectrum. Furthermore both are highly abundant in the Earth's crust

and are easily extracted which translates in low costs of the PEC. In both cases the efficiency for solar water splitting compared to other transition metal oxides is relatively high.[5]

The liquid-jet electronic structure measurements of the (hematite Fe_2O_3 , anatase TiO_2) nanoparticle—water interface are reported in Chapters 5 and 6 respectively. For the α-Fe_2O_3 nanoparticle, water is found to be dissociatively adsorbed at the surface in acidic solutions, while for the TiO_2 nanoparticle, water is molecularly adsorbed in the acidic chemical environment and it interacts dissociatively with the surface at slightly basic pH. In latter case, a complementary study using photon-emission spectroscopy (here we detect emitted X-ray photons) is performed and reported in Chapter 7. Due to the large penetration depth of X-rays, this method is highly bulk sensitive and assists in quantifying the water dissociation on the TiO_2 surface. The results are combined with those of the photoelectron to determine the composition of the Stern layer and of the diffuse layer around the TiO_2 nanoparticle in aqueous solution. In addition, I estimate the Debye length for this specific sample.

1.1 Thesis Outline

This thesis consists of eight chapters:

Chapter 1: Introduction and Motivation: The problems of the energy crisis, environmental pollution and global warming are caused by the reliance on fossil fuels as the essential energy sources. We need to switch from this fuel to a clean and renewable energy source based on sunlight. The promises and challenges of converting solar energy into H_2 fuel via photoelectrochemical cells are explained. One of those challenges is the lack of knowledge about the transition metal oxide—water interface, which is the main motivation of this study. Finally, I elaborate on the specific selection of the hematite iron oxide and the anatase titanium dioxide, the materials examined in this thesis.

Chapter 2: X-ray Spectroscopy: In this chapter, I focus on describing the basic theories of photoelectron spectroscopy which is the main technique used in this study. I differentiate between the initiated X-ray photoionization and the photoexcitation processes and I discuss the different non-radiative relaxation processes via Auger-electron emission. After that, I comment on the inelastic mean free path of the electrons in aqueous solution and its effect on the (limited) probing depth of the photoelectron spectroscopy measurements. I also briefly introduce the photon-emission (photon-out) spectroscopy by giving an overview on the different radiative relaxation processes upon photoionization/photoexcitation by X-ray radiation.

Chapter 3: Experimental Techniques: This section focuses on the technical description of the experimental techniques used in this thesis. I start by describing the SOL^3 PES setup which is used to collect the photoemission spectra shown in this study. Complementary photon-emission measurements are conducted using the LiXEdrom experimental setup which is briefly explained as well. Also, the liquid micro-jet technique, by which the liquid samples are introduced into the vacuum chamber of the SOL^3 PES and the LiXEdrom, is discussed. Lastly, the benefit of using a tunable X-ray source from a synchrotron radiation facility, like BESSY II, is elaborated. I specifically highlight the technical parameters of the soft X-ray beam provided by the U49-2/PGM-1 beamline that was used in this study.

Chapter 4: Photoemission and Photon-emission Spectroscopies from Liquid Water: This chapter presents the photoemission and photon-emission measurements of liquid water. These respective spectra serve as references for discussing the results presented in the subsequent chapters.

N.B.: The term "photoemission" is used here to cover all the electron-out processes by direct photoelectron emission as well as the secondary electron emission (i.e.: electron emission by autoionization, such as Auger decay, and secondary electrons) resulting from electronic relaxation. It should not be confused with the term "photon-emission", which is a photon-out process.

Chapter 5: Electronic Structure of the Hematite Fe_2O_3 Nanoparticle—Aqueous Solution Interface: This chapter starts with an introduction reviewing the importance of hematite Fe_2O_3 as a photocatalytic material, the challenges of investigating the Fe_2O_3 — water interfacial electronic structure, the related reported literature and our approach to measuring it. In the Methods and Materials section, the specific experimental parameters used to collect the results shown are described and a detailed description of the investigated samples is provided. The Results and Discussion section is divided into four parts: (i) valence photoelectron spectra, (ii) O 1s resonant photoemission and partial-electron-yield XA spectra, (iii) O 1s core-level photoelectron spectra, and (iv) Fe 2p photoemission and PEY-XA spectra. In each part, the corresponding results are presented and discussed. That is followed by the Conclusion section. The chapter closes with an Appendix section.

Chapter 6: Electronic Structure of the Anatase TiO_2 Nanoparticle—Aqueous Solution Interface: Analogous to the pervious chapter, the introduction reviews the titanium dioxide's promising role as photocatalytic material, the debate about the nature of water (molecular/dissociative) adsorption on this surface, the difficulties and attempts to probe

the TiO_2—water interface by photoelectron spectroscopy, and our approach to measuring this interfacial electronic structure using TiO_2 nanoparticle colloidal aqueous solutions. Also, the specific experimental parameters used, and a detailed description of the investigated samples are mentioned in the Methods and Materials section. This is followed by the results and discussion of the (i) Ti L-edge PEY-XA spectra, (ii) O 1s off-resonant photoemission spectra, and (iii) O K-edge photoemission and PEY-XA spectra. This chapter ends with the Conclusion section and an Appendix.

Chapter 7: X-ray Spectroscopic Characterization of the Electric Double Layer (EDL) around TiO_2 Nanoparticles Stabilized in NH_4OH Aqueous Solution: This chapter is an extension of the TiO_2 –water interface study. Here I focus only on the dissociative water interaction, described in Chapter 6, occurring for the above neutral pH ~ 7.8. The introduction section motivates the importance of enhancing the water dissociation efficiency by separating the produced (OH^-) and (H^+) species from each other through diffusion into the surrounding aqueous environment. This section also explains the possible parities of the composed electric double layer around a charged surface (TiO_2 nanoparticle) in aqueous solution and its effect on the aqueous ion distribution. The Methods and Materials section states the experimental parameters used during the photoemission and the photon-emission measurements using the SOL^3PES and the LiXedrom, respectively, and provides a detailed description of the investigated samples. In the Results and Discussion section, the measurements are presented and discussed, divided into three parts: (i) N 1s Off-resonant Photoemission and PEY-XA Spectra, (ii) O 1s Off-resonant Photoemission Spectra, and (iii) O K-edge PFY-XA Spectra. This chapter ends with a Conclusion Section and an Appendix Section.

Chapter 8: Summary and Outlook: After summarizing the findings of this study, I propose a means of harvesting the H^+ generated from the water dissociative interaction with the TiO_2 surface as a way to future applications. Then, I present selected completed side-projects that I participated in during my PhD which are relevant to this study. Next, I present selected results from my currently conducted studies of similar NP(aq) systems (magnetite iron oxide—aqueous interface and cerium dioxide—aqueous interface) based on the findings reported so far. Lastly, I give an outlook on future studies of the NP(aq) systems using tender X-rays (1.5-12 KeV).

Chapter 2
X-ray Spectroscopy

In this chapter, I explain the main theoretical concepts that form the basis for the experimental measurements presented in this thesis. Starting from the soft X-ray interaction with matter, I differentiate between the photoionization and the photoexcitation of the sample upon interacting with X-ray photons. I also discuss the different radiative and non-radiative relaxation processes. Firstly, I focus on explaining the non-radiative relaxation processes via Auger-electron emission (the second order photoemission), distinguishing between the normal, participator and spectator Auger decay channels. Thereafter, I describe electron scattering and its effect on the photoemission spectroscopy probing depth. Lastly, I briefly comment on the radiative relaxation processes in photoionized and photoexcited matter.

2.1 X-ray Radiation

X-ray radiation, also known as Röntgen radiation, is a part of the electromagnetic spectrum that was discovered in 1895 by Conrad Röntgen.[34] It has a wavelength range of *Å*ngstroms up to nanometers, shorter than UV photons and longer than gamma rays. Because of their short wavelengths X-ray beams are ideally suited for the investigation of the structure of matter. The photon energy is described by the Planck-Einstein relation.

$$E = h\nu = \frac{hc}{\lambda_{ph}} \qquad \text{Eq. (2.1)}$$

where E is the photon energy, h is Planck's constant, ν is the frequency of the X-ray wave, λ_{ph} is the wavelength and c is the speed of light. X-ray photons can interact with matter either by absorption, or scattering. I focus in the following section only on the absorption process, in which an X-ray photon is absorbed and an electron is ejected from the atom or molecule of the material. In order to ionize the molecule this X-ray photon must have an energy exceeding the binding energy of the electron in its molecular orbital. The whole process is called photoelectric absorption or photoionization.

2.2 Photoionization

Photoionization is again a photon-in – electron-out process, where a sample is irradiated with X-ray photons ($h\nu$), and electrons are ejected from the system. By measuring the kinetic energy (E_{Kin}) of the emitted electrons, one obtains the binding energy (E_B) of the initial electronic state from the following equation:

$$E_B = E_{Kin} - h\nu \qquad \text{Eq.(2.2)}$$

In this presentation, E_B is relative to the vacuum level which is defined as the reference zero. E_B and E_{Kin} are represented in Figure 2-1. Low-energy photons are capable to eject electrons from the valence levels having binding energies below 40 eV. In contrast, a high energy X-ray photon can probe both, valence and core electronic orbitals.

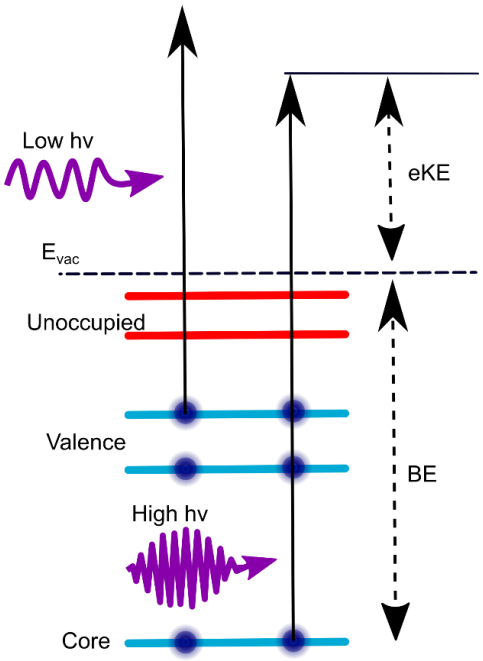

Figure 2- 1

Schematic energy diagram showing the photoionization process of an atom. The occupied energy levels are shown in light blue color, the unoccupied energy levels are shown in red, and the electrons are represented by dark blue balls. The binding energy and the kinetic energy are presented on the right-hand side. A low energy photon can eject only valence electrons while a high energy X-ray photon can ionize both core or valence electrons. This Figure is adapted and modified from reference [35].

The photoionization process of a condensed material is typically described via a three-step model. Here, the X-ray photon absorption and electron excitation into a final state inside the matter are considered the first step. Then, in the second step, this electron is travelling through the sample. Finally, it escapes from the surface into vacuum (third step). A more realistic approach is the one-step model where the excited electron travels into a damped energy state. This damping state is taking into account the limited inelastic mean free path of the electron.[36] The latter is described in detail in Section 2.4.

For the theoretical interpretation of the photoelectron process several factors must be considered: (1) the interaction of the incident photon with the emitted photoelectron, (2) the interaction of the ejected photoelectron with the remaining electrons in the system and how they are reorganized due to the creation of an electron vacancy, and (3) the continuous nuclear motion effect[37-38]. However, such detailed treatment of the photoionization process is not subject of this thesis and it is sufficient to explain the measurements presented in Chapters (5, 6 and 7) based on the following assumptions:

- **The independent particle model:** The photoelectron interaction with its surrounding electrons in the system is completely neglected. The photoelectron is assumed to travel near the electrons and nuclei in an electrostatic potential.[39] This is accurate enough in a weakly correlated system where no electron-electron interaction occurs, as in aqueous solutions.

- **The sudden approximation:** This approximation assumes that the photoelectron is fast enough to leave the system without being affected by the valence shell reorganization. This is true only for high kinetic-energy electrons which can escape within the core-hole lifetime (few femtosecond time scale). This assumption is valid for photoelectrons with high kinetic energies of hundreds of eV, i.e., for large photon energies[40] used in this study.

- **The Born-Oppenheimer approximation:** Based on the Born-Oppenheimer approach, atomic nuclei motion can be separated from the electron dynamics. As a direct photoelectron emission process happens within attoseconds,[41] which is at least two orders of magnitude faster than the atomic movement,[42] the whole process is happening in the ground-state geometry.

Based on those assumptions, the electron—electron interaction and the effects of nuclear motion on the photoionization process are completely neglected. Only the photon absorption and the emission of one electron should be considered in the Hamiltonian (H_0) of the process. We can therefore describe the perturbated Hamiltonian (H') as follows:

$$H' = \frac{e}{mc}\,\vec{A}\,.\,\vec{p} \qquad \text{Eq.(2.3)}$$

where $\vec{A}$ is the vector potential of the photon, $\vec{p}$ is the electron movement momentum operator ($\vec{p} = \text{i}\hbar\nabla$), c is the speed of light, *e* and *m* are the charge and mass of the electron, respectively.[43-44] Another expression of Eq.(2.3) would be:

$$H' = \frac{\text{i}\hbar e}{mc}\,\vec{A}\,.\,\nabla \qquad \text{Eq.(2.4)}$$

The intensity of the photoemission signal collected upon the photoionization process is directly dependent on the transition probability of one electron in an (N) electrons system from an initial state (i) with wave function (Ψ_i) to a final state (f) with wavefunction (Ψ_f). This transition probability is given by Fermi's Golden Rule:

$$W_t = \frac{2\pi}{\hbar} \left|\langle \Psi_f \left| H' \right| \Psi_i \rangle\right|^2 . \partial(E_f - E_i - \hbar\omega) \qquad \text{Eq.(2.5)}$$

$\hbar$ is the reduced Planck constant and $\hbar\omega$ is the photon energy.[43-44]

Equations 2.3 – 2.5 are the essential basics of the photoionization process and they are sufficient to interpret the direct valence band and core level photoelectron spectra presented in this thesis.

2.3 Relaxation Processes via Electron Emission

In case of an ionization process as well as in an excitation process (see Section 2.3.1), the emission/excitation of a core-level electron is accompanied by the creation of a hole in the initial energy state. This electronically highly excited system will relax back into its electronic ground state, either via radiative or non-radiative decay channels. In the Section 2.3.1, I describe the non-radiative relaxation process, while the radiative relaxation channels are briefly introduced in Section 2.5. I distinguish here between the normal Auger electron emission (following an ionization process) and the resonant Auger electron emission (following an excitation process). I focus on the so-called resonance photoelectron spectroscopy and explain the resulting photoemission relaxation processes via participator and spectator Auger decays. There are other so-called non-local autoionization processes, like Intermolecular Coulombic Decay (ICD) or Electron Transfer Mediated Decay (ETMD), where neighboring atoms are involved (see Figure 2-2, F and G). However, these processes are not relevant to this study.

Figure 2-2 illustrates the different relaxation channels. In (A), the photoionization process for an electron from the core level in a single molecule or atom is sketched. The lowest unoccupied molecular orbital (LUMO) is located below the vacuum level and energetically above the highest occupied molecular orbital (HOMO). In this photoionization process, the X-ray photon is absorbed by a core/inner-valence level electron. The electron is then ejected above the vacuum level into the continuum, and a normal Auger-electron emission would be subsequently emitted, as will be explained in the next Section 2.3.1.

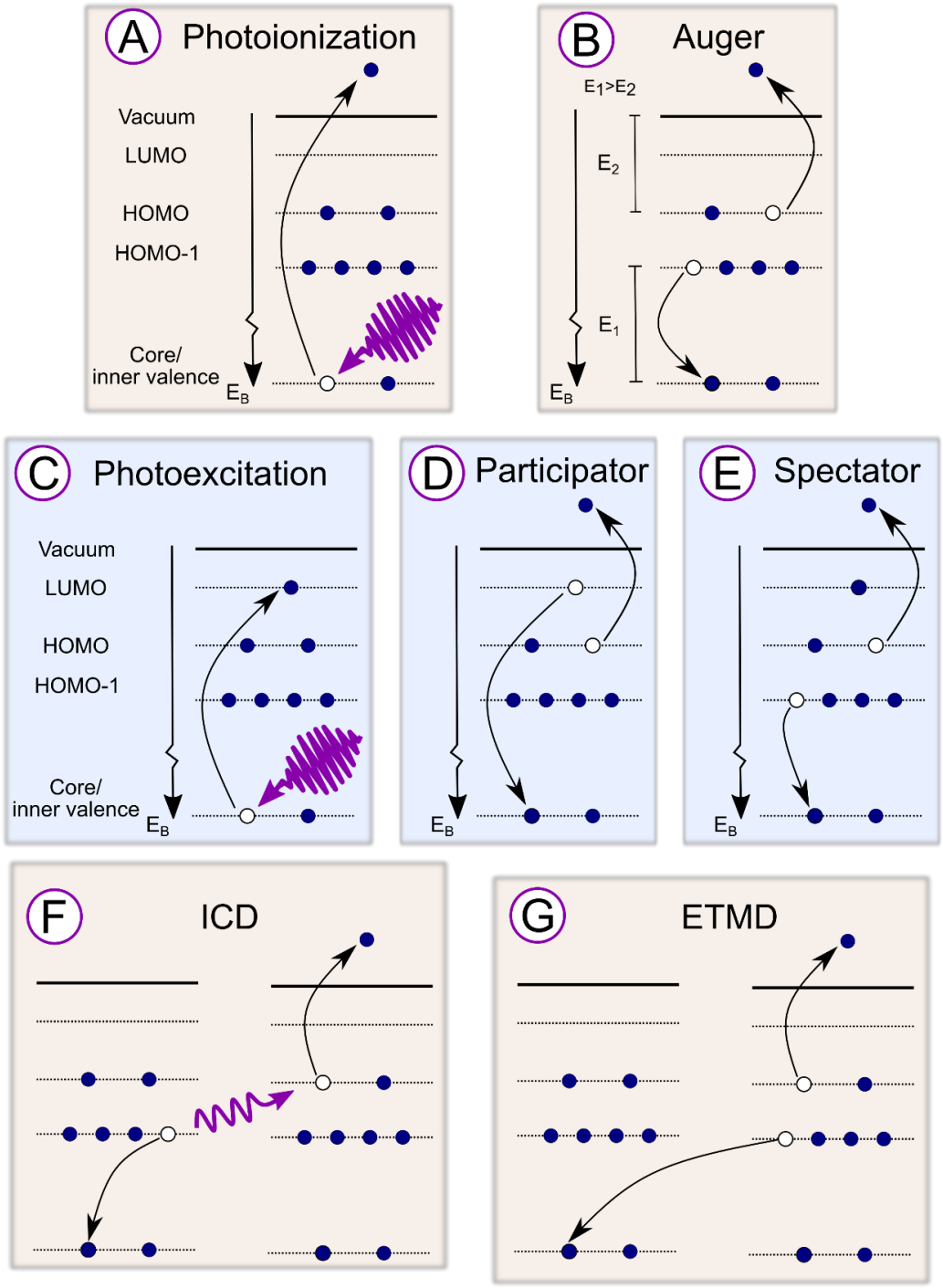

Figure 2- 2

Schematic representation of the photoionization, the photoexcitation and the non-radiative relaxation processes. The photoionization of a single atom (presented in A) could relax via Auger process (B), however an photoionized atom in a medium could relax via intermolecular coulombic decay (F) or electron transfer mediated decay (G) channels. On the other side, a photoexcited atom like (C), would relax via participator (D) or spectator (E) Auger decay. Detailed explanation of these processes is described in the text.

2.3.1 Auger-Electron Spectroscopy and Resonant Photoelectron Spectroscopy

Auger spectroscopy is named after Pierre Auger, who explained this second order photoelectron emission in 1926.[45] In Figure 2-2 (B), a normal Auger electron emission process is sketched. After an electron from a core level is ejected from the system, an electron from a higher energy level refills the core hole, and transfers its energy to a third electron, which is ejected to the continuum, leaving the atom behind with two holes. The kinetic energy of the emitted Auger electron is determined by the energy difference between the electronic states involved in the process and is completely independent from the excitation photon energy. i.e. an Auger emission line is very element specific.

The whole Auger process is mediated by the Coulomb interaction between the primary core hole and the valence shell electrons[46-47] that makes it the most probably decay channel for light atoms, where the Coulomb interaction is larger than the electrostatic potential of the atomic core.[48] For a heavy element, an X-ray emission relaxation process is more dominating as the electrostatic potential exceeds the hole-electron Coulomb interaction.[48]

Likewise, in the photoionization process, the intensity of an Auger line is depending on the Auger transition probability and it is given by equation 2.6:

$$W_A = \frac{2\pi}{\hbar} \left| \iint X_f^*(\boldsymbol{r_1})\, \Psi_f^*(\boldsymbol{r_2})\, \frac{e^2}{|r_1 - r_2|}\, X_i(\boldsymbol{r_1})\, \Psi_i(\boldsymbol{r_2})\, d\boldsymbol{r_1}\, d\boldsymbol{r_2} \right|^2 \qquad \text{Eq.(2.6)}$$

The two electrons involved in the Auger process have initial (i) and final (f) energy state wavefunctions $X_i(\boldsymbol{r_1})$,$\Psi_i(\boldsymbol{r_2})$, $X_f^*(\boldsymbol{r_1})$ and $\Psi_f^*(\boldsymbol{r_2})$. Please note that $X_f^*(\boldsymbol{r_1})$ is the formal hole energy state while $\Psi_f^*(\boldsymbol{r_2})$ is a continuum energy state.[49]

The creation of a core hole is not necessarily the result of an electron ejection, it also could be generated due to an excitation of core electron into a valence orbital, which is either unoccupied or partially occupied as shown in Figure 2-2(C). This case is called "resonant excitation", here the excitation photon energy is matching the energy difference between the core level and a valence level within the atom. At this resonance photon energy, the atom becomes excited, but not ionized and will relax via radiative or non-radiative processes. The latter is of greater interest for interpreting the results in this study and it has two types: participator and spectator Auger processes. For both cases, two holes are created in the atom and one electron is emitted. In the participator process, (Figure 2-2 (D)) the promoted electron relaxes back to its initial energy state (participate in the relaxation process) while transferring its energy to a second electron, which escapes the system. For the spectator process shown in Figure 2-2 (E), the promoted electron only spectates the relaxation of a second electron, transferring its energy to a third electron, which is leaving the system. The spectator and the participator Auger electrons are distinct from each other by their kinetic energy as shown experimentally in Section (4.2)

for liquid water. Note that the final states of participator resonant Auger-electrons are indistinguishable from that of photoionization emission i.e., coherent superposition of outgoing electron waves of the participator Auger emission and the photoionization emission; In the light of this, the process can also be called a resonantly enhanced photoionization channel. The resonant photoemission spectroscopy has proven to be a powerful tool for probing the ultrafast charge delocalization[50] and in this thesis, it is successful in highly enhancing the signal from the nanoparticle surface fully immersed in liquid water and from the solid–liquid interface species, as will be presented in the result chapters 4 and 5.

There are also other important relaxation channels like the intermolecular Coulombic decay (ICD) and the electron transfer medicated decay (ETMD),[51] however, those processes are not studied in this thesis. As the photoionized atom is not isolated, neighboring molecules can contribute in the relaxation processes. For the ICD process shown in Figure 2-2 (F), after the photoionization of the molecule, a second electron fills the core hole and its energy is transferred to a neighboring molecule, followed by an electron ejection. In the final state every molecular site has one hole. In the ETMD process presented in Figure 2-2 (G), an electron from a neighboring molecule fills the core hole. A second electron is then emitted with the respective excess energy. In this process, both holes are on the neighboring molecular site.

2.4 Electron Scattering

As described throughout in Chapter 2, soft X-ray photoemission is a very powerful technique for material characterization, as it is highly element-specific with tunable surface sensitivity. In this section, I explain how electron scattering affects the photoemission spectrum, and what information we can obtain from solid surfaces covered by many layers of water as in the case of NPs dispersed in aqueous solution.

A soft X-ray beam (e.g., from a synchrotron radiation source like BESSY II) has an attenuation length of 1-10 μm when penetrating into the sample.[52-53] However, the emitted electrons can only escape from the most upper few nm below the sample surface. In general, electrons travelling in a medium have a rather short inelastic mean free path (IMFP), which is highly dependent on their kinetic energies. The IMFP is defined as the distance between two inelastic scattering events. The experimentally accessible parameter is the electron effective attenuation length (EAL), which is the distance after which the number of electrons with a certain kinetic energy drops to 1/e due to (in)elastic scattering.[54-55] This EAL quantity is representing a lower bound for the IMFP.[35] IMFP and EAL are related by the following equation (when ignoring the emission angle dependence):

$$\mathrm{EAL} = \left(1 - 0.028\sqrt{z}\right)[0.501 + 0.068 \ln E_{Kin}]\ \mathrm{IMFP}, \qquad \text{Eq.(2.7)}$$

Where Z is the atomic number and E_{Kin} is the kinetic energy of the emitted electron in eV.[56] These quantities are almost identical in the case of weak elastic scattering. However, it is

experimentally difficult to distinguish between the elastic and inelastic scattering contributions in the total photoelectron signal. Theoretically, the EAL was reported 30% lower than the IMFP using statistical path length simulation models [54, 56]. For this study as well as for many other experiments, determination of the EAL is fully sufficient.[55]

The left-hand side of Figure 2-3, schematically illustrates how electrons emitted in bulk water and near the water–vacuum interface are affected by inelastic and elastic scattering for two different kinetic energy regimes. Low-kinetic energy electrons (shown in green color) can only be detected if they are emitted close to the liquid–vacuum boundary, the electrons generated in the bulk will scatter away and will likely not reach the photoelectron detector. In red color, the high-kinetic energy electrons can escape from the interface as well as from the bulk. The right-hand side of Figure 2-3 illustrates the steeper exponential decrease of the low-kinetic energy electrons (green curve) compared to the high-kinetic energy electrons (red curve) as a function of the liquid water depth. As a result, the ratio of the surface vs the bulk contribution is for low kinetic energies larger than for high kinetic energies.

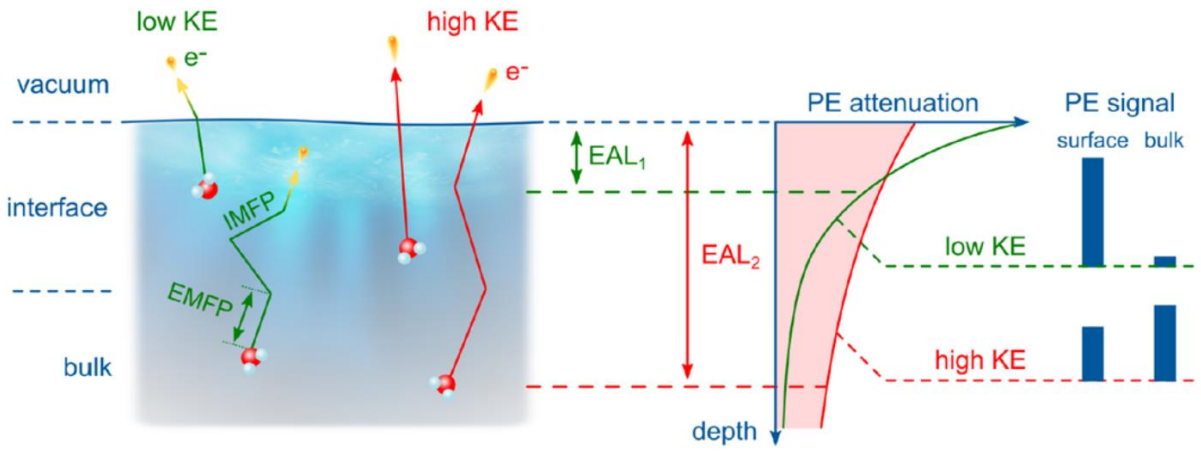

Figure 2- 3

Schematic illustration of the inelastic mean free path (IMFP) and the electron effective attenuation length (EAL) of emitted photoelectrons in liquid water. Electrons are deflected by elastic scattering and lose their kinetic energy via inelastic collisions. The PE signal gets exponentially attenuated with depth as presented by the green and red curves for low and high kinetic energy electrons, respectively. The area under the curves is shown on the right-hand side as function of surface and bulk PE signal. This Figure is taken from reference[57].

Several efforts have been made to spectroscopically estimate IMFP. Even though, it was expected to be dependent on the sample nature, Seah and Dench in 1979 reported a "universal curve" based on an extensive database measured for selected metals[56, 58] (qualitatively similar to the grey curve in Figure 2-4). However, the photoemission probing depth for liquid water is still unresolved. Figure 2-4 is presenting different results for EAL and IMFP as a function of electron kinetic energy for liquid water. The blue and green EAL curves used experimental measurement of the O 1s core orbital photoelectron signal intensities of pure water, which were derived independently, all by liquid PES, to estimate the probing depth for photoemission[55, 59-60]. The grey IMFP1 curve was obtained by constructing a Bethe surface from liquid water inelastic X-ray scattering data (see reference[60] for a more detailed description), which reproduced the shape of the universal curve for solid samples. The red dashed IMFP curve is estimated by comparing PE measurements from aqueous electrolyte and molecular dynamics simulations of the depth profile of the solute ions.[59] Despite this uncertainty of the IMFP, it is sufficient for the present study to have a rough estimation of photoemission probing depth in liquid water.

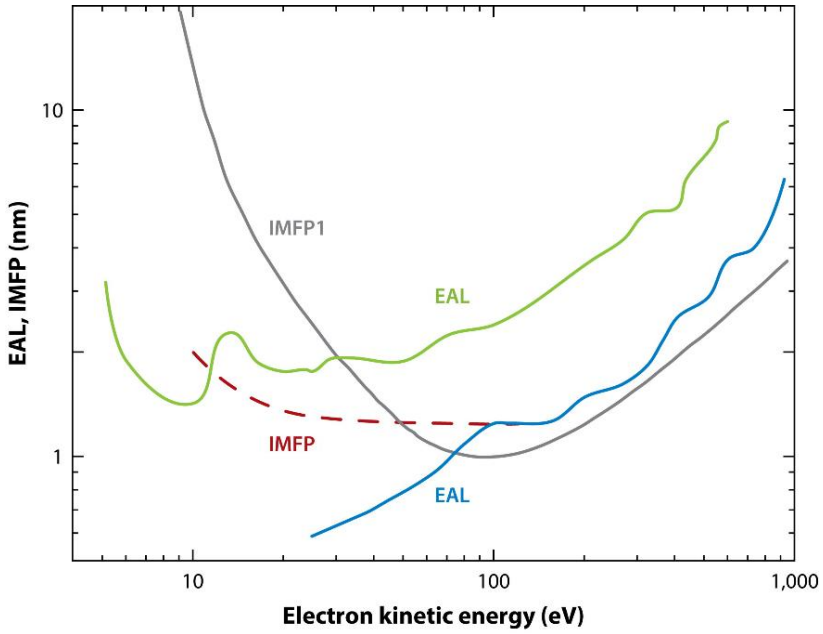

Figure 2- 4

Experimentally derived effective attenuation length (EAL) and simulated inelastic mean free path (IMFP) curves for liquid water. Details are described in the main text. This Figure is taken from reference[35].

In this thesis, the main interest is in the (resonant) Auger decay channels when sweeping through the oxygen K-edge, which results in roughly 500 eV kinetic energy electrons. This translates into an inelastic mean free path of the electrons on the order of a few nanometer (3-5 nm) depending on which reference curve in Figure 2-4 is considered. Such small IMFPs make it difficult to get reasonable signal from nanoparticles fully immersed in liquid water: electrons now need to escape through the solution-vacuum interface and through or from the NPs-solution interface.

However, for small enough size of the NPs (< 30 nm diameter), a relatively high density profile of nanoparticles at the water—vapor boundary can be established, enabling the detection of emitted photoelectrons from the nanoparticle surface. Currently, there is no other way to investigate the nanoparticle–(bulk) water interface other than using the liquid jet technique.

2.5 Relaxation Processes via Photon-Emission

In this section, I briefly summarize the radiative relaxation process upon photoionization or photoexcitation of an atom or molecule. Besides the normal Auger electron emission, the system can also emit a photon via X-ray fluorescence while refilling the core-hole (see Figure 2-5 (B)). As explained in Section 2.3, the resonant photoexcitation will also produce a core-hole (see Figure 2-5(C)). It is followed by one of two probable radiative decay processes. The first is called resonant elastic X-ray scattering and is characterized by the fallback of the initially promoted electron to the core-orbital emitting the same amount of energy as it has received from the absorption (see Figure 2-5(D)). The second case is called resonant inelastic X-ray scattering and describes the case that any other electron refills the core hole, resulting in the emission of an X-ray photon with less energy than the absorbed one (see figure 2-5 (E)).

In general, the quantum yield for fluorescence is much lower than for Auger emission for light elements (i.e. low atomic numbers).[61] On the other hand, the probing depth of photon-emission spectroscopic techniques is much larger compared to photoelectron-based techniques. Accordingly, photon-emission spectroscopy provides bulk sensitive measurements with reasonable signal intensity. It is complementary to photoelectron spectroscopy and useful for the study of the nanoparticle–bulk aqueous solution systems as shown in Chapter 7.

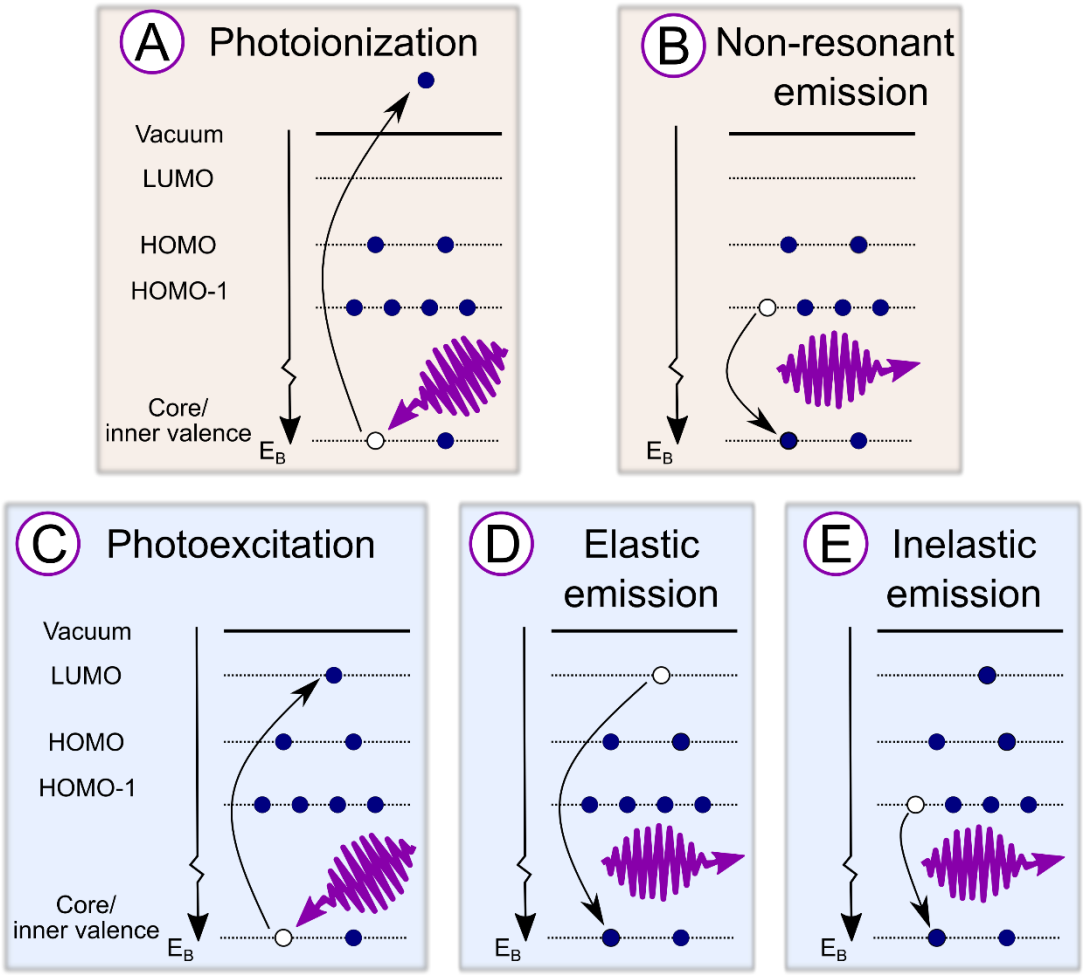

Figure 2- 5

Schematic representation of the photoionization, photoexcitation, and radiative relaxation processes. The photoionized single atom (presented in A) can relax via a non-resonant X-ray emission process (B). A photoexcited single atom (C) can either relax via resonant elastic X-ray scattering (D), or via resonant inelastic X-ray scattering (E). See text for more details.

Chapter 3
Experimental Techniques

This thesis reports measurements that have been done with two different experimental setups (SOL^3 PES and LiXEdrom) both at the beamline U49-PGM1 of the synchrotron radiation facility BESSY II Berlin, Germany. The photoemission studies were performed with the SOL^3 PES while the photon-emission spectra were detected with the LiXEdrom setup. In this chapter, both experimental setups are described, as well as the liquid sample introduction system (liquid micro-jet). I also provide a short introduction into synchrotron radiation, which is used as an X-ray excitation and ionization source in this study, with a special focus on the U49-PGM1 beamline parameters.

3.1 SOL^3 PES Experimental Setup

SOL^3 setup is an abbreviation of ***Sol****id*, ***Sol****ution*, and ***Sol****ar*. This reflects our main research goals, i.e., exploring the solid—solution interface using photons; optionally in the solar spectrum. My very first measurements from the TiO_2 nanoparticle—aqueous interface, performed during the commissioning beamtime of the SOL^3 setup in April 2016, are published as proof of concept accompanied with the experimental setup description in ref.[62] In brief, the SOL^3 PES setup consists of three main parts: (1) The interaction chamber, (2) the electron analyzer, and (3) the differential pumping unit.

3.1.1 Interaction Chamber

Figure 3-1 represents schematically the interaction chamber (IC) of the SOL^3 PES setup. It is made of non-magnetic stainless-steel material with a dimension of 27x27x42 cm^3. The hemispherical electron analyzer is mounted perpendicularly to both the X-ray beam and the liquid jet axis. The IC is equipped with a gate valve towards the entrance of the X-ray beam from the differential pumping unit, while the liquid jet is housed on an X,Y,Z manipulator. The latter makes the alignment of the sample easier under the electron analyzer pinhole and along the X-ray beam axis to achieve higher PE signals during the measurements.

In addition, a three-pair Helmholtz coil assembly is surrounding the IC along the three main axis (illustrated in left bottom of Figure 3-1), to compensate the earth magnetic field at the interaction point (highlighted by a blue circle in Figure 3-1). The X-ray beam focal point meets the laminar liquid jet in front of the electron analyzer orifice.

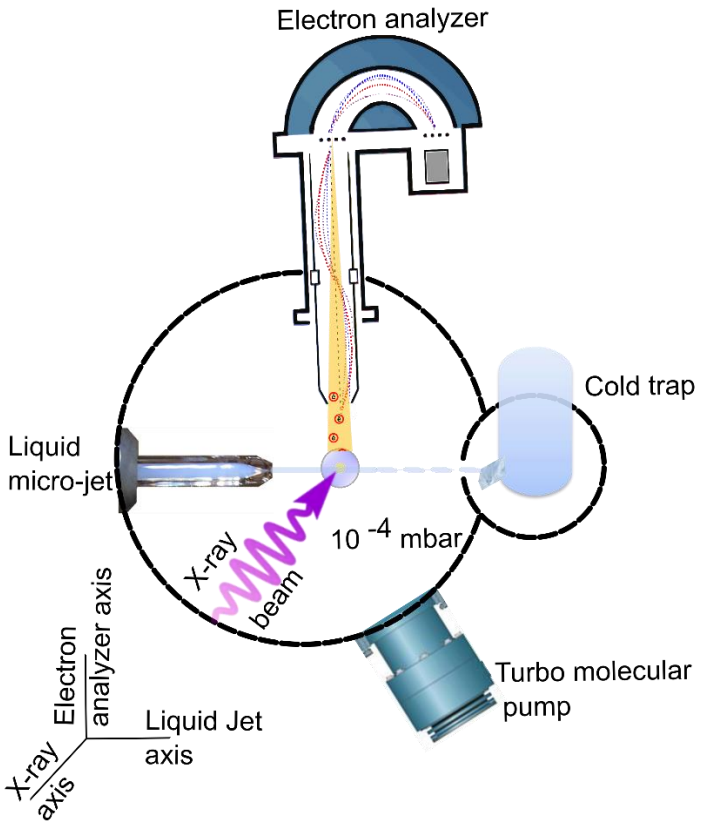

Figure 3- 1

Schematic view of the interaction chamber of the SOL[3] PES experimental setup. The Liquid jet is mounted on an XYZ manipulator to proper align its position at the intersection point under the hemispherical electron analyzer pinhole. The vacuum is in the 10^{-4} mbar regime using a turbomolecular pump in combination with cold trap.

In order to maintain suitable vacuum conditions (pressure ~10^{-6} mbar), a 1600 l/s turbomolecular pump is used. Under liquid jet condition, the IC is coupled with a sample catcher chamber that has a narrow inlet for the liquid beam. A cold trap (cylindrical metallic tube with ~1000 cm^2 surface area) is filled with liquid nitrogen to collect the frozen samples and is located inside the sample catcher chamber. The sample catcher chamber is easy to disassemble, facilitating the required frequent cleaning. The IC also provides a port for an additional cold trap in front of the turbomolecular pump. Under such conditions, the pressure is usually kept at ~ 10^{-4} mbar when the liquid jet is running. It is also important to mention that experiments could be executed at the SOL[3] PES setup at up to 20 mbar (near ambient pressure regime). Typical scenarios for experiments at elevated pressures are: (1) highly volatile samples from a normal liquid microjet, (2) large surface area or mixed liquid samples using a flat jet design,[63] (3) liquid − gas interaction studies using a liquid jet coupled with a gas dosing

system,[64] (4) or investigations at the liquid − solid crystalline interface as function of relative H_2O humidity.[29]

The whole IC can be rotated from 90° to zero° relative to the floor plane. This enables us to detect electrons emitted at different angles with respect to the X-ray beam polarization plane to study the electron angular distribution of different molecular orbitals. In this thesis photoelectron angular distribution experiments were not performed.

3.1.2 Electron Analyzer

A hemispherical electron analyzer (EA) consists of three main parts: (1) an electrostatic lens unit (the drift stage) that refocuses the electrons entering the analyzer; this unit also provides efficient differential pumping, (2) two concentric outer and inner hemispheres with approximately 200 mm radius (for the outer hemisphere)[62] and an changeable inlet slit with widths ranging from 0.2 mm to 4 mm (controlling the energy resolution).[62, 65] (3) Behind the exit slit, the detector unit is mounted. This 2-dimensional detector consists of a micro-channel plate (MCP) and a 40 mm-diameter phosphor screen coupled to a charged coupled device (CCD) camera.[62]

SOL^3 PES is equipped with a "ScientaOmicron R4000 HiPP-2" high-resolution hemispherical electron energy analyzer designed to detect electron energies in the approximately 5 to 6000 eV range, and capable to perform near-ambient-pressure measurements, up to tens of millibars.

The emitted electrons at the interaction point pass the skimmer orifice (entrance into the analyzer), which acts as a first pinhole for the drift stage (see Figure 3-2 (A)). Inside the drift stage the electrostatic lenses accelerate or retard the electrons before reaching the inlet slit of the hemispherical analyzer, where the electrons are forced to follow a circular trajectory by the electrostatic field between the two concentric hemispherical lenses. Only electrons with a specific kinetic energy (the so-called pass energy, E_P) reach the exit slit and are counted by the electron detector. The pass energy in the Scienta R4000 HiPP-2 electron analyzer can be chosen between the following values: 5, 10, 20, 50, 100, 200, and 500 eV. This pass energy is fixed during the measurements. A larger pass energy allows a higher transmission, resulting in higher signal intensity in shorter time, however at the expense of energy resolution. In contrast, a small pass energy allows measurement of high-energy resolution spectra, but signal intensity is smaller. There are additional restrictions, e.g. pass energies must be smaller than 1/3 of the kinetic energy of the electrons detected. In order to scan over a range of kinetic energies, the drift stage de-/accelerate the electrons to reach the entrance aperture (A_E) of the hemispherical analyzer with a matching energy to the pass energy (±8% distribution[66]).

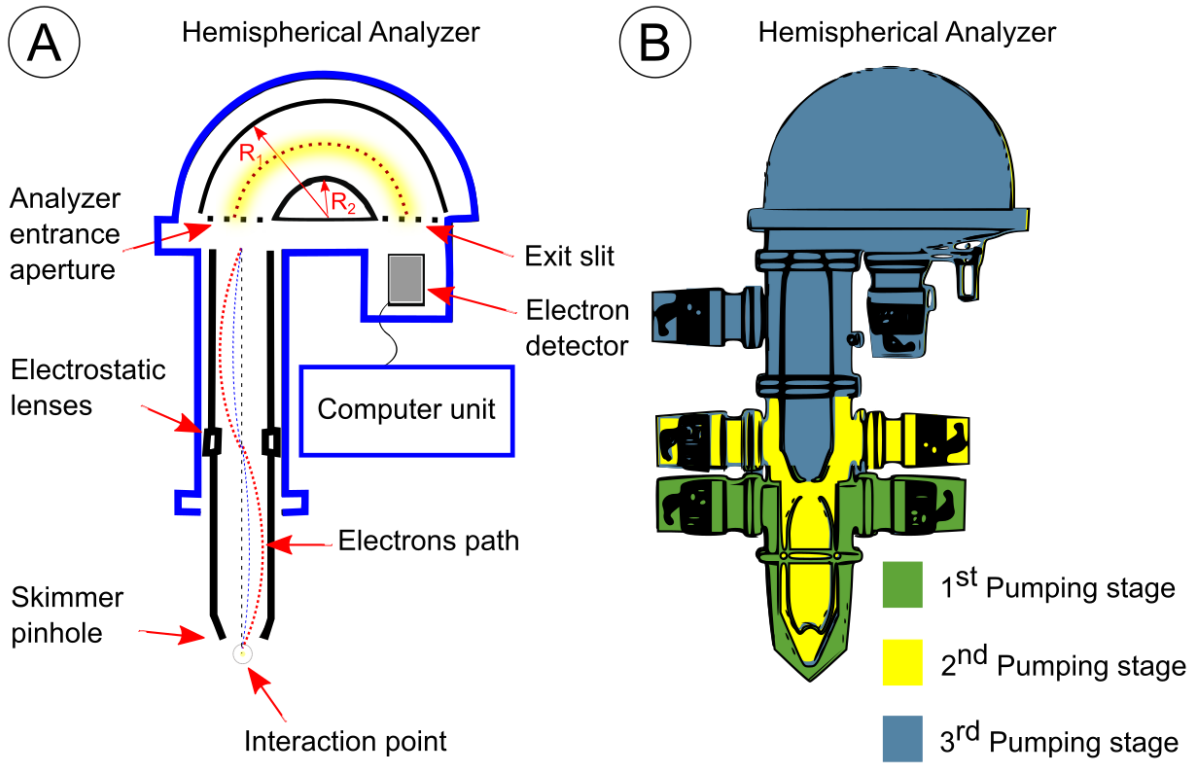

Figure 3- 2

Schematic of the electron analyzer of the SOL[3] PES experimental setup. In A, the main parts of the electron analyzer are illustrated as well as some of the electron trajectories. In B, the differential vacuum pumping zones are shown. B is modified from reference [66].

All the high voltage elements in the hemispherical analyzer have to be kept in ultra-high vacuum during operation, which is incompatible with the nature of liquid jet measurements (in ~10^{-4} mbar regime) or even near-ambient pressure measurements. To account for this pressure difference, the drift stage also acts as a three-stage differential pumping unit (see Figure 3-2 (B)). The pressure in the 1st pumping stage is typically ~ 10^{-5} to 10^{-6} mbar, in the 2nd pumping stage it is one order of magnitude better (~ 10^{-6} to 10^{-7} mbar), and finally in the 3rd pumping stage it reaches values between ~ 10^{-7} to 10^{-9} mbar. There are two 250 l/s turbo molecular pumps (Pfeiffer Vacuum, HiPace 300) attached at every stage, in addition to one HiPace 300 pump at the hemispherical analyzer. Every stage is backed up by an oil-free 10 l/s scroll pump (Edwards XDS 35i).[62]

The Scienta Omicron R4000 HiPP-2 offers two data acquisition modes: transmission mode and angular mode. The transmission mode is used for spatial mapping across homogeneous surfaces. This mode provides an overall transmission magnification factor of 5 with a spatial resolution of 300 µm. In contrast, the angular mode maps the angular distribution of the photoelectrons. A refocusing design of the pre-lens unit enables a simultaneous detection over 22 degrees. The angular resolution is

dependent on the emission spot size, with smaller spot sizes giving the highest resolution. A 0.1 mm spot yields better than 0.3° angular resolution.

The electron analyzer energy resolution (ΔE) of the Scienta Omicron R4000 HiPP-2,[66] in a first approximation, can be described by the following equation:

$$\Delta E = \frac{S * E_P}{2r_0} \qquad \text{Eq.(3.1)}$$

E_P is the pass energy (eV), r_0 is the radius of the hemispherical analyzer (200 mm), and S is the entrance slit in mm in the energy dispersion direction.[66] Equation 3.1 assumes a perfect analyzer and does not take mechanical imperfection, surface potentials etc. into account. For this analyzer, S can be changed between nine different sizes, ranging from 0.2 to 4 mm.[62] Usually, the slit is kept to 1.5 mm, which provides a good compromise between energy resolution and electron transmission.

3.1.3 Differential Pumping Unit

The differential pumping unit (DPU) is located between the interaction chamber and the refocusing chamber of the beamline (see Figure 3-3). Its function is to keep the vacuum at the beamline side in good condition (10^{-9} mbar) during XPS experiments in the interaction chamber even at elevated pressures of up to 20 mbar. It consists of three sections, which are pumped individually by one 250 l/s turbo molecular pump in the first section and two 80 l/s turbo pumps in the other two sections. The first section is also equipped with a liquid nitrogen cold trap. The sections are separated by 1, 2, and 3 mm concentric pinholes (from the IC to the beamline). To guide the X-ray beam through these pinholes and at the same time hit the sample at the required imaging distance of 0.5 mm in front of the analyzer aperture cone, the DP is adjustable in all three translation axes and also rotatable by +/-5° with respect to the synchrotron-light axis. Passing the synchrotron light through the DP is assisted by a fluorescence film, covering the areas around the pinholes, that gets illuminated when hit by X-ray.

The DP unit is separated from the IC by a gate valve, which is open during the measurements and manually locked when breaking the vacuum in the IC is necessary. This is usually the case for disassembling the sample catcher chamber and cleaning the IC (after liquid jet measurements), inserting a sample holder (e.g., liquid jet manipulator, solid sample holder, electrochemical flow cell, etc.), and also for rotating the IC relative to the X-ray beam polarization plane.

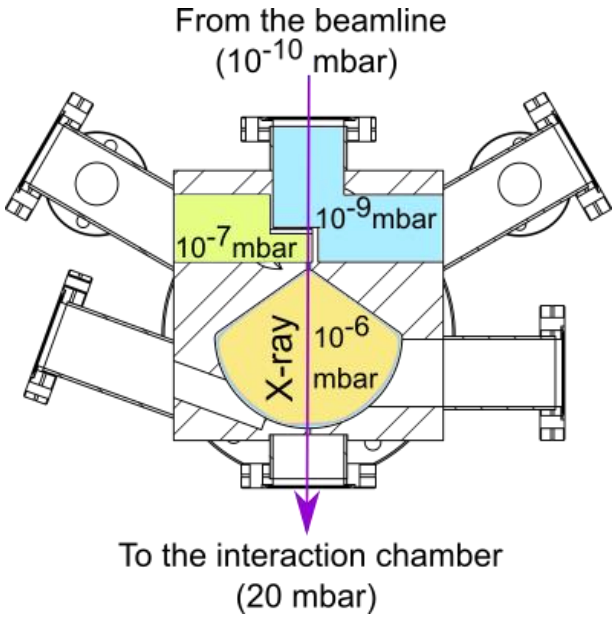

Figure 3- 3

The differential pumping unit is divided into three regions, which are connected with each other by 1-3 mm pinholes. It keeps the pressure at the beamline side in the 10^{-9} mbar regime – even at near-ambient pressures conditions in the interaction chamber.

3.2 LiXEdrom Experimental Setup

The LiXEdrom experimental setup was used for the photon-emission measurements presented in Chapter 7. A schematic of this experimental station is shown in Figure 3-4. It consists of three parts: **(i) The interaction chamber:** A liquid jet is mounted on an XYZ manipulator normal to the X-ray beam. The liquid shoots vertically down into an ISO-K 100 tube that resides in a liquid nitrogen bath. Here, the liquid-jet freezes out when hitting the inner wall. The pressure inside the interaction chamber is kept at 10^{-5} mbar using a 1500 l/s turbo-molecular pump and an additional cold trap. **(ii) The differential pumping section:** This section is located behind the interaction chamber (not shown in the figure). Analogous to the SOL^3 PES differential pumping section, it serves to differentiate the pressure between the interaction chamber and the first part of the beamline. A typical pressure in the differential pumping section during experiments is 10^{-9} mbar. A gate valve between the interaction chamber and the differential pumping section is kept open during the measurements and closed when breaking the vacuum in the interaction chamber is needed (for insertion/removal of the sample holder or clean-up of the sample cold trap). **(iii) The detector:** The LiXEdrom detector section is divided into two parts: the dispersion element and the photon detector. It is separated from the interaction chamber by a gate valve that can be closed during the insertion of the sample to preserve the vacuum inside the detector section and opened during the measurements (in the 10^{-7} mbar regime for the

dispersion element and 10^{-9} mbar regime at the photon detector). The LiXEdrom is supplied by two diffraction gratings, acting as light dispersion elements. They are spherical gratings with variable line spacing (VLS) with line densities of 1200 l/mm and 2400 l/mm, respectively, mounted on a holder inside a vacuum chamber, covering the photon energy ranges between 200-500 eV and 400-1200 eV. In this study, I used the 2400 l/mm grating to record the photon emission from the oxygen K-edge (~ 530 eV photon energy). The LiXEdrom photon detector consists of a micro-channel plate (MCP), phosphor screen and a charge coupled device (CCD) camera as shown in Figure 3-5. Once the photons hit the MCP surface, electrons are generated due to the photoelectric effect. The high electrical voltage applied throughout the MCP tubes leads to an electron avalanche, i.e. every single generated electron is accelerated and releases further electrons from the MCP walls, leading to a gain of 10^4 (see Figure 3-5 right hand side). By impinging on the phosphor screen, a fluorescence image is created that is captured by the CCD camera.

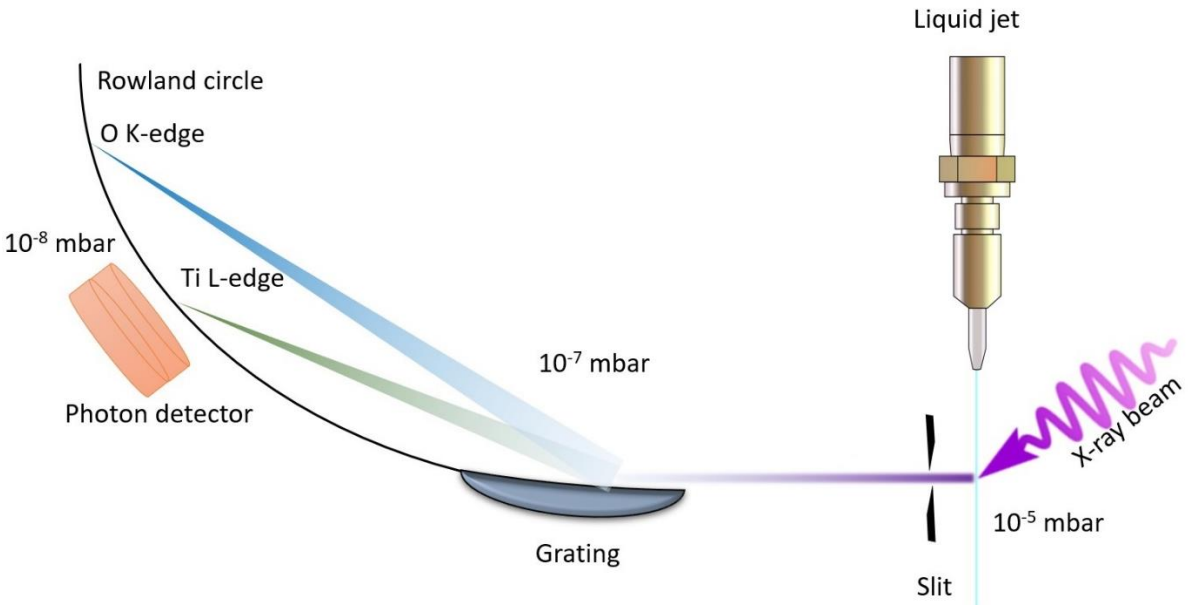

Figure 3- 4

A schematic diagram of the LiXEdrom experimental station. The X-ray beam interacts with the liquid sample in a point, which acts like an emission source for the grating, that disperse the light. This dispersed light beam is then detected by a photon detector, which is placed in a Rowland geometry with respect to the grating and the sample-beam interaction point.

The LiXEdrom components are arranged in a Roland circle geometry. Thus, the interaction point between the X-ray beam and the liquid jet acts like a light source to the grating; and the photon

detector is mounted on a motorized manipulator that provides an X,Y and rotational motion. It is connected to the grating via a metal bellow.

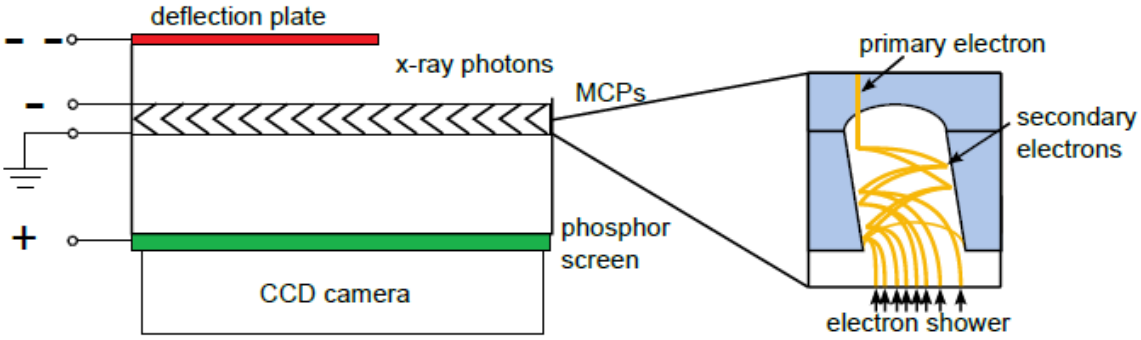

Figure 3- 5

A schematic diagram of the LiXEdrom photon detector. The zoom-in on the right side shows schematically the photoelectron multiplication inside an MCP channel. This figure is adapted from reference [67].

3.3 Liquid Microjet Sample Introduction System

For a long time, detection of photoemission spectra from highly volatile liquids was hardly possible due to the difficulty of transferring the emitted photoelectron from the liquid surface through the vapor phase to the electron analyzer[32, 68] (see Section 2.4). Also, the typical large evaporation rate of liquids had prevented to obtain the required vacuum without consuming the investigated sample itself.[69] A breakthrough came with the demonstration of the first valence level photoemission spectra of liquid water and aqueous ions from a microjet setup using He I line radiation for excitation, in 1997 by Faubel et al.[69] He developed a technique to introduce a liquid to the vacuum forming a truly laminar aqueous-phase surface. This microjet setup provides a very thin, fast flowing liquid jet filament while maintaining a 10^{-5} mbar pressure.[69] Here, the thin liquid filament is injected into the vacuum chamber, gets ionized by soft X-ray radiation and the outgoing photoelectrons are then detected by, e.g., a hemispherical electron analyzer (see Section 3.1.2). Alternatively, photon-emission spectra can be measured from a jet by using a diode or a photon detector unit (see Section 3.2).

The liquid microjet introduction system used for my studies is illustrated in Figure 3-6. The jet is produced by pressurizing the sample solution through a fused silica nozzle (***A***) which has a typical inner diameter between 5 and 50 µm. Several factors are crucial for a stable flow rate and a smooth laminar surface region of the jet: (1) A steady flow rate is achieved by a variable backing pressure, applied by a High-Performance Liquid Chromatography (HPLC; Techlab Model Economy) pump (***B***) connected to the (pure) water reservoir (***C***). (2) A degassed solution is used to avoid air and gas

bubbles, which could lead to flow interruptions of the jet and ultimately to a freezing tip of the nozzle inside the vacuum chamber. (3) A very clear solution without any micro-suspended particles/ impurities will prevent nozzle clogging. This is done by filtrating the sample before reaching the nozzle through an inline filter with 2 µm pore size. (**D**) An external filtration process should be applied before inserting the liquid sample in the reservoir (***C***).

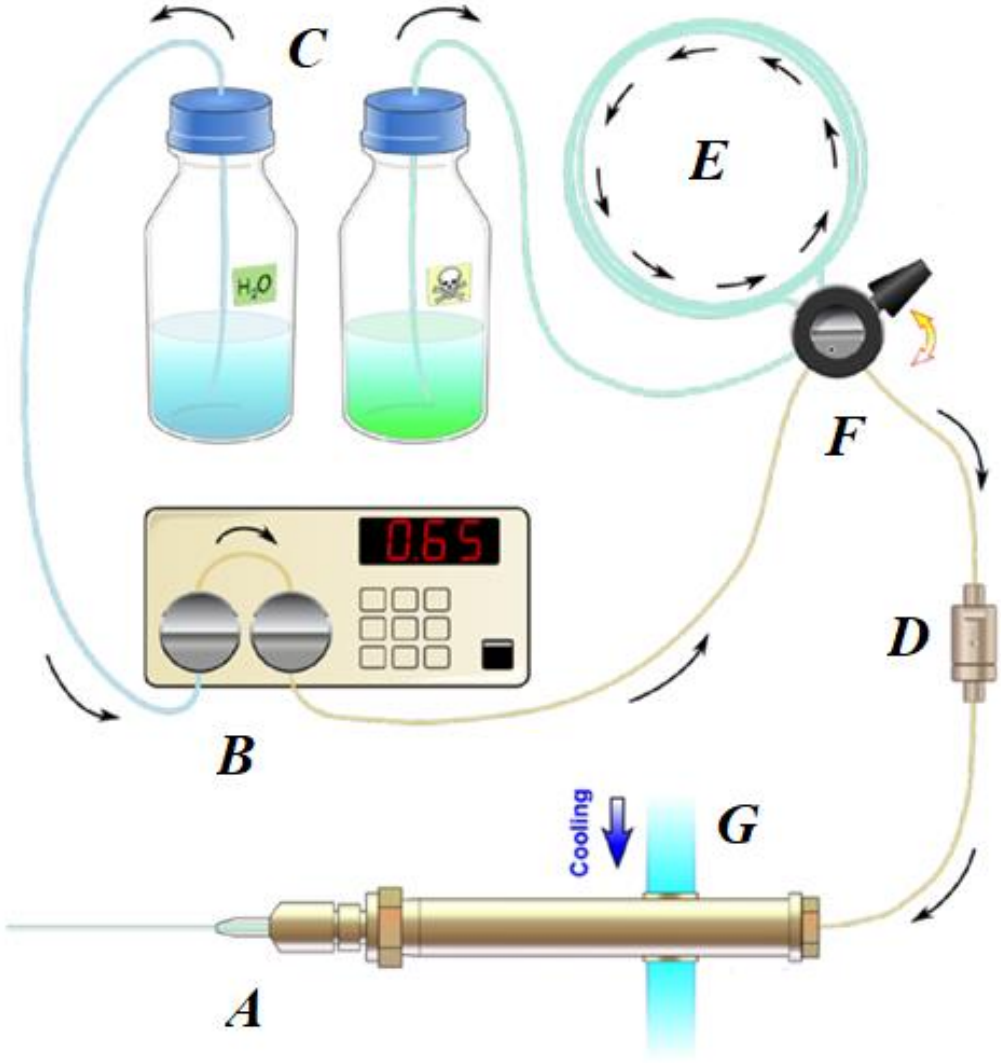

Figure 3- 6

Schematic of the liquid jet introduction system. The figure is adapted from reference [70].

In order to measure highly acidic, basic or salty samples without interaction with the stainless steel parts of the HPLC pump, we implement a loop system (***E***) between the HPLC pump (***B***) and the nozzle (***A***). The plastic tubes in the loop system, which are in direct contact with the solution being investigated, are made of the chemically inert materials Fluorinated Ethylene Propylene (FEP) and

Poly-Ether Ether Ketone (PEEK). By switching a four-way switch (***F***), the loop capillary is loaded from the sample reservoir (***C***) with the aid of an external peristaltic pump (not shown in Figure 3-6). After loading and switching again the four-way switch (***F***) the water from the reservoir C, running through the HPLC pump, goes to the loop system and pushes the sample solution to the nozzle (***A***). An additional loop system can be connected to the switch (***F***) to reduce the measurement deadtime during sample filling. Typically, the sample solution is cooled to (5 - 15°C) by a cooling device (Julabo F12 ED chillor) (***G***). This leads to a reduced evaporation rate of the liquid sample and increases the electron inelastic mean free path around the liquid jet at the interaction point.

3.4 Synchrotron Radiation

Synchrotron radiation is the electromagnetic radiation that is emitted tangentially along the trajectory of charged particles travelling near the speed of light, when deflected from their straight path, typically by (strong) magnetic fields. Synchrotron radiation can occur naturally, e.g. in supernovae remnants like the Crab Nebula, or it can be generated artificially, e.g. in electron storage rings. The first of its kind was a "betatron" built in the 1940th, for electron acceleration.[71-72] Nowadays, storage rings in the 3rd generation are world-wide in place, capable of producing ultra-high brilliance synchrotron radiation thanks to the development of insertion devices like undulators and wigglers. A schematic of an undulator is shown in Figure 3-7. It consists of an array of dipole magnets with alternating polarity, where the electron beam travels along a sinusoidal trajectory.[73] Electrons lose energy by emitting radiation every time they change their direction.[74-75] Due to relativistic effects and the constructive interference of this radiation a highly collimated photon beam with a few energetic narrow peaks, the so-called harmonics (see the inset of Figure 3-7) is generated. The distance between the north and south poles of a magnet inside the undulator is called the undulator gap. By changing the gap of the undulator, one can control the photon energy of the harmonic peaks. The odd harmonic peaks are the ones used in the experiments.[75] A quality parameter for an X-ray photon beam generated from an undulator is the brilliance. This term reflects the number of photons per area of radiation, per solid angle of the radiation cone, and per unit time.

BESSY II (Berliner Elektronenspeicherring-Gesellschaft für Synchrotronstrahlung) is one of the 3rd generation synchrotron radiation facilities and it was used to carry out the experiments presented in this thesis. It offers ultra-bright photon beams in the wavelength range of infrared up to hard X-rays with the highest brilliance in the soft X-ray regime. Experiments at up to 46 beamlines can be performed independently, and at 26 stations at the same time. There are two beamlines at BESSY II (UE52-SGM-1, and U49/2-PGM-1) that provide the required high photon flux in the soft X-ray regime and a small focal spot size for the liquid jet experiments (see 3.4.1). In Figure 3-8, the electron trajectory inside the BESSY II accelerator and the storage ring is illustrated. Free electrons

are generated by heating a cathode (electron gun) and then accelerated to 100 keV in an electric field. Before 2014, electrons were further accelerated by a microtron and after 2014 by a high frequency linear accelerator to 50 MeV. These 50 MeV electrons are then 'kicked' into a synchrotron ring with a 96 m circumference, the so-called booster, where the magnetic field, generated from 16 dipole magnets, is synchronously increased until the electrons energy reach 1.7 GeV. The electrons – now bunched at packages – are further injected into the larger storage ring, which has a circumference of 240 m. Here, the electrons are forced on a circular path by bending magnets, quadrupole and hexapole magnets, with the insertion devices (undulators and wigglers) sitting in the straight sections between the magnets.

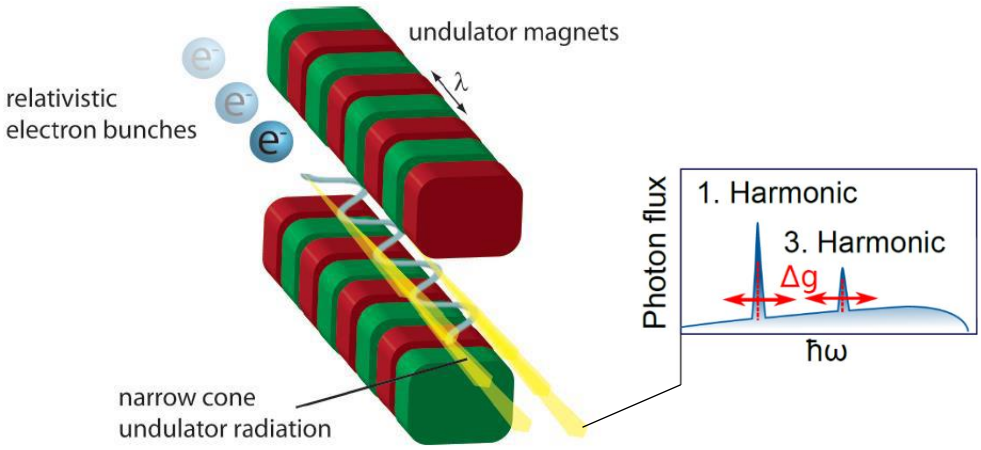

Figure 3-7

Schematic description of the creation of synchrotron radiation within an undulator, taken from reference [76]. In the inset the various harmonic lines are shown, adapted from reference[77].

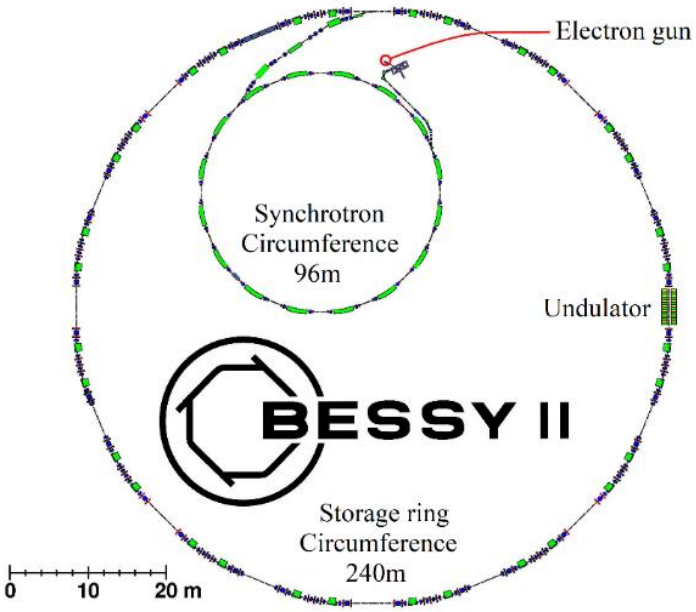

Figure 3- 8

A schematic diagram of the BESSY II synchrotron facility. Electrons are generated by an electron gun and accelerated to reach 99.9% of the speed of light before being injected in the storage ring. Figure is taken from reference[78].

3.4.1 U49-2/PGM-1 Beamline

Liquid jet photoelectron measurements require specific X-ray beam parameters like a small focal size, high photon flux, and variable soft X-ray energy. The U49-2/PGM-1 beamline meets those requirements. Figure 3-9 presents a schematic side and top view of all optical elements of the beamline, which are in an ultra-high vacuum environment. A brilliant, coherent, and pulsed X-ray beam with possible energies between 80 and 1600 eV is generated inside the U49/2 undulator – an insertion device consisting of multiple strong permanent magnets each 24.5 mm wide with periodic polarity. From there the synchrotron light is guided towards the U49/2-PGM-1 beamline, where it passes a series of collimating optical elements. The beam is then monochromatized by the pre-mirror M_2 coupled to an exchangeable plane grating of 600 l/mm and 1200 l/mm before reaching the focusing cylindrical mirror M_3. The exit slit is adjustable from 5 µm up to 2 mm. As the energy resolution of the beamline directly correlates with the exit slit size a good compromise between resolution and photon flux is 50-100 µm. The mirror M_4 refocuses the X-ray beam. The final focal size is under optimal conditions 'beamline exit slit'(vertical) times 100 µm (horizontal), with a lower value of 22 µm in the vertical direction.[79] The technical parameters of the U49-2/PGM-1 beamline are summarized in table 3-1.

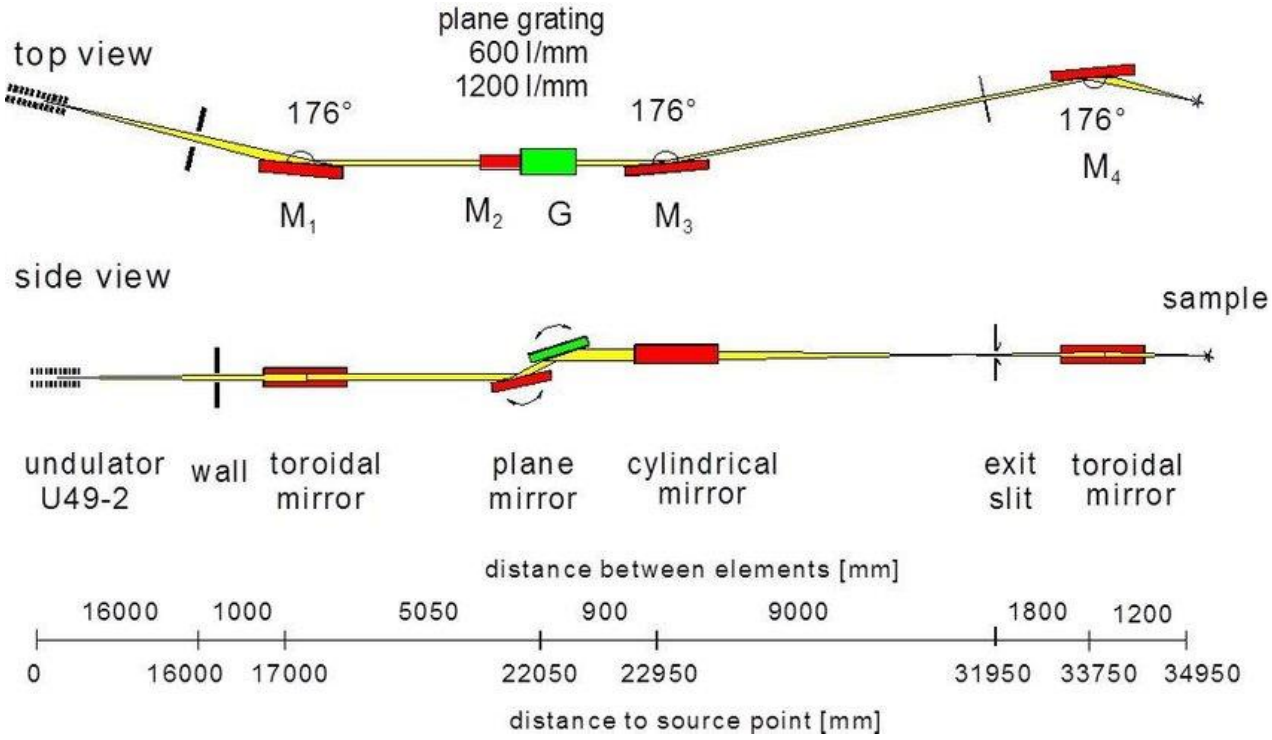

Figure 3- 9

Optical layout of the U49-2/PGM-1 beamline, adapted from reference [79].

Energy range	85 - 1600 eV
Energy resolution	25,000 (85 - 500 eV) 15,000 (500 - 1,500 eV)
Flux	10^{13} ph/s (85 – 500 eV) 10^{12} ph/s (500- 1500 eV)
Polarization	Horizontal
Divergence	2 mrad horizontal 2 mrad vertical
Focus size	100 µm x 22 µm
Focus distance	959 mm from the last valve
Focus height	1417 mm from the floor level
Fixed end station	NO

Table 3- 1

The technical parameters of the U49-2/PGM-1 beamline.

Chapter 4
Photoemission and Photon-Emission Spectra from Liquid Water

Liquid water is the main solvent for all the samples measured in this thesis, and its spectral features are used as energy references for all the measured spectra in Chapters 5, 6 and 7. This chapter reviews photoemission and photon-emission spectra obtained from liquid water using the microjet technique. First, I present and discuss the valence and O 1s core-level photoelectron spectra from liquid and gas-phase water. Then, I show that these liquid water spectral features serve as an accurate reference for binding energy determination. This requires reviewing the result from a recent study (to which I contributed) on the effect of ion concentration in aqueous solution on the electronic structure of the liquid water. Afterwards, I present a series of resonant valence PE spectra measured around the O 1s resonance photon energies of H_2O(l). In these spectra, I differentiate the photoemission resonance signals (spectator, participator and normal Auger electrons) based on the earlier explained Auger emissions in Section 2.3. Next, I introduce the so-called partial electron yield X-ray absorption (PEY-XA) spectrum generated by integrating the aforementioned series of valence band spectra. Analogous to the PEY-XA spectrum, I present the O K-edge partial fluorescence yield X-ray absorption (PFY-XA) spectrum. This spectrum is generated by integrating the intensity of the photon-emission yield upon the water electron's relaxation from the valence to the O 1s core orbital. Using a contour-map representation of the intensity of the emitted photons as the function of emitted photon energy and excitation photon energy, I assign the observed spectral features to their corresponding radiative relaxation channels explained in Section 2.5.

4.1 Valence Band and O 1s Core-Level Photoelectron Spectra

In this section, I present the valence and core-level PES spectra from liquid and gas-phase water, assign the spectral peaks to their corresponding electronic states, and I discuss why the water $1b_1$ peak position is an accurate energy reference.

Figure 4-1, bottom, displays the valence and O 1s core-level photoelectron spectra from 0.05 M NaI aqueous solution measured at 150 and 575 eV photon energy, respectively. The latter photon energy is high enough to ionize the O 1s core-level. This low-concentration salt solution is needed to avoid sample charging upon interacting with the X-ray photons which can produce peak shifts and broadenings and to compensate for electronic charging[80]. Such a procedure is typically adopted in liquid jet photoelectron measurements when solutions are non- or poorly conductive.

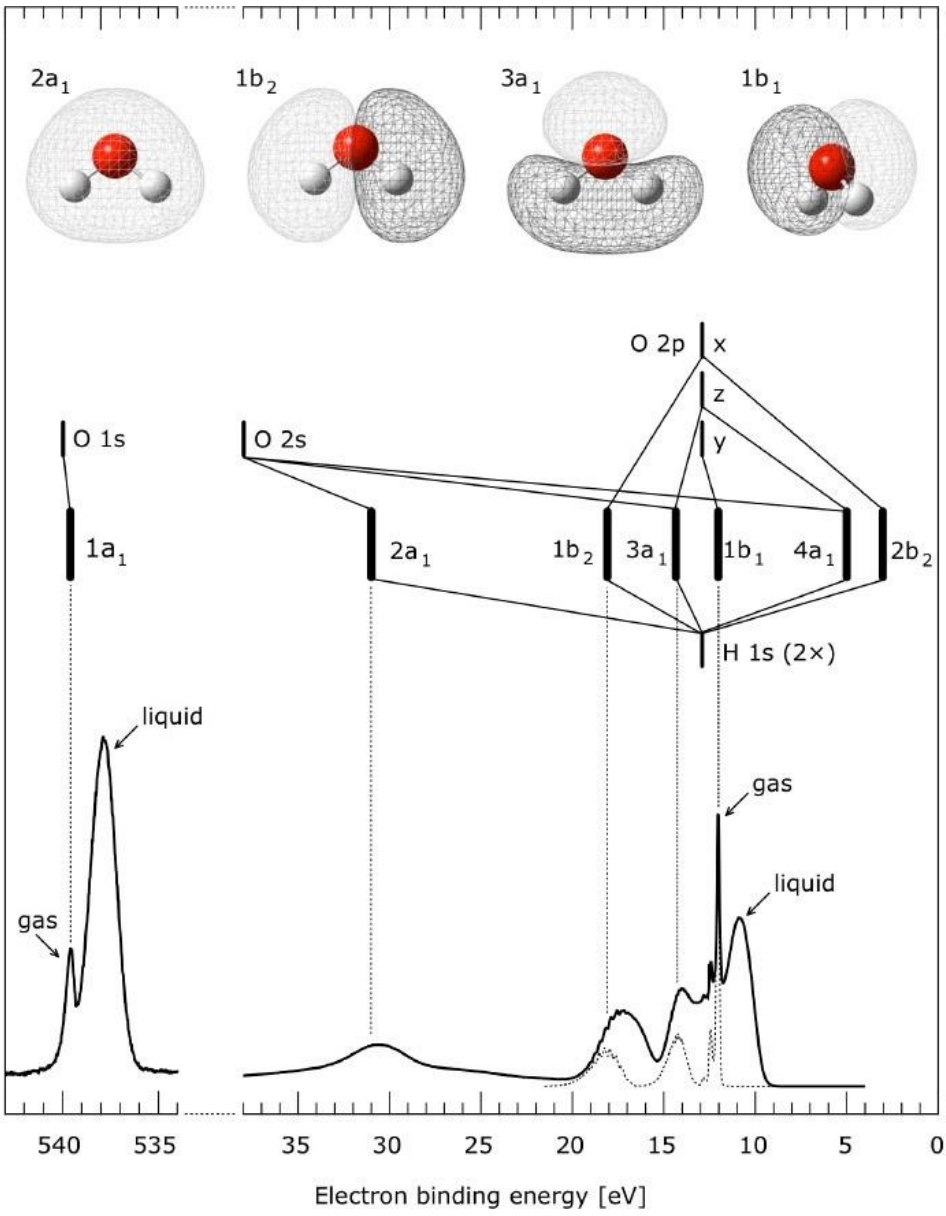

Figure 4- 1

Top: Energy-level diagram and molecular orbital scheme of the H_2O molecule. The valence molecular orbitals of water are reprinted from ref.[81]*. All atomic and molecular levels are positioned according to their binding energies (taken from Ref* [82] *for the atoms and from Refs* [83-84] *for H_2O) on the energy scale. Bottom left hand side: Liquid-jet O1s core-level PE spectrum from liquid water (probed with 575 eV photon energy) exhibiting two peaks at 538.1 eV form $H_2O(l)$ and at 539.9 eV form $H_2O(g)$. Bottom right hand side: Liquid-jet PE spectrum from liquid water in the valence band regions (measured using 150 eV photon energy). Here, the gas-phase valence spectrum (recorded using 175 eV photon energy) of water is shown by dotted curve. Dashed lines assign all gas peaks to their respective molecular orbital. The $4a_1$ and $2b_2$ orbitals are unoccupied orbitals and therefore not visible in the PE spectrum. This Figure is adapted from reference* [85].

Photoelectron spectra from a liquid water jet inevitably exhibit signal from both liquid and gas-phase water. The relative intensity of the latter depends on focal size of the photon beam and can be kept as low as 5% when the focal size is on the order of the jet diameter. In order to isolate the gas contribution from liquid water, the jet position is typically moved away from the X-ray beam focus (the interaction point, see Section 3.1.1). The resulting valence spectrum, obtained for 175 eV photon energy is shown by a dotted line below the liquid water valence spectrum in Figure 4-1. For both liquid and gas-phase valence spectra, peaks at the low binding energies are produced from the ionization of the molecular valence orbitals of the H_2O, $1b_1$, $3a_1$, $1b_2$, and $2a_1$. The respective peaks for the liquid phase are shifted by approximately 1.4 eV toward lower energy and exhibit larger widths in comparison to the gas-phase peaks due to water's dielectric screening and a large distribution of hydration configuration, respectively. A full energy-level diagram of gas-phase H_2O is presented in the middle of Figure 4-1, and at the top, the shapes and characters of the four occupied valence molecular orbitals of an isolated water molecule are illustrated. Peaks at the high-binding energy side in Figure 4-1 identify the O 1s core-level spectrum from the liquid water. It exhibits peaks at 538.1 eV form H_2O(l) and at 539.9 eV form H_2O(g). The liquid-phase peak is used for energy calibration for all the O 1s core-level measurements of different samples in this thesis.

Our typical energy reference for all measured valence PES spectra using aqueous solution microjets is the $1b_1$ liquid water peak. It is well separated from the corresponding gas-phase peak and it has been reported at 11.16 eV binding energy.[86] This value was taken from a spectrum recorded for neat liquid water. This procedure is only valid if the solute has no effect on the water valence energies. Recently, our group has combined liquid jet measurements with molecular dynamical and quantum chemical calculations to answer these questions.[80] Figure 4-2 shows valence PE spectra measured for 0.5 and 8 M NaI aqueous solutions to assess the electronic structure changes when going from liquid water to the viscous, almost crystalline-like liquid phase.[80] It is found that the solute peaks Na^+ 2p, I^- 4d and I^- 5p and also the water $1b_1$ peak position stay aligned.[80] The absence of any shift then implies that the $1b_1$ peak of liquid water is a robust energy reference for photoemission measurements from aqueous solution using microjet.[80]

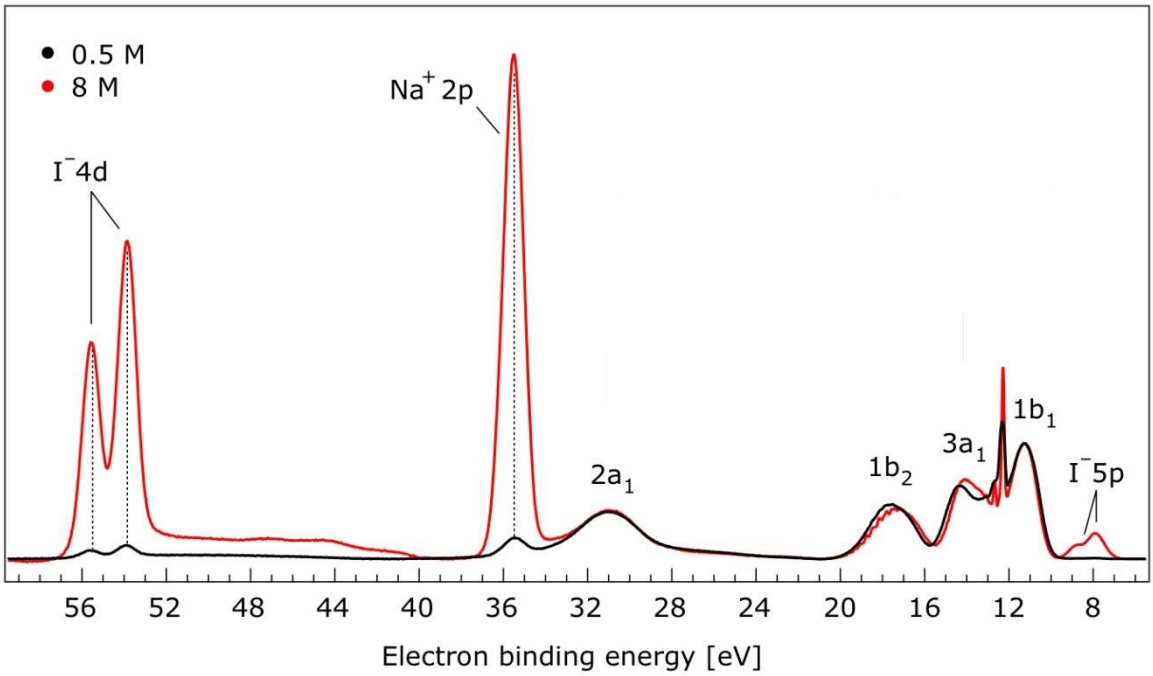

Figure 4- 2

Valence photoelectron spectra of 0.5 M (black) and 8.0 M (red) NaI (aq) measured at 198.0 eV photon energy. A linear background was subtracted from both spectra in order to account for the contributions of the inelastically scattered electrons. Both spectra appear to be closely energetically aligned at the Na^+ 2p and I^- 4d peaks (as indicated by dashed lines) after shifting the peak of the liquid water$1b_1$ peaks to 11.16 eV. This Figure is adapted from ref.[80]

4.2 O K-edge Partial Electron Yield X-ray Absorption Spectra

Figure 4-3,(left), shows a series of valence PES spectra measured from liquid water for photon energies below and at the ionization threshold of the O 1s core-level. The excitation energy is indicated on the right side. At 524 eV excitation energy, which is well below the ionization energy, the valence spectrum reproduces the typical water electronic structure of Figure 4-1, except for some relative intensity change due to different ionization cross sections. When the excitation photon energy matches the resonance (535 eV), corresponding to the photoexcitation of a core electron from the O 1s into the $4a_1$ molecular orbital (LUMO)[87], one also observes electrons created by Auger decay in the spectrum. Valence spectra measured at a core-level resonance photon energy are referred as resonant photoemission (RPE) spectra. Two types of Auger-electron processes can be distinguished in the spectra, spectator and participator Auger photoemission (indicated with arrows in Figure 4-3); these two Auger processes have been introduced in Section 2.3.1. The participator Auger electron has the identical kinetic energy as the photoelectron emitted from the HOMO orbital involved in the Auger

decay (a resonantly enhanced photoionization channel). In contrast, spectator Auger electrons have lower kinetic energy (appearing at higher binding energy) than the emitted direct photoelectron.

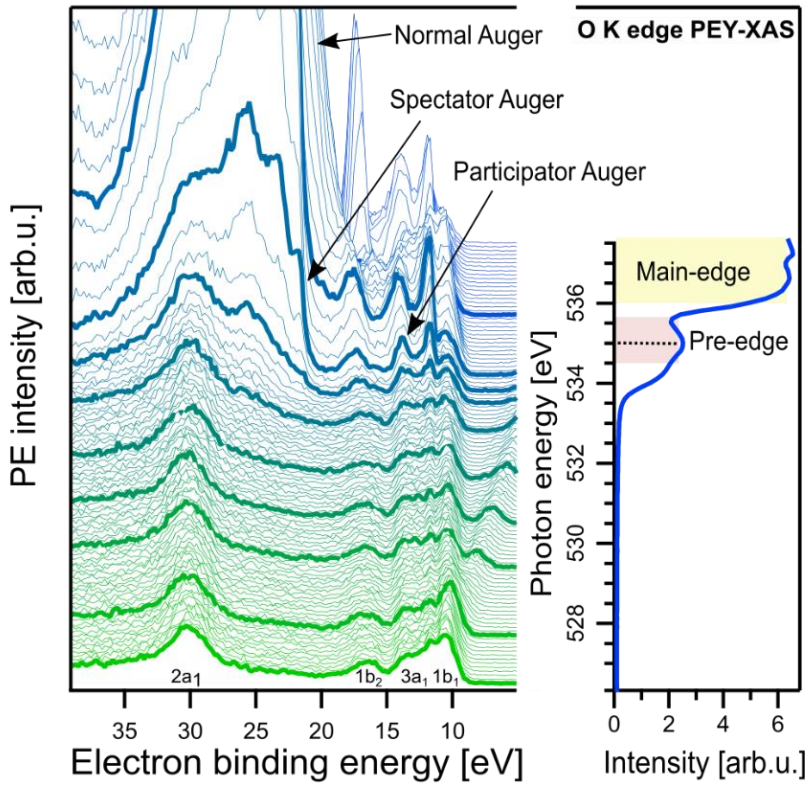

Figure 4- 3

A Series of valence photoelectron spectra of 0.05 M NaCl aqueous solution measured below and on resonance photon energies for the O 1s core orbital. All orbitals are labeled. The produced partial electron yield-X-ray Absorption (PEY-XA) spectrum is shown on the right-hand side. At resonant photon energy (535 eV), examples of the participator and spectator Auger electron signals are indicated. These signals give rise to the pre-edge peak (red-shaded area) in the PEY-XA spectrum. Above the ionization photon energy (537 eV) normal Auger electron signals are producing the main edge peak (yellow-shaded area).

By further increasing the excitation photon energy above the water O 1s ionization threshold, the system will relax via normal Auger emission (discussed in Section 2.3.1). This channel gives rise to the large signal, indicated by the arrow labeled normal Auger.

XA measurements can be achieved by observing the second-order relaxation processes (radiative or non-radiative) via photoemission or photon-emission over specific binding energy/ kinetic energy or photon energy window (partial yield) or over the whole energy range (total yield). In the following, I discuss the partial electron yield XA spectrum obtained by recording the second-

order photoemission signal intensity (appearing in the valence-spectrum window) as a function of the photon energy across the O K-edge. In the subsequent section, the spectrum recorded using the photon-emission is presented and discussed.

The so-called partial electron yield X-ray absorption (PEY-XA) over the O K-edge is presented on the right hand side of Figure 4-3. This spectrum is generated by integrating the signal intensity for each RPE spectrum shown on the left as a function of its photon energy. It consists of two spectral features which are called the pre-edge (red-shaded area) and the main edge (yellow-shaded area). The identical valence spectra which have only direct photoelectron signals, produce a constant background; while the various spectra exhibiting second order photoemission signals from the resonant Auger emission generate the pre-edge at 535 eV photon energy (red-shaded area). Also, the main edge (yellow-shaded area) is the result of the normal Auger electrons in the valence band region. As aforementioned, this PEY-XA spectrum is observing the relaxation processes happening over the valence band window. Other Auger relaxation channels could also be detected and would reproduce the XA spectrum as well, which is adopted later in Chapter 5 for the Fe L-edge XA spectra where the electron emission over the valence band region and the 3p core-orbital region are integrated separately (Section 5.3.4). The comparison of these two differently-integrated XA spectra can reveal information about the valence electron delocalization of the hematite iron oxide into the aqueous environment.

Analogous to the valence band spectrum in Figure 4.1, the vapor phase has a contribution in all RPE spectra presented in Figure 4.3, including the PEY-XA spectrum. In the latter spectrum, the vapor phase peaks appears at roughly 534.4 and 536.2 eV photon energy just below the water pre-edge and main edge. A detailed explanation of the gas phase influence on the O K-edge PEY-XA spectrum is shown later in Section 5.3.2. There, we compare the vapor phase and liquid phase spectra with the hematite NP solution measurement and we also comment on the effect of the beamline focus size. Our main interest for all the O K-edge PEY-XA spectra of the NP samples focuses on the 528-533 eV photon energy range where we observe oxygen species of NP Lattice oxides, OH^-, NO_3^- and this range is free from water signals.

4.3 O K-edge Partial Fluorescence Yield X-ray Absorption Spectra

Similar to the PEY-XA spectrum, I present and discuss here the partial fluorescence yield X-ray absorption (PFY-XA) spectrum. This is obtained by observing the second order radiative relaxation process (photon intensity) over the valence band energy region upon tuning the excitation energy across the O 1s resonance. These radiative relaxation decay channels are also called resonant inelastic X-ray scattering (RIXS) spectroscopy. Figure 4-4 left hand side shows a 2D contour map where the emitted photon energy (on the X axis) and its intensity (following the color code shown in the inset) are given as a function of the excitation photon energy (on the Y axis). Below 532 eV photon

energy, no fluorescence is emitted. At the photoexcitation energy of 535 eV, the O 1s electron is promoted to the $4a_1$ (empty) valence orbital. The system then relaxes via resonant elastic X-ray emission (marked by a white line on the map) and inelastic X-ray emission. Both signals are detected and presented in Figure 4-4. The difference between those two relaxation processes is explained in Section 2.5. Briefly, the elastic emission produces photons with identical energy as the excitation photon energy, but the inelastically emitted photon is less in energy compared to the excitation photon energy. By tuning the incident photon energy to the ionization threshold, the non-resonant X-ray emission is observed. On the right hand side of Figure 4-4, the integrated fluorescence signal of the emitted photon is presented as function of the excitation photon energy. Again, two main features are highlighted: the pre-edge (red-shaded area) and the main edge (yellow-shaded area), similar to the PEY-XA spectrum (Figure 4-3) except for the different peak intensity ratio that is due to the strong saturation effect in photon yield detections. Usually the pre-edge at 535 eV is used for energy calibration and intensity normalization of the spectra from different samples (as adopted in Chapter 7).

It is important to note that the vapor phase contribution in this PFY-XA spectrum is much smaller, almost invisible compared to the partial electron yield. This is due to the much higher probing depth of this technique and hence, the vapor signal is very minor with respect to the bulk water photon-emission signals.

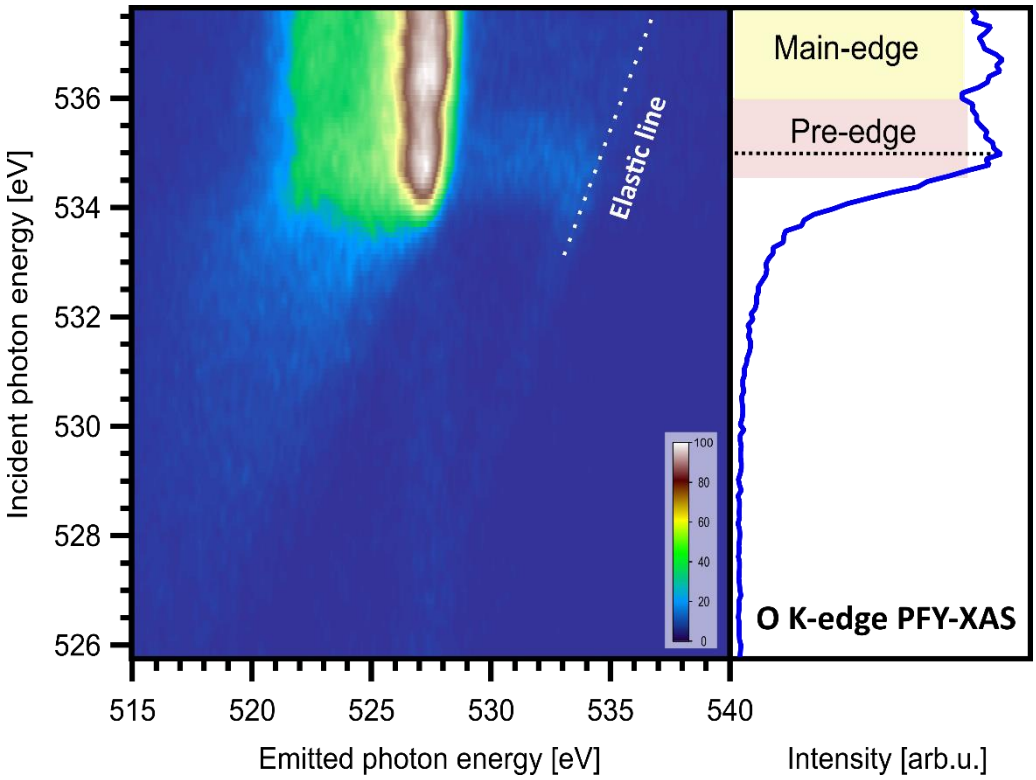

Figure 4- 4

A series of photon-emission spectra of liquid water measured below and on resonance photon energies for the O 1s core orbital are presented as 2D contour map (the incident photon energy, emitted photon energy vs the intensity in color code). The produced partial fluorescence yield X-ray Absorption (PFY-XA) spectrum is shown on the right hand side. At photoexcitation energy (535 eV), the resonant elastic and non-elastic X-ray emission produce the pre-edge peak (red-shaded area). At higher photon energy, the water molecules are ionized and non-resonant photon emission is reflected on the PFY-XA as the main edge peak (yellow-shaded area).

Chapter 5

Electronic Structure of the Hematite Fe_2O_3 Nanoparticle – Aqueous Interface

This part of the thesis is taken from the following publication:

Molecular Species Forming at the α-Fe_2O_3 Nanoparticle–Aqueous Solution Interface

Hebatallah Ali, Robert Seidel, Marvin N. Pohl and Bernd Winter

Chemical Science 2018**, 9**, 4511-4523, **DOI:** 10.1039/C7SC05156E

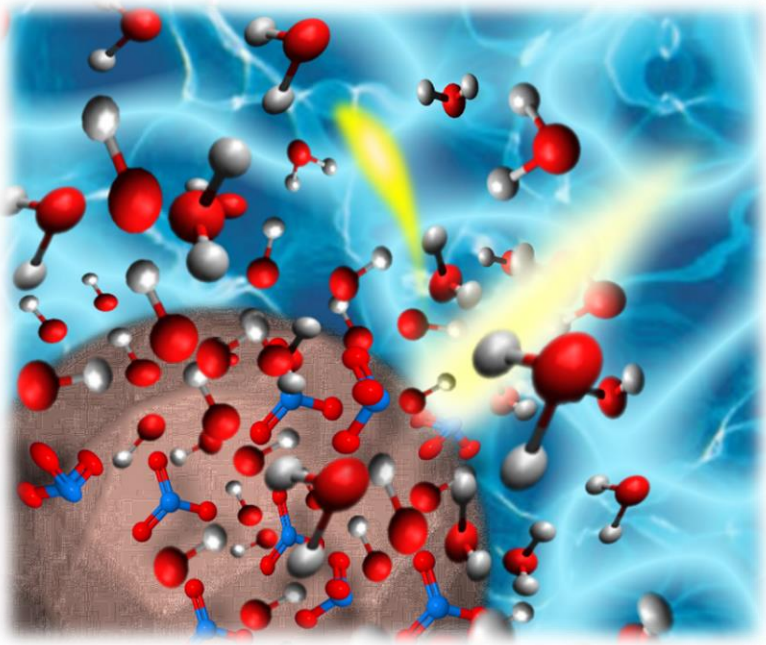

Local electronic-structure interaction, dissociative water adsorption, and electron-delocalization time at the α-Fe_2O_3 nanoparticle–aqueous solution interface are revealed from liquid-jet photoelectron spectroscopy at the oxygen-1s and iron-2p resonances.

5.1 Introduction

Iron oxides are highly abundant metal-oxide minerals on Earth[15] and play a prominent role in many environmental and technological processes,[88-92] relevant for instance in mineralogy and atmospheric science, including corrosion, catalysis, crystal growth and dissolution, as well as photo-electrochemical water splitting. Particularly the latter is of large interest in current energy research, and a central goal is to determine the atomic / molecular and electronic structure of the interface between transition-metal oxide surface and liquid water. Here we focus on photoelectron (PE) spectroscopy to determine the electronic structure.

Experimentally, photoelectron-spectroscopy investigations of the solution – solid interface remain challenging, and so are any other electron-based imaging and spectroscopy techniques routinely used in surface-science studies, requiring considerable adjustment for aqueous phase applications. In recent years several experimental developments have been demonstrated. These are (1) ambient pressure photoelectron (AP-PE) spectroscopy,[93-97] (2) photoelectron spectroscopy from liquid cells consisting of a few layers thick graphene (oxide) membrane with large transmission for electrons in the < 500 eV kinetic energy (KE) range,[31, 98-99] and (3) liquid-microjet PE spectroscopy.[32-33, 86, 100-105] AP-PE spectroscopy detects electrons ejected from the solid surface covered with a few-layer water film, stabilized at approximately 20 mbar water atmosphere. Such near-ambient pressure measurements require experimental conditions that enable collision-free travel of the electrons escaping the solution to the electron analyzer; *i.e.*, long enough electron mean free path must be ensured. The same also applies to the liquid-jet experiments, which are however typically performed at much lower pressure, ~10^{-4} mbar, and requirements for differential pumping are not as strict. Application of PE spectroscopy, arguably the most important electronic-structure technique, with its unique sensitivity to the atomic chemical environment, then enables detection of the molecular species at the solution – solid interface. The species are identified by their respective electron binding energies (BE), and in some cases by the electronic relaxation processes such as Auger decay or other autoionization channels, which is a central aspect of the present study. One of the main scientific challenges is to explore how exactly water interacts with a solid surface. This includes an understanding of the possible rearrangements of the solid surface structure, connected with catalyzed water dissociation, which would ultimately enable the control of surface properties.

This chapter reports on hematite, α-Fe_2O_3, nanoparticles (NPs) in aqueous solution. Hematite is the thermodynamically most stable iron oxide, and its interaction with water is promising for photocatalytic (cheap) solar H_2 production.[106-113] Several experimental [114-120] and theoretical [121-124] studies have been reported for single crystal surfaces. There are likely to exist six possible surface terminations of hematite [121] which can be classified into two categories, oxygen and iron terminations. Relative stabilities depend on temperature and oxygen pressure during the preparation process of the

crystalline surface.[125] However, a detailed understanding of the hematite termination remains unresolved.[126-127] There is general consensus that gaseous H_2O dissociates at the hematite surface at both high[18] and low[128] vapor exposure. Note that almost all experimental studies have been performed for gas-phase water adsorption in ultra-high vacuum[15-18, 128] or at ambient pressure.[129-130] Dissociative water adsorption is also found in density functional theory [131-134] and molecular dynamics (MD) simulations.[135]

The electronic structure of the hematite – liquid-water interface has been investigated rather little. On the experimental side we are aware of one single but significant AP-PE spectroscopy measurement from the hematite – liquid-water interface.[136] It was concluded that H_2O adsorption on the α-Fe_2O_3(0001) surface at near ambient-pressure conditions leads to hydroxylation at very low relative humidity (RH). With increasing RH, the OH coverage increases up to one monolayer, and thereafter H_2O adsorbs molecularly on top of the hydroxylated surface. Based on measured uptake curves of OH and H_2O as a function of RH the authors suggest cooperative effects among water molecules that lead to water dissociation. The water-catalyzed dissociation is argued to result from the stabilization of the dissociated state due to the strong hydrogen bond between H_2O and OH which lowers the kinetic barrier for water dissociation.[136] Finally, observed small oxygen-1s binding energy shifts of adsorbed OH as a function of water coverage are possible indications of the occurrence of different OH species or α-Fe_2O_3(0001) surface reconstruction. We would also like to point out an MD simulation of hematite NPs in water.[137] Smaller NPs (1.6 nm) were observed to exhibit larger disorder of the crystalline structure, and also the immediate two water layers are less ordered than for the larger (2.7 nm) particles studied. These results are in accord with a combined vibrational spectroscopy and MD simulations study.[22]

In the present study, I perform liquid-jet PE spectroscopy measurements in conjunction with soft-X-rays from hematite NPs dispersed in aqueous solution. This is the *all-in-solution* approach to investigate the electronic structure of the Fe_2O_3 – water interface, and no such attempt has been reported previously. Although we expect that the actual O 1s photoelectron spectrum from dissociated H_2O at the NP surface will not provide consequential new information with regard to the aforementioned AP-PE study from hematite crystal,[136] there is however an interest in aqueous suspension of hematite NPs for potential (photo)electrochemical applications. We also like to point out that liquid jet studies have the advantage that photon beam damage or impurities (often carbon) encountered in AP studies are essentially absent in flowing samples. Yet, NP (aq) studies remain challenging and complicated for several reasons. One issue is the preparation of aqueous solutions in which the NPs are prevented from aggregation. Another concern is the small electron escape depth in aqueous solution [35, 59-60] which would suggest that detection of electrons with kinetic energies below approximately 500-700 eV (approximately covering the energies of the Auger electrons considered in

this work), originating from the NPs in solution, is unfeasible. Regarding the first point, preparation of stable NP (aq) suspension requires addition of a stabilizer, typically by pH variation. Only if the surfaces are charged the particles will be electrostatically repelled from each other, and do not form aggregates that sediment out. Inevitably, the adsorption of charged molecules at the NP surface implies that the neat Fe_2O_3 NP–water interface would be difficult to explore; this also applies to previously reported aqueous-phase NP studies.[138-139] In the present case α-Fe_2O_3 NPs, 6 nm diameter, are stabilized in 0.05 and 0.1 M HNO_3 aqueous solution, yielding a positive zeta potential. At this acidic pH the NP surface will interact with NO_3^- anions; at these low concentrations all HNO_3 molecules in the solution dissociate into NO_3^- and $H^+(H_3O^+)$.[140] It is thus crucial to explore and establish experimental conditions that reasonably balance the stabilizer concentration with a large enough number of NP surface sites for interaction with H_2O molecules. With respect to the second point, we show here that liquid-jet PE spectroscopy is capable to detect the electronic structure of the hematite NP–aqueous solution interface despite the small electron mean free path in solution.[35] Specifically, from a combination of core-level and resonant (oxygen 1s and the iron 2p edges) valence PE measurements, and also from analysis of the derived partial-electron-yield X-ray absorption (PEY-XA) spectra we observe the small signal from adsorbed OH species which can be distinguished from the nitrate species, NO_3^- (aq) and NO_3^- (ads). Furthermore, the interfacial electron signal can be distinguished from the electrons emitted from the interior of the aqueous-phase NPs.

5.2 Methods and Materials

The photoemission measurements were conducted using the SOL^3 liquid-jet PE spectroscopy setup[62] at the U49 PGM soft-X-ray beamline of the synchrotron-radiation facility BESSY II, Berlin. Electrons were detected in a direction perpendicular to the polarization vector of the X-ray beam, with the latter intersecting the horizontal liquid jet also at 90° angle. The liquid jet was produced by pushing the aqueous solution at a flow rate of 1.2 ml/min and at approximately 25 bar through a 35-µm inner-diameter quartz capillary into the vacuum chamber. This diameter is considerably larger compared to the typically 15-20 µm in most of our previous liquid-jet PE spectroscopy studies,[33, 100] but the larger size was found here to deliver more stable jets in the case of NP solutions. The jet temperature at the position of interaction with the X-rays (approximately 0.3 mm downstream of the glass capillary) was approximately 2-5 °C. This is a crude estimate, accounting for the reservoir temperature of 10-15 °C and the varying relative amount of measured water gas-phase signal intensity when ionizing the liquid jet further downstream. An exact determination of the jet temperature has been reported for 10-µm diameter based on a measurement of the velocity distribution of evaporating water molecules, yielding a temperature of ∼6 °C. [141] Under liquid-jet operation conditions a pressure of 7.5×10^{-4} mbar was maintained in the interaction chamber using a molecular turbo pump (1600 l/s) and two liquid-nitrogen cold traps. Using an 80-µm exit slit of the beamline the energy resolution at 500 eV photon energy

(near the oxygen K-edge) was better than 130 meV, and at 700 eV photon energy (iron L-edge) the resolution was better than 200 meV. The focal size of the X-ray beam was approximately 60 x 60 μm^2. Electrons were detected with a HiPP-2 (ScientaOmicron) hemispherical energy analyzer which is part of SOL[3]. The 500-μm-diameter detector orifice was at 0.5 mm distance from the liquid jet. With the analyzer pass-energy set to 100 eV the energy resolution was approximately 100 meV in our experiments.

Iron oxide, α-hematite (Fe_2O_3), nanoparticles of 6 nm diameter dispersed in 0.05 and 0.1 M HNO_3 aqueous solutions, were purchased from PlasmaChem [http://www.plasmachem.com]. The following three NP solutions were studied: 5 wt% NPs in 0.1 M HNO_3 aqueous solutions (pH 1.55), 10 wt% NPs in 0.1 (pH 1.9) and 0.05 M (pH 2.0) HNO_3 aqueous solutions. The 0.05 M stabilizer concentration was found to correspond to the smallest amount of stabilizer, NO_3^-, at which the NPs stay separated.

5.3 Results and Discussion

5.3.1 Valence Photoelectron Spectra

Figure 5-1(A) presents the valence PE spectra from a 6-nm hematite α-Fe_2O_3 NPs, 5 wt%, aqueous solution with added HNO_3 (0.1 M), measured at photon energies 710.5 (in black) and 704.5 (blue) eV. The former energy is resonant with the lowest-energy Fe 2p → valence excitation, and the latter energy corresponds to off-resonant valence ionization. Spectra shown in the Figure are displayed on the binding energy (BE) axis, with energies given relative to the vacuum level.[33] Both spectra are presented as measured but a Shirley background has been subtracted to remove signal from inelastically scattered electrons. (Unless otherwise noted, the Shirley method is used throughout this thesis; It assumes that the background intensity at a given kinetic energy is proportional to a ratio of the integrated photoelectron signals at higher kinetic energies.[142-143]) Relative intensities of the two spectra are displayed to yield the same height of the water $2a_1$ peak (near 32 eV BE) as this inner-valence peak remains unaffected by the resonant excitation. The spectral energy positions corresponding to ionization of water orbitals $1b_1$, $3a_1$, $1b_2$, and $2a_1$ are labeled.

The most striking observation in Figure 5-1(A) is the absence of the low-energy emission band near 8.5 eV BE for the off-resonant ionization. This immediately illustrates the increased sensitivity of resonant PE (RPE) spectroscopy to otherwise weak photoelectron signals. As shown in previous studies on Fe^{3+} [139] and Ti^{3+} [144] aqueous solutions, the direct valence ionization and the (valence → 2p participator) Auger decay produce the same final states. This leads to the coherent superposition of the outgoing electron waves for the two different channels and causes the observed signal enhancement.[50] Hence the off-resonant PE spectrum in Figure 5-1(A) is essentially the spectrum of

neat water, and I can analyze the 710.5-eV RPE spectrum by eliminating the water contributions. For that I first fit the 704.5-eV (off-resonant) spectrum with the known water photoelectron peak positions and widths (determined for the much lower ionization energy of 180 eV [32]); intensities are kept as free parameters to account for unknown variations of ionization cross sections when increasing the photon energy.

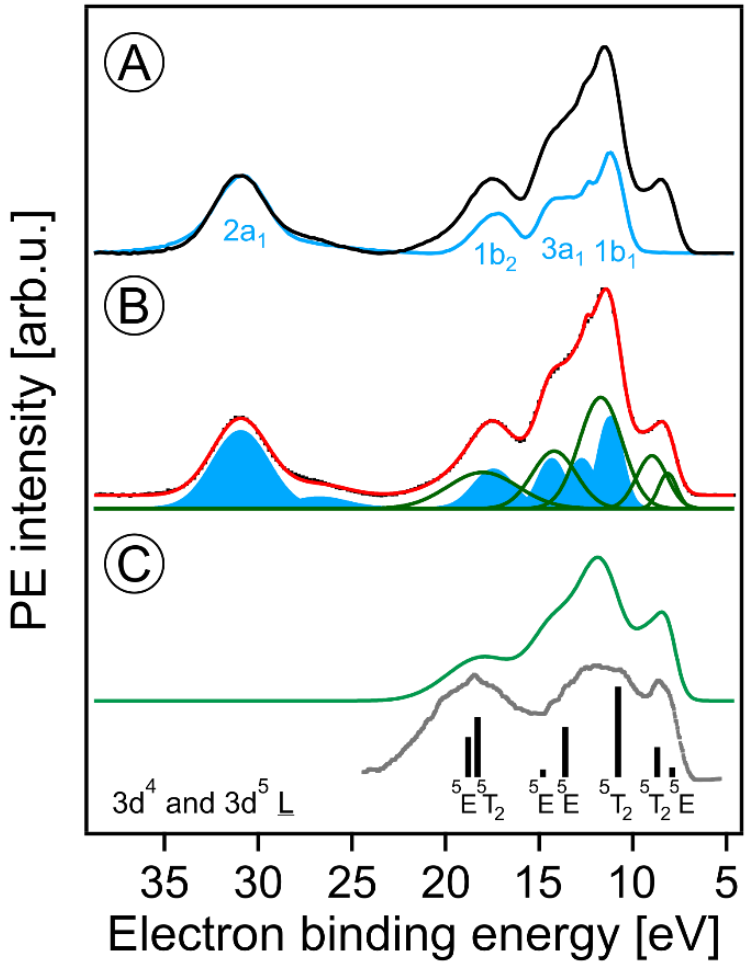

Figure 5- 1

(A) Valence photoelectron spectra from a 5 wt% α-Fe_2O_3 NP aqueous solution obtained at the iron 2p resonant photon energy 710.5 eV (black) and at the off-resonant photon energy 704.5 eV (blue). A Shirley background has been subtracted. Contributions from water ionization are labelled. (B) Decomposition of the 710.5 eV spectrum of (A) into contributions from water (blue-filled Gaussians) and iron (green Gaussians). The black-dotted line is the total fit. (C) The green spectrum represents solute-only spectral contributions; it is the sum of the green Gaussians in (B). The grey line is the photoelectron spectrum from solid α-Fe_2O_3 measured in ultrahigh vacuum; from ref [145]. The black sticks are calculated energy positions and weights from ref [146]. Both the grey spectrum and the calculated energies were shifted by the work function (5.4 ± 0.2 eV) [18] as to match the liquid-jet spectra which are presented with reference to the vacuum level.

The respective water contributions are presented by the blue Gaussians in Figure 5-1(B). The signal arising from NP ionization is then accounted for by introducing five unique additional Gaussians (green curves); the total fit in Figure 5-1(B), shown in red, accurately reproduces the 710-eV RPE spectrum. In Figure 5-1(C), I present the spectrum resulting from summing up the Gaussians in Figure 5-1(B) that represent signal from NP ionization. A detailed interpretation will be provided below with the help of PE spectra measured at the oxygen 1s edge. We note that the experimental NP valence spectrum is in an overall fair agreement with a previously reported valence PE spectrum from crystalline α-hematite [145] (in grey) measured in ultra-high vacuum. There are clearly distinct differences though. Most noticeable is the occurrence of extra PE signal near 14.5 eV BE, which is due to the effect of the aqueous solution on the Fe 3d – O 2p hybridization which causes a strong ligand-to-iron charge transfer[50] in this metal oxide.

The major conclusion from Figures 5-1(A) and 5-1(B) is that electron emission from the Fe_2O_3 NPs is definitely detectable in the present liquid-jet experiments. This is not self-evident because of aforementioned small electron mean free paths in aqueous solutions at the present KEs;[35, 59] this will be detailed later. The lowest-ionization energy peak in Figure 5-1(B) (due to the highest-occupied molecular orbital, HOMO, which is of metal 3d nature) of the solution cannot be fit by a single peak. I assign the two Gaussians, at 8.2 eV and 9 eV BE, to the t_{2g} (with 3-electron occupancy) and e_g (2 electrons) levels which arise from the iron $3d^5$ high-spin levels in an octahedral ligand field.[147] To support this assignment, I need to collect more electronic structure information though, for instance from the PEY-XA spectra which provide the 10Dq values. Moreover, I must explore whether the observed energies are due to electrons emitted from the NP surface or the interior. It should be noted that the 8.2 and 9 eV energy positions are smaller than the respective iron t_{2g} and e_g energies, 8.9 and 10.2 eV, reported for aqueous Fe^{3+} cation.[50] On the other hand, a single peak at 10.3 eV BE was observed in a later liquid-jet PE study.[148] Such differences between the iron-oxide NP and the iron hexa-aqua complex can be attributed to the different ligand fields arising from the specific local environments. Previously reported valence PE spectra from the α-Fe_2O_3 (1012) crystalline surface in ultra-high vacuum also exhibit a broad unresolved HOMO peak near 8.5 eV,[145] similar to the spectrum in Figure 5-1(A). Also, a very recent valence PE spectroscopy study from a powder of 7-nm diameter iron-oxide NPs exhibits a single broad Fe 3d derived peak.[149] Yet, theoretical calculations[146] do reproduce the split as shown by the sticks in Figure 5-1(C).

5.3.2 O 1s Resonant Photoemission and Partial-Electron-Yield XA Spectra

I now explore the photoemission spectra measured for photon energies near the oxygen 1s core-level ionization threshold. These (valence) RPE spectra contain contributions from direct valence photoionization and from non-radiative relaxation channels, associated with the oxygen 1s core-hole refill. Results from 5 wt% α-Fe_2O_3 NPs of 6 nm diameter, dispersed in 0.1 M HNO_3 aqueous solution (same solution as in Figure 5-1), are presented in Figure 5-2(A). At photon energies < 528.0 eV one essentially measures the valence PE spectra from neat water; compare the discussion on Figure 5-1(A). All spectral changes occurring for increasing photon energies are then associated with the oxygen 1s electron promotion into the partially occupied t_{2g}, e_g, and empty valence orbitals. The first absorption peak of neat water (O 1s → $4a_1$; pre-peak) occurs at 535.0 eV photon energy,[150-151] with an absorption onset at approximately 533.0 eV. In order to accurately determine the full absorption spectrum, I look at the respective O 1s PEY-XA spectrum, presented in Figure 5-2(B), which was obtained by integrating the signal intensity of each RPE spectrum between 15 and 27 eV BE. The steep water absorption onset at 533.0 eV is clearly visible. All other features, at 532.2 eV (peak ***a***), 531.5 eV (small shoulder ***b***), and 530 eV (peak ***c***) must arise from oxygen-containing species other than bulk-phase H_2O, and these are of particular interest here.

The origin of the absorption peaks ***a***-***c*** can be explained by an analysis of the accompanying changes among the respective RPE spectra. For convenience, I project the RPE spectra in Figure 5-2(A) onto a color-coded 2-dimensional representation. The resulting photon-energy *versus* electron BE map is shown in Figure 5-2(C). In addition, I present in Figure 5-2(D) the single RPE spectrum measured at resonance ***c***, as this helps to better visualize this small feature. Absorption peak ***a*** is caused by an intensity increase near 17 eV BE, and also by a band of at least six overlapping peaks in the 21.0-24.5 eV BE range, as can be seen by the changing color at 532.2 eV excitation photon energy in the encircled area. These energies correspond to spectator Auger electrons from aqueous-phase NO_3^- as has been measured previously for HNO_3 aqueous solutions.[62] The PE spectrum at 532.2 eV resonance (peak ***a***) from a 0.5 M HNO_3 aqueous solution will be shown later, when I determine the spectral contributions from surface-adsorbed species.

Since the hematite-NP surface is positively charged, as inferred from the measured zeta potential of +30 mV, NO_3^- molecules will inevitably bind at the surface. Evidence for that is indeed found in the O 1s X-ray absorption spectrum, shown in Figure 5-3, where we present results from 10 wt% NP / 0.1 M HNO_3, 0.5 M HNO_3, 0.5 M NaOH aqueous solutions, and from neat liquid water; in addition, the O 1s XA spectrum from gas-phase H_2O is shown. The liquid water spectrum (blue line), presented in the inset figure, is a PEY-XA spectrum which was previously measured in our laboratory with a smaller capillary (15 μm diameter compared to 35 μm here) to form the liquid jet. Furthermore, in that study a smaller (23 x 12 μm^2) X-ray focus was available.

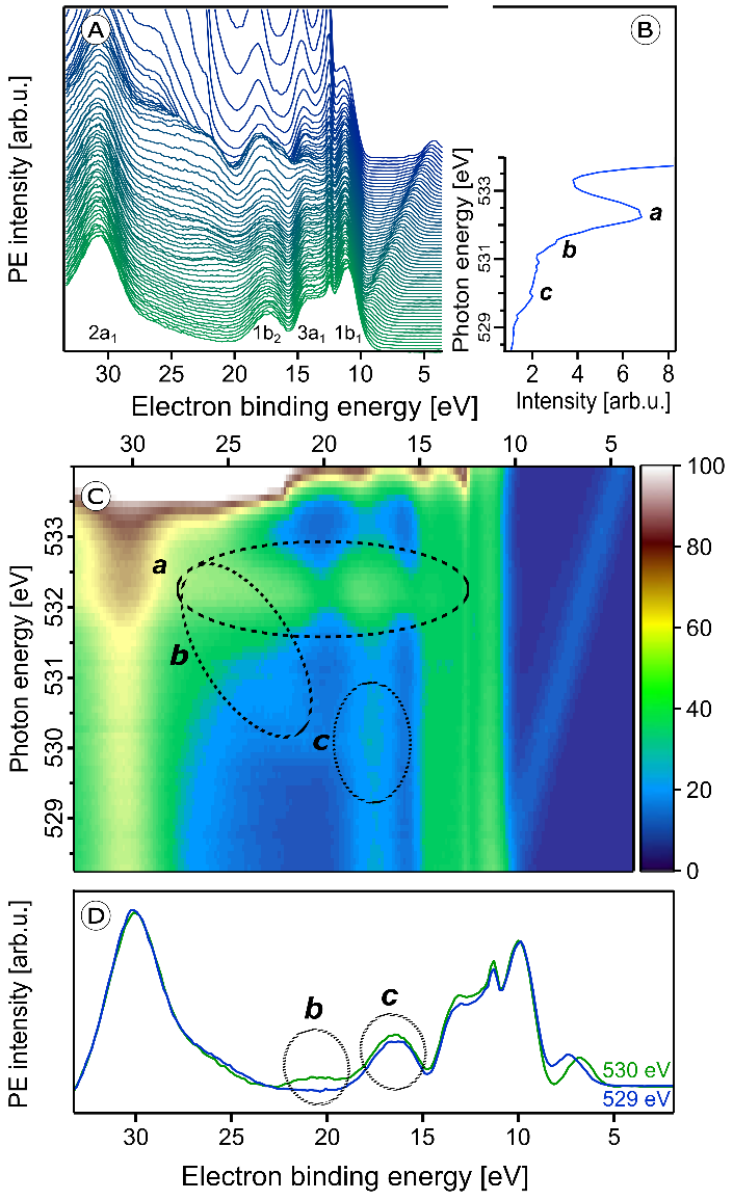

Figure 5- 2

(A) Series of oxygen 1s resonant photoelectron (RPE) spectra from 5 wt% α-Fe_2O_3 NPs in 0.1 M HNO_3 aqueous solution. (B) Resulting partial electron yield X-ray absorption (PEY-XA) spectrum. Peak ***a*** *(532.2 eV) is the absorption of NO_3^-. Bands* ***b*** *(531.5 eV) and* ***c*** *(530.0 eV) are absorptions by lattice oxide of the hematite NPs. (C) Contour map of the oxygen 1s RPE spectra shown in (A); spectral intensities are given by the color code on the right side. Absorptions* ***a***, ***b***, *and* ***c****, are marked by the three black circles. (D) RPE spectrum from Figure 5- 2(A) for photon energy 530.0 eV (c resonance) together with the off-resonant valence PE spectrum measured at 529.0 eV. Important to note is the slightly larger intensity in the 530-eV spectrum at 17.5 eV BE (bottom tier) which is the same contribution that gives rise to the weak signal enhancement, labeled* ***c****, in Figure 5-2(C). More details are provided in Figure A-5-1 of the Appendix section.*

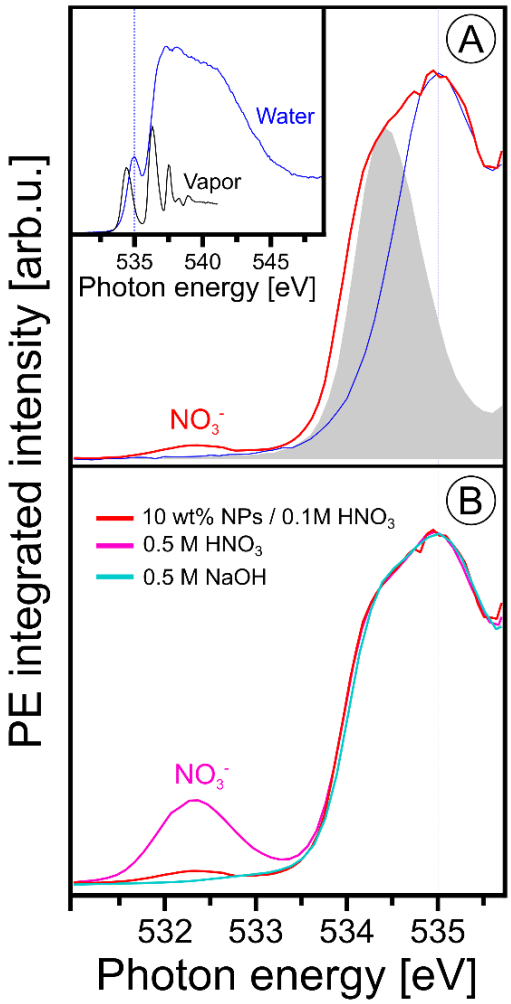

Figure 5- 3

(A) Oxygen 1s PEY-XA spectra from 10 wt% NP / 0.1 M HNO_3 aqueous solution (in red) and from neat water measured under conditions that considerably suppress the spectral contributions from gas-phase water; see discussion in Experimental section. Spectral intensities are adjusted to yield the same heights of the water pre-edge peak, at 535.0 eV. The grey-shaded peak is the leading absorption of gas-phase water; the full spectrum is presented in the inset figure where we also show an extended range of the liquid water spectrum. The latter was obtained from signal integration of the leading Auger peak that overlaps with the valence PE band; the procedure has been discussed in ref [152]. (B) Oxygen 1s PEY-XA spectra from 0.5 M NaOH (light blue), from 0.5 M HNO_3 (pink), and from 10 wt% NP / 0.1 M HNO_3 aqueous solutions. All spectra in (B) were measured using the same large-diameter glass capillary. Note that under these experimental conditions the absorption peak of hydroxide is not resolved (reported near 533 eV [153-154]), and furthermore the small signal from hydroxide strongly overlaps with the large water gas-phase absorption.

Both effects are the reason for a large contribution of gas-phase H_2O to the aqueous solution XA spectra in the present study, which is clearly seen in Figure 5-3(A) displaying the spectra from the NP solution (in red) and from water (from inset figure), for both gas-phase (grey-shaded peak) and liquid water (blue line) on top of each other. The large shoulder at 534.4 eV observed in Figure 5-3(A) is thus the signal from gas-phase water, and from comparison with the XA spectrum from 0.5 M NaOH (light blue line in Figure 5-3(B)) which exhibits small signal near 533 eV, I see that contributions from gaseous water and OH^- (aq) strongly overlap. Since the hydroxide concentration in the NP solutions is so small, a meaningful quantification of its signal on the large water background thus seems unreasonable. Yet, an attempt to single out OH signal based on subtraction of gas-phase signal from the NP (aq) XA spectrum is presented in Figure A-5-2 of the (Appendix Section 5.5). It shows measurements from three different NP solutions, each representing a different fraction of surface sites available for H_2O adsorption. The analysis indeed suggests a small signal from hydroxide at 533 eV, and there is also an indication that the signal intensity may increase with the available surface sites. More details on the data analysis are provided in the Appendix Section 5.5. Unlike the OH^- X-ray absorption, NO_3^- absorbs at considerable lower energies than water, near 532.3 eV, as can be seen from the XA spectrum from 0.5 M HNO_3 aqueous solution in Figure 5-3(B). Hence, NO_3^- can be easily identified in the NP (aq) XA spectra.

In order to obtain a more significant spectroscopic signature from hydroxide adsorbed at the NP – solution interface I next consider the RPE spectra measured at the X-ray absorption maximum, 532.2 eV (peak ***a***; Figure 5-3). These spectra are barely affected by gas-phase water, and I can detect adsorbed hydroxide and nitrate simultaneously. Results are shown in Figure 5-4 for the same solutions briefly mentioned in the previous paragraph where I discussed the XA spectra. As introduced along with Figure A-5-2 the NPs in the different solutions differ by the amount of adsorbed nitrate, and hence the fraction of available adsorption sites for water varies, which is controlled by the concentration of the NPs and the concentration of stabilizing HNO_3. The nitrate-to-free surface sites ratios studied here are approximately 1:1 (labeled [1:1] in Figure 5-4) for 5 wt% NP in 0.1 M HNO_3, 1:2 ([1:2]) for 10 wt% NP in 0.1 M HNO_3, and 1:4 ([1:4]) for 10 wt% NP in 0.05 M HNO_3. For reference, Figure 5- 4 also includes the spectra from 0.5 M HNO_3 and 0.5 M NaOH aqueous solutions, the latter is measured at 532.8 eV excitation energy (close to peak ***a***). All spectra are displayed with the corresponding off-resonant spectra subtracted which singles out the spectral features that get enhanced. Note that subtraction of the large water signal is the reason for the rather poor signal statistics. As-measured RPE spectra are shown in Figure A-5-3 of the Appendix Section 5.5. One important observation from Figure 5-4 is that the RPE spectrum for highest NO_3^- (ads) concentration (ratio 1:1) is almost the same as the one from bare HNO_3 aqueous solution. In both cases four main photoemission bands are observed, at approximately 16.0, 18.0, 22.5, and 24.5 eV BE (all within the

red-shaded area), arising from various Auger-electron decays upon O 1s → valence excitation at 532.2 eV photon energy.

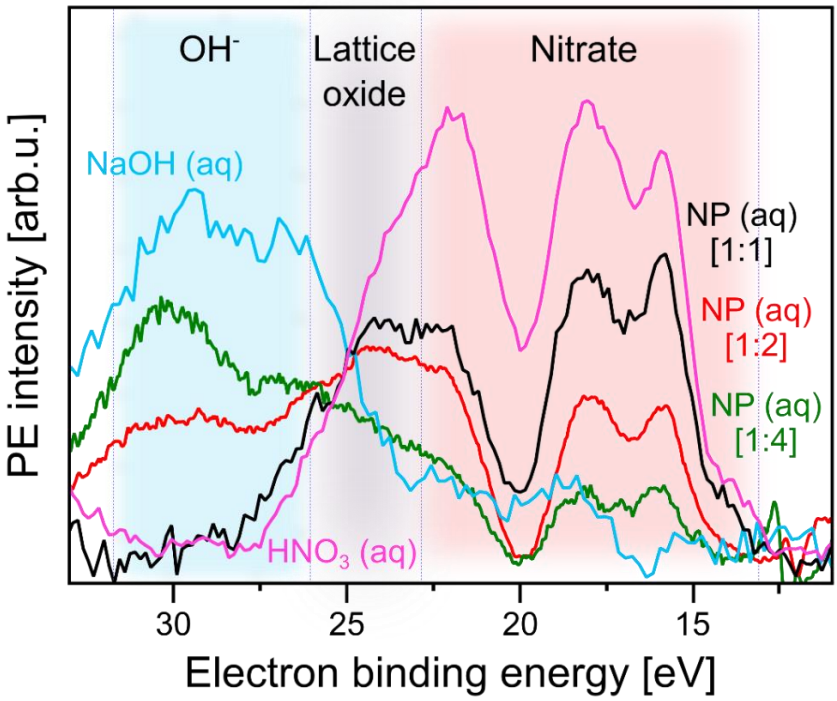

Figure 5- 4

*Photoelectron spectra at resonance a (532.2 eV) from three α-Fe_2O_3 NPs aqueous solutions, as well as from 0.5 M HNO_3 and 0.5 M NaOH (measured at 532.8 eV, near **a**) aqueous solutions. In all cases the respective off-resonant photoelectron spectrum has been subtracted. Results for the following NP solutions are shown: Purple: 0.5 M HNO_3. Black: 5 wt% NP in 0.1 M HNO_3 [1:1]. Red: 10 wt% NP in 0.1 M HNO_3 [1:2]. Green: 10 wt% NP in 0.05 M HNO_3 [1:4]. The additional spectrum from 0.5 M NaOH is shown in blue. The shaded areas mark spectral regions which are dominated by contributions from a single species: Blue region: OH^-. Grey region: lattice oxide. Red region: NO_3^-. In square brackets the ratios of number of adsorbed NO_3^- to number of available surface sites of the hematite NPs are shown. These ratios are estimates based on the total surface of the NPs in a given volume, and assuming a density of adsorption sites of 5.6 nm^{-2} which is the value reported for crystalline hematite;[130] see also description of Figure A-5-2 where I analyze the XA spectra from the same solutions.*

The fact that the spectra present close resemblance indicates that the electronic structure of NO_3^- (aq) changes little upon adsorption at the NP surface. The 4-peak structure of the HNO_3 (aq) spectrum can be qualitatively attributed to Auger processes that involve orbitals with NO_3^- character. These have

energies of approximately 9.5, 16.0, 19.5 eV BE, as determined from an (off-resonant; 200 eV photon energy) valence PE spectrum from 1M HNO_3 aqueous solution presented in Figure A-5-4 (in the Appendix Section 5.5). The leading peak at 15.5 eV is due to a participator Auger decay. A more accurate assignment of the NO_3^- Auger-electron spectrum would require quantification of screening effects of the core hole, and also consideration of the nitrogen *versus* oxygen characters of the orbitals.[155]

With increasing number of available H_2O adsorption sites on the NP surface (ratio 1:4) the RPE spectrum (green in Figure 5-4) still exhibits a similar overall shape as the one from NO_3^- (aq) but relative peak intensities in the 15-20 eV BE range change, and peak energies tend to shift slightly. In addition, peaks seem to broaden but this effect cannot be quantified due to insufficient signal statistics. These changes are attributed to the occurrence of signal from adsorbed OH^- which is concluded from comparison with the 0.5 M NaOH aqueous solution. The respective RPE spectrum (in blue) exhibits a rather similar overall shape as the one from the [1:4] NP solution (green). I particularly point out the appearance of a 28.5 eV BE peak (blue-shaded area) for the latter solution which is an unequivocal signature of OH^- (compare blue spectrum). The differences of all spectral intensities are argued to arise primarily from the varying relative ratios of adsorbed NO_3^- over OH^-. But I also expect small energy differences between free and adsorbed hydroxide, and I also note that in the NP spectrum the 28.5-eV OH^- peak overlaps with the electron emission from NP lattice oxygen (23-28 eV BE region; grey-shaded), although this signal has larger intensity at the slightly lower absorption energy corresponding to peak ***b*** (531.5 eV) in Figure 5-2(C).

I return to Figure 5-2 to discuss X-ray absorption peaks ***b*** and ***c***. Both oxygen-1s excitations must arise from the Fe_2O_3 NPs (aq), and I now differentiate between the contributions from the NP – solution interface *versus* those from the NP interior (bulk). As seen from Figure 5-2(C) absorption ***b*** (see also Figure A-5-1) correlates with a signal increase in the RPE spectra near 23 eV BE, whereas ***c*** correlates with a very small increase of the 17.5-eV BE peak. In an attempt to somewhat enhance the visibility of absorption ***c***, I display in Figure 5-2(D) the relevant single RPE spectrum, at 530.0 eV excitation energy, selected from Figure 5-2(A). This spectrum is compared with the off-resonant PE spectrum measured at 529.0 eV, and one notices a small signal increase at the 17.5 eV BE. In Figure A-5-1 of the Appendix Section 5.5 I show that this increase vanishes when the photon energy is raised slightly above the ***c*** resonance.

From comparison with L-edge X-ray absorption spectra from hematite crystal measured at ~10^{-4} mbar water pressure,[156] I assign absorptions ***b*** and ***c*** to the O 1s → t_{2g} (at 530.0 eV) and O 1s → e_g (at 531.5 eV) transitions, respectively. The energy difference yields 10Dq = 1.5 eV. Previous XA

spectroscopy studies from α-Fe_2O_3 [16] have reported very similar absorption energies of 530.2 and 531.6 eV, respectively, *i.e.*, 10Dq = 1.4 eV.[17, 157-162] Another study, of supported 8- and 30-nm hematite NPs [163] finds absorption maxima at 530.4 (for O 2p – Fe t_{2g}) and 531.8 eV (for O 2p – Fe e_g) photon energies. In the same work, also crystalline hematite has been investigated, and the authors observed the identical 10Dq value of 1.38 eV, concluding that there is no evidence for a size-driven effect. The slightly larger 10Dq (1.5 eV) in the present study is thus argued to result from the hematite NP's modified electronic structure in the presence of an aqueous solution. This conclusion will be corroborated by RPE measurements at the iron 2p (L) edge. With above assignments to electron promotion into t_{2g} and e_g states, which are separated by 1.5 eV, one would expect similar RPE spectra for ***b*** and ***c*** excitations. But this is not observed experimentally. Referring to the computed electronic states of $(FeO_6)^{9-}$, [16, 147] and considering solely involvement of t_{2g} states the peak at 17.5 eV BE (corresponding to ~512 eV kinetic energy) could be qualitatively understood as arising from O^{2-} 1s-$1t_{2g}1t_{2g}$ spectator Auger decay. Here, excitation from the oxygen 1s core-level into the empty $2t_{2g}$ (spin down) level is followed by core-hole refill from the $1t_{2g}$ level, and electron release from $1t_{2g}$. Similarly, for the O^{2-} 1s → $4e_g$ excitation at 531.5 eV the peak at ~22.5 eV BE (corresponding to ~509 eV kinetic energy) can be explained by O^{2-} 1s-$3e_g3e_g$ spectator Auger decay. I am unable though to provide a more quantitative explanation based on the available data.

5.3.3 O 1s Core-Level Photoelectron Spectra

In the previous section surface bound NO_3^- and OH^- species were shown to give rise to characteristic signals in the O 1s RPE valence spectra. I now explore the signature of these species in the non-resonant O 1s PE spectra, shown in Figure 5-5(A). The spectra were obtained from the 6-nm diameter Fe_2O_3 NPs (10 wt% aqueous solutions) for the two HNO_3 concentrations 0.1 M (in red) and 0.05 M (in green). For comparison, the spectrum from 0.05 M NaCl aqueous solution containing no NPs, and essentially representing neat water, is presented as well (in blue). The spectra are normalized to their peak maxima, as shown in the inset of Figure 5-5(A). A photon energy of 1200 eV was used to deliberately generate O 1s photoelectrons with approximately 650 eV KE, which is similar to the electron energies detected in case of the Fe 2p RPE spectra shown in Figure 5-1. This assures a comparable probing depth into the solution for both cases. And more important, the inelastic mean free path of the ~700 eV photoelectrons is obviously large enough to detect electrons born at the NP (aq) surface and even originating inside the NPs (aq). However, the exact probing depth into the particles as well as the distance of the NPs from the solution surface cannot be quantified here. For recent estimates of electron mean free paths in liquid water and aqueous solutions we refer to references.[59-60]

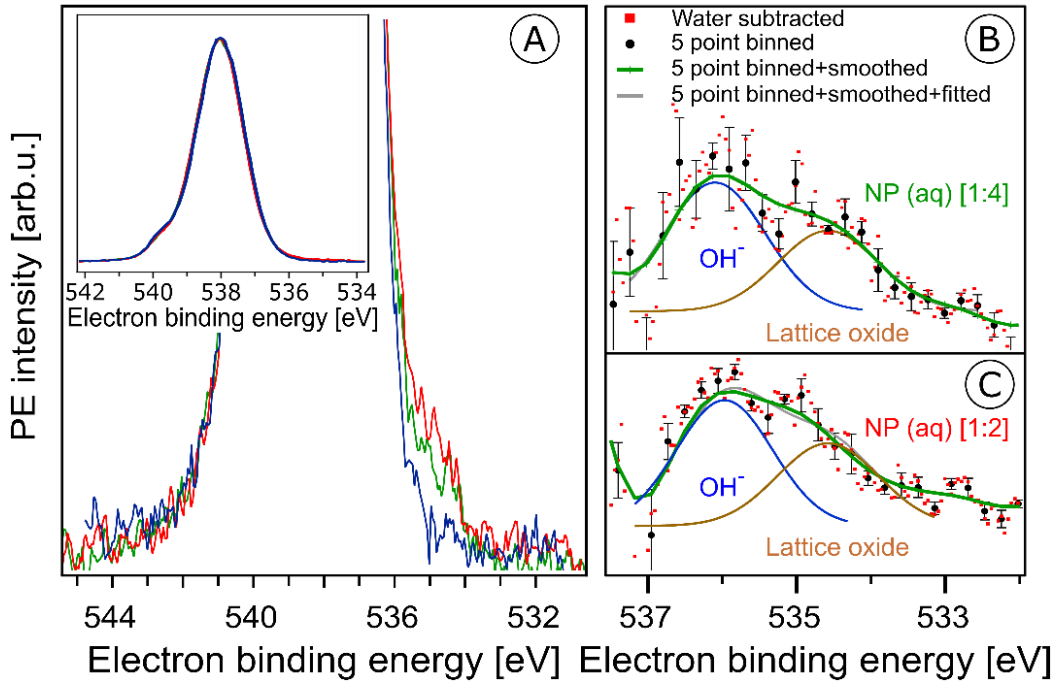

Figure 5- 5

(A) Oxygen 1s photoelectron spectra from the 10 wt% hematite NPs in 0.1 M HNO_3 aqueous solution (corresponding to [1:2]; red curve), and in 0.05 M HNO_3 aqueous solution (corresponding to [1:4]; green curve). For reference, the spectrum from 0.05 M NaCl aqueous solution (blue curve) is also shown. Photon energy was 1200 eV. In the main figure, the O 1s peak has been cut at about 25% of its intensity. The full peaks, and the intensity normalization is seen in the inset figure. (B), (C) Oxygen 1s photoelectron spectra in the 538-532 eV binding energy region which covers the O 1s photoelectron peaks from OH^- (536.1 eV) and lattice oxide (534.7 eV). (B) shows results for the 10 wt% hematite NPs / 0.05 M HNO_3 aqueous solution (corresponding to [1:4]), and (C) for 10 wt% hematite NPs / 0.1 M HNO_3 aqueous solution (corresponding to [1:2]) after subtraction of the 0.05 M NaCl aqueous solution spectrum (red dots). Black dots in (B) and (C) result from five-point-binning of the red dots, and the green line results from additional smoothing. Error bars, representing the standard deviation from five-point-binning, are still fairly large. They are too large to reveal the expected increase in the OH-to-lattice oxide signal ratio when going from [1:2] to [1:4] solution. See also Figure A-5-5 for the raw data.

PE spectra from the two NP solutions (Figure 5-5(A)) are seen to be by far dominated by photoelectrons from liquid water, giving rise to the strong peak at 538.0 eV BE.[164] A small shoulder at 540.0 eV BE arises from ionization of gas-phase water. The photoelectron signal contributions from oxygen species, primarily OH^- bound to the NP (aq), appear at lower BE than water, and the intensity is very small, slightly greater than the baseline signal. An enlarged view of the spectral region of

interest (with the water spectrum subtracted) is presented in Figures A-5-5(A) (NP / 0.1 M HNO_3) and A-5-5(B) (NP / 0.05 M HNO_3). These spectra exhibit very poor statistics though, and in order to demonstrate that the data are yet statistically significant the as-measured individual data points (of Figure A-5-5) were binned and the resulting error bars have been determined. Results for five-point binning are presented in Figures 5-5(B) and 5-5(C), where I also provide error bars and Gaussian fits to reproduce the observed double-peak spectrum. A more detailed description of the data handling is given in the caption of Figure 5-5. The higher-BE peak at 536.1eV (1.0 eV width), which is 1.9 eV smaller BE than liquid water, can be assigned to adsorbed OH^-, in agreement with several reported surface hydroxyl species formed on the hematite crystal surface. [15, 26, 126, 165] Note that NO_3^- can be ruled out because its O 1s signal contributes to the O 1s (aq) peak at 538.1 eV and cannot be deconvoluted due to the high concentration of bulk water.[138, 166] My assignment also agrees with a previous liquid-jet PE measurement from 4 molar NaOH aqueous solution, reporting a 536.0-eV O1s BE of OH^- (aq).[153] As in the case of the O 1s RPE spectra (Figure 5-4), a distinction between aqueous-phase OH^- and the adsorbed hydroxide is not possible on the grounds of the PE spectra of Figure 5-5. However, our assignment of adsorbed OH is justified by the acidic pH of the NP solutions. Perhaps another indication is the slight increase of OH signal for the [1:4] solution in qualitative agreement with the resonant O 1s photoelectron spectra of Figure 5-4. The lower-BE peak at 534.7 eV (*i.e.*, 3.3 eV smaller BE than liquid water) and approximately 1 eV width is attributed to the O 1s BE of the lattice oxygen of the hematite NPs (aq). This is in agreement with the energy difference found in an ambient-pressure PE study of a few-monolayer liquid water film on top crystalline α-Fe_2O_3 (0001).[136] A remaining and somewhat puzzling observation from Figures 5-5(B) and 5-5(C) is that the O 1s signal intensities from the lattice oxide and from surface OH^- are rather similar. Our explanation is that at the electron kinetic energies relevant here the electron inelastic mean free path approximately matches the distance between NP surface and the solution surface. This is a reasonable assumption, based on reported estimates of the mean free path in aqueous solutions[35] which strongly encourages liquid-jet PE spectroscopy studies with tender X-rays to probe deeper into both the solution and into the NPs.

5.3.4 Fe 2p Photoemission and PEY-XA Spectra

In the following I explore the photoemission spectra for excitation energies resonant with the Fe 2p → valence transitions. The idea of these measurements is analogous to the oxygen 1s excitation discussed along with Figure 5-2. I am thus interested in the evolution of the RPE spectra when varying the photon energy across the Fe 2p (only $2p_{3/2}$, *i.e.*, the L_3 edge is considered here) resonance, and how this reflects in the Fe L_3-edge PEY-XA spectra. XA spectra will be obtained for two different

relaxation channels, one corresponding to the refill of the 2p core-hole by a valence electron, and in the other case the refill is by another core-level electron. The specific Auger decay channels are 2p-3d3d and 2p-3p3p which lead to electron emission in the 672–715 eV and 560–600 eV kinetic energy ranges, respectively. Hence, signal integration of the RPE spectra within these boundaries yields the respective PEY-XA spectra. In (2p-3d3d) PEY the electron refilling the core hole originates from an iron 3d valence orbital (spectra are denoted as $P^{V}EY$). The 3d orbitals carry information on the mixing with ligand-centered orbitals. On the other hand, in (2p-3p3p) PEY the core-hole is refilled by electrons from the deeper Fe 3p orbitals which only weakly interact with the ligands (spectra are denoted as $P^{C}EY$). Here we use the same nomenclature as in our previous study from $FeCl_2$ aqueous solutions.[167] Illustrations of the two Auger processes will be presented in Figure 5-6.

Figures 5-6(A) and 5-6(C) present Fe 2p RPE maps from 10 wt% α- Fe_2O_3 NPs in 0.1 M HNO_3 aqueous solution, covering the 2p-3p3p and 2p-3d3d Auger decay channels; individual spectra were recorded for photon energies between 707-717 eV. Figures 5-6(B) and 5-6(D) display the respective $P^{C}EY$- and $P^{V}EY$-XA spectra. Note that Figure 5-6(A) displays data as KEs while Figure 5-6(C) presents BEs in the 5-25 eV range energy, which corresponds to 682-712 eV KE. Valence spectra in Figure 5-6(C) are dominated by an off-resonant water-signal background, appearing as vertical bands. The spectra in Figure 5-6(A) have no off-resonant signal contribution, and solely exhibit resonant signals from 2p-3p3p and in part from 2p-3s3d Auger emissions. Therefore, in the latter case the KE axis is more appropriate since Auger electrons do not depend on the photon energy. Both PEY-XA spectra exhibit a pre-peak at 709 eV photon energy, and a main peak at 710.5 eV. These are the Fe $2p_{3/2} \rightarrow t_{2g}$ and Fe $2p_{3/2} \rightarrow e_g$ resonances characteristic for Fe^{3+}.

Figure 5-7 presents the $P^{V}EY$- and $P^{C}EY$-XA spectra on top of each other, and one observes a considerably smaller pre-peak in the $P^{V}EY$-XA spectrum; intensities are displayed such that the e_g peaks have the same height (to be discussed later). In addition to the different intensities of the pre-peaks, one notices a somewhat smaller intensity in the post-edge region at 709–714 eV. The pre-peak arises from the electronic interactions between the iron site and the local environment, *i.e.*, with the solvation-shell water molecules and the lattice oxygen atoms of the hematite NP. The excited electron can thus engage in additional relaxation processes such as electron delocalization and energy transfer.[167-168] As a consequence, the $P^{V}EY$-XA spectrum may differ considerably from the $P^{C}EY$-XA spectrum which is in fact a better representation of the true X-ray absorption spectrum that would be obtained in a transmission measurement. The delocalized excited electron has a lower probability to refill the Fe 2p hole within its lifetime (sub-10 fs), and hence the PEY is state-dependent, scaling with the extent of delocalization. The observed differences between the $P^{V}EY$- and $P^{C}EY$-XA spectra (Figure 5-7) thus correlate with the orbital extensions.[168] Core-level 3p orbitals are strongly localized and are not or barely involved in iron–ligand orbital mixing.

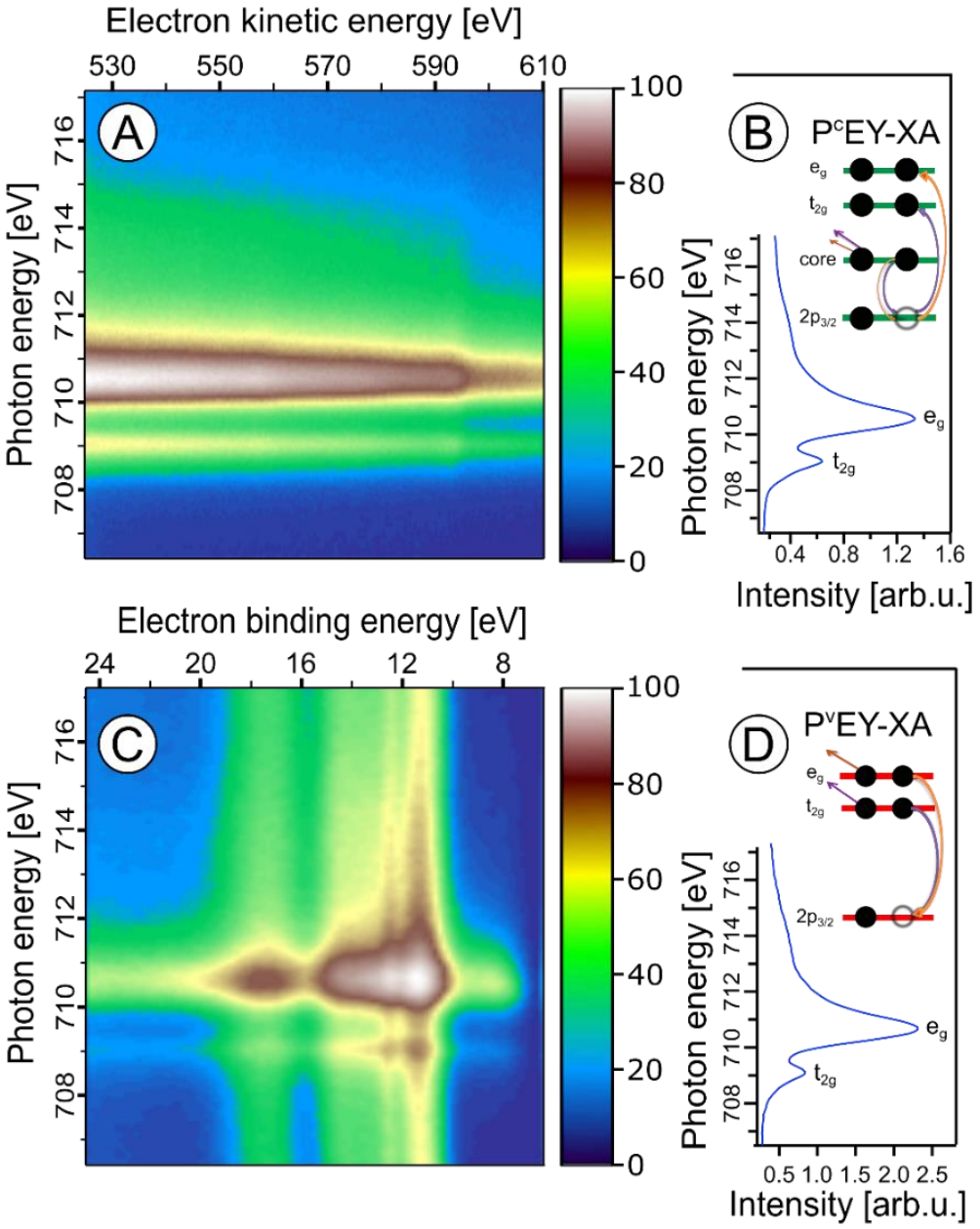

Figure 5- 6

Fe $2p_{3/2}$ resonant photoelectron spectra from 10 wt% α- Fe_2O_3 NPs in 0.1 M HNO_3 aqueous solution, covering the 2p-3p3p (A) and 2p-3d3d (C) Auger-electron emissions after Fe $2p_{3/2} \rightarrow t_{2g}$ and $2p \rightarrow e_g$ excitation, respectively. Spectra were recorded for photon energies between 707-716 eV. The respective P^CEY- and P^VEY-XA spectra, and illustrations of the relevant energies, excitations and the relaxation channels are displayed in (B) and (D).

In contrast, 3d orbitals are large, and there is considerable mixing with water lone-pair orbitals as well as with the NP lattice oxygen-2p orbitals which was already seen from Figure 5-1. Our interpretation is corroborated by the changes that occur in the RPE spectra measured at the e_g *versus* the t_{2g} resonance. These two RPE spectra are shown in Figure 5-8. In both cases the off-resonant valence PE spectrum, measured at 707 eV (bottom tier in Figure 5-8), has been subtracted. To quantify the spectral changes that occur for the two resonances we fit the spectra (center and top tiers in Figure 5-8) using the same Gaussians as in Figure 5-1(B), *i.e.*, energy positions and peak widths are kept constant, and the only free fit parameter is the intensity. The most noticeable observation is the decrease of the t_{2g} signal intensity relative to the e_g signal which is exactly what one expects. Due to the overlap of the metal t_{2g} levels with the O 2p levels of hematite (already seen in Figure 5-1(C)) the electron excited into t_{2g} appears to relax by a different path, thus quenching the 2p-3d3d Auger channel. On the other hand, when populating the e_g states, which have less overlap with the oxygen orbitals, the excited electron promptly refills the Fe 2p hole via the 2p-3d3d Auger channel. These qualitative considerations are in agreement with theoretical calculations, reporting for bulk hematite stronger hybridization between Fe t_{2g} and O 2p orbitals than between e_g and O 2p, 48% *versus* 35% oxygen character.[147]

I can go a step further and quantify the observed electron delocalization to estimate the charge transfer, or electron delocalization rate. Fast charge transfer, which inhibits the charge recombination at the surface (for instance of a transition-metal-oxide electrode), is crucial for efficient device performance under photoelectrochemical conditions. With the Fe 2p lifetime, τ_{core}, assuming an exponential Auger decay rate, and an exponential electron delocalization governed by the charge transfer time, τ_{CT}, the latter can be expressed as $\tau_{CT} = \tau_{core} \cdot (f_{Auger}^{-1} - 1)$.[169-170] Here, f_{Auger} is the fraction of normal Auger-electron signal with respect to the signal from non-local decay processes, the charge-transfer channels of autoionization. τ_{core} = 1.6 fs (1.8 fs) as calculated from the natural line width of Fe 2p, Γ = 0.41 eV [171] (0.36 eV [172]). I determine the normal Auger fraction from the local and non-local signal contributions. Disentangling these signals from Figure 5-8 is not straight-forward because both e_g and t_{2g} mix with ligand orbitals, and hence there is no obvious way of scaling the relative spectral intensities. Arguably, the more accurate procedure is to use the peak areas of the P^CEY- and P^VEY-XA spectra of Figure 5-7.

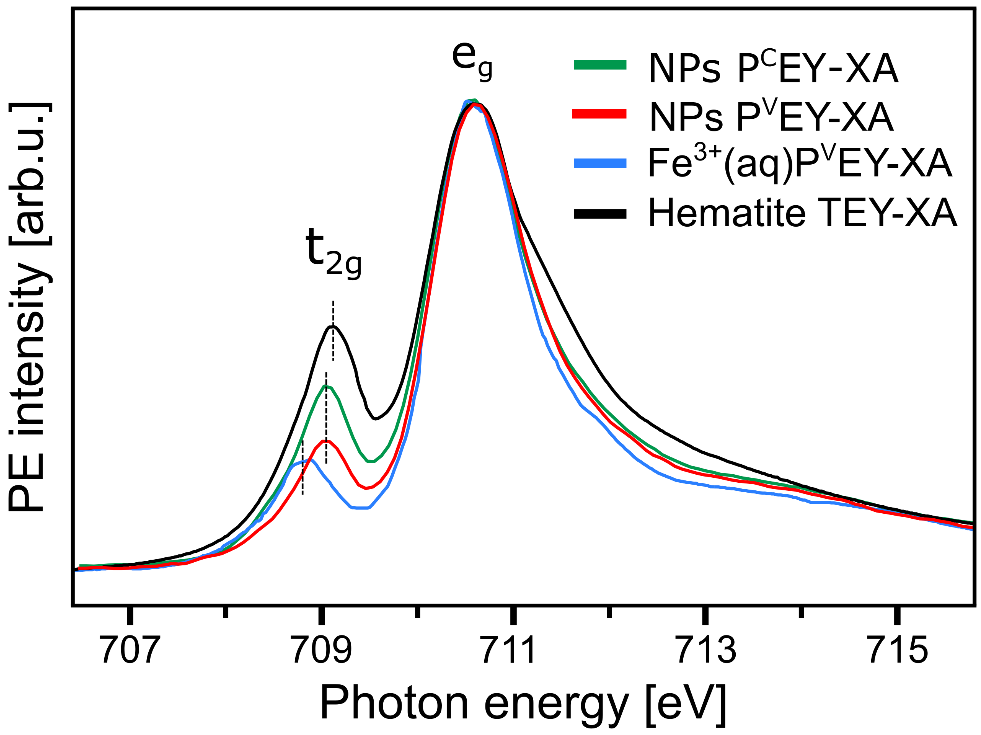

Figure 5- 7

Comparison of the Fe L_3-edge P^CEY- and P^VEY-XA spectra (in green and red) from 10 wt% α-Fe_2O_3 NPs in 0.1 M HNO_3 aqueous solution (of Figure 5-6) with the Fe L_3-edge P^VEY-XA spectrum from 1 M $FeCl_3$ aqueous solution (in blue), [50] and with the total-electron-yield spectrum from solid hematite sample (in black).[16] Spectra are displayed to yield the same height of the most intense absorption band, at 710.5 eV photon energy.

In this case, assuming that the intensity normalization at the e_g peak is reasonable, the difference in the pre-peak intensity of the t_{2g} absorption does scale quantitatively with the electron delocalization. To be more accurate, I argue that the P^CEY-XA spectrum is a very good representation of an actual X-ray absorption spectrum.[167-168] Any difference between P^CEY- and P^VEY-XA spectra must thus be due to delocalization of the 3d electrons. From the areas of the t_{2g} XA peaks we then find $f_{Auger} = 0.6$ which yields $\tau_{CT} \sim 1$ fs. We are not aware of a previous report of this quantity which would be very difficult to access by other experimental techniques, requiring sub-femtosecond laser pulses.

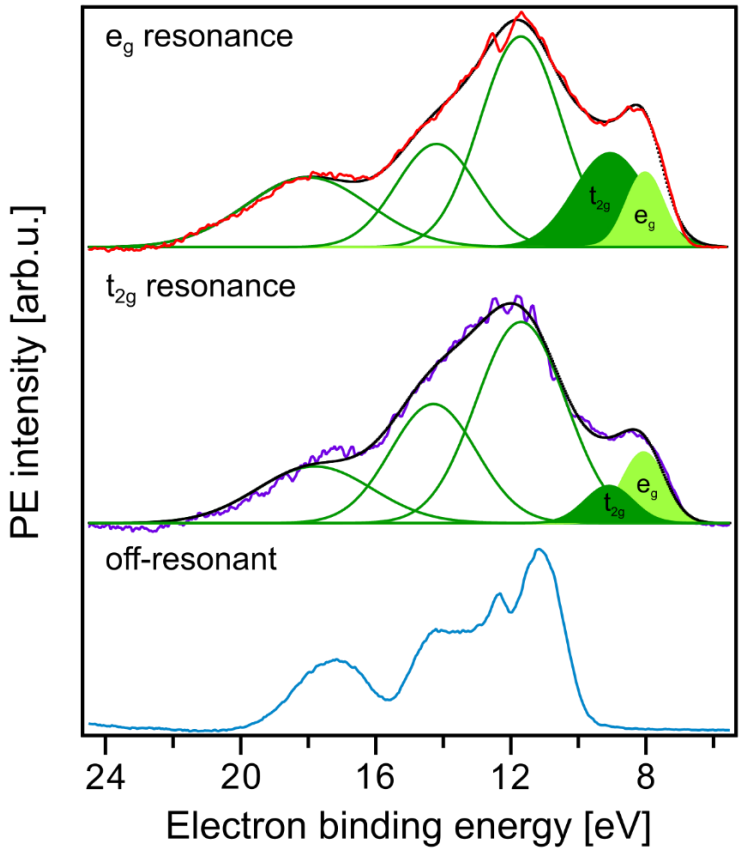

Figure 5- 8

Fe $2p_{3/2}$ resonant photoelectron spectra from 10 wt% α-Fe_2O_3 NPs in 0.1 M HNO_3 aqueous solution measured at the e_g (710.5 eV) and the t_{2g} (709.0 eV) resonances, (A) and (B), respectively. In both cases the off-resonant photoelectron spectrum obtained at 706.0 eV photon energy, shown in (C), has been subtracted. Green curves in (A) and (B) are the Gaussians that represent the spectral contributions from the NPs; compare Figure 5-1(B).

A question that arises is how 10Dq (the e_g-t_{2g} energy difference) from NPs (aq) (see Figure 5-7) compares with values for atomic Fe^{3+} in aqueous solution (blue) and bulk-solid-phase hematite (black) under high-vacuum conditions; the XA spectra for the latter are also presented in Figure 5-7. In all cases the iron charge-state is Fe^{3+}. For nanoparticles in aqueous solution I derive from Figure 5-7 a 10Dq value of 1.5 eV (the same is obtained for the O 1s edge XAS) which is slightly larger than for crystalline hematite, 10Dq = 1.38 eV,[163] but it is smaller than for the Fe^{3+} atomic ions in aqueous solution, where 10Dq = 1.8 eV. A quantitative interpretation of the different values would be difficult but I argue that the main effect is due to the NP – solution interface. This is because aforementioned previous O 1s absorption studies have found an identical 10Dq value (1.38 eV) for bulk-solid hematite and for dry 8 and 30 nm diameter hematite NPs.[163] Hence, the smaller 10Dq is a property of the surface of the aqueous-phase NPs. The Fe 2p PEY-XA spectra are thus sensitive to the interfacial structure,

and yet the quantitative characterization of the ligand field, without a good understanding of the surface structure and the existing molecular species, is elusive. A similar qualitative argument probably holds to explain the intensity variation in the 711-714 eV photon-energy region (Figure 5-7) – the spectral fingerprint region of excited-state charge transfer.[173] Intensities follow the same trend as the t_{2g} absorption intensity, although the effect is negligibly small when comparing $P^{V}EY$ compared to $P^{C}EY$. The latter would be expected if I assume that the ground-state iron t_{2g} – oxygen 2p orbital overlap is only little affected by the electron excited into a higher lying state. This assumption also justifies aforementioned normalization of the spectra at the $2p \rightarrow e_g$ absorption in Figure 5-7. The observed considerably larger intensity, near 712 eV absorption energy, for crystalline hematite compared with the NP solutions, and even more so Fe^{3+} (aq), suggests that ground-state charge transfer from the ligand to the iron cation is smaller in solution, implying less orbital overlap. Arguably, water or hydroxide, either absorbed at the nanoparticle surface or located within the first hydration shell in case of the Fe^{3+} (aq) monomer, have a smaller charge-transfer probability compared to O^{2-} ligands in the bulk hematite. To confirm this interpretation theoretical calculations are needed to quantify charge transfer, including electron donation and back-donation between the different electronic ground-state configurations.

5.4 Conclusions

I demonstrated that liquid-jet soft-X-ray PE spectroscopy is a powerful method that enables the detailed investigation of the electronic-structure interaction of hematite nanoparticles with an aqueous solution. This is a remarkable result because of the rather short probing depth of the emitted (photo)electrons in aqueous solutions. An experimental challenge of the present work has been to stabilize hematite NPs at sufficiently large concentration with an as small as possible number of stabilizing molecules adsorbed at the NP surface. Using a combination of soft-X-ray photoemission techniques (direct and resonant ionization, and autoionization) electrons from both the surface and the interior of the aqueous-phase NPs can be detected. From the oxygen 1s PE spectra I obtain the electron binding energy from dissociated water, at 536.1 eV, which is in good agreement with the energies of hydroxyl species reported in an ambient-pressure PE-spectroscopy study of the Fe_2O_3(0001) hematite – liquid water interface.[136] However, the new spectroscopic information from our NP study is revealed from resonant PE spectra at the oxygen 1s and iron 2p edges. The former spectra provide a complementary and very sensitive electronic structure signature of oxygen-containing molecules adsorbed at the NP surface. Performing photoemission measurements at the iron 2p edge we were able to detect the lowest ionization energy of the solution, which corresponds to the ionization of the iron 3d-derived e_g and t_{2g} orbitals. This is an important quantity for understanding chemical reactions in aqueous solution. I also determined the e_g-t_{2g} energy difference (10Dq value) from the partial-electron

yield iron 2p XA spectra obtained from an analysis of the Auger electron signal. 10Dq is a measure of the Fe^{3+} local environment, which is found here to be uniquely sensitive to the iron interactions with both hematite oxygen and water / oxygen interfacial species. Unfortunately, I cannot provide a quantitative interpretation of the energy shifts. But I expect that this experimental findings will motivate theoretical modeling of the rather complex hematite – water interface, taking into account iron spin interactions. An aspect related to the iron 2p RPE measurements is the possibility to obtain (PEY) XA spectra for different autoionization channels which can be used to estimate the ultrafast electron delocalization times of electrons excited into metal 3d orbitals.

One promising future experimental route is the application of tender X-rays (1.5-12 KeV) in liquid-jet photoemission which allows probing deeper into solution and into the NPs (aq). This will greatly enhance the signal intensity detected from the NP – solution interface, enabling further characterization of the dissociated water species and their interactions with the NPs. With regard to the latter point it will be also interesting to explore non-local relaxation processes upon water O 1s ionization with their large sensitivity to hydration structure and hydrogen-bond strength.[174] The presented liquid-jet studies demonstrate promising applicability for the investigation of the electronic structure of other NPs, including transition-metal-oxide, also noble metals and other materials, dispersed in various electrolyte solutions over a large range of concentrations.

5.5 Appendix

5.5.1 Lattice-Oxygen O 1s Absorption Spectra from α-Fe_2O_3 NP Aqueous Solution

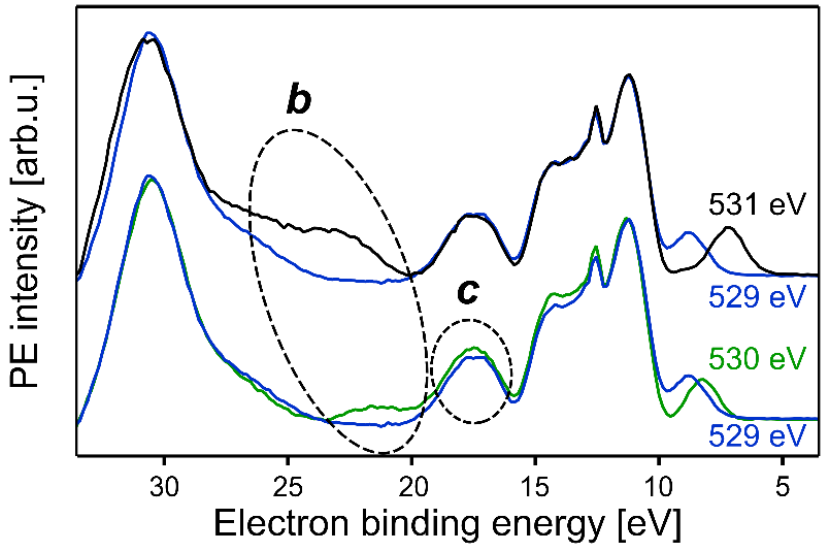

Figure A-5- 1

*Selected RPE spectra from 5 wt% NP / 0.1 M HNO_3 aqueous solution which are taken from Figure 5-2(A) for photon energies 530.0 eV (**c** resonance) and 531.0 eV (energy between **c** and **b** resonances). Each spectrum is presented together with the off-resonant valence PE spectrum measured at 529.0 eV. Important to notice is the slightly larger intensity in the 530-eV spectrum at 17.5 eV BE (bottom tier), which disappears shortly above the resonance (top tier). This is the same contribution that gives rise to the weak signal enhancement, labeled **c**, in Figure 5-2(C). All peaks appearing in the < 10 eV BE region result from water O 1s ionization by the second-order light (2x hv) which is not blocked at the beamline.*

5.5.2 Nitrate and Hydroxide O 1s Absorption Spectra from Fe_2O_3 NP Aqueous Solutions

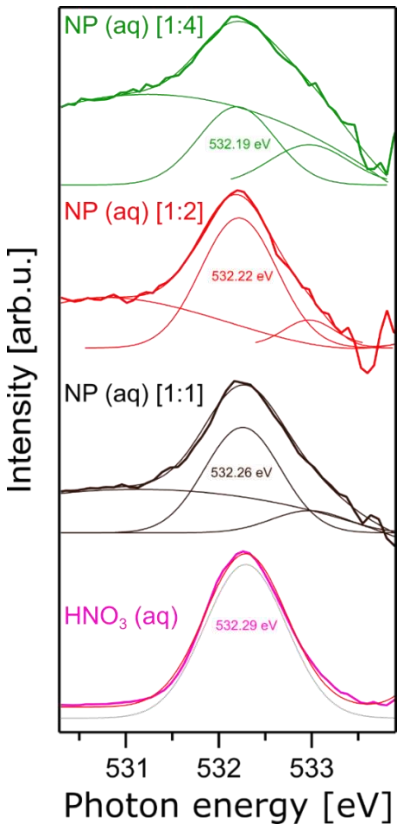

Figure A-5- 2

*PEY-XA spectra from 0.5 M HNO_3 aqueous solution and from three NP solutions, 5 wt% NP / 0.1 M HNO_3, 10 wt% NP / 0.1 M HNO_3, and 10 wt% NP / 0.05 M HNO_3. The presented photon energy region 531-534 eV corresponds to absorption **a** in Figure 5-2(B). Spectra were generated by integration of the respective RPE spectral intensities as a function of photon energy as explained for Figure 5-2 in the main text. In Figure A-5-2 the spectra from different solutions were energy-calibrated and intensity-normalized at the O 1s liquid water pre-peak at 535.0 eV photon energy, after subtraction of the water-vapor absorption spectrum; compare Figure 5-3(A) in the manuscript. For the 5 wt% solution the ratio of available NO_3^- molecules to adsorption sites at the NP (6 nm diameter) surface is approximately 1:1. That is, the surface of the NPs is expected to be fully covered by adsorbed nitrate, and the concentration of aqueous-phase NO_3^- (aq) should be very low. Then, at 10 wt% NP concentration in 0.1 M HNO_3 and in 0.05 M HNO_3, the nitrate-to-surface site ratio decreases to 1:2 and 1:4, implying that H_2O molecules can now interact directly with the NP surface, forming OH interfacial species. Above ratios are a coarse estimate based on the total surface of the NPs in a given volume, and assuming a density of adsorption sites of 5.6 nm^{-2} which is the value reported for crystalline hematite. [130] Smaller ratios were not investigated as to avoid agglomeration of the NPs; all measurements presented here were performed from freshly prepared NP solutions.*

5.5.3 Adsorbed Nitrate and Hydroxide on the NP Surface Observed in the O 1s RPE Spectra from Fe_2O_3 NP Aqueous Solutions

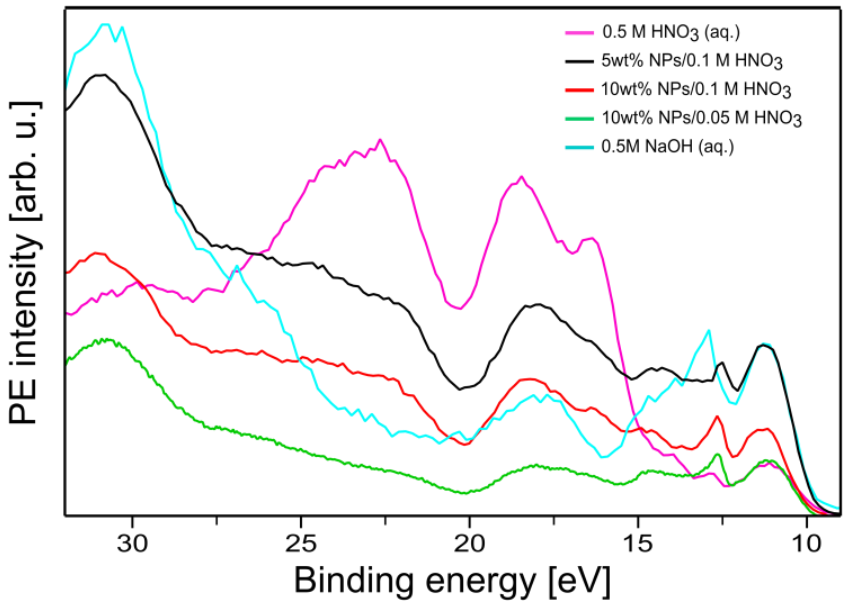

Figure A-5- 3

*Photoelectron spectra at resonance **a** (532.2 eV) for the same three α-Fe_2O_3 NPs aqueous solutions considered in Figure A-5-2. In addition, spectra from 0.5 M HNO_3 and 0.5 M NaOH (measured at near **a**) aqueous solution, are shown. Unlike in Figure 5-4 spectra are shown as measured without the off-resonant photoelectron spectrum subtracted. Otherwise Figure A-5-3 and Figure 5-4 are identical.*

5.5.4 Valence Photoelectron Spectra from 1 M HNO_3 Aqueous Solution

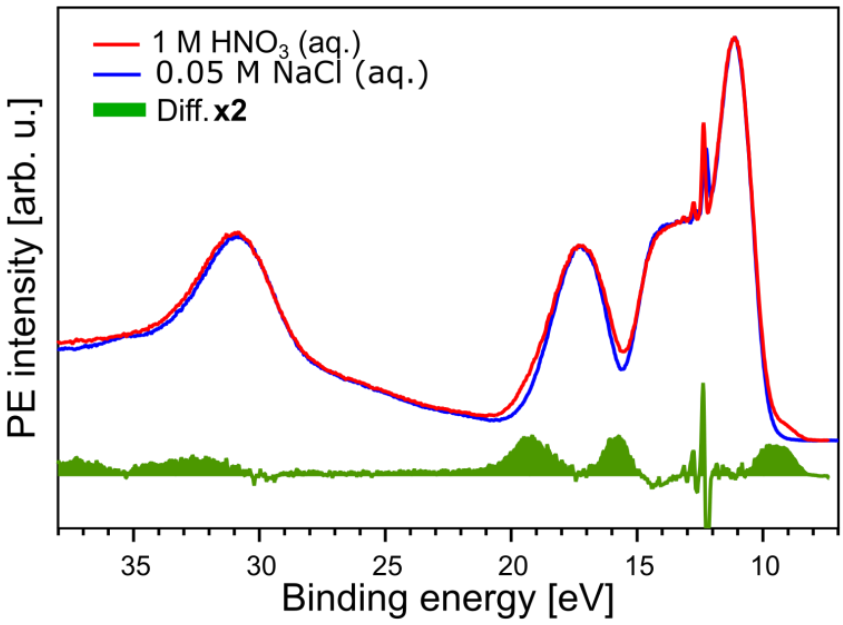

Figure A-5- 4

Valence photoelectron spectra from 1 M HNO3 and from 0.05 M NaCl (which is essentially the spectrum from neat liquid water) aqueous solutions measured at 200 eV photon energy. The green curve is the difference spectrum, HNO_3 minus NaCl, and highlights the signal contributions from ionization of NO_3^- (aq). Peaks occur at 9.5, 16.0, 19.5 eV binding energy; these energies are in good agreement with computed energies.[155]

5.5.5 O 1s Photoelectron Spectra from Fe_2O_3 NP Aqueous Solution

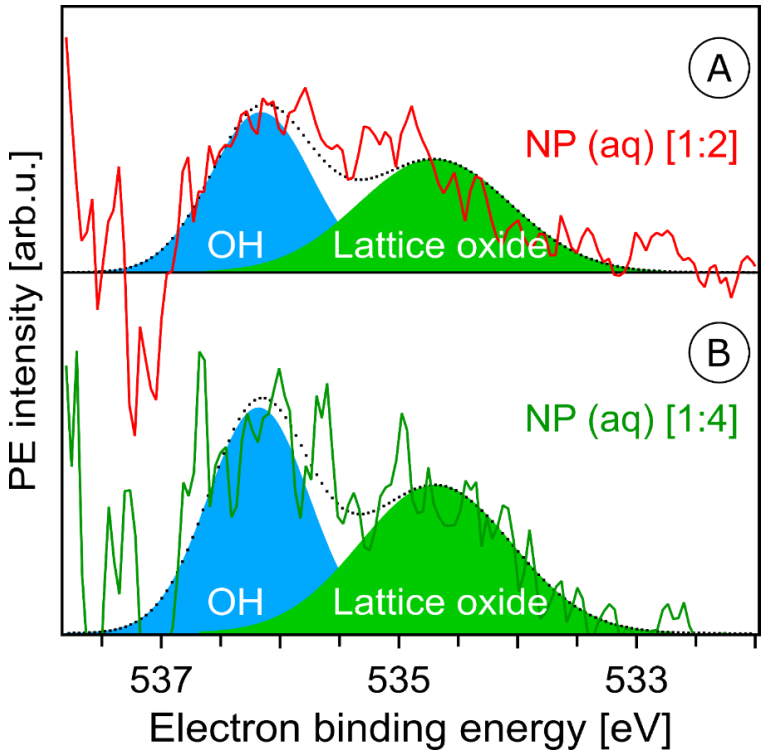

Figure A-5- 5

Oxygen 1s photoelectron spectra from the 10 wt% hematite NPs in 0.1 M HNO_3 aqueous solution showing the 538-532 eV binding energy region which covers the O 1s photoelectron spectra from OH^- (536.1 eV) and lattice oxide (534.7 eV). Ionization photon energy was 1200 eV. In this figure we present the raw data, whereas in Figures 5-5(B) and 5-5(C) we show the same data for 5-point binning. Each contribution is presented by a Gaussian, and the total fit is shown by the dotted curve. (A) shows results for the 10 wt% hematite NPs / 0.1 M HNO_3 aqueous solution (corresponding to [1:2]), and (B) for 10 wt% hematite NPs / 0.05 M HNO_3 aqueous solution (corresponding to [1:4]) after subtraction of the 0.05 M NaCl aqueous solution spectrum.

The table below presents the positions and areas of both the hydroxide and lattice-oxide O1s photoelectron peaks along with the respective error bars of the raw data.

NPs in 0.1 M HNO_3 aq. solution	Peak [eV]	Area [arb. u.]
Lattice Oxide	534.8 ± 0.2	114.4 ± 32
OH^-	536.2 ± 0.1	91.2 ± 29

NPs in 0.05M HNO_3 aq. solution	Peak [eV]	Area [arb. u.]
Lattice Oxide	534.7 ± 0.2	139.2 ± 31
OH^-	536.2 ± 0.1	140.2 ± 30

Chapter 6

Electronic Structure of the Anatase TiO_2 Nanoparticle—Aqueous Interface

This part of the thesis is taken from the following publication:

Electronic Structure of Aqueous-Phase Anatase Titanium Dioxide Nanoparticles Probed by Liquid Jet Photoelectron Spectroscopy

Hebatallah Ali, Robert Seidel, Arno Bergmann and Bernd Winter

Journal of Materials Chemistry A 2019, **7**, 6665-6675, **DOI:** 10.1039/C8TA09414D

This article was selected for the themed collection: ***2019 Journal of Materials Chemistry A HOT Papers,*** and appears as the front cover of the ***Issue 12, 2019***.

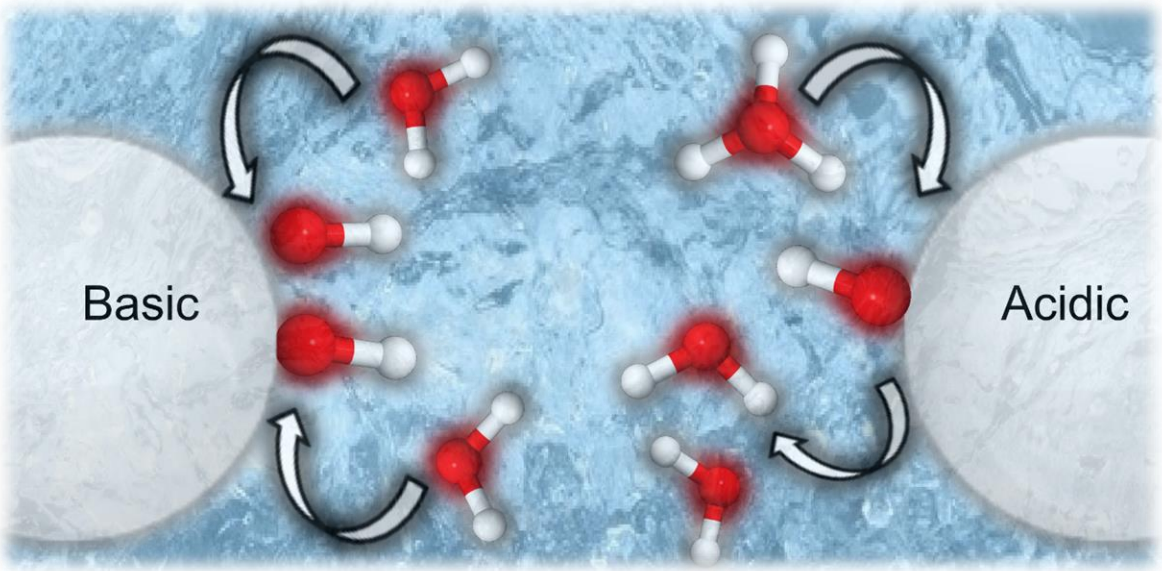

Proposed pH-dependent mechanism of TiO_2 – water interaction.

6.1 Introduction

Titanium dioxide, TiO_2, with its three phases in nature, anatase, rutile and brookite, is one of the most important transition metal oxides.[175] It offers wide-range properties for science and industry applications, and furthermore it is a chemically stable, abundant and cheap material.[176] Exhibiting a large bandgap of 3.2 eV TiO_2 absorbs light in the UV region [177-178] which explains the extensive study of this material in photoelectric and photochemical research.[1, 179] In 1972, Fujishima and Honda studied the water photolysis on the TiO_2 electrode surface which can be described by the reaction $H_2O + 2h\nu \rightarrow ½\ O_2 + H_2$.[8] This photochemical reaction thus provides a clean and sustainable way for hydrogen fuel production from solar energy. Many subsequent works have focused on the water electrolysis to develop efficient photoelectrochemical cells (PEC) for solar hydrogen generation by immersing two electrodes (TiO_2 photoanode and a cathode). [177, 180-186] The challenge in these studies is to minimize the unwanted back-reaction, *i.e.*, the recombination or non-separation of hydrogen and oxygen atoms which reduces the PEC's efficiency. An ideally performing device, minimally suffering from electric current losses, would assure that the initial charge separation is very fast (on the femtosecond timescale) to slow down the back-reaction.[187] Despite active research the conversion efficiency from solar to electric power with current PECs is still low, reaching up to 17%,[187-188] and prevents this path for solar hydrogen generation from being economically and commercially viable.[189-190]

As the TiO_2 electrode is immersed in an aqueous environment it is essential to gain a detailed understanding of the electronic properties of the TiO_2 – water interface, and this has motivated many investigations of the water adsorption behavior on single crystals, in rutile as well as in anatase phase. [93, 177, 191-196] Likewise, the present study aims at determining the electronic structure of this interfacial layer. The novel approach here is to access the interface by soft X-ray photoelectron (PE) spectroscopy which has not been accomplished previously for a TiO_2 surface fully contained in liquid water. The reason is that the detection of photoelectrons in a high-vapor pressure environment has only recently become possible with the introduction of the liquid microjet technique [139, 197-199] and of ambient pressure photoelectron spectroscopy (AP-PES). [27, 29, 93, 97, 136] Liquid jets are ideally suited to study NPs dispersed in aqueous solutions [139, 197-199] while the latter technique typically refers to condensation of few monolayers (ML) liquid water on a solid substrate at suitable relative humidity. [27, 29, 93, 97, 136] Also, photoelectrons have been detected from liquid cells equipped with a few-nanometer thick graphene membrane to separate the liquid from vacuum. [98-99, 200]

The TiO_2 anatase phase has been found to exhibit higher photocatalytic activity [201] and higher efficiency in photo-electrochemistry applications,[202-203] and is also more stable in the nanometer regime.[204-205] However, on macroscopic size scale, rutile is the most stable phase,[175, 206] and has been studied more intensively, both theoretically [177, 191] and experimentally.[93, 207-208] Yet, the nature of the water adsorption on the TiO_2 surfaces remains unclear; depending on the specific study water has been

concluded to adsorb (1) dissociatively, (2) molecularly, or (3) mixed at the TiO_2 interface.[93, 177, 191-194, 209-213] Furthermore, the adsorption mechanisms for these different cases were proposed to depend on whether or not the (vacuum) surface is defect-free. A defect surface site refers to a missing oxygen atom in the crystal structure (oxygen vacancy), and is easily created by electron bombardment, ion sputtering, or thermal annealing.[214] In aqueous phase the situation is quite different; defects on the titania surface will be healed upon interaction with the water molecules. [93, 138] Oxygen vacancies are accompanied by a change of the titanium charge state ($Ti^{4+} \rightarrow Ti^{3+}$) and the occurrence of color centers, [214] which are the most active surface sites for water dissociation (mechanism (1)). [214-216] Defects on the TiO_2 surface are conveniently detected by Ti^{3+} signal,[93, 192] a procedure also adapted here. For the interpretation of the results obtained in the present work it is useful to briefly review the different adsorption mechanisms.

Dissociative adsorption (mechanism (1)) of TiO_2 – water interaction depends entirely on the existence of surface defects; water molecules dissociate only at oxygen vacancy defects. The thus generated hydroxyl species fills the oxygen vacancies (denoted OH_t), leaving the hydrogen to bond to a neighbor lattice oxygen atom (OH_b) and forming what is termed paired hydroxyl groups.[208] Ketteler et al.[93] observed this paired OH for 0.25 ML coverage on rutile (110) using AP-PES. In addition, the authors detected an O 1s photoelectron signal from adsorbed molecular water at less than 1 ML coverage, with an approximately 0.5 eV lower binding energy (BE) as compared to bulk water. This PE peak could correspond to hydroxyl or to molecularly adsorbed water; also pseudo-dissociated water has been suggested.[93] In the latter process, the paired hydroxyl groups re-form a water molecule by back-reaction. At higher coverage, water has been shown to adsorb molecularly, bonding to the OH groups that act as hydrogen-donors.[93] A similar conclusion has been drawn from PE spectroscopy measurements from TiO_2 nanoparticles (NP) exposed to water vapor; experiments were conducted using an aerosol generator.[217] Mechanism (1) can hence be represented as $H_2O + O_b \leftrightarrow OH_b + OH_t$.[218-219] The interconversion energy of the dissociated hydroxyl pair relative to the water molecule (back-reaction) has been estimated as $\Delta E = 0.035 \pm 0.003$ eV, based on a combination of supersonic molecular-beam experiments, scanning tunneling microscopy, and *ab initio* molecular dynamics.[218] Given this very small energy difference between the two states, the re-formation of adsorbed water molecule is slightly more likely over the paired hydroxyl configuration, but not dominating.[219] In this mechanism, OH_t was assumed to form a covalent bond with the TiO_2 surface.[93] This interpretation is based on the detected energy of the O 1s and Ti 2p peak positions, both being different for the hydrated TiO_2 rutile crystal surface compared to the bulk crystal.[207]

In the second proposed mechanism (2) of the TiO_2 / water interaction, water is molecularly adsorbed on the surface at very specific geometries where the water oxygen atom binds to Ti^{4+} sites and its hydrogens bind to two neighboring lattice oxygen atoms.[220] This raises the question whether water dissociates exclusively at oxygen vacancies or whether dissociation can also occur at Ti^{4+} sites.

Here, the third mechanism (3) of TiO_2 – water interaction comes into play, and is legitimated by experiments on defect-free surfaces of rutile[210, 221] and anatase,[192-193, 209] both showing a mixed adsorption behavior, with OH signal being small relative to the signal from molecularly adsorbed water. Specifically, Walle et al.[192] reported that the first water layer is composed of 0.47±0.05 ML OH and 0.77±0.55 ML molecular water for the anatase TiO_2(101) defect-free surface; the OH coverage stays nearly constant for higher water exposure. In a theoretical work, Zheng et al studied the stability of the dissociated OH species on titanium sites using density function theory (DFT) on rutile (110) surface edge.[222] The authors report that its lifetime is highly dependent on the location of the hydrogen species (the second product of the water dissociation) and that the recombination/reformation of water molecule is possible.[222] This mechanism is the most closely related one to the present study as detailed later in the results section.

Here, I present PE measurements from anatase-phase TiO_2 NPs dispersed in liquid water which I refer to as the "*all-in-solution*" surface-study approach. This is complicated though by the fact that NPs are not soluble in water due to large surface potential. They tend to aggregate and sediment out near the point of zero charge (PZC) which is at pH ~6.4 for the anatase surface.[223] That is, when the surface is neutral, NPs reduce their surface energy by aggregating and thereby reducing their surface area. Such unwanted effects are avoided by adding stabilizers to the aqueous solutions, which inevitably leads to change of pH. In this study we use three different stabilizers, Cl^-, NO_3^-, resulting in a positive surface zeta potential of the TiO_2 NP (the potential between TiO_2 surface and the surrounding aqueous solution), and NH_4^+ yielding a negative surface zeta potential. Under these conditions the NPs are stable in aqueous solution, and stable liquid microjets for the photoemission experiments can be obtained. Evidently, I am mostly interested in conditions where the stabilizer concentration is low enough such that a sufficiently large fraction of free NP surface sites is available for water adsorption. This fraction can be estimated from the adsorbed ML density on TiO_2 (110) (5.2 nm^{-2} [93, 192]). Then, one of our major questions is whether water adsorbs molecularly or dissociatively on the TiO_2 anatase NP defect-free surface where no Ti^{3+} sites are present. The other, equally important question is how the adsorption nature depends on pH, explored here for basic and acidic pH. This latter aspect has not been addressed experimentally before. We are aware of a single density functional theory (DFT) molecular dynamic work studying the acidity of the surface groups relevant in the water interaction with rutile (110) surface.[224] It was predicted that the fraction of terminal water molecules ($TiOH_2$) is small at neutral pH, and the surface pK_a for this site has been estimated to be 9. In contrast, pK_a of -1 was estimated for the surface hydroxide bridge groups (Ti_2OH^+). Most interesting for the present work is the $TiOH_2$ case. Deprotonation of $TiOH_2$ to $TiOH^-$, which is coupled with the protonation of H_2O in the liquid water, is paralleled by the reverse reaction where the solution proton is transferred to a $TiOH^-$ surface group [224] ($TiOH^- + H_3O^+ \rightarrow TiOH_2 + H_2O$). I can hence expect that

in a basic solution environment this reverse reaction is insignificant. Qualitatively, such a behavior is supported by our combined resonant and non-resonant PE spectroscopy, as well as partial-electron yield X-ray absorption (PEY-XA) measurements from TiO_2 NP (aq) at different pHs.

6.2 Methods and Materials

Photoelectron measurements of TiO_2 NP solutions (*i.e.*, colloidal dispersions) were conducted using the SOL^3 PES setup[62] at the U49/2-PGM-1 soft X-ray beamline, at the synchrotron radiation facility BESSY II, Berlin. Briefly, synchrotron light, liquid jet and the photoelectron detection are orthogonal to each other. The X-ray light at this beamline is linearly polarized in the floor plane which is the plane spanned by jet propagation and light propagation. Focal size is approximately 60 x 20 μm^2. Solutions were injected into the interaction vacuum chamber through a 25 μm glass capillary. Liquid flow rate was 0.7 ml/min using a backing pressure of 10 bars. The liquid jet hits the X-ray beam at 0.5 mm distance from the capillary tip, and this interaction point is at 500 μm distance from the detector orifice. The pressure in this chamber was kept at approximately 3.0 x 10^{-4} mbar by using a turbo molecular pump (1600 l s^{-1}) and two liquid nitrogen cold traps. At 500 eV photon energy, using 80 μm beamline exit slit, the energy resolution in our measurement is higher than 130 meV.

Four sets of anatase TiO_2 NP solutions were studied. The NP sizes used in this study were given by the samples that were commercially available. In addition to different NP sizes, the different vendors also use different stabilizers as well as different stabilizer concentrations. Then, together with the finding that anatase-phase TiO_2 NPs, for 2-200 nm diameter, have been demonstrated to exhibit no noticeable size effects on the electronic structure [225] it is possible to solely vary the ratio of free-to-stabilizer covered surface sites as a single parameter.

Dry NPs: 20 nm diameter, 99.5% anatase TiO_2 NP sample purchased from Io-Li-Tec, Germany. This sample was used for the total electron yield measurements of the Ti L- edge XA and the O K-edge XA spectra for examining the similarity between XA spectra the anatase-phase TiO_2 NPs in dry environment and TiO_2 single crystal reported in literature.

TiO_2 NPs in HCl aqueous solution: (acidic solutions without free surface sites) 10 nm, 99.9% pure anatase TiO_2 NPs coated with Cl^-, purchased from Mknano, Canada, was used to prepare the 20 wt% TiO_2 NP in 0.5 M HCl aqueous solution (yielding pH 1.2) and in 1 M HCl aqueous solution (yielding pH 0.7). In both samples, the NPs are fully covered by Cl^- ions with NP surface sites relative to stabilizer ions ratio $[1:1]^{Cl-}$ and $[1:2]^{Cl-}$ respectively. In all these cases water cannot interact with the actual TiO_2 NP. Our measurements from the HCl-stabilized NP solutions thus provide valuable reference O 1s non-resonant, resonant XPS and PEY-XAS spectra of the TiO_2 NPs, in the absence of interfacial oxygen species.

TiO_2 NPs in HNO_3 aqueous solution: (acidic solutions with free / no free surface sites) 20 wt%, 6 nm TiO_2 NPs in 0.5 M HNO_3 aqueous solution (yielding pH 1.2) and in 0.25 M HNO_3 aqueous solution (pH 0.9), purchased from PlasmaChem, Germany, which have TiO_2 surface sites relative to the stabilizer ratios of $[1:1]^{NO3-}$ and $[2:1]^{NO3-}$, respectively. Furthermore, in order to increase the $[x:y]^{NO3-}$ ratio, a 20 wt%, 3 nm TiO_2 NP in 0.6 M HNO_3 aqueous solution (pH 0.7) yielding $[4:1]^{NO3-}$ was used; this ready-to-use solution was purchased from NYACOL, USA.

TiO_2 NPs in NH_4OH aqueous solution: (basic solutions with free surface sites) 20 wt%, 20 nm TiO_2 NP in 0.3 M NH_4OH aqueous solution (pH 7.8; slightly above the neutral water pH) was obtained from NYACOL, USA. In addition, we added 0.5 M NH_4OH to this NPs(aq) solution to obtain 20 wt%, 20 nm TiO_2 NP in 0.8 M NH_4OH aqueous solution (pH 9.8). This leads to ratios $[2:1]^{NH4+}$ and $[1:1.5]^{NH4+}$, respectively. The latter sample is used to support our proposed TiO_2/water interaction mechanism, as discussed in the results section. It is interesting to mention that the estimated $[2:1]^{NH4+}$ratio is in good agreement with measurements of the surface zeta potential. It is -16.9 mV for the $[2:1]^{NH4+}$ solution (measured with "Zetasizer Nano ZS" spectrometer) and can be compared with a value of +30 mV [226] for fully covered anatase TiO_2 NPs surface in aqueous solution.

6.3 Results and Discussion

6.3.1 Ti L-edge PEY-XA Spectra

I start by exploring the X-ray absorption (XA) spectra from aqueous-phase TiO_2 NPs measured at the Ti^{4+} 2p → valence $3d^0$ resonance. We note that an electron-yield absorption spectrum essentially captures electrons that are emitted in an electronic relaxation process, which is mostly Auger decay. One typically assumes that the Auger-electron yield is proportional to the actual XA. [167-168] In the present work I detect the partial electron yield corresponding to the refill of a Ti 2p hole by a 3p electron and subsequent ejection of another 3p electron (Ti LMM Auger channel); this (resonant) Auger signal appears in the 360-420 eV kinetic energy range. More specifically, by integrating the signal intensity over this energy range as a function of the excitation energy I obtain the so-called partial electron yield XA (PEY-XA) spectrum. For the questions addressed here, the small difference that may occur between PEY and total electron yield (TEY) detection [168] is irrelevant; the important point here is that I can experimentally track the electronic structure changes that lead to the measured XA spectra. Figure 6-1 shows the Ti L-edge PEY-XA spectra from several NP solutions, $[1:1]^{Cl-}$, $[1:1]^{NO3-}$, $[4:1]^{NO3-}$ and $[2:1]^{NH4+}$. I present one sample from each set described in the experimental section. Only for the NO_3^- sample set, two samples provided from different companies, are shown ($[4:1]^{NO3-}$ and $[1:1]^{NO3-}$). In addition, the dry NPs (shown in the bottom of Figure 6-1) XA spectrum was measured by detecting the drain current while sweeping the photon energies over the Ti L-edge.

This is one way to obtain total electron yields, and throughout the text I will refer to the TEY-XA spectrum, serving as reference.

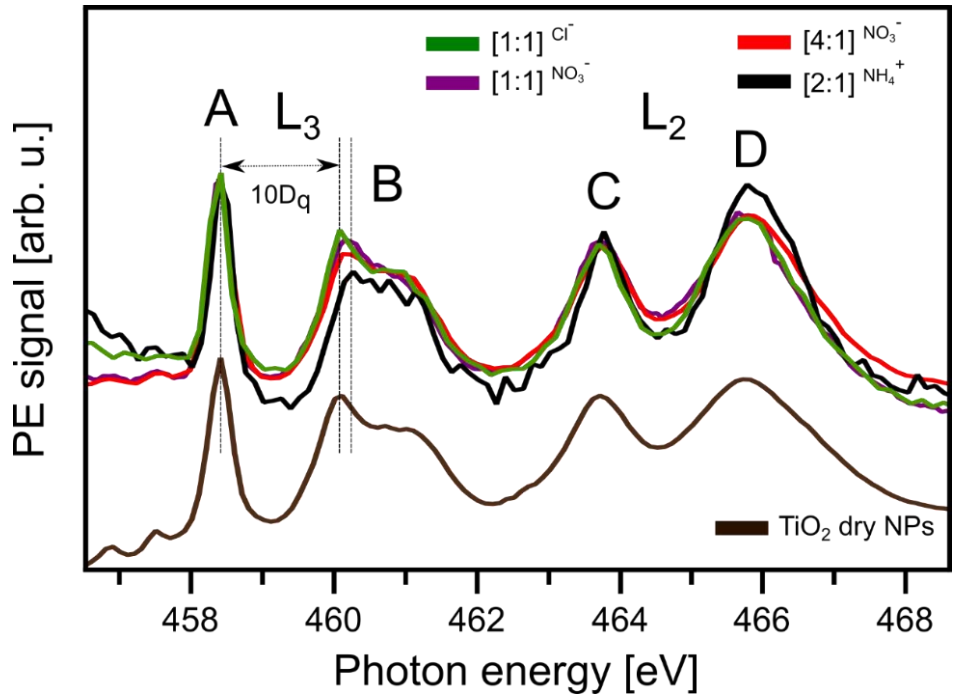

Figure 6- 1

(top): Ti L-edge PEY-XA spectra from anatase TiO_2 NPs dissolved in different aqueous solutions. Here [x:y]ion indicates the stabilizer ion that has been used, and inside the bracket the ratio of available NP surface sites to surface sites covered by the stabilizer ion is shown. Labels A-D refer to the most prominent absorption bands. The splitting of the L_3 edge feature, 10Dq, is indicated. (bottom): Ti L-edge TEY-XA spectra from dry anatase TiO_2 NPs.

The measured L-edge XA spectra, presented in Figure 6-1, can be divided into two regions, L_2 ($2p_{1/2}$) and L_3 ($2p_{3/2}$) edges, due to the 2p spin orbital coupling splitting. Results are shown for NP solutions $[1:1]^{Cl-}$, $[1:1]^{NO3-}$, $[4:1]^{NO3-}$, and $[2:1]^{NH4+}$. Here, we largely focus on the L_3 region. Our first observation is that the spectra from all solutions are nearly identical. The first prominent absorption band *A* results from the Ti $2p_{3/2} \rightarrow 3d\ t_{2g}$ transition, and band *B* is the Ti $2p_{3/2} \rightarrow 3d\ e_g$ transition. The energy difference between *A* and *B* which quantifies the crystal field splitting, 10Dq, of the empty 3d orbital hybridized with the surrounding oxygen atoms, is indicated. Since 10Dq is sensitive to the Ti–O distance [227] its value is an indicator of changes in the Ti local environment. Arguably more important is the overall shape of the L-edge XA spectrum, the details of which being characteristic for a given TiO_2 phase (Anatase, Rutile, or Brookite). We see that the NP spectra in Figure 6-1 match the TEY-

XA spectrum from dry 20 nm NPs which is also presented, at the bottom of Figure 6-1, rather well. And the latter spectrum perfectly reproduces the XA spectrum from anatase-phase TiO_2 crystal.[228-230] I particularly point out that the broadening of the e_g L_2 (as well as the sub-splitting of the e_g L_3 edge), which is very sensitive to the crystal phase, is the same in all spectra and reproduces the shape and width reported in the literature.[228-230] I can thus rule out any NP phase transition in the aqueous solutions, and also oxygen defects are not detected which would manifest in contributions from Ti^{3+} signal.

To further confirm the non-existence of Ti^{3+} I have also recorded the valence spectra at the various resonances, A, B, C, D identified in Figure 6-1. The results are exemplarily shown for the $[2:1]^{NH4+}$ solution in Figure A-6-1 of the Appendix Section 6.5 where I also present an off-resonant spectrum measured slightly below the resonance, at 457 eV photon energy. In none of the spectra I observe any signature of the 2p – 3d3d (LVV) Ti^{3+} Auger decay as judged from comparison with our previous study of atomic Ti^{3+} in $TiCl_3$ aqueous solution.[144] Our conclusion is also supported by reported valence spectra from pure crystalline anatase TiO_2 (containing no Ti^{3+}) and from Li^+-doped TiO_2 in which case Ti^{3+} forms.[231] Hence, the spectra in Figure A-6-1 prove that the Ti 3d orbital is empty, and the aqueous-phase NPs are indeed purely anatase-phase TiO_2. Adsorption mechanism (1), described in the Introduction Section 6.1, is thus irrelevant for the TiO_2 NP – aqueous solution interface. One further observation from Figure 6-1 that is noteworthy to mention is that 10Dq appears to be slightly larger for the $[2:1]^{NH4+}$ solution than for all other solutions. In Figure A-6-2 of the Appendix Section 6.5 I have averaged the $[4:1]^{NO3-}$, $[1:1]^{Cl-}$, and $[1:1]^{NO3-}$ solution spectra for better visualization of this pH-dependent effect. Arguably, this is an indication that NH_4^+, unlike the other stabilizing ions, has some specific effect on the interfacial structure. Indeed, a distinct adsorption behavior of H_2O occurs in the NH_4^+-stabilized NP solutions as we will show below.

6.3.2 O 1s Off-resonant Photoemission Spectra

Figure 6-2 presents the (regular) oxygen 1s core-level photoelectron spectra measured at 1200 eV photon energy for all our NPs solutions. Here I have included the reference spectrum from O 1s spectrum from 0.05M NaCl aqueous solution, representative of neat liquid water. I find that all PE spectra (Figure 6-2(A)), again with the one exception of NH_4^+ (Figure 6-2(B)) are almost identical, exhibiting the main bulk water peak at 538.1 eV BE, [86] relative to the vacuum level, the water gas-phase (a shoulder) at 540.0 eV, and an additional small peak at 534.9 eV BE from lattice oxygen of the TiO_2 NPs, in agreement with the reported value for the TiO_2 rutile crystal with few layers of water prepared at suitable relative humidity.[93] Similar to our previous study of aqueous-phase hematite NPs stabilized with NO_3^-, [197] the PE signal from the NO_3^- cannot be observed (at 538.1 eV binding energy[166]) at such a low concentration because of overlap with large signal intensity from bulk water.

[138, 166] The OH^- signal, on the other hand gives rise to a peak at 536.0 eV BE (determined in the aforementioned ambient-pressure PE study from rutile TiO_2 single crystal[93]) which is distinguishable from NO_3^- and water. But there is no indication of adsorbed OH^- despite available free adsorption sites for interaction with water, for instance in the case of the $[4:1]^{NO3-}$ and $[2:1]^{NO3-}$. I thus conclude (and will later corroborate) that water does not dissociate on the TiO_2 NP surface but rather adsorbs molecularly; yet, a small but negligible amount of dissociated water may exist at the NP surface. This is opposite to α-Fe_2O_3 NPs, where water dissociates when the NPs are stabilized by NO_3^-.[197] (See Figure 5-5) Note that also adsorbed water, similar to NO_3^-, has a O 1s BE strongly overlapping with bulk water (0.5 eV lower BE than bulk water[93]) which makes the detection of this contribution impossible in a liquid-jet experiment.

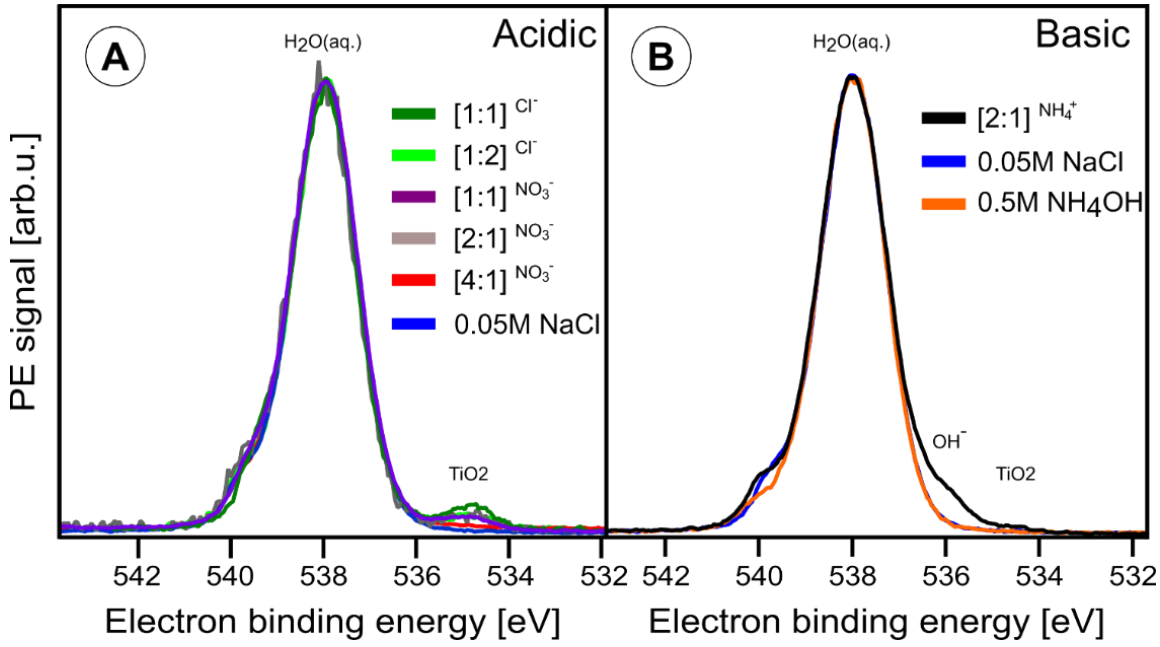

Figure 6- 2

Oxygen 1s photoelectron spectra of the different anatase TiO_2 NP aqueous solutions, measured at 1200 eV photon energy. As in Figure 6-1, [x:y]ion indicates the stabilizer ion that has been used, and inside the bracket the ratio of free NP surface sites to surface sites covered by the stabilizer ion is shown. NP size is given in the experimental section. (A) Acidic NP solutions: [1:1]Cl^- (pH 1.2), [1:2]Cl^- (pH 0.7), [1:1]NO_3^- (pH 1.2), [2:1]NO_3^- (pH 0.9) and, [4:1]NO_3^- (pH 0.7). Also shown is the spectrum from 0.05 M NaCl. (B) Basic solution: [1:1]NH_4^+ (pH 7.8). Also shown are the O 1s spectra from 0.05 M NaCl and 0.5 M NH_4OH aqueous solutions.

I now turn to the $[2:1]^{NH4+}$ NP solution (Figure 6-2(B)) where I observe a weak signal at 536.0 eV BE which identifies adsorbed OH^- species. This energy is in agreement with the previously reported value for adsorbed hydroxyl on a TiO_2 surface under near ambient pressure conditions.[29, 93, 213]. Comparing with reference O 1s PE spectra from 0.5 M NH_4OH aqueous solution (pH 11.7) and 0.05 M NaCl aqueous solution, containing no NPs, the OH^- signal is seen to vanish. This implies that it is not produced by the NH_4^+ interaction with bulk water. Note that the higher-concentration solution, 0.5M NH_4OH (compared to 0.3 M NH_4OH), does not even show the slightest evidence of OH^- signal. Hence, the 536.0-eV BE signal must result from water interaction with the TiO_2 free surface sites. Since the pH of the $[2:1]^{NH4+}$ NP solution is 7.8, *i.e.*, the concentration of free OH^- in the solution is roughly 10^{-7} mol/L, the detected OH^- species must be immobilized within the TiO_2 NP – solution interface rather than being free in the solution. One also infers from Figure 6-2 that dissociation of water on the TiO_2 NP surface depends on solution pH, a hypothesis I will verify with the help of oxygen K-edge PEY-XA spectra. In the present case of approximately 650 eV O 1s photoelectrons the top-most layers of the NPs, including their adsorbed molecular layer, are probed. The relatively large OH^- signal intensity compared to the lattice oxide signal in Figure 6-2(B) is attributed to the exponentially decreasing electron signal contribution as a function of distance from the (covered) NP surface – aqueous solution interface.

6.3.3 O K-edge Photoemission and PEY-XA Spectra

Analogous to the Ti L-edge PEY-XA measurements, I also study the valence photoemission signal (detected in the 510-525 eV kinetic energy range), sweeping the photon energy across the O 1s resonance. Figure 6-3(A) presents the O 1s PEY-XA spectra from five selected NP solutions, $[1:1]^{Cl-}$, $[1:2]^{Cl-}$, $[4:1]^{NO3-}$, $[2:1]^{NH4+}$, and $[1:1.5]^{NH4+}$. In Figure 6-3(B) I show the respective spectra from four relevant reference salt aqueous solutions, 0.5 M HNO_3 (pH -0.2), 0.5 M NH_4OH (pH 11.7), 0.5 M NaOH (pH 13.7), and 0.05 M NaCl (pH 7). Figure 6-3(C) shows the TEY-XA spectrum from the dry TiO_2 NPs which was however recorded by measuring the resulting electric current through the sample.

In Figures 6-3(A) and 6-3(B), the large peak at 535 eV photon energy is due to the liquid water absorption pre-peak (O 1s → $4a_1$ transition [150]) which is used here for energy calibration and intensity normalization. The shoulder at 534.5 eV photon energy is the respective H_2O gas-phase absorption. This contribution is seen to vary among different solutions, which is due to a combination of changing vapor pressure upon pH variation and perhaps slight misalignment of the liquid jet when switching solutions. In addition to the water absorption bands several smaller peaks, ***a*** (near 531.2 eV), ***b*** (532.3eV), ***c*** (532.8), and ***d*** (533.8), can be seen in both Figures 6-3(A) and 6-3(B). More specifically, and starting with the TEY-XA spectrum from dry NPs (Figure 6-3(C)), the two main bands, ***a*** (531.2

eV) and ***d*** (533.8 eV), are the absorptions O 1s → O 2p–Ti 3d (t_{2g} and e_g); these metal orbitals are hybridized with lattice O 2p. [162, 225, 232-234] I next consider the solutions [1:1]$^{Cl-}$ and [1:2]$^{Cl-}$ for which no free adsorption sites on the NP surfaces are available.

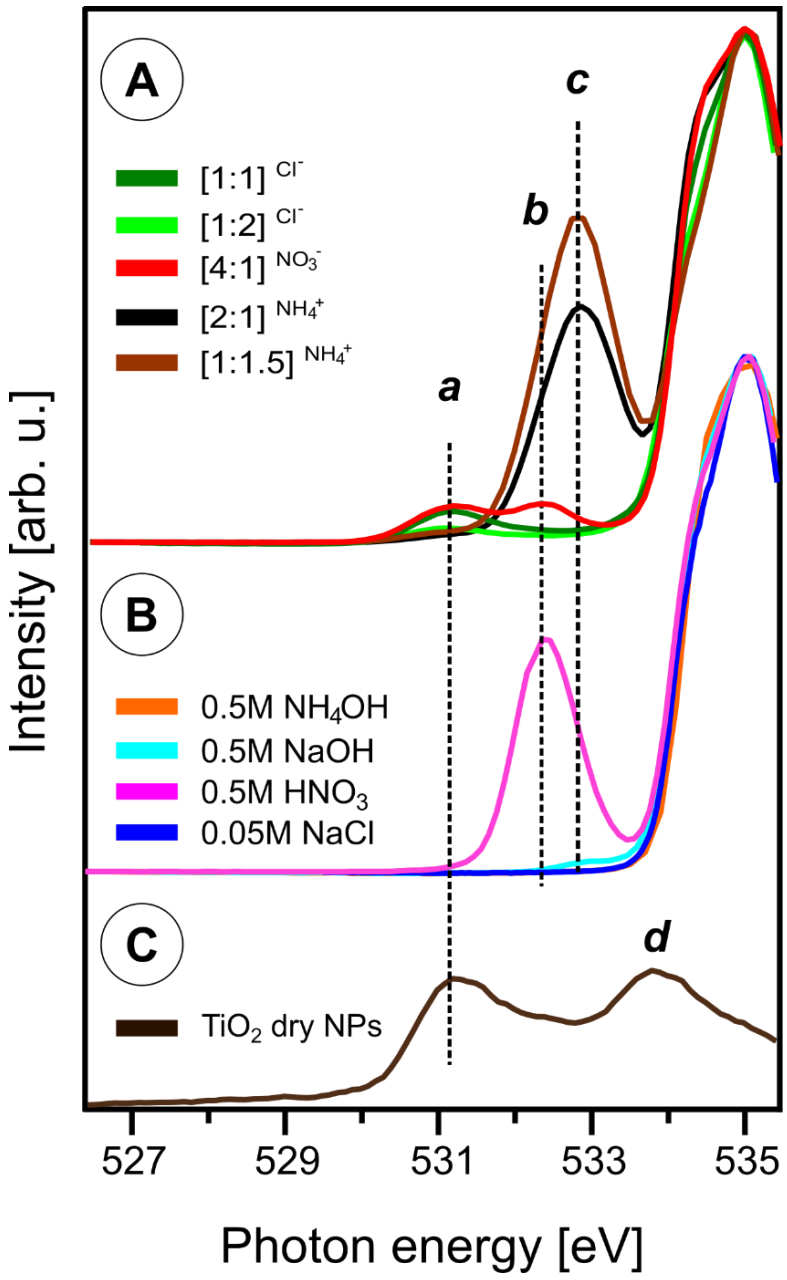

Figure 6- 3

(A) O 1s PEY-XA spectra from different anatase TiO_2 NP aqueous solutions; compare caption of Figure 6-2 for the solution labels. Intensities are normalized at the water pre-peak band at 535.0 eV. (B) O 1s PEY-XA spectra from reference solutions, as labeled. (C) TEY-XA spectra from dry anatase TiO_2 NPs. Assignment of absorption bands: ***a*** *and* ***d*** *(TiO_2 lattice oxide),* ***b*** *(NO_3^-),* ***c*** *(OH^-).*

The respective spectra thus serve as reference, representative of an O 1s XA spectrum in the absence of interfacial oxygen-containing species, and they are also useful to quantify the stabilizer ion and concentration effects on the detected signal intensities. Not surprisingly, these spectra exhibit just absorption ***a***, corresponding to the TiO_2 NP bulk, and band ***d*** stays undetected, hidden under the water pre-edge peak. Small energy shift of band ***a*** with respect to the dry NPs is likely caused by the Cl^- decoration. Turning now to the $[4:1]^{NO3-}$ NP solution – I expect molecular water adsorption (as concluded from Figure 6-2(A)) – an additional band ***b*** (at 532.3 eV photon energy) is observed. The same band occurs in the XA spectrum from 0.5M HNO_3 aqueous solution (Figure 6-3(B)), and I can unequivocally assign band ***b*** to interfacial NO_3^- species. For the $[2:1]^{NH4+}$ and $[1:1.5]^{NH4+}$ NP solutions I find an intense band ***c*** (at 532.8 eV photon energy), *i.e.*, at slightly larger absorption than ***b***, and the intensity of band ***a*** is now very small. Comparing with the XA spectrum from 0.5M NaOH aqueous solution (pH ~13.7) in Figure 6-3(B), where I also find an absorption band (although small) at position ***c***, shows that this band is due to free OH^- (also in agreement with references [153-154]). The comparison with NaOH solution was necessary here because the OH^- signal from 0.5M NH_4OH solution (our reference discussed along with Figure 6-2) is below our detection limit. Note that NaOH is a stronger base than NH_4OH. As a further remark, I point out that the intensities of interfacial OH^- in the NP (aq) solutions is so much larger than the signal of the free OH^- in the reference solutions (particularly 0.5 M NaOH). This result would seem non-intuitive given the NP solution pH of 7.8. I attribute the large OH signal to immobilized dissociated H_2O at or near the TiO_2 surface; alternatively, this effect might be a consequence of the NPs position relative to the solution – vacuum interface to be detailed below. Complementary resonant X-ray scattering (RIXS) studies are presented in Section 7. 3.3 to clarify the origin of this large signal from TiO_2 NPs in aqueous solution, at basic pH.

In order to explore the water–NP interaction mechanism, I performed O 1s RPE spectroscopy measurements at three selected excitation energies, the t_{2g} lattice oxide (absorption ***a***), the interfacial NO_3^- (***b***) and OH^- (***c***). My initial focus is to identify the spectral contributions from the lattice oxide as this will guide me in singling out contributions from interfacial species. In Figure 6-4, I present the RPE spectra from all our NP solutions measured at ***a*** (531.2 eV), and in addition I show the off-resonance spectrum from $[2:1]^{NH4+}$ NP solution. All spectra are displayed with a Shirley background subtracted. The off-resonance spectrum reproduces the water valence spectrum (in blue), [32] and solute signal is below our detection limit. The most relevant feature in this comparison is the electron signal near 22.5 eV (grey-shaded) which results from Auger electron emission. It is specifically the spectator Auger decay, O^{-2} $1s\text{-}1t_{2g}\text{-}1t_{2g}$, occurring at 508.7 eV kinetic energy (equivalent to 22.5 eV BE), and has been assigned with the help of the TiO_6^{-8} molecular orbital diagram from reference[235]. The other

spectral features at approximately 18.0 and 24.5 eV BE are also due to spectator Auger decay but are not further considered here as their intensities are too small for a quantitative analysis of the interfacial species.

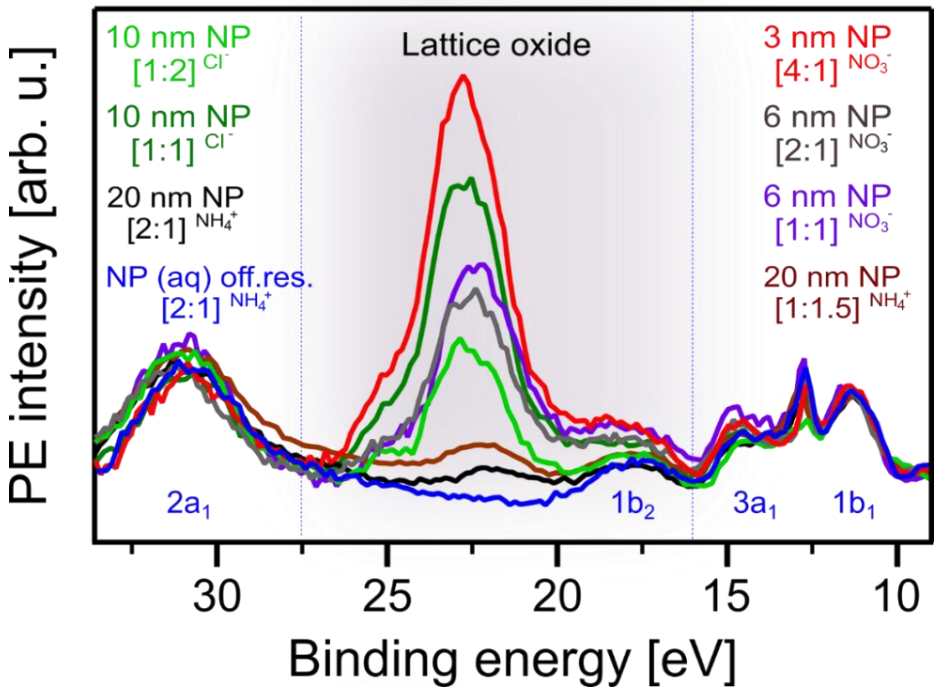

Figure 6- 4

*Valence resonant photoelectron (RPE) spectra from different anatase TiO_2 NP aqueous solutions measured at the O_2^- resonance, **a** (531.2 eV photon energy; compare Figure 6-3). Also presented is the off resonance spectrum from [2:1]NH_4^+ NP solution, measured at 530.0 eV photon energy. Solutions are labeled as explained in the caption of Figure 6-1. Here, we have added the NP diameters. The grey-shaded area highlights the contributions from the spectator Auger electrons originating from the TiO_2 lattice oxide.*

The next observation from Figure 6-4 is the considerable intensity variation of the lattice oxide absorption band among the different solutions. At the applied 531.2-eV photon energy (resonance ***a*** in Figure 6-3) the electron inelastic mean free path can be assumed to be less than 3 nm,[35] implying that the NPs are located within this range from the solution – vacuum interface. Arguably, there are several parameters that have direct influence on the exact position of a nanoparticle in the measured solutions, including particle size, stabilizer ion and concentration. The current experiment was not designed to systematically study such effects since the different solutions in this work usually differ by more than one parameter. However, the lattice signal contributions tend to be larger for the smaller

NPs, which might be an indication of smaller NPs having a larger affinity for the solution interface. On the other hand, the comparison between the 10 nm $[1:1]^{Cl-}$ and the 6 nm $[1:1]^{NO3-}$ NP solutions would suggest the opposite, indicating that the distance of the NPs from the solution surface depends on the complex interplay between size, charge, and adsorbate, and specifically on the respective nature of the so-called diffusive layer.[236] It is reminded that electronic-structure size effects (see Methods and Materials Section 6.2) in the NP size range considered here can be expected to be negligible.

Having analyzed the oxygen signal from the NPs, based on the O 1s RPE spectra at the lattice oxide resonance, ***a***, I now turn to explore the contribution from oxygen-containing molecular species at the NP / water interface. I start with the acidic solution. Figure 6-5 shows RPE spectra measured at the NO_3^- resonance, ***b***, for the $[1:1]^{NO3-}$, $[2:1]^{NO3-}$, and $[4:1]^{NO3-}$ NP aqueous solutions. For comparison I also include a spectrum from the 0.5 M HNO_3 aqueous solution. All spectra are displayed with a Shirley background subtracted. As in Figure 6-4 the signal near 30 eV ($2a_1$) and 11 eV ($1b_1$) is due to water, [237] and the latter was used for signal intensity normalization. The interesting features are the broad electron emissions in the 13-24 eV BE range due to NO_3^-. As in the previous work on hematite NPs [197] (see Figure 5-4) the same four main photoemission bands are observed, at approximately 16.0, 18.0, 22.5, and 24.5 eV BE (all within the red-shaded area), assigned to various Auger-electron decays upon O 1s → valence excitation at 532.2 eV photon energy.[197] The 24.5-eV peak strongly overlaps with the lattice oxide peak (black-shaded area); compare Figure 6-4. This peak can be most clearly observed for the $[4:1]^{NO3-}$ NP solution, in which case NO_3^- contribution is the lowest; see experimental section. On the other hand, the NO_3^- signal increasingly dominates when going from $[4:1]^{NO3-}$ to $[1:1]^{NO3-}$ solutions. In fact, relative intensities (red-shaded area) almost quantitatively track our estimated NP surface sites-to-stabilizer ratios. Most important for the present study are however the $[2:1]^{NO3-}$ and $[4:1]^{NO3-}$ solutions which provide free surface sites for water to interact with the TiO_2 surface. If this interaction were dissociative, Auger signal from adsorbed OH^- should appear in the 25-32 eV binding energy finger-print region (blue-shaded area) analogue to the hematite NPs (aq) study;[197] this is because of the considerable spectral overlap between resonances ***b*** and ***c*** (of adsorbed NO_3^- and OH^-, respectively), seen in Figure 6-3(A). Obviously no signal of adsorbed OH^- is observed here, corroborating our above finding (from the O1s non-resonant spectra, Figure 6-2(A), and O K-edge XAS, Figure 6-3) that water adsorbs molecularly on the surface of the TiO_2 in acidic environment. In the next paragraph I discuss the interaction in basic solution.

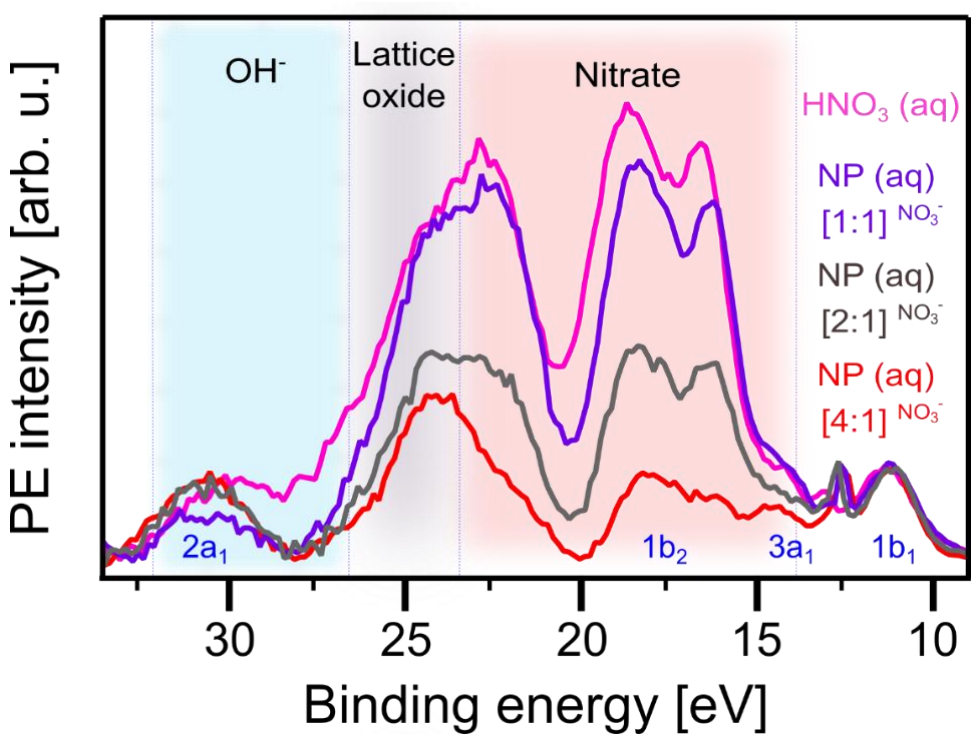

Figure 6- 5

*Valence resonant photoelectron (RPE) spectra from different anatase TiO_2 NP aqueous solutions measured at the NO_3^- resonance, **b** (523.2 eV photon energy; compare Figure 6-3). Also presented is the spectrum from 0.5 M HNO_3 aqueous solution. Different shades indicate the regions of Auger-electron emission from different species: NO_3^- (red-shaded), lattice oxide (grey-shaded), OH^- (blue-shaded).*

Figure 6-6 shows the respective O 1s RPE spectra from the basic $[2:1]^{NH4+}$ and $[1:1.5]^{NH4+}$ NP solutions. Measurements were performed right at the OH^- resonance (peak ***c***, 532.8 eV photon energy), rather than at resonance ***b***, which increases the spectral sensitivity to adsorbed OH^-. The figure also includes an off-resonance spectrum from the $[2:1]^{NH4+}$ NP solution measured at 530 eV photon energy as well as a reference spectrum from 0.5 M NaOH aqueous solution. All the spectra are Shirley-background subtracted. Again, the off-resonance spectrum (in dark blue) reproduces the water valence peaks.[32] The NaOH spectrum (light blue) exhibits the resonantly enhanced OH^- signal, dominated by Auger-electron emission, in the 15-25 eV BE range (corresponding to 505-514 eV kinetic energy range).[153] This signal contribution is found to be much larger in the spectra from the NP solutions, with an intensity being an order of magnitude larger than the signal from the water valence band. I note though that near the 25-eV BE position (grey-shaded area) the OH^- signal considerably overlaps with the electron emission from lattice oxide (see also Figure 6-4 and 6-5). The

remarkably large OH^- signal for the NP solutions, with pH 7.8 ($[2:1]^{NH4+}$) and 9.7 ($[1:1.5]^{NH4+}$), is a clear indication that this signal cannot be due to free OH^- in aqueous solution, and rather arises from OH^- bound to the aqueous-phase NP surface. It is useful to recall our observation from Figure 6-1 that in the case of the $[2:1]^{NH4+}$ NP solution 10Dq is larger than for all other NP solutions. Together with our findings in Figure 6-6 this corroborates that the split can be associated with the different specific interactions between a H_2O molecule and a Ti site at the anatase surface. Our final observation from Figure 6-6 is the slight increase of the OH^- signal when increasing the NH_4^+ concentration from 0.3 M ($[2:1]^{NH4+}$) to 0.8 M ($[1:1.5]^{NH4+}$), which is paralleled by an increase of the OH^- XA-band intensity as was shown in Figure 6-3(A). This effect will be discussed next.

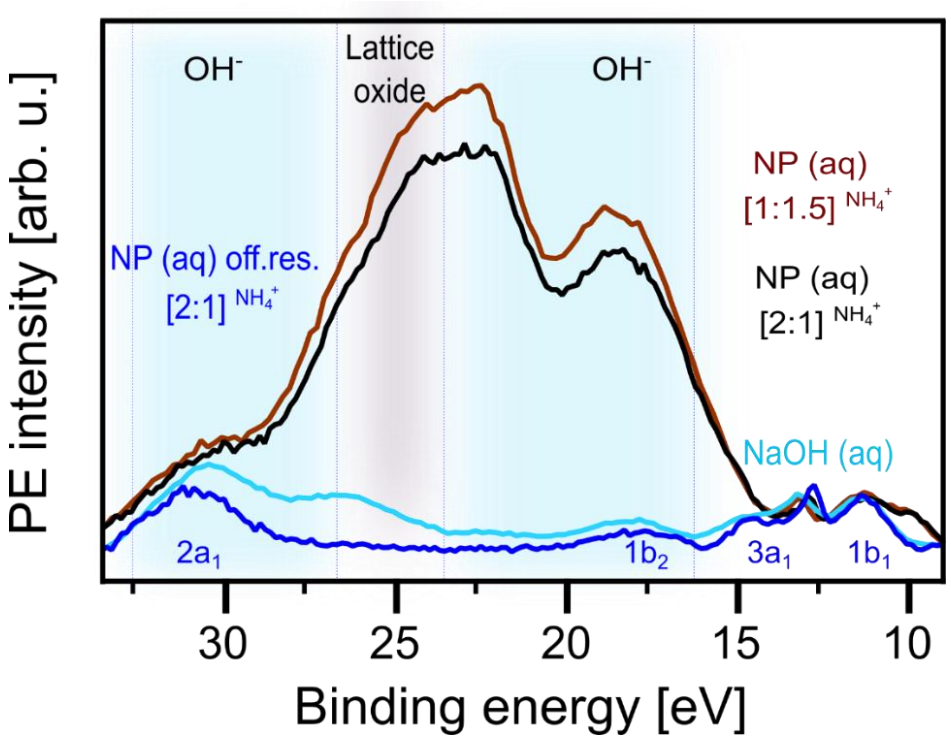

Figure 6- 6

*Valence resonant photoelectron (RPE) spectra from different anatase TiO_2 NP aqueous solutions measured at the OH^- resonance, **c** (532.8 eV photon energy; compare Figure 6-3). Also presented is the spectrum from 0.5 M NaOH aqueous solution, and in addition the off-resonance spectrum measured at 530 eV photon energy from the $[2:1]NH_4^+$ NP is shown. Different shades indicate the regions of Auger-electron emission from different species: lattice oxide (grey-shaded), OH^- (blue-shaded).*

My observations, from Figures (6-1) to (6-6), lead me to propose the following pH-dependent adsorption mechanisms for water on the anatase NP surface, illustrated in Figure 6-7. Here I depict the interaction in the acidic environment in the top tier, and in basic solution in the bottom tier. My starting point is the hypothetical (prepared) adsorption of a water molecule for both cases. This is followed by the dissociation of H_2O at the defect-free anatase surface, forming a hydroxyl / H^+ pair similar to the processes discussed in references, [192] and explained in the introduction. Above, I have inferred from the changes of 10Dq that water dissociates at the Ti surface sites of the TiO_2 NP. One crucial difference between acidic and basic environments is then the probability to stabilize the (paired) proton in the vicinity of OH^- at the surface. In fact, aforementioned simulation of the dissociative/ associative water adsorption on rutile TiO_2 using DFT calculations[222] concludes that the stability of hydroxylated configuration is largely dependent on the locations of the H^+ species, and the recombination of water molecules from hydroxyls is observed in the fully hydroxylated condition. I argue that this is what our data show. Under acidic conditions the free proton is locally rather confined due to hydronium molecules, and recombination to form water is likely. This is illustrated in the acidic-environment model (top tier of the second step), in Figure 6-7. Possibly, also the surrounding hydronium in water may transfer a proton to a surface OH^- molecule (center tier of the second step). In any case, our experiments suggest that the lifetime of hydroxyl is very short, and this species can thus not be detected here. In contrast, such recombination is less likely in basic solution where H^+ quickly diffuses away from the surface, and the OH^- lifetime is sufficiently large. This situation is illustrated at the right side of the bottom tier of Figure 6-7. My model mechanism would also account for the increase of OH^- signal suggested by the spectrum of the $[1{:}1.5]^{NH4+}$ NP solution in Figure 6-6. Here, due to larger pH the proton delocalization is even larger, which leads to the stabilization of more hydroxyl groups at the TiO_2 surface.

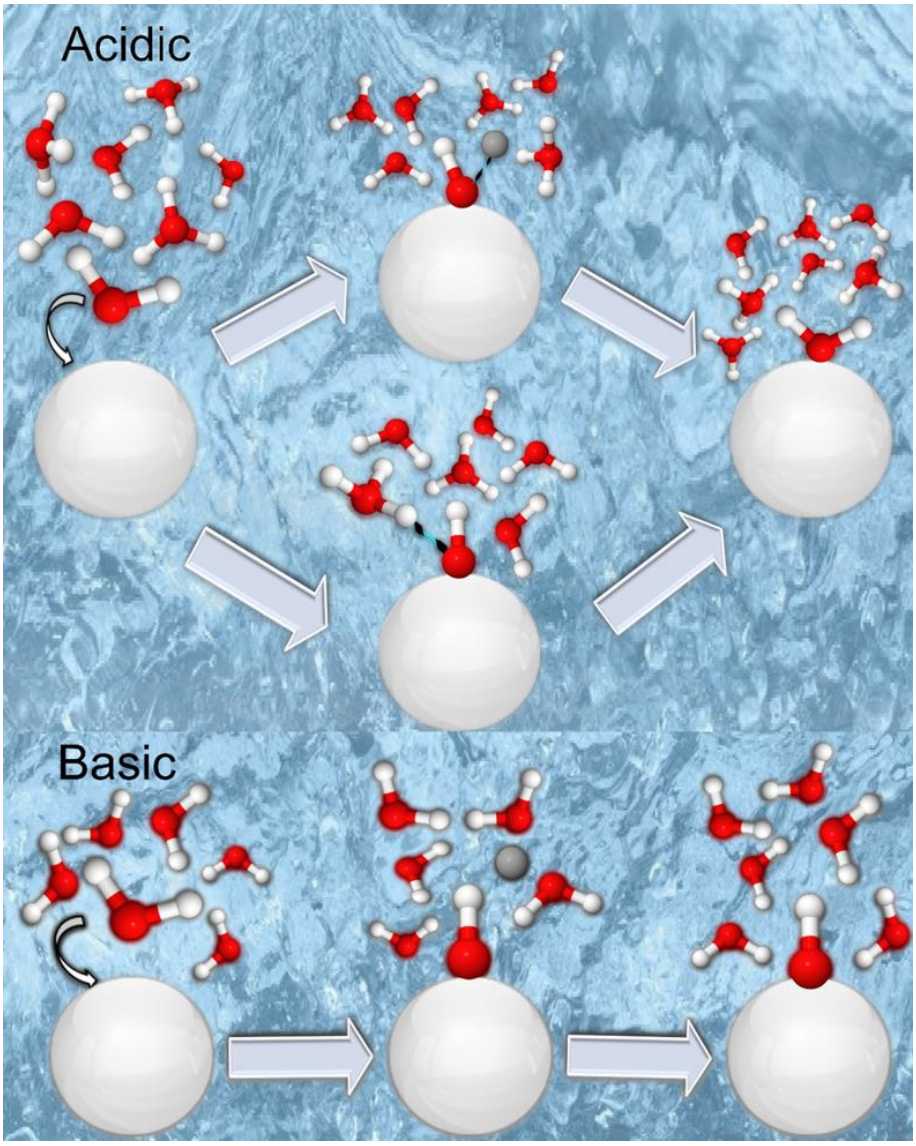

Figure 6- 7

Illustration of the proposed TiO_2 – water interaction in acidic (top tier) and basic (bottom tier) aqueous solutions. TiO_2 NPs are represented by the large white spheres. Water and hydronium oxygens are shown in red, bonded hydrogen atoms in white, and a single free hydrogen (proton) in solution is shown in light-grey. The hydroxyl stability on the NP surface depends on its probability to form a water molecule by capture a free H^+ or via proton transfer from a surrounding hydronium. This probability is largest in acidic environment, either by recombination of the dissociated H^+ and OH^- pairs (top panel in the acidic model second step) or by proton transfer from the surrounding hydronium (bottom tier in the acidic model second step). Such recombination and proton transfer processes do not occur in a basic or above neutral chemical environment; the basic-pH interaction model is illustrated in the bottom-most tier of the Figure.

6.4 Conclusions

I have examined the solid–liquid interface of titania NPs in aqueous solutions of different pH. By measuring the Ti L-edge XA spectra I confirmed that in all solutions studied here the NPs exhibit an anatase TiO_2 phase. Molecularly adsorbed H_2O molecules were found on the NP surface in the acidic solution. However, dissociative water interaction, leading to OH^- species at the TiO_2 surface, is observed for the near-neutral solutions. This behavior is inferred from the oxygen 1s core level non-resonant PE spectra, and corroborated by the O K edge XA as well as the resonant PE spectra. Specifically, the RPE spectra are a sensitive probe of the NP lattice oxide, and of the existence or absence of NO_3^- and OH^- interfacial species. The detailed spectral analysis of the 10Dq value suggests that water interacts with the Ti sites of the NPs surface. My results lead to propose that at acidic pH the protonation of adsorbed OH^- at the Ti-site of the defect-free anatase NP surface is fast, leading to molecularly adsorbed water as dominant species. This is either by recombination of the proton, which stays rather localized at the site where it was born, with surface OH^-, or by proton transfer from hydronium to a surface OH^-. On the other hand, at basic pH, the proton can easily diffuse away from the surface which makes the reformation of adsorbed H_2O unlikely. An interesting aspect of these findings is that the pH variation provides a means to control the molecular *versus* dissociative water interaction with anatase surfaces. This finding is in agreement with previous theoretical studies on the stability of hydroxylated configurations[222], and on the proton transfer between the TiO_2 surface and hydronium in solution.[224]

I also like to stress that the liquid-jet PE technique is truly complementary to ambient-pressure PE spectroscopy, with the latter ideally suited for investigation of crystalline surfaces covered by several water or aqueous solution monolayers at neutral pH. As shown here, investigation of the respective nanoparticles (TiO_2) fully dispersed in an aqueous solution enables unique access to study the TiO_2 – water interface as a function of pH. Moreover, the application of the multiple aspects of photoemission (beyond the mere measurement of photoelectron spectra) in ambient-pressure studies remains challenging. And yet, future investigations of catalytically-relevant NPs (aq), including also hybrid system like core-shell nanoparticles[238], or tailored nanoparticle properties in material research would benefit from measurements in the tender or even hard X-ray regime in order to better characterize the distribution of NPs at the aqueous solution – vacuum interface.

6.5 Appendix

6.5.1 Valence Band Photoelectron Spectra Measured On-resonant and Off-resonant at the Ti L-edge for the [2:1]$^{NH4+}$ NP(aq) Solution

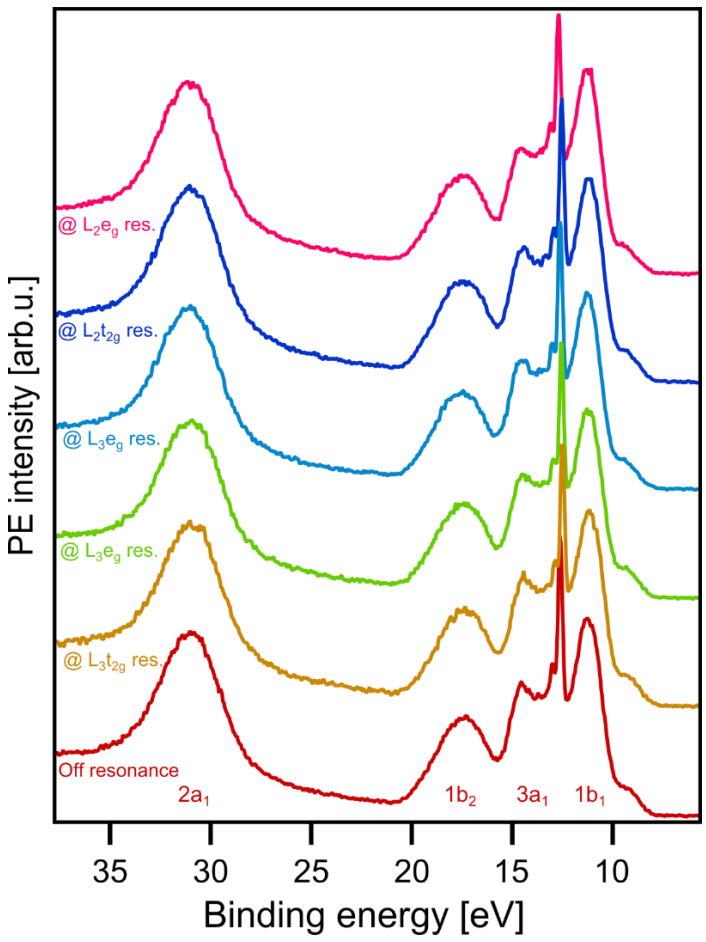

Figure A-6- 1

Valence band photoelectron spectra measured at off-resonance and on-resonance (A, B, C and D in Figure 6-1) photon energies for the [2:1]$^{NH4+}$ sample. The off-resonance spectrum was measured at 457 eV photon energy, while the on-resonance spectra were recorded at marked peaks in Figure 6-1: A (L_3t_{2g}), B (L_3e_g at two positions due to the sub-splitting), C (L_2t_{2g}) and D (L_2e_g). All spectra are almost identical, exhibiting no signal from Ti^{3+}.

6.5.2 The $10D_q$ Energy Splitting of the Ti 3d Orbital Detected from TiO_2 NP Aqueous Solutions

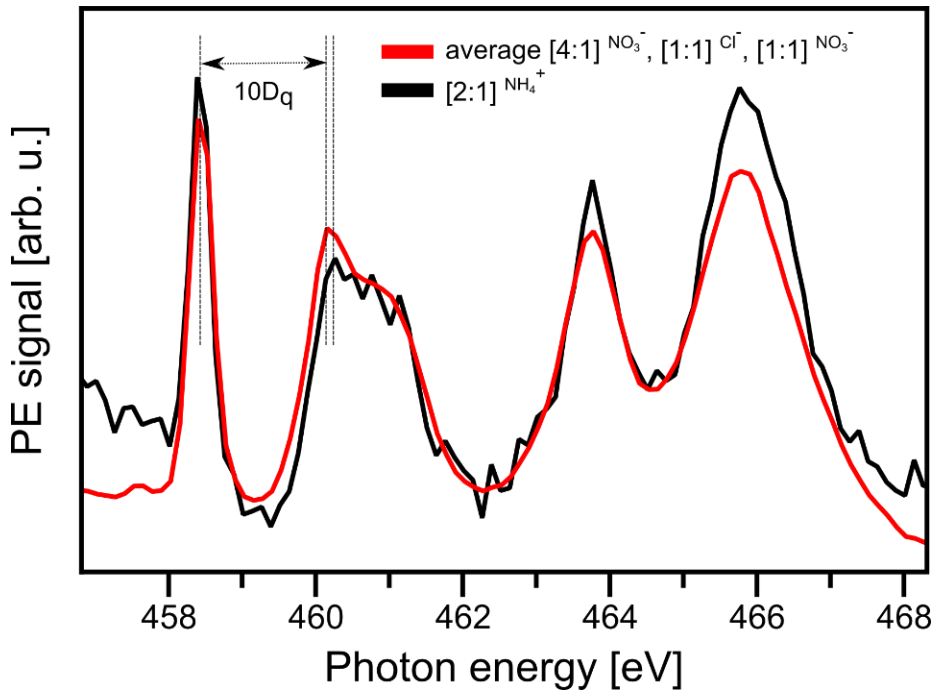

Figure A-6- 2

Ti L-edge PEY-XA spectrum in black from anatase TiO_2 NPs $[2:1]^{NH4+}$ sample in comparison with an average spectrum of the TiO_2 NPs $[4:1]^{NO3-}$, $[1:1]^{Cl-}$ and $[1:1]^{NO3-}$ solutions shown in Figure 6-1. The $10D_q$ splitting is indicated by dashed lines.

Chapter 7

X-ray Spectroscopic Characterization of the Electric Double Layer (EDL) around TiO_2 Nanoparticles Stabilized in NH_4OH Aqueous Solution

This part of the thesis is taken from the following publication:

In-Situ X-ray Spectroscopy of the Electric Double Layer around TiO_2 Nanoparticles Dispersed in Aqueous Solution: Implications for H_2 Generation

Hebatallah Ali, Ronny Golnak, Robert Seidel, Bernd Winter and Jie Xiao

ACS Applied Nano Materials 2020, **3** (1), 264-273, **DOI:** 10.1021/acsanm.9b01939

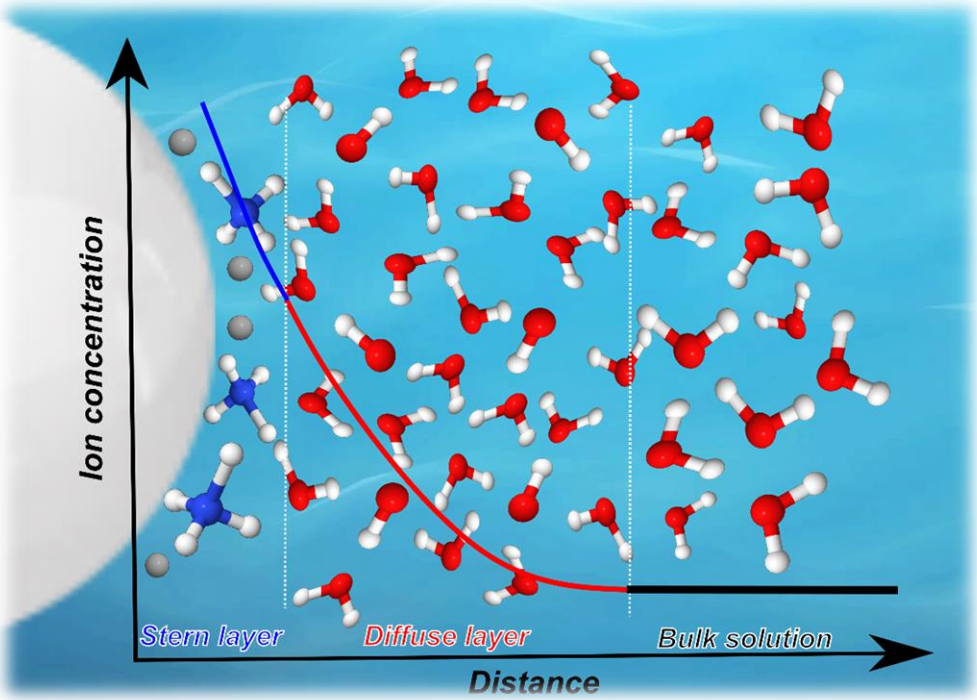

Composition of the EDL around TiO_2 nanoparticles dispersed in NH_4OH aqueous solution.

7.1 Introduction

Titanium dioxide (TiO_2) is a promising material to catalyze water dissociation for the production of H_2 fuel as a clean and renewable energy source.[177, 185, 189, 239-240] Among the three TiO_2 phases, brooktile, rutile and anatase, the latter phase exhibits the highest photocatalytic activity[241-242] and chemical stability in various aqueous environments.[243] Many efforts have been made to improve the TiO_2-catalyzed energy conversion efficiency in water-splitting reactions.[177, 180-186] However, the fast back-reaction of proton (H^+) and hydroxide (OH^-) recombination into water molecules reduces the efficiency significantly.[189] Spatial separation of proton from hydroxide is therefore very critical for the enhancement of the water dissociation efficiency and device performance. This separation of the dissociation products, H^+ and OH^- ions, in the vicinity of the TiO_2 – water interface requires a true aqueous environment (rather than a few monolayers of water coverage) that enables ions to diffuse away from the interface. In fact, the electric double layer (EDL) that forms at the TiO_2 – water interface will strongly influence ion distributions and mobilities. Several models have been proposed to describe the EDL, including the Helmholtz model,[244] the Gouy-Chapman model,[245-246] and the Gouy-Chapman-Stern model[247]. In the Helmholtz model, the EDL is treated analogously to a static electric capacitor[248-249] where all counter-ions are postulated to be confined to the TiO_2 surface, and all co-ions are repelled. Ion mobility in solution is completely ignored in this model.[248-249] It is, however, taken into account in the Gouy-Chapman model that postulates a diffuse layer located at the interface where the ion concentration away from the interface follows the Boltzmann distribution.[249] This model assumes that ions are point charges, occupying no space, and this can lead to an overestimation of surface charge.[249] The Gouy-Chapman-Stern model,[247] based on the two previous models, which is also the model we adopt in this study to discuss the acquired spectra, introduces an additional layer, the Stern layer, where some or all counter-ions are confined at the TiO_2 surface. The remaining counter-ions or co-ions, depending on the electrolyte concentration, are mobile and form the diffuse layer.[250] As in the Gouy-Chapman model, ions are Boltzmann-distributed across the layer. The thickness of the EDL in the Gouy-Chapman-Stern model is defined as the Debye length, which is strongly dependent on the electrolyte concentration.[248]

Although the charge parity of the EDL at the TiO_2 – water interface in dilute aqueous solution has been extensively investigated by various methods,[251-254] we still lack a quantitative molecular-level experimental insight into the detailed EDL structure, including the Debye length (electrostatic screening length). Soft X-ray spectroscopy studies that can directly reveal element-specific electronic structure of interfacial species are still scarce for solid surfaces in contact with real (bulk) aqueous solution. In recent years, the development of ambient pressure X-ray photoelectron spectroscopy (AP-PES) has allowed for instance probing of the EDL for a thin electrolyte film on top of a polycrystalline gold electrode created by the so-called “dip-and-pull method” by using tender X-ray radiation for ionization.[255] In the aforementioned study, the Debye length, measured as a function of the KOH

electrolyte concentration, has been reported to decrease monotonically from 30.4 nm at 0.1 mM to approximately 1.9 nm near 80 mM concentration.[255] Despite extensive experimental efforts, PES studies seeking to reveal the EDL dimension have remained limited to nanometer-thick water coverage, in which case ion mobility and ion adsorption/desorption at the TiO_2 surface will be different than in bulk solution.[256] In-situ probing of the TiO_2 surface fully contained in liquid water is therefore of great importance, but experimentally challenging.

In this study, X-ray photoelectron spectroscopy (PES) and partial electron/fluorescence yield X-ray absorption spectroscopy (PEY/PFY-XAS) measurements are conducted on anatase-phase TiO_2 nanoparticles (NPs) dispersed in NH_4OH aqueous solution. Our system represents a TiO_2 surface fully immersed in aqueous solution at slightly basic pH (~7.8), for which we recently demonstrated dissociative water adsorption at the NP – solution interface.[257] Here, we report complementary electron-yield and photon-yield detections to quantify the amount of water dissociation at the TiO_2 – water interface, and estimate the Debye length. The NP solution has a concentration of 20 wt% corresponding to an average separation distance between the dispersed NPs of approximately 80 μm resulting from van der Waals (vdW) interaction between the NPs. In this case of high NP concentration, the Stern layer is composed of stabilizer NH_4^+ ions (discussed later along with Figure 7-2), and NP aggregation and the lack of it can be well described by the Derjaguin, Landau, Verwey and Overbeek (DLVO) theory.[248-249] Accordingly, at high electrolyte concentration, the NP interaction potential barrier is lowered and a minimum (secondary energy barrier with oppositely charged ions) in the potential curve can lead to a slow NP aggregation.[249] For electrolyte concentrations above the so-called critical coagulation value, the energy barrier reduces to below zero and triggers NPs to aggregate rapidly.[249] The TiO_2 NP colloidal solution in the present study falls into the category of relatively high concentration, but still being below the critical value. We briefly review the expected nature of the EDL, and how it depends on electrolyte concentration. As illustrated in the cartoon of Figure 7-1(A), at low electrolyte concentration positive charge (these are the NH_4^+ cations) accommodates at the NP surface to establish charge neutrality of the NP + EDL entity. In a simplified picture, Figure 7-1(B), of high electrolyte concentrations negative charge from the electrolyte (OH^- in our case) will approach the NPs more closely, and stay associated with the NPs within the EDL. The primary goal of the present study is to use PES together with the more bulk-sensitive PFY-XA spectroscopy to identify the molecular nature of the EDL, including composition of oppositely charged ions, and to even estimate the thickness of the EDL and infer hydration structure details.

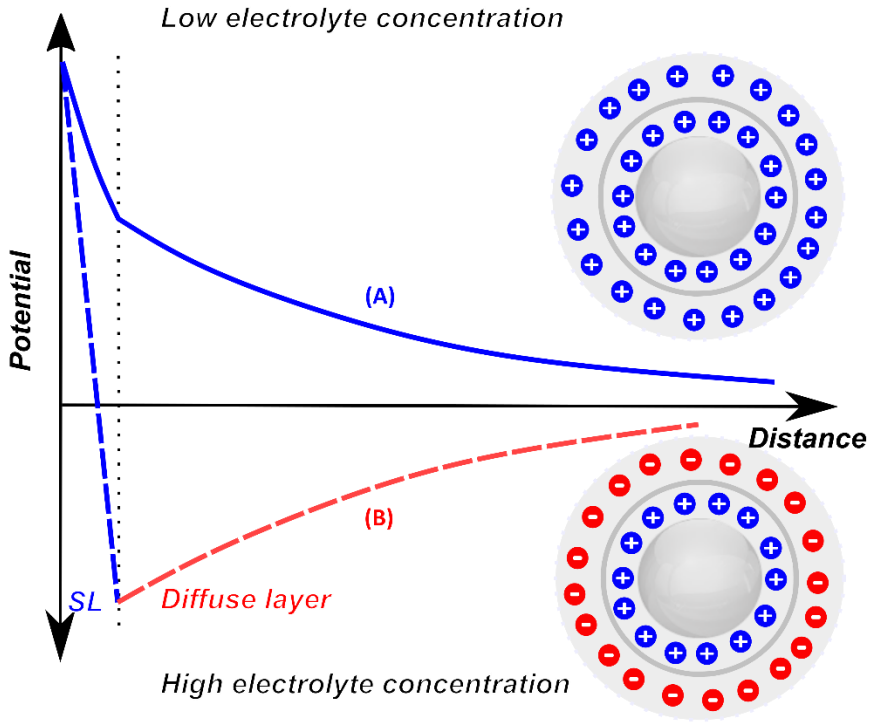

Figure 7-1

Potential curves of the EDL surrounding the nanoparticle: (A) low electrolyte concentration, and (B) high electrolyte concentration (adsorbing counter-ions) leading to charge reversal. The figure is partially adapted from reference [250].

7.2 Methods and Materials

Both the PES and PEY-XAS measurements were conducted with the SOL^{3}PES setup,[62] and PFY-XAS studies were performed with the LiXedrom setup,[258] at the synchrotron-radiation facility BESSY II, Berlin. For all measurements we used the soft X-ray beamline U49/2-PGM1. A 20 wt% colloidal solution of 20 nm diameter anatase-phase TiO_2 NPs dispersed in 0.3 M NH_4OH aqueous solution was acquired from NYACOL, USA, and introduced into the experimental vacuum chambers by applying liquid microjet technique.[86] I also investigated 0.5 and 2 M NH_4OH, and 5 M NaOH aqueous solutions, as well as a 20 wt% colloidal solution of 10 nm diameter anatase-phase TiO_2 NPs dispersed in 0.5 M HCl aqueous solution purchased from MK Nano, Canada, which all served as references for spectral comparisons. Note that the NP surface in 0.5 M HCl aqueous solution is fully covered by adsorbed Cl^- ions, and water cannot interact with the TiO_2 NP. This provides a useful spectroscopic reference, and has been applied in several previous liquid microjet PES studies.[62, 138-139, 197-198, 259] According to the concentrations of the TiO_2 NP (20 wt%) and NH_4OH (0.3 M) aqueous solutions, the NP diameter (20 nm), and with the reported adsorption density of approximately 5.2

molecule/nm^2 on the TiO_2 surface,[93, 192] I estimate that approximately half of the total NP surface is covered by NH_4^+ stabilizer ions. This leaves the other half of TiO_2 surface sites available for interaction with water. In the following, the term $[X:Y]^{st}$ is used to indicate the ratio between the available TiO_2 surface sites X and adsorbed stabilizer ions Y, and st denotes the stabilizer ion. $[2:1]^{NH4+}$ and $[1:1]^{Cl-}$ thus denote the NP solutions where half of the NP surface is covered by NH_4^+ and fully covered by Cl^- ions, respectively.

7.3 Results and Discussion

7.3.1 N 1s Off-resonant Photoemission and PEY-XA Spectra

In an ammonia aqueous solution, hydrated ammonia undergoes a chemical equilibrium reaction with liquid water, $NH_3(aq) + H_2O \leftrightarrow NH_4^+(aq) + OH^-$, (Equation (7-1)), making the solution basic. This reaction is dependent on temperature and pH, and an equilibrium between NH_3 and NH_4^+ species is established at approximately pH 9 (pKa ~ 9) at 24°C.[260-261] A 0.3 M NH_4OH aqueous solution (containing no TiO_2 NPs) has pH 11.3. When TiO_2 NPs are dispersed into the solution, NH_4^+ stabilizer ions adsorb at the NP surface[248] (see Figure 7-1). As a result, there is no free NH_4^+ in the solution. NH_4^+ adsorption thus perturbs the ammonium – ammonia chemical equilibrium (Equation 7-1) which leads to the production of more OH^-. However, the measured pH of the $[2:1]^{NH4+}$ NP colloidal solution is 7.8, just slightly above neutral pH. This surprising observation implies the presence of additional reactions, other than the ammonium – ammonia equilibrium, that occur in the solution and affect the number of OH^- ions. In order to determine these additional reactions, I first investigate NH_4^+ ions in the presence of TiO_2 NPs and subsequently compare with NH_4OH aqueous solution (without TiO_2 NPs added) by measuring the PEY-XA at the N K-edge and PE spectra of N 1s orbital. I then explore the OH^- species by recording the O 1s PE spectra from the 5 M NaOH, 0.5 M NH_4OH, $[2:1]^{NH4+}$ NP aqueous solutions, and $[2:1]^{NH4+}$ NP aqueous solution with 0.5 M NaOH added. Finally, I derive the hydroxide hydration configuration for the $[2:1]^{NH4+}$ NP aqueous solution based on its O K-edge PFY-XA spectrum in comparison with the spectra of $[1:1]^{Cl-}$ NP and 1.5 M NaOH aqueous solutions.

Figure 7-2(A) shows the N K-edge PEY-XA spectra of the $[2:1]^{NH4+}$ NP solution and 2 M NH_4OH aqueous solution (pH ~12), respectively. These two spectra are generated by integrating the signal intensity of the valence-band photoelectron spectra (not shown here) as a function of photon energy; see, *e.g.*, ref [167] for a more detailed explanation. Observed spectral differences reveal the existence of different nitrogen-containing species in the two solutions. The spectrum of the 2 M NH_4OH solution (Figure 7-2(A), bottom) primarily exhibits spectral features characteristic of neutral gas-phase ammonia (NH_3).[262] This can be explained by the ammonium – ammonia equilibrium reaction (Equation 7-1). At high pH ~12, the equilibrium reaction moves towards the $NH_3(aq)$ side,

and due to ammonia's high volatility[260-261] and the rather short probing depth of soft X-ray PES, the spectrum is then dominated by NH_3(g) signal. Note that Henry's constant for the hydrated NH_3 is relatively high, 59 mol/atm at 25°C.[263] Under the experimental condition, NH_3(aq) is below the detection limit whose main feature would be expected to appear between the first two peaks of gas phase followed by an intense absorption step edge[262], which is not the case for the bottom spectrum of Figure 7-2(A). Our observation is in agreement with the previous N 1s Auger-electron/autoionization PE study from a 2.6 M NH_3 aqueous solution.[264] Turning now to the N K-edge PEY-XA spectrum of the $[2:1]^{NH4+}$ NP solution (Figure 7-2(A), top), I find reasonable resemblance to the reported spectrum of NH_4^+ aqueous solution,[43] but better agreement is obtained when comparing to the dry NH_4^+ salts.[265-266] Considering the nearly neutral pH of this solution, it suggests that NH_4^+ ions are adsorbed at the TiO_2 NP surfaces acting as a stabilizer.

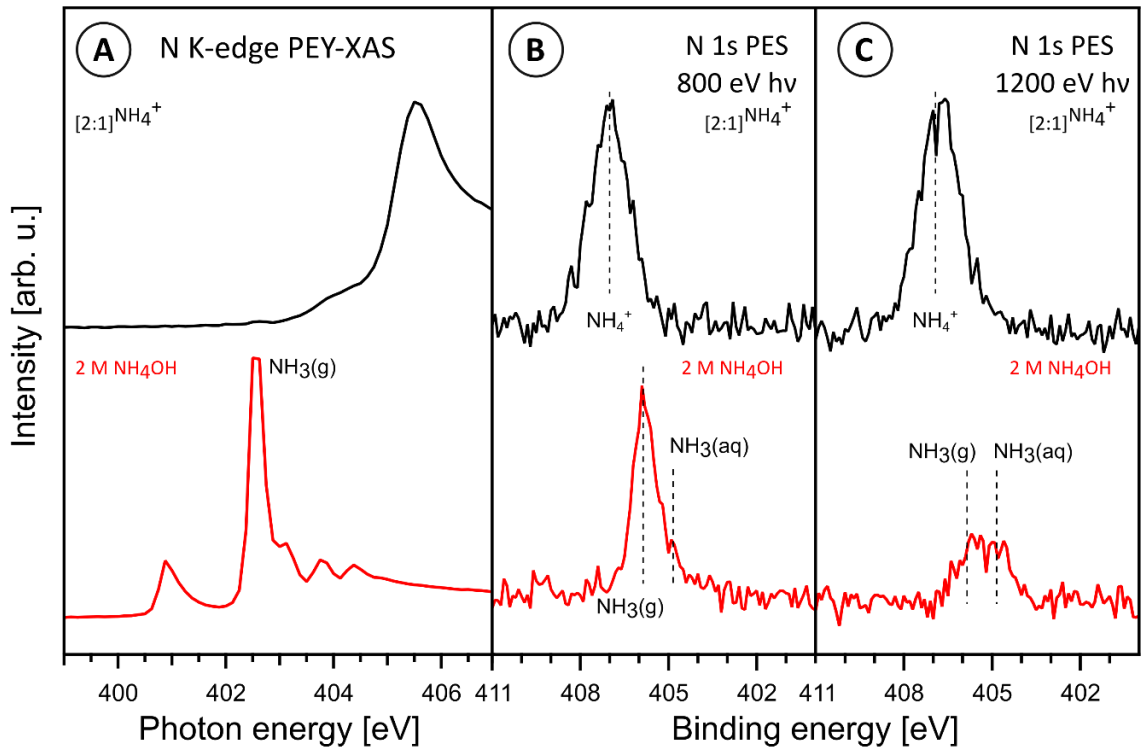

Figure 7-2

(A) Nitrogen K-edge PEY-XA spectra from $[2:1]^{NH4+}$ NP (black, top) and 2 M NH_4OH (red, bottom) aqueous solutions, and the respective N 1s photoelectron spectra measured at 800 eV (B) and 1200 eV (C) photon energies. Spectral contributions of NH_3(g), NH_3(aq), and NH_4^+ are labeled.

Our conclusion on the nature of the nitrogen-containing species is corroborated by the N 1s PE spectra from the same two solutions which are also presented in Figure 7-2. Measurements were performed at two photon energies, 800 eV (Figure 7-2(B)) and 1200 eV (Figure 7-2(C)). The latter energy probes deeper into the solutions due to the larger kinetic energies of the photoelectrons resulting in a larger electron inelastic mean free path (IMFP).[35] Beginning with the 800-eV spectrum taken from the 2 M NH_4OH solution (Figure 7-2(B), bottom), one observes a large peak at 405.9 eV binding energy (BE) which arises from N 1s ionization of gas-phase ammonia, NH_3(g). Signal from NH_3(aq) is weak, giving rise to a small shoulder at 404.8 eV BE. In contrast, the 800-eV PE spectrum of the $[2{:}1]^{NH4+}$ NP solution (Figure 7-2(B), top) exhibits a single peak at larger BE of 407.0 eV which originates from N 1s ionization of adsorbed ammonium stabilizer, NH_4^+. This is exactly what one would expect based on Figure 7-2(A), top. Note also that in both cases the energies of the detected electrons are rather similar. That is, the kinetic energy (KE) of the N 1s photoelectrons (excited by 800 eV photon energy) and of the N 1s Auger electrons (from which the PEY-XA spectrum in Figure 7-2(A), bottom, has been obtained) are approximately 400 eV. At this energy the electron probing depth is thus too small to detect a noticeable signal from NH_3(aq). Increasing the photon energy from 800 to 1200 eV has a minor effect on the PE spectrum of $[2{:}1]^{NH4+}$ solution (Figure 7-2(C), top), but one observes a drastic change of the spectrum from the 2 M NH_4OH solution (Figure 7-2(C), bottom). Due to the increased probing depth, the spectrum of the 2 M NH_4OH solution now exhibits, in addition to the NH_3(g) signal at 405.9 eV, a second peak at 404.8 eV of similar intensity arising from NH_3(aq). This implies that the majority of NH_4^+ in the $[2{:}1]^{NH4+}$ NP solution cannot be assigned to species solvated in bulk solution. If this were the case, a significant amount of NH_3(g) (and some NH_3(aq) at 1200 eV excitation energy) signal would be detected due to the ammonia – ammonium equilibrium (Equation 7-1). Therefore, Figure 7-2 reveals that almost all NH_4^+ ions in the $[2{:}1]^{NH4+}$ NP solution are adsorbed on the TiO_2 NP surface, covering about half of the available surface area, as mentioned above. The adsorbed NH_4^+ ions constitute a positively charged Stern layer of the EDL. The thickness of this Stern layer is on the order of the diameter of the NH_4^+ ion which is approximately 0.35 nm, assuming a 0.175 nm NH_4^+ ionic radius.[267]

7.3.2 O1s Off-resonant Photoemission Spectra

I next focus on the nature of the oxygen-containing species, and I am particularly interested in identifying dissociated water and estimating the amount of OH^- anions, from which an approximate length of the diffuse layer can be inferred. For that I have measured the oxygen 1s PE (Figure 7-3) and oxygen K-edge PFY-XA (Figure 7-4) spectra from the same $[2{:}1]^{NH4+}$ NP solution. In addition, I present the respective spectra from two reference aqueous solutions, 5 M NaOH and 0.5 M NH_4OH. 5 M NaOH solution is used to establish the OH^- PES peak position, and to identify the effect of OH^-

on the water structure through changes of the water O 1s PE peak. Note that 0.5 M concentration is reasonably close to the 0.3 M NH_4OH concentration which is used to stabilize the aqueous-phase TiO_2 NPs. All PE spectra were measured at 1200 eV photon energy, *i.e.*, at the same energy which we have applied to increase the probing depth into the solution in the case of the N 1s PE measurements (Figure 7-2(C)). Spectra are displayed to yield the same heights of the strongest peak. Figure 7-3(A) shows the O 1s PE spectrum from the 5 M NaOH aqueous solution. Three major oxygen features can be observed, the dominating liquid-water peak at 538.1 eV BE,[86] the water-vapor contribution at 539.9 eV,[164, 268] and hydrated OH^- giving rise to a shoulder at 535.8 eV.[269] These contributions are highlighted by the respective Gaussian fits shown in different colors; see figure caption for details. The O 1s PE spectrum from the other reference solution, 0.5 M NH_4OH, shown in Figure 7-3(B) exhibits no OH^- signal at this low OH^- concentration; this is also true for a NaOH aqueous solution of the same concentration.[269] Another important difference between the spectra of lower (0.5 M) and higher (5 M) OH^- concentrations is the change of the water O 1s peak width. The full width at half maximum (FWHM) of the low-concentration spectrum is approximately 1.6 eV (which is almost the same as for neat liquid water[164]), and increases by 12.5 % (0.2 eV wider) for the higher concentration. Qualitatively, such a broadening is in accord with a theoretical finding that hydration of hydroxide affects the electronic structure of water,[270] and it also agrees with previous experimental and computational PFY-XA study of hydroxide aqueous solution[154] which will be detailed below along with the discussion of Figure 7-4.

The O 1s PE spectrum of the $[2:1]^{NH4+}$ NP solution, shown in Figure 7-3(C), is rather similar to the spectrum of the 5 M NaOH aqueous solution. However, there is an additional small peak from the TiO_2 lattice oxygen at 534.8 eV BE, and furthermore the following subtle but important spectral differences can be observed. (1) The OH^- signal intensity from the NP solution amounts to almost 70% of that from the 5 M NaOH solution. According to the spectrum of 0.5 M NH_4OH (Figure 7-3(B)), which corresponds to an even higher OH^- concentration than the $[2:1]^{NH4+}$ NP solution, one would expect to observe no OH^- signal, let alone to exhibit an intensity comparable to the 5 M NaOH aqueous solution. (2) The FWHM of the water O 1s PE peak is very similar to the one from neat water, and the peak is not broadened unlike in the case of the 5 M NaOH aqueous solution. (3) The OH^- peak position is at slightly smaller (by 0.5 eV) BE compared to the PE spectrum from 5 M NaOH aqueous solution (Figure 7-3(A)). All relevant BEs, FWHMs, and peak areas are provided in Table A-7-1 of the Appendix Section 7.5.

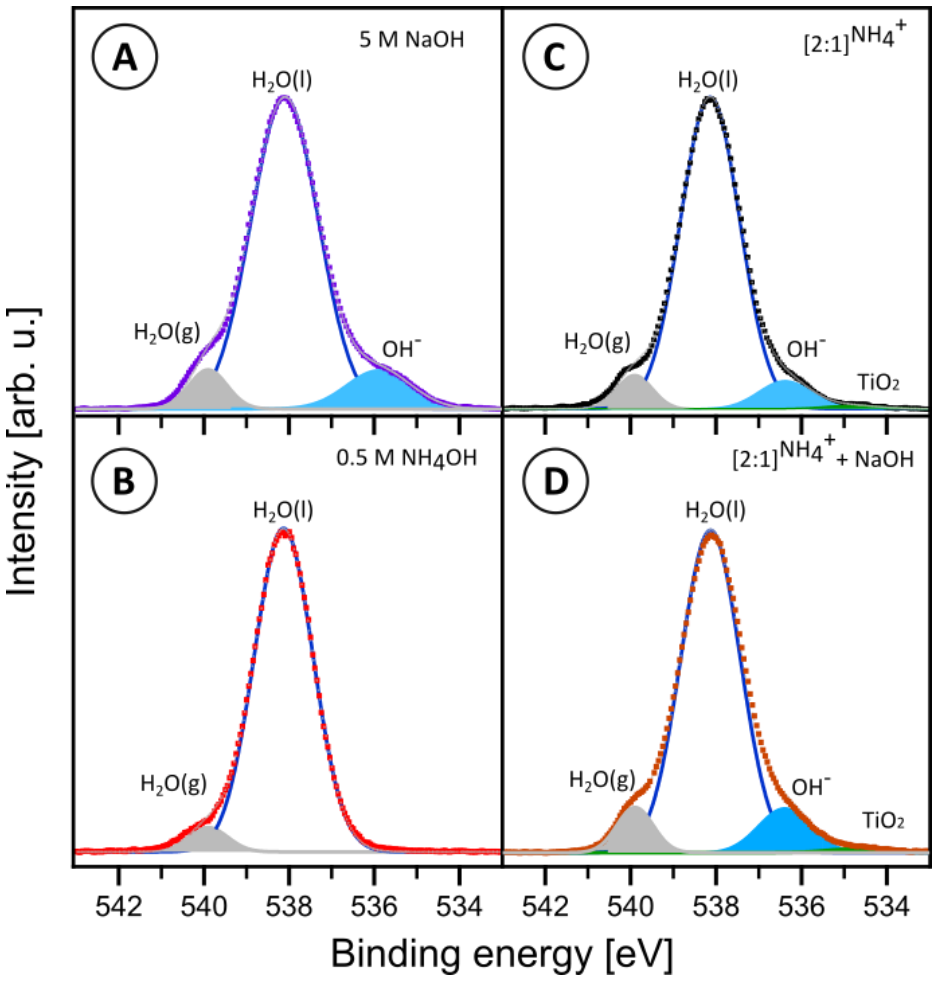

Figure 7-3

O 1s PE spectra of 5 M NaOH (A), 0.5 M NH_4OH (taken from ref. [257]) (B), $[2:1]^{NH4+}$ NP (taken from ref. [257]) (C), and $[2:1]^{NH4+}$ NP + 0.5 M NaOH (D) aqueous solutions measured at 1200 eV photon energy. Note that solution in (D) has pH of only 9.8 whereas the pure 0.5 M NaOH solution has pH 13.7. All spectra are fitted with multiple Gaussian functions that each represent the different oxygen species: liquid water ($H_2O(l)$), gas-phase water ($H_2O(g)$), OH^-, TiO_2. Spectra are presented on the binding energy scale, and intensities of the different spectra are displayed to yield the same peak height of the liquid-water peak. Dots are the measured data, and the solid red lines are the total fits. The detailed fitting parameters are presented in Table A-1 in the Appendix (Section 7.5).

Observation (1) indicates that in the NP solution the number of OH^- significantly exceeds the number that would be provided from 0.3 M concentration, and yet the pH of the $[2:1]^{NH4+}$ NP solution is only 7.8. Observations (2) and (3) imply that OH^- species in the NP solution are accommodated in a different chemical environment than the hydrated OH^- in water at basic pH. In the previous work,

on the same $[2:1]^{NH4+}$ NP aqueous solution,[257] I have reported that water dissociates at the TiO_2 NP surface (Chapter 6) which can qualitatively explain the increase of OH^- signals (observation (1)) in the spectrum. Note though that observation (1) is at odds with the fact that the pH of the $[2:1]^{NH4+}$ NP solution is only 7.8. It thus implies that most of the OH^- molecules in the NP solution must be trapped around the TiO_2 NPs by the positive Stern layer, forming the diffuse layer of the EDL; these confined OH^- species make no contribution to the pH measurement. Analogous to my previous photoemission study of aqueous-phase TiO_2 NPs,[257] I have also measured the $[2:1]^{NH4+}$ NP solution with 0.5 M NaOH added (Figure 7-3(D)) to show that the intensity of the OH^- peak at 536.3 eV continues to increase, becoming as large as for the 5 M NaOH solution. However, the pH is ~ 9.8 and the added amount of hydroxide could not produce such signal enhancement. This further corroborates our conclusion that a large amount of OH^- is indeed produced by additional water dissociation at the TiO_2 surface. The implications of observations (2) and (3) together with the findings of Figure 7-3(D) will be detailed in the following paragraphs, where I acquire additional support from PFY-XA measurements. The latter is indispensable here as it is a bulk-sensitive method, enabling a realistic estimate of the amount of OH^- present in the NP solution.

7.3.3 O K-edge PFY-XA Spectra

The O K-edge PFY-XA spectrum of the $[2:1]^{NH4+}$ NP solution, with the assistance of the reference PFY-XA spectra of $[1:1]^{Cl-}$ NP solution, neat water, and 1.5 M NaOH aqueous solution, allow for a quantitative estimation of the OH^- amount in the NP solution. All PFY-XA spectra, shown in Figure 7-4, were generated by integrating the X-ray emission intensities resulting from valence band to core transitions (O 2p → 1s) following resonant excitation at the O K-edge. Note that the PFY-XA spectrum of 1.5 M NaOH aqueous solution, shown in Figures 7-4(B) and 7-4(D) has been adapted from ref.[271]. This spectrum helps to quantify the amount of OH^- in the NP solutions, which will be explained later. Figure 7-4(A) shows the spectra from the $[2:1]^{NH4+}$ NP solution and the $[1:1]^{Cl-}$ NP solution. Since the latter solution corresponds to the fully Cl^--covered NP surface, water cannot interact with TiO_2. Hence, the difference spectrum (dotted curve), $[2:1]^{NH4+}$ NP minus $[1:1]^{Cl-}$ NP, reveals the signal solely due to OH^-. I label this signal contribution OH^-(i*). Then in Figure 7-4(B), I compare OH^-(i*) with the OH^- signal obtained from the neat 1.5 M NaOH aqueous solution (no NPs contained). For that I subtract the PFY-XA spectrum of neat water (shown in blue) from the one of the NaOH solution (in brown). This difference spectrum is presented at the bottom of Figure 7-4(B). Unlike in Figure 7-4(A), one now observes two contributions, centered at 532.8 and 534.1 eV photon energy, labeled OH^-(i) and OH^-(ii), respectively. These two OH^- contributions have been previously

reported for 4 and 6 M KOH aqueous solutions, and were attributed, based on computations, to the hydroxide hydration complexes in tri-coordinated (tetrahedral-coordinated) $OH^-(H_2O)_3$ and in planar 4-fold coordinated (hyper-coordinated) $OH^-(H_2O)_4$ configurations, respectively.[154] The tetrahedral configuration produces a single pre-edge peak at 532.5 eV photon energy (matching the OH^-(i) peak position in Figure 7-4(B)), whereas the hyper-coordinated configuration gives rise to a pre-edge peak at 534.5 eV (coinciding with OH^-(ii) in Figure 7-4(B)), as well as to OH^-(i).[154] The good agreement between the computed energies for OH^-(i) with the experimental energy of OH^-(i*) strongly suggests that not only is the OH^- hydration configuration near the NP surface different than in bulk water, but the tri-coordinated structure dominates. Note that the occurrence of different OH^- configurations would be qualitatively consistent with the different O1s BEs found in the NP solution compared to the 5 M NaOH solution (Figure 7-3(A) and 7-3(C)). Our suggested hydroxide hydration configuration within the EDL is corroborated by a Car-Parrinello molecular dynamics (CPMD) simulation, finding that the fraction of 3- and 4-coordinated structures depends strongly on the OH^- concentration. At low concentration, OH^- ions are surrounded by abundant water molecules and the $OH^-(H_2O)_4$ hyper-coordinated configuration is preferred; the tetrahedral complex $OH^-(H_2O)_3$ quickly (within 2-3 ps) interconverts to $OH^-(H_2O)_4$.[272-273] At high concentration, fewer water molecules are available to coordinate OH^-, making the $OH^-(H_2O)_3$ configuration more favorable.[274] I argue that the OH^- concentration in the diffuse layer is high, although I have yet to quantify the concentration, and the 3-coordinated structure thus dominates. This interpretation is supported by a nuclear magnetic resonance study of the water molecule distribution around TiO_2 NPs, showing strong confinement of water molecules with low mobility and reactivity within the first few layers above the TiO_2 surface.[275]

Having characterized the OH^- hydration configurations and their contributions to the PFY-XA spectra, I now quantify the amount of OH^- within the EDL. The O K-edge PFY-XA spectra of $[2:1]^{NH4+}$ NP (Figure 7-4(A)) and 1.5 M NaOH solutions (Figure 7-4(B)) solutions are then fitted with Gaussians, each representing the respective oxygen component, as shown in Figure 7-4(C) and (D). In both cases, the well-known water pre-edge peak at 535.0 eV[87] is presented in blue (no filling) and is used for intensity normalization; the relative intensity of this signal will be used to estimate the OH^- concentration. In Figure 7-4(C) the two TiO_2 oxygen features at 531.1 and 533.3 eV (green Gaussians), resulting from O 2p orbital hybridization with Ti t_{2g} and e_g orbitals,[162, 225, 232-234] are fitted under the constraints of the same peak positions, widths, and intensity ratio that are obtained from the fitting parameters of the reference PFY-XA spectrum of the $[1:1]^{Cl-}$ NP solution (no OH^- signal) shown in Figure A-7-1 and Table A-7-2 in the Appendix Section 7.5.

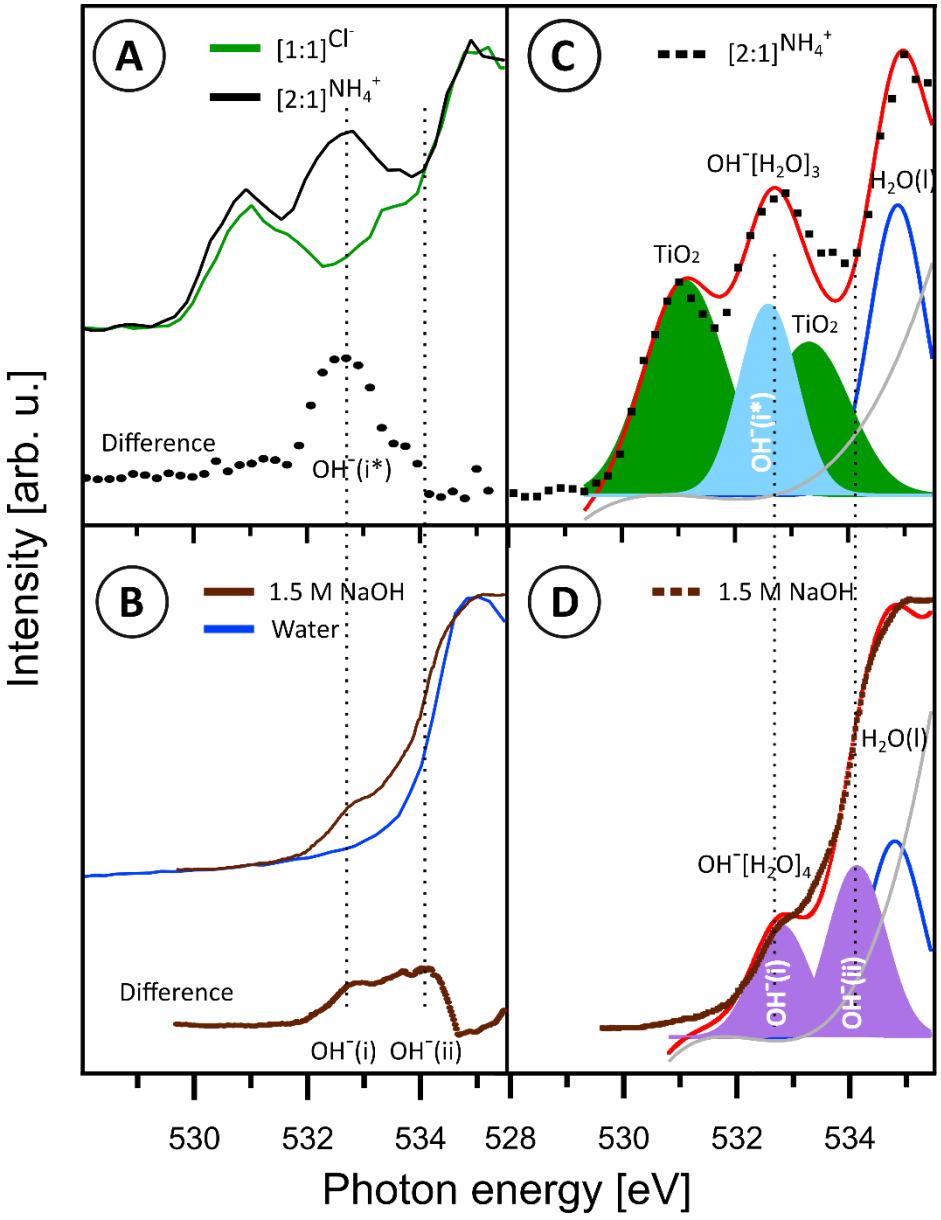

Figure 7-4

O K-edge PFY-XA spectra from [2:1]$^{NH4+}$ NP and [1:1]$^{Cl-}$ NP aqueous solutions, along with the respective spectral difference (A), and from 1.5 M NaOH aqueous solution (taken from ref. [271]) and neat liquid water, as well as their spectral difference (B). In (B) intensities are normalized at the water pre-edge. The Gaussian fits of the [2:1]$^{NH4+}$ NP and 1.5 M NaOH spectra are presented in (C) and (D), respectively. Different filling colors refer to different oxygen species: liquid-water oxygen (no filling), gas-phase water (grey), OH^- (blue and purple), TiO_2 lattice oxygen (e_g and t_{2g}, green). The two spectral backgrounds in C and D are fitted with a cubic function, indicated by grey curves (see also Figure A-7-1 in the Appendix (Section 7.5)). The detailed fit parameters are presented in Table A-7-2 in the Appendix (Section 7.5).

It is clear that the fitted Gaussian at 532.6 eV (light blue; Figure 7-4(C)), which accounts for OH^- signal, is needed to yield a good total fit (red line) of the overall spectrum. The 532.6-eV peak position perfectly matches the position of the computed tetrahedral species $OH^-(H_2O)_3$ (feature OH^- (i) at 532.5 eV photon energy),[154] in agreement with our above, more qualitative analysis. I notice that in my previous O 1s PE spectroscopy study of TiO_2 NP aqueous solution,[257] the obtained PEY-XA spectra exhibit somewhat smaller OH^- signal with respect to the water pre-edge intensity. Also, the TiO_2 signal is considerably smaller in the electron-yield measurements. It is this signal-intensity discrimination intrinsic to the (rather surface-sensitive) PES study that did not allow for a quantitative estimate of the relative concentration of the (oxygen) species of interest. In contrast, the signals obtained with bulk-sensitive PFY are argued to quantitatively reflect the total TiO_2 lattice and OH^- concentrations in solutions.

In Figure 7-4(D) I present the individual contributions of OH^-(i) and OH^-(ii) to the PFY-XA spectrum from 1.5 M NaOH aqueous solution (of Figure 7-4(B)), where I am guided by the analysis of ref [154]. I first fit the water pre-edge peak (see Figure A-7-1 and its caption), and then include two Gaussian peaks, representing OH^-(i) and OH^-(ii). The obtained peak positions (532.8 and 534.1 eV photon energy) are in very good agreement with the energies computed for the hyper-coordinated hydroxide.[154] For estimating the OH^- amount in the NP solution, I then compare the Gaussian peak area of tetrahedral (light blue peak in Figure 7-4(C)) with the area of hyper-coordinated (light violet peaks in Figure 7-4(D)) OH^- species, from which an approximately 0.6 M OH^- concentration for the $[2:1]^{NH4+}$ NP aqueous solution is derived. Here, I have used the OH^--to-H_2O (pre-peak) intensity ratio of Figure 7-4(D) as a calibration point; see the fitting parameters in Table A-7-2 and related calculation details in the Appendix Section 7.5.

I recall that the 0.3 M NH_4OH aqueous solution has the pH 11.3, whereas the pH of $[2:1]^{NH4+}$ NP solution (prepared in 0.3 M NH_4OH aqueous solution) is only 7.8. Despite this near-neutral pH, the OH^- concentration in the NP solution estimated to be 0.6 M, and almost all these anions are confined within the EDL. Given that at 0.3 M NH_4^+ concentration about half the TiO_2 NP surface sites are covered (estimated from 5.2 ions adsorbed/nm^2),[93, 192] 0.6 M $OH^-(H_2O)_3$ would be enough to exceed one monolayer coverage, forming the diffuse layer. This raises several questions: (1) How thick is the diffuse layer, (2) what is the origin of the 0.6 M OH^- concentration, and (3) what role does the produced H^+ (from water dissociation) play in this interfacial system? To answer these questions I propose two scenarios, as schematically presented in Figure 7-5.

Scenario A (Figure 7-5(A)) proposes that 0.3 M NH_4OH solution contributes maximum 0.3 M OH^- concentration to the diffuse layer (bulk OH^- drawn toward the NPs by Coulombic attraction of the Stern layer), and the other 0.3 M OH^- is provided by water dissociation at the TiO_2 NP surface. Indeed, our previous liquid microjet PES study of the same [2:1]$^{NH4+}$ TiO_2 NP colloidal solution has already shown that OH^- can be produced in basic solution from water dissociation,[257] and subsequent OH^- liberation (into the diffuse layer) allows for further dissociation. The amount of OH^- that can be accommodated in the diffuse layer depends on the effective charge of the Stern layer, and one crucial question is whether H^+ (from water dissociation) is part of the Stern layer. As discussed in the Introduction Section 7.1, fast H^+ – OH^- recombination is one of the major obstacles limiting the efficiency of water dissociation reactions. In the present case, this problem is by-passed, when we assume that H^+ is bound at the TiO_2 surface. This confinement of H^+ increases the Stern layer charge and keeps the extra negative OH^- species stay close, within the diffuse layer. Such a mechanism would be consistent with a previous scanning tunneling microscopy study finding that H^+ bonds to the oxygen sites of TiO_2 surfaces.[211]

In Scenario B (Figure 7-5(B)), the 0.6 M OH^- concentration is assumed to be fully produced by water dissociation at the TiO_2 NP surfaces. Due to the limited number of anchoring oxygen sites for water on the TiO_2 surface, the excess amount of OH^- can be rationalized when assuming that some fraction of H^+ ions produced at the interface migrates through the diffuse layer, and recombines to form water in the bulk solution. This latter neutralization would explain the observed relatively low pH 9.8 when adding NaOH to the NP solution (see Figure 7-3(D), and respective figure caption). Note that some fraction of H^+ will inevitably recombine with OH^- in the diffuse layer, and the resulting loss of OH^- molecules can be replenished because H^+ release from the TiO_2 surface vacates adsorption sites for further water dissociation reaction, which in turn generates additional OH^- in the diffuse layer. Even if we do not understand the detailed mechanism of such efficient diffusion through the diffuse layer (although very thin; discussed below), OH^- in the bulk solution, as well as in the diffuse layer, must play an important role in initiating the release of H^+ from the TiO_2 surface. This dynamical cycle of continuous freeing surface sites for water adsorption, and the subsequent release of H^+, followed by recombination, will reach an equilibrium once the bulk solution is nearly neutralized. Similar observations have been made from a photoelectrochemical cell (PEC) study under external electric potential.[5, 276-277] Water dissociation was found to occur at the TiO_2 working electrode, followed by H^+ diffusion through an electrolyte solution to the counter electrode; the nature of the EDL at the working electrode – electrolyte interface has not been addressed.

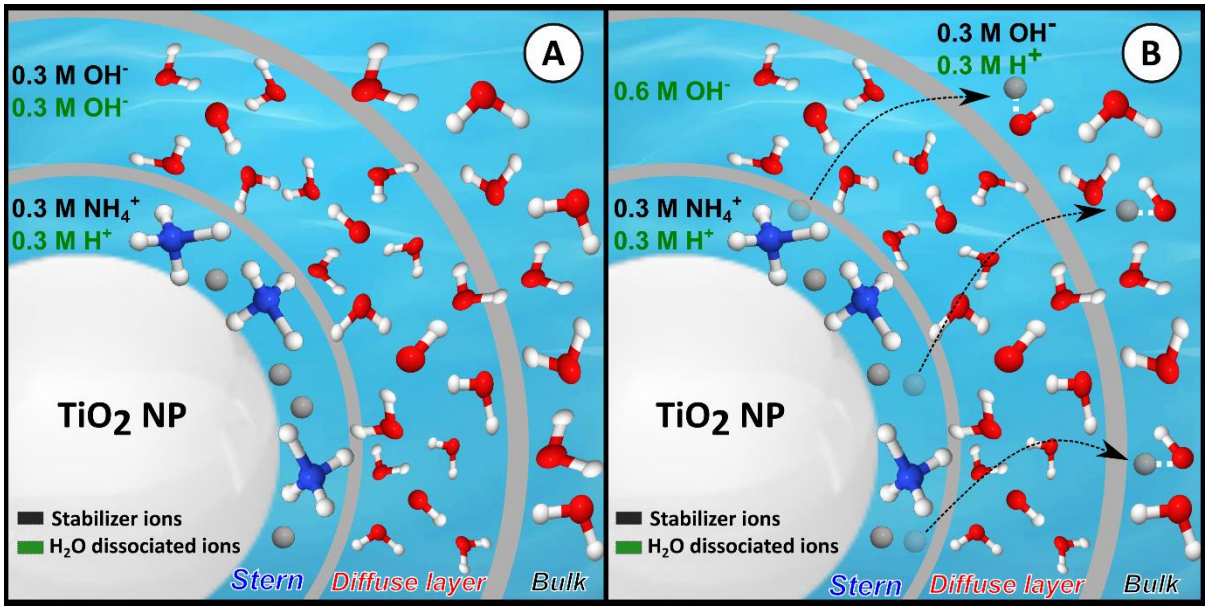

Figure 7-5

Schematic representation of the charge (NH_4^+, OH^-) distribution in the EDL around a TiO_2 NP. (A) In Scenario A, 0.3 M H_2O have dissociated at the TiO_2 surface producing H^+ ions that become part of the Stern layer as well as producing 0.3 M OH^- in the diffuse layer. All other OH^-, also residing within the diffuse layer, originate from the bulk solution (from the 0.3 M NH_4OH stabilizer). (B) Scenario B assumes that 0.6 M H_2O are dissociated and form 0.6 M OH^- ions in the diffuse layer. The corresponding 0.6 M H^+ are divided into 0.3 M H^+ that are bound to the oxygen sites on the TiO_2 surface, and the other 0.3 M H^+ quickly diffuse into the bulk solution and neutralize the solution.

Finally, the thickness of the diffuse layer is estimated based on the 0.22 nm O–O bond length reported for the $OH^-(H_2O)_n$ complex.[154] The 0.6 M tetrahedral $OH^-(H_2O)_3$ complex derived from the quantitative analysis of the PFY-XA spectra in Figure 7-4 can then form an at least 0.44-nm-thick diffuse layer, corresponding to one complete densely-packed monolayer (with 0.3 M NH_4^+ covering half of the TiO_2 NP surface). The actual thickness of the diffuse layer is, however, likely to extend beyond 0.44 nm due to the mobility of $OH^-(H_2O)_3$ ions. Hence, the Debye length should be > 0.8 nm; this comprises the > 0.44 nm diffuse layer and ~ 0.35 nm Stern layer. Previous electrochemical studies have investigated the interaction force between two electrodes immersed in ionic liquid and in NaCl aqueous solution, and obtained a semi-parabolic relationship between the interaction force, from which the Debye length can be inferred as a function of electrolyte concentration. The results of ref. [278] show that the Debye length reaches an undetectably small value at 0.1 M electrolyte concentration,

and then goes up to approximately 1.5 nm for ~2.0 M concentration in the case of NaCl aqueous solution, and to approximately 6 nm for ~2.0 M concentration ionic liquid solution in propylene, respectively.[278] Our > 0.8 nm Debye length estimated for the $[2:1]^{NH4+}$ colloidal solution agrees with this reported Debye length vs. concentration relation,[278] although we cannot precisely determine the overall electrolyte concentration.

7.4 Conclusion

I have applied in-situ X-ray spectroscopy to characterize the electric double layer (EDL) around 20-nm TiO_2 NPs dispersed and stabilized in NH_4OH aqueous solution. My studies thus capture the interaction of bulk electrolyte solution with a TiO_2 surface. By combining PES, PEY-XAS and PFY-XAS, I find that at low concentration of NH_4^+ stabilizer ions – but still assuring that NPs do not aggregate – there remains sufficient NP surface area to interact with water. My PES and PEY-XAS measurements at the N 1s and O 1s core levels, along with the measured pH, identify the Stern layer to consist of NH_4^+ stabilizer ions, and the diffuse layer being composed of OH^-. Moreover, the PFY measurements at the O K-edge reveal an unexpected large amount of OH^- in the NP aqueous solution (despite near-neutral pH) that can only be explained by water dissociation. These OH^- species are proposed to form an approximately > 0.44-nm-thick diffuse layer, charge-balanced by a ~ 0.35-nm Stern layer of NH_4^+. The PFY measurements furthermore strongly suggest a prevailing 3-coordinated OH^- hydration structure, $OH^-(H_2O)_3$, within the diffuse layer which is not the case for OH^- hydration in bulk-solution where the 4-coordinated structure, $OH^-(H_2O)_4$, is more probable. I conclude by proposing two models in which the dissociation product H^+ is either anchored at the TiO_2 – solution interface (Scenario A), or it quickly escapes into the bulk solution (Scenario B), both consequently preventing the unwanted $H^+ – OH^-$ recombination. Scenario B is probably a more realistic description of the dynamics of dissociative water adsorption / H^+ release and recombination cycle, although elements of both models are likely relevant. In addition, the present work marks an important advance in the spectroscopic characterization of the EDL, including the molecular interactions of aqueous solution with solid surfaces that are relevant for energy-material research. My method can be readily applied to surfaces other than studied here.

7.5 Appendix

7.5.1 Fitting Parameter of O1s PE Spectra in Figure 7-3

	0.5 M NH_4OH			5 M NaOH		
	Position	**FWHM**	**Area**	**Position**	**FWHM**	**Area**
H_2O(l)	538.1	1.6	100	538.1	1.8	100
H_2O(g)	539.9	1.0	4.9	539.9	1.0	7.0
TiO_2	-	-	-	-	-	-
OH^-	-	-	-	535.8	1.8	11.8
	TiO_2 [2:1]$^{NH4+}$			**TiO_2 [2:1]$^{NH4+}$ + NaOH**		
	Position	**FWHM**	**Area**	**Position**	**FWHM**	**Area**
H_2O(l)	538.1	1.6	100	538.1	1.6	100
H_2O(g)	539.9	1.0	6.7	539.9	1.0	8.5
TiO_2	534.8	1.4	1.0	534.8	1.4	0.9
OH^-	536.3	1.4	8.0	536.3	1.4	12.3

Table A-7-1

Fitting parameters of PE spectra in Figure 3. All fitted areas are normalized according to the fitted area of H_2O(l) peak at 538.1 eV which is set to 100.

7.5.2 PFY-XA Spectra of Neat Water and TiO_2 NPs $[1:1]^{Cl^-}$ Aqueous Solutions

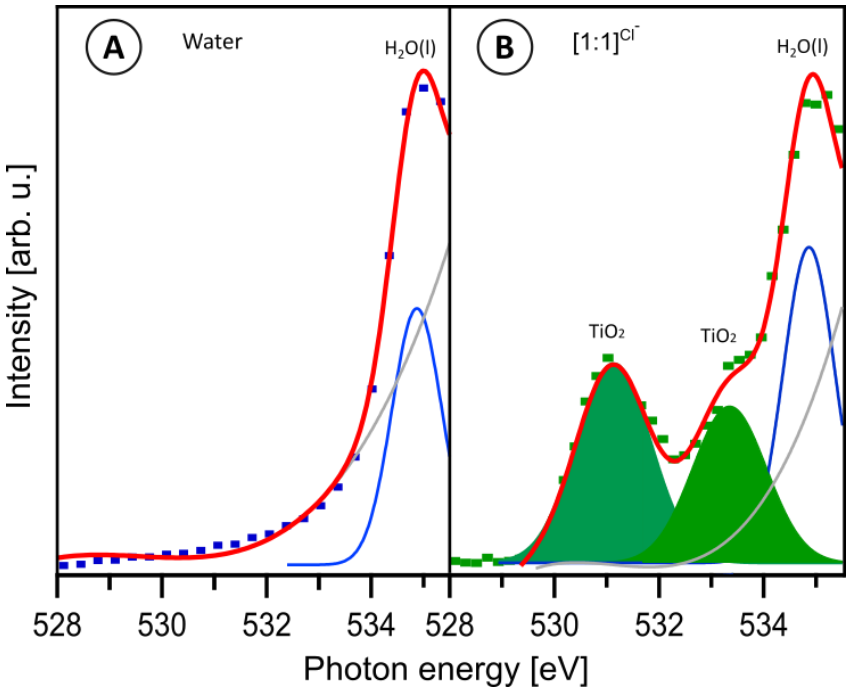

Figure A-7-1

PFY-XA spectra of neat water (A) and $[1:1]^{Cl^-}$ aqueous solution (B), identical to the blue and green spectra presented in Figure 7-3(B) and 7-3(A), respectively. Gaussian fittings are conducted for both spectra, in which the water pre-peak at 535.0 eV (blue components) and TiO_2 lattice O at 531.1 and 533.3 eV (green components) are indicated. The background curves are fitted with a cubic function, marked in grey color. The fitting parameters of the water pre-peak and background function in A are applied to the PFY-XA spectrum fitting in B, as well as those in Figure 7-3(C) and 7-3(D). The detailed fitting results are listed in Table A-7-2.

7.5.3 Fitting Parameter of O K-edge PFY-XA Spectra in Figure 7-4 and Figure A-7-1

	Water			TiO_2 [1:1]$^{Cl-}$		
	Position	**FWHM**	**Area**	**Position**	**FWHM**	**Area**
H_2O(l)	535.0	1.1	100	535.0	1.1	100
O 2p-Ti 3d t_{2g}	-	-	-	531.1	1.6	90.2
O 2p-Ti 3d e_g	-	-	-	533.3	1.6	71.0
	TiO_2 [2:1]$^{NH4+}$			**1.5 M NaOH**		
	Position	**FWHM**	**Area**	**Position**	**FWHM**	**Area**
H_2O(l)	535.0	1.1	100	535.0	1.1	100
O 2p-Ti 3d t_{2g}	531.1	1.6	104.7	-	-	-
O 2p-Ti 3d e_g	533.3	1.6	74.4	-	-	-
$OH^-(H_2O)_3$	532.6	1.1	65.1	-	-	-
$OH^-(H_2O)_4$	-	-	-	532.8	1.1	57.0
$OH^-(H_2O)_4$	-	-	-	534.1	1.1	86.4

Table A-7-2

Fitting parameters of PFY-XA spectra in Figure 7-4 and A-7-1. All fitted areas are normalized according to the fitted area of H_2O(l) peak at 535.0 eV which is set to 100.

7.5.4 Calculation Details of the OH^- Molarity in the TiO_2 NPs $[2:1]^{NH4+}$ Aqueous Solution:

According to the fitting results presented in Table A-7-2, the total area of the two fitted $OH^-(H_2O)_4$ components from the 1.5 M NaOH aqueous solution 57.0 + 86.4 = 143.4 is compared to the corresponding $OH^-(H_2O)_3$ area of the $[2:1]^{NH4+}$ solution 65.1. As the water peaks in both solutions are used as a common reference, a correction factor that considers the different water weights in each solution is applied. Given that the mass density of the $[2:1]^{NH4+}$ solution is 1100 g/l and weight percentage of NP is 20wt%, the water weight in a given volume, say 1 liter, is calculated to be 1100 g × 80% = 880 g (the weight of 0.3 M NH_4OH is negligible). The water weight in one liter of 1.5 M NaOH aqueous solution is 1000 g. Therefore, the molarity x of $OH^-(H_2O)_3$ in the $[2:1]^{NH4+}$ solution can be estimated by x/1.5 M = (65.1 × 880 g)/(143.4 × 1000 g), which gives x = 0.6 M.

Chapter 8
Summary and Outlook

During the course of my PhD studies, I focused on characterizing the electronic structure of the transition metal oxide – aqueous interface for hematite iron oxide (α-Fe_2O_3) and anatase titanium dioxide (TiO_2) nanoparticles. A key aspect was the nature of water adsorption at these interfaces. In this chapter, I summarize the findings based on the measurements shown in chapters 5, 6 and 7, and I propose a harvesting methodology of the H_2 fuel from the dissociative TiO_2 — water interaction. Then, I briefly highlight the results from some other projects that I have been involved in. These projects are not the main focus of this study, but the findings are of general relevance for liquid-jet PES. Then in the outlook Section, I describe the current efforts to investigate other NP systems e.g., magnetite iron oxide and cerium dioxide nanoparticle aqueous solutions, building on the experience accumulated with α-Fe_2O_3 and TiO_2 NPs. Also, the future perspectives for further characterization of the systems studied in this thesis are presented.

8.1 Summary of the Results

The electronic structure of the interfacial layer between the (6 nm diameter) hematite iron oxide nanoparticles and aqueous solution was reported in Chapter 5 using the liquid microjet technique coupled to soft X-ray photoelectron spectroscopy. This method is sufficiently sensitive to detect the adsorbed hydroxide species, resulting from the water dissociation at the nanoparticle surface in aqueous solution (in acidic condition). The photoelectron signals of adsorbed OH^- were obtained at the O 1s resonant, non-resonant and from partial electron yield X-ray absorption. In addition, the Fe $2p_{3/2}$ resonant excitation was explored. This L_3-edge detection is sensitive to the surrounding chemical environment of the Fe^{3+} ions at the nanoparticle—aqueous interface which is manifested in the 10*Dq* value, a measure of the ligand-field strength. By recording the L_3 edge PEY-XA spectra from different iron Auger-decay channels, the t_{2g} (3d electrons) peak intensity variation was assigned to different extents of electron delocalization. From the experimental fraction of local *versus* non-local autoionization signals, the charge transfer time from the interfacial Fe^{3+} into the environment is found to be approximately 1 fs.

Analogous to the hematite system, the nature of water interaction with the anatase TiO_2 nanoparticles surfaces was reported in Chapter 6. The electronic structure of the nanoparticles of different size (3, 6, 10 and 20 nm diameter), dispersed in different aqueous solutions (different pH) was investigated in order to identify the molecular species adsorbed at the NP— aqueous solution

interface. From the Ti 2p resonant photoemission (PEY-XA) an anatase-phase transformation or the occurrence of Ti^{3+} sites due to surface oxygen defects could be ruled out. The O 1s non-resonant and on-resonant photoelectron spectra allow to distinguish the molecular and dissociative water adsorption on the TiO_2 NP (aq) surface. The latter measurements demonstrate that water is adsorbed molecularly at low pH, and is interacting dissociatevely at the TiO_2 NP (aq) surface for slightly basic solution. Based on these findings, I propose an anatase TiO_2—water interaction mechanism that explicitly takes the local solution chemical environment into account.

Using in-situ X-ray spectroscopy, the electric double layer around 20-nm TiO_2 NPs dispersed and stabilized in NH_4OH aqueous solution was characterized in Chapter 7. From a combination of PE and PEY-XA spectra at the N 1s core level, the Stern layer was identified to consist of NH_4^+ stabilizer ions. The concentration of NH_4^+ ions is low enough to cover only half of the TiO_2 surface sites, which allows water interaction with the NPs. This less than one monolayer thick Stern layer is approximately ~ 0.35-nm thick. Also, the combination of PE and PFY-XA measurements at the O K-edge revealed an unexpected large OH^- amount in the NP aqueous solution which is not consistent with the pH of 7.8. This large OH^- concentration is attributed to the dissociative water interaction with the TiO_2 surface in such a chemical environment (based on Chapter 6 findings). From the measured PFY-XA spectra, I quantify the hydroxide amount in the NP aqueous solution ~ 0.6 M trapped in > 0.44-nm-thick diffuse layer around the Stern layer. Also, I show that these hydroxide groups are forming a tetrahedral hydrated configuration structure $OH^-(H_2O)_3$ which is different from the hyper-coordinated hydroxyl hydrated complexes $OH^-(H_2O)_4$ forming in bulk hydroxide solutions. Lastly, I proposed two structural models of the EDL around the TiO_2 NPs, where the dissociated produced H^+ is anchored at the NP surface or diffuses into the bulk solution, respectively. Both models prevent H^+ and OH^- from recombination. The second proposed mechanism is probably more favorable as it potentially provides a means to produce more dissociation by adding an electric bias to the bulk solution. I have shown that adding NH_4OH or NaOH to the NPs (aq) solution (see Figure 6-7 and Figure 7-3) provides a means to extract the H^+ away from the NP surface in aqueous solution (Figure 7-5 (B)).[279] The next step is to provide an external negative potential equivalent to the OH^-, attracting generated H^+ to leave the NP surface in order to free the catalytic sites for further water dissociation.

8.2 Other Projects

In parallel to the transition metal oxide NP—water interaction studies, I participated in other projects, some of which have been published. Here, I briefly mention only those that are somewhat related to my main topic.

- **Advances in Liquid Phase Soft-X-ray Photoemission Spectroscopy: A New Experimental Setup at BESSY II**.

  This work is describing the SOL^3 PES experimental station, its technical features, and reports some proof-of-concept measurements. I here cite the abstract of the article[62], and then briefly highlight the important role of this experimental setup for conducting my NP(aq) studies **"***A state-of-the-art experimental setup for soft X-ray photo- and Auger-electron spectroscopy from liquid phase has been built for operation at the synchrotron-light facility BESSY II, Berlin. The experimental station is named SOL^3, which is derived from solid, solution, and solar, and refers to the aim of studying solid–liquid interfaces, optionally irradiated by photons in the solar spectrum. SOL^3 is equipped with a high-transmission hemispherical electron analyzer for detecting electrons emitted from small molecular aggregates, nanoparticles, or biochemical molecules and their components in (aqueous) solutions, either in vacuum or in an ambient pressure environment. In addition to conventional energy-resolved electron detection, SOL^3 enables detection of electron angular distributions by the combination of a ±11° acceptance angle of the electron analyzer and a rotation of the analyzer in the polarization plane of the incoming synchrotron-light beam. The present manuscript describes the technical features of SOL^3, and we also report the very first measurements of soft-X-ray photoemission spectra from a liquid microjet of neat liquid water and of TiO_2-nanoparticle aqueous solution obtained with this new setup, highlighting the necessity for state-of-the-art electron detection*.**"**

  The presented resonant photoelectron spectra (in Chapters 5 and 6) are the pioneer in solid-liquid interface studies. This aspect is crucial for probing the electronic structure of the adsorbed molecular species on the NP(aq) surfaces as a function of pH, which has not been attempted before.

- **Do water's electrons care about electrolytes?**

  This project investigated if the electrolyte ions have an effect on the electronic structure of the surrounding water molecules and whether the photoelectron spectrum of neat liquid water can be used as an energy reference to calibrate other aqueous solution photoelectron spectra. I already mentioned this study briefly in Chapter 4. The main goal of that work, as summarized in the abstract of ref.[80], is: "*Ions have a profound effect on the geometrical structure of liquid water and an aqueous environment is known to change the electronic structure of ions. Here we combine photoelectron spectroscopy measurements from liquid microjets with molecular dynamical and quantum chemical calculations to address the*

reverse question, to what extent do ions affect the electronic structure of liquid water? We study aqueous solutions of sodium iodide (NaI) over a wide concentration range, from nearly pure water to 8 M solutions, recording spectra in the 5 to 60 eV binding energy range to include all water valence and the solute Na^+ 2p, I^- 4d, and I^- 5p orbital ionization peaks. We observe that the electron binding energies of the solute ions change only slightly as a function of electrolyte concentration, less than 150 ± 60 meV over an ~8 M range. Furthermore, the photoelectron spectrum of liquid water is surprisingly mildly affected as we transform the sample from a dilute aqueous salt solution to a viscous, crystalline-like phase. The most noticeable spectral changes are a negative binding energy shift of the water $1b_2$ ionizing transition (up to −370 ± 60 meV) and a narrowing of the flat-top shape water $3a_1$ ionization feature (up to 450 ± 90 meV). A novel computationally efficient technique is introduced to calculate liquid-state photoemission spectra using small clusters from molecular dynamics (MD) simulations embedded in dielectric continuum. This theoretical treatment captured the characteristic positions and structures of the aqueous photoemission peaks, reproducing the experimentally observed narrowing of the water $3a_1$ feature and weak sensitivity of the water binding energies to electrolyte concentration. The calculations allowed us to attribute the small binding energy shifts to ion-induced disruptions of intermolecular electronic interactions. Furthermore, they demonstrate the importance of considering concentration-dependent screening lengths for a correct description of the electronic structure of solvated systems. Accounting for electronic screening, the calculations highlight the minimal effect of electrolyte concentration on the $1b_1$ binding energy reference, in accord with the experiments. This leads us to a key finding that the isolated, lowest-binding-energy, $1b_1$, photoemission feature of liquid water is a robust energetic reference for aqueous liquid microjet photoemission studies."

With the water $1b_1$ binding energy being a confirmed robust energy reference, I was able to accurately determine the binding energies of the NPs as well as of the adsorbed interfacial molecular species.

8.3 Outlook

In this section, I present several perspectives and my thoughts of current and future experiments and applications. First, I report on two ongoing studies of two other metal-oxide nanoparticle aqueous systems. I conclude by elaborating on the advantage of applying tender X-rays, for the study of aqueous-phase NPs.

With the hematite iron oxide and the titanium dioxide – aqueous interface studies I have demonstrated that the liquid microjet technique combined with the soft X-ray photoelectron

spectroscopy is a powerful analytical technique to characterize the interfacial layer between nanoparticles and aqueous solution. I have applied the same techniques to the Fe_3O_4 NPs and CeO_2 NPs to probe their solid surface interaction with solvent and solute ions. The findings are summarized below:

- **Magnetite Iron Oxide Nanoparticle—Aqueous Solution Interface**

  Magnetite iron oxide (Fe_3O_4) exhibits strong magnetic properties (magnetic moment of 4 μ_B per formula cell[126]) which makes it a promising electrode material for energy storage application, such as supercapacitors[280-281]. Also, its nanoparticle structures are being intensively exploited as ferrofluids in magnetic refrigeration[282], and used in magnetic resonance imaging[283] and cancer therapy[284-285]. Iron (II, III) oxide (Fe_3O_4) has an inverse spinel structure where the Fe^{2+} is octahedrally coordinated while the Fe^{3+} cations are divided between octahedral and tetrahedral coordination (accurate ratio of every coordination is addressed in the following text). The total ratio of Fe^{2+}/Fe^{3+} is 1:2. When this value decreases, the Fe_3O_4 partially loses its magnetic properties. According to Néel's theory of ferrimagnetism, the magnetic moment of Fe_3O_4 uniquely arises from the Fe^{2+} ions; The Fe^{3+} cation moments cancel each other on each sublattice (tetrahedral and octahedral sublattice).[126, 286] The Fe^{2+} cations are known to be easily oxidized to Fe^{3+}, by exposure to air, humidity, or in acidic aqueous solution. Therefore, magnetite nanoparticles are not sustainable in aqueous solution, and they start losing their magnetic properties. In fact, magnetite would transform into maghemite (γ-Fe_2O_3), where the Fe^{2+}/Fe^{3+} ratio drops to zero (magnetic moment of 2.5 μ_B per formula unit), then adapt to the most stable form of iron oxide, hematite (α-Fe_2O_3).[126] Such a transformation affects almost all the magnetite iron oxide applications, especially the ones performed in aqueous solution. This oxidation behavior of Fe^{2+}, resulting in iron oxide phase transformation, has been the motivation for several works [287-289] as well as for my NP study. Specifically, I aim to quantify and compare the Fe^{2+}/Fe^{3+} ratios for magnetite NPs under different Fe^{2+} oxidization conditions:

  (i) **NPs extensively exposed to Fe^{2+} oxidization condition:** Magnetite NPs dispersed in an acidic aqueous solution. Two Fe^{2+}/Fe^{3+} ratios were obtained: (1) At the NPs—aqueous interface (by preforming liquid jet PES measurements) as well as (2) from the NP interior (by fully digestion of the NPs).

  (ii) **NPs shortly exposed to Fe^{2+} oxidization condition:** Dried Fe_3O_4 NPs(aq) from the aqueous solution in **(i)**, and the dried NPs (aq) after distilled water washing.

  (iii) **NPs never exposed to Fe^{2+} oxidization condition:** Dry NPs (this ratio is reported in the literature[290] by our collaborator Kevin M. Rosso (Pacific Northwest National Laboratory, USA)).

First, characteristic measurements were performed for conditions **(i)** and (**ii)** to ensure the same particle shape and size after chemical treatment, washing and drying. Measurements included (1) X-ray diffraction (XRD) and Scanning electron microscopy (SEM) from the dried Fe_3O_4 NPs(aq) after being dissolved in acidic aqueous solution **(NPs shortly exposed to Fe^{2+} oxidization condition (ii))**, and (2) dynamic light scattering (DLS)) for Fe_3O_4 NPs dispersed in HNO_3 aqueous solution (**NPs extensively exposed to Fe^{2+} oxidization condition(i)).** DLS measurements were performed twice for the latter sample, since part of the experiment was done at BESSY II, Berlin, while additional studies were done at the Pacific Northwest National Laboratory, USA, which made a re-examination of the sample stability mandatory.

In the following, I present liquid jet photoemission spectra from magnetite NP aqueous solution, aiming at determining the Fe^{2+}/Fe^{3+} ratio. Figure 8-1 presents the Fe L_3-edge PEY-XA spectrum obtained by integrating the photoemission signals over the 2p-3p3p Auger decay channel (compare Figure 5-6) for 10 wt% (20 nm) Fe_3O_4 nanoparticles stabilized in HNO_3 aqueous solution (black curve). In an attempt to interpret the spectrum we consider the previously reported ab-initio based multireference configuration interaction (MRCI) calculations for the $Fe(II)O_6$,$Fe(III)O_6$ and $Fe(III)O_4$ clusters on the Fe L-edge[290] (shown in green, blue and orange, respectively). We thus compare the measured PEY-XA spectrum with the total fit of the three characteristic individual spectra which represent the spectral contribution of the octahedral configurated Fe^{2+}, octahedral configurated Fe^{3+} and tetrahedral configurated Fe^{3+}. The fitting residual (linear combination fitting of theoretical component spectra) is presented in red color. The fit yields a contribution of 25.9%, 37.0% and 37.1% of $Fe(II)O_6$,$Fe(III)O_6$ and $Fe(III)O_4$ respectively **(for NPs highly exposed to Fe^{2+} oxidization condition at the NPs—aqueous interface (i))**. This can be compared with 37.21%, 29.37% and 33.42% reported for the dry magnetite NPs measured by bulk-sensitive technique, total electron yield X-ray absorption[290] **(NPs never exposed to Fe^{2+} oxidization condition (iii))**. Given the surface sensitivity of the liquid-jet PE measurements, the large change of the Fe^{2+} contribution in the PEY-XA spectrum suggests that these cations are slowly oxidized at the magnetite nanoparticles surface.

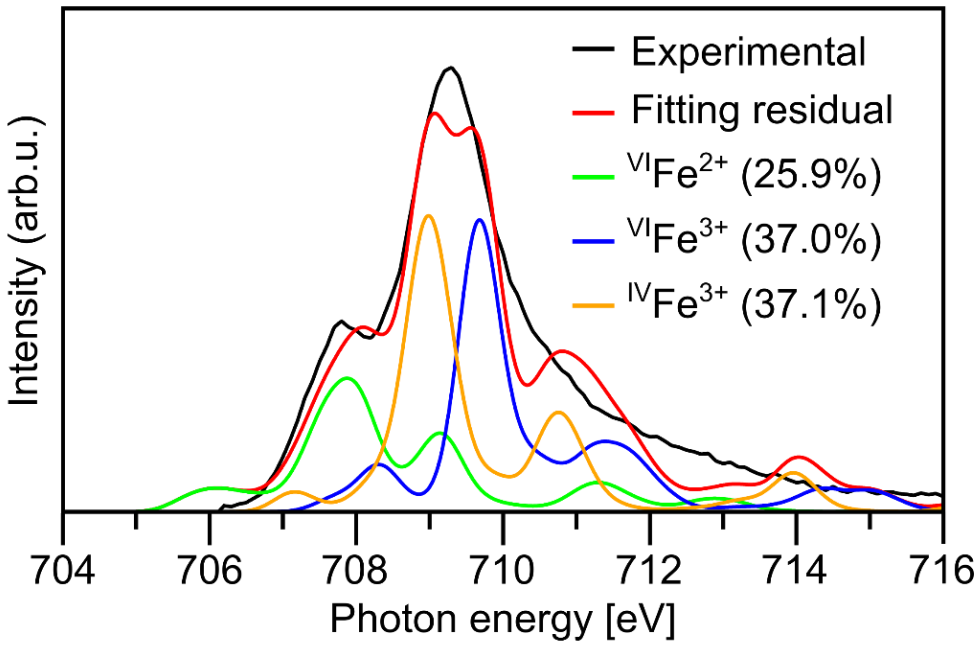

Figure 8 - 1

Black: Measured Fe L_3 edge PEY-XA spectrum from 10 wt% (20 nm) Fe_3O_4 NPs in HNO_3 aqueous solution, covering the 2p-3p3p Auger-electron emissions after Fe $2p_{3/2} \rightarrow t_{2g}$ and $2p_{3/2} \rightarrow e_g$ excitation. Spectra were recorded for photon energies between 704-716 eV. Green, blue, and orange: singular contribution from the octahedral configurated Fe^{2+}, octahedral configurated $Fe^{3+}$and tetrahedral configurated Fe^{3+}, respectively. Red: linear combination of the theoretical component spectra (fitting residual). More detailed in the text.

In addition, the Rosso group has performed X-ray absorption near-edge structure (XANES) measurements as well as X-ray magnetic circular dichroism (XMCD) studies at the Fe L-edge from the dried Fe_3O_4 NPs(aq) and from the one dried sample after distilled water washing **(NPs shortly exposed to Fe^{2+} oxidization condition (ii))**. The obtained Fe^{2+}/Fe^{3+} ratios are compared with the one reported from the dried NPs and from NPs(aq). Furthermore, a full digestion of the nanoparticles **(for NPs highly exposed to Fe^{2+} oxidization condition (i))** based on Ferrozine method[291] revealed the Fe^{2+}/Fe^{3+} ratio from the NPs' interior. This ratio was found to be much less than the interfacial Fe^{2+}/Fe^{3+} ratio, suggesting a diffusion of the Fe^{2+} cations from the NP interior to the surface. Such a behavior was previously observed for magnetite microspheres after the growth of metal-organic framework, around the Fe_3O_4 [292]. A manuscript on our findings is in preparation.

- **Cerium Dioxide Nanoparticle—Aqueous Solution Interface**

The electronic and optical properties of cerium dioxide (CeO_2) make this material interesting for many applications, such as thermal barrier coating, ionic conductors, and again for H_2 fuel production[293] and solar cells.[294-295] Especially with regard to the latter, the 3.2 eV band gap renders this materials of considerable interest for the thermochemical splitting of liquid water.[296] It is thus crucial to explore the electronic structure of the CeO_2—water interface. Many experimental and theoretical studies were indeed dedicated to characterize the nature of water adsorption on the CeO_2 surfaces.[297-302] Yet, it remains unclear whether water is molecularly, dissociatively, or mixed adsorbed at the surface.[297] A better characterization of this CeO_2—aqueous interface was the main motivation of exploring aqueous-phase ceria NPs by liquid-jet photoelectron spectroscopy. Figure 8-2 presents the valence photoelectron spectra measured on- and off resonant (in red and blue curves), respectively at the Ce^{4+} $3d_{5/2}$ transition to the valence orbital from a 20 wt% 3nm CeO_2 nanoparticle stabilized in HNO_3 aqueous solution. The spectra are energy calibrated with reference to the $1b_1$ peak of liquid water (11.16 eV binding energy[32]), and they are presented after a Shirley background subtraction. The intensities are displayed to yield the same heights of the $2a_1$ water peak as it represents an isolated peak which is not affected at resonance. A similar procedure was adopted in the α-Fe_2O_3 NPs(aq) study (see Section 5.3.1).

The most noticeable peak at the low binding energy side, at approximately 9 eV, is attributed to two components, the Ce 5d – O 2p and Ce 4f- O 2p hybridizations, based on the reported valence band spectra of cerium dioxide single crystal[303]. The broad electron emission near 25 eV binding energy can be attributed to the contribution from Ce 5p, O 2s and Ce 5s, respectively[303]. This implies that liquid-jet PES is capable to detect electrons emitted from the CeO_2 NP (aq). Moreover, we have succeeded to detect signals from interfacial oxygen species resulting from the adsorption of water. Analogous to the α-Fe_2O_3 NPs (aq) O 1s RPE and PE measurements shown in Figures 5-4 and 5-5, CeO_2 NPs (aq) solutions with reduced amount of NO_3^- stabilizer ions relative to the available NPs surface sites were recently measured to investigate the nature of water adsorption on the NPs surface. The data analysis is in process and manuscript on this work is in preparation.

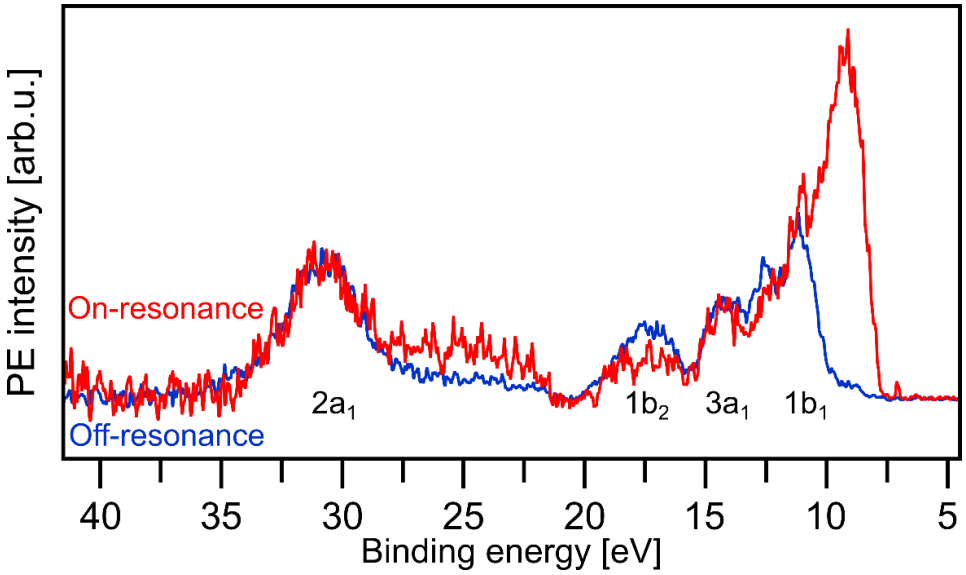

Figure 8 - 2

Valence photoelectron spectra from a 20 wt% 3nm CeO_2 NP aqueous solution obtained at the cerium $3d_{5/3}$ resonance photon energy 884 eV photon energy (in red color) and at the off-resonance photon energy 870 eV (blue). A Shirley background has been subtracted from the spectra. The water valence photoelectron contributions are labelled.

It will be very useful to preform analogous studies using tender X-rays (1.5-12 KeV). This allows probing deeper into solution to quantify the density profile of the NPs at the liquid—vapor interface, and to increase the absolute signal intensity from the interfacial species. For that, I am planning NP liquid jet experiments at the Galaxies beamline of the SOLEIL synchrotron facility (Paris, France). That beamline delivers up to 12 keV photon energy[304] corresponding to approximately IMFP of 11-12 nm[305] which is a factor of 2-4 larger than for the present X-ray studies.

Future perspectives may extend to explore hybrid core-shell nanoparticle aqueous solutions (for example: ZnO/Fe_2O_3 and Fe_2O_3/TiO_2). This would be a mimicking systems of the core-shell photoelectrodes recently examined in PEC. Such heterojunction structure formed between the core and shell materials has shown to significantly improve the separation of the charge carrier and the OER[306-307] (see Figure 1-1). Studying these tailored NP—water interactions would benefit advance the developments of photoelectrochemical cells.

References

1. Schneider, J.; Matsuoka, M.; Takeuchi, M.; Zhang, J.; Horiuchi, Y.; Anpo, M.; Bahnemann, D. W., Understanding TiO_2 photocatalysis: mechanisms and materials. *Chem. Rev. (Washington, DC, U. S.)* **2014,** *114* (19), 9919-9986.
2. Nehring, R., Traversing the mountaintop: world fossil fuel production to 2050. *Philosophical Transactions of the Royal Society B: Biological Sciences* **2009,** *364* (1532), 3067-3079.
3. Berner, R. A., The long-term carbon cycle, fossil fuels and atmospheric composition. *Nature* **2003,** *426* (6964), 323.
4. Wang, W.; Tadé, M. O.; Shao, Z., Research progress of perovskite materials in photocatalysis- and photovoltaics-related energy conversion and environmental treatment. *Chem. Soc. Rev.* **2015,** *44* (15), 5371-5408.
5. Wang, D. A. C., Guozhong, *Nanomaterials for Energy Conversion and Storage*. 2018.
6. Dincer, I.; Zamfirescu, C., *Sustainable energy systems and applications*. Springer Science & Business Media: 2011.
7. Lewis, N. S., Toward cost-effective solar energy use. *Science* **2007,** *315* (5813), 798-801.
8. Fujishima, A.; Honda, K., Electrochemical evidence for the mechanism of the primary stage of photosynthesis. *Bull. Chem. Soc. Jpn.* **1971,** *44* (4), 1148-1150.
9. Maeda, K., Photocatalytic water splitting using semiconductor particles: history and recent developments. *Journal of Photochemistry and Photobiology C: Photochemistry Reviews* **2011,** *12* (4), 237-268.
10. Van de Krol, R., Principles of photoelectrochemical cells. *Photoelectrochemical Hydrogen Production* **2011,** *102*, 13.
11. Deák, P.; Kullgren, J.; Aradi, B.; Frauenheim, T.; Kavan, L., Water splitting and the band edge positions of TiO_2. *Electrochim. Acta* **2016,** *199*, 27-34.
12. Atabaev, T. S.; Hossain, M. A.; Lee, D.; Kim, H.-K.; Hwang, Y.-H., Pt-coated TiO_2 nanorods for photoelectrochemical water splitting applications. *Results in Physics* **2016,** *6*, 373-376.
13. Macdonald, T. J.; Ambroz, F.; Batmunkh, M.; Li, Y.; Kim, D.; Contini, C.; Poduval, R.; Liu, H.; Shapter, J. G.; Papakonstantinou, I., TiO_2 nanofiber photoelectrochemical cells loaded with sub-12 nm AuNPs: Size dependent performance evaluation. *Materials today energy* **2018,** *9*, 254-263.
14. Bae, D.; Seger, B.; Vesborg, P. C.; Hansen, O.; Chorkendorff, I., Strategies for stable water splitting via protected photoelectrodes. *Chem. Soc. Rev.* **2017,** *46* (7), 1933-1954.
15. Junta-Rosso, J. L.; Hochella, M. F., The chemistry of hematite 001 surfaces. *Geochim. Cosmochim. Acta* **1996,** *60* (2), 305-314.

16. Todd, E.; Sherman, D.; Purton, J., Surface oxidation of chalcopyrite ($CuFeS_2$) under ambient atmospheric and aqueous (pH 2-10) conditions: Cu, Fe L-and O K-edge X-ray spectroscopy. *Geochim. Cosmochim. Acta* **2003,** *67* (12), 2137-2146.
17. Todd, E.; Sherman, D.; Purton, J., Surface oxidation of pyrite under ambient atmospheric and aqueous (pH= 2 to 10) conditions: electronic structure and mineralogy from X-ray absorption spectroscopy. *Geochim. Cosmochim. Acta* **2003,** *67* (5), 881-893.
18. Kurtz, R. L.; Henrich, V. E., Surface electronic structure and chemisorption on corundum transition-metal oxides: α-Fe_2O_3. *Phys. Rev. B* **1987,** *36* (6), 3413.
19. Henderson, M. A., The interaction of water with solid surfaces: fundamental aspects revisited. *Surf. Sci. Rep.* **2002,** *46* (1-8), 1-308.
20. Thiel, P. A.; Madey, T. E., The interaction of water with solid surfaces: fundamental aspects. *Surf. Sci. Rep.* **1987,** *7* (6-8), 211-385.
21. Hodgson, A.; Haq, S., Water adsorption and the wetting of metal surfaces. *Surf. Sci. Rep.* **2009,** *64* (9), 381-451.
22. Boily, J.-F. o.; Yeşilbaş, M.; Md. Musleh Uddin, M.; Baiqing, L.; Trushkina, Y.; Salazar-Alvarez, G. n., Thin Water Films at Multifaceted Hematite Particle Surfaces. *Langmuir* **2015,** *31* (48), 13127-13137.
23. Boily, J.-F.; Shchukarev, A., X-ray photoelectron spectroscopy of fast-frozen hematite colloids in aqueous solutions. 2. Tracing the relationship between surface charge and electrolyte adsorption. *J. Phys. Chem. C* **2010,** *114* (6), 2613-2616.
24. Shimizu, K.; Shchukarev, A.; Boily, J.-F. o., X-ray photoelectron spectroscopy of fast-frozen hematite colloids in aqueous solutions. 3. Stabilization of ammonium species by surface (hydr)oxo groups. *J. Phys. Chem. C* **2011,** *115* (14), 6796-6801.
25. Shimizu, K.; Shchukarev, A.; Kozin, P. A.; Boily, J.-F., X-ray photoelectron spectroscopy of fast-frozen hematite colloids in aqueous solutions. 4. Coexistence of alkali metal (Na^+, K^+, Rb^+, Cs^+) and chloride ions. *Surf. Sci.* **2012,** *606* (13-14), 1005-1009.
26. Shimizu, K.; Shchukarev, A.; Kozin, P. A.; Boily, J.-F. o., X-ray Photoelectron Spectroscopy of Fast-Frozen Hematite Colloids in Aqueous Solutions. 5. Halide Ion (F^-, Cl^-, Br^-, I^-) Adsorption. *Langmuir* **2013,** *29* (8), 2623-2630.
27. Andersson, K.; Ketteler, G.; Bluhm, H.; Yamamoto, S.; Ogasawara, H.; Pettersson, L. G.; Salmeron, M.; Nilsson, A., Autocatalytic water dissociation on Cu(110) at near ambient conditions. *J. Am. Chem. Soc.* **2008,** *130* (9), 2793-2797.
28. Jürgensen, A.; Esser, N.; Hergenröder, R., Near ambient pressure XPS with a conventional X-ray source. *Surf. Interface Anal.* **2012,** *44* (8), 1100-1103.
29. Yamamoto, S.; Bluhm, H.; Andersson, K.; Ketteler, G.; Ogasawara, H.; Salmeron, M.; Nilsson, A., In situ X-ray photoelectron spectroscopy studies of water on metals and oxides at ambient conditions. *J. Phys.: Condens. Matter* **2008,** *20* (18), 184025.

30. Kerherve, G.; Regoutz, A.; Bentley, D.; Hood, C.; Feeley, K.; Knight, S.; Robson, A.; Turner, C.; Singh, N.; Pontefract, J., Laboratory-based high pressure X-ray photoelectron spectroscopy: A novel and flexible reaction cell approach. *Rev. Sci. Instrum.* **2017,** *88* (3), 033102.
31. Velasco-Velez, J. J.; Pfeifer, V.; Hävecker, M.; Weatherup, R. S.; Arrigo, R.; Chuang, C. H.; Stotz, E.; Weinberg, G.; Salmeron, M.; Schlögl, R., Photoelectron spectroscopy at the graphene–liquid interface reveals the electronic structure of an electrodeposited cobalt/graphene electrocatalyst. *Angewandte Chemie International Edition* **2015,** *54* (48), 14554-14558.
32. Winter, B.; Weber, R.; Widdra, W.; Dittmar, M.; Faubel, M.; Hertel, I., Full valence band photoemission from liquid water using EUV synchrotron radiation. *J. Phys. Chem. A* **2004,** *108* (14), 2625-2632.
33. Winter, B.; Faubel, M., Photoemission from liquid aqueous solutions. *Chem. Rev. (Washington, DC, U. S.)* **2006,** *106* (4), 1176-1211.
34. Siegbahn, K., From X-ray to electron spectroscopy and new trends. *J. Electron Spectrosc. Relat. Phenom.* **1990,** *51*, 11-36.
35. Seidel, R.; Winter, B.; Bradforth, S. E., Valence electronic structure of aqueous solutions: Insights from photoelectron spectroscopy. *Annu. Rev. Phys. Chem.* **2016,** *67*, 283-305.
36. Almbladh, C.-O. In *Photoemission beyond the sudden approximation*, J. Phys.: Conf. Ser., IOP Publishing: 2006; p 127.
37. Dehmer, J.; Dill, D.; Wallace, S., Shape-resonance-enhanced nuclear-motion effects in molecular photoionization. *Phys. Rev. Lett.* **1979,** *43* (14), 1005.
38. Raseev, G.; Le Rouzo, H.; Lefebvre-Brion, H., Partial photoionization cross section and photoelectron angular distribution for the $X^2\Sigma_g^+$ state of N_2^+ in the static-exchange approximation. *J.Chem. Phys.* **1980,** *72* (10), 5701-5709.
39. Schaich, W., Theory of photoemission: Independent particle model. In *Photoemission in Solids I*, Springer: 1978; pp 105-134.
40. Hedin, L.; Lee, J., Sudden approximation in photoemission and beyond. *J. Electron Spectrosc. Relat. Phenom.* **2002,** *124* (2-3), 289-315.
41. Schultze, M.; Fieß, M.; Karpowicz, N.; Gagnon, J.; Korbman, M.; Hofstetter, M.; Neppl, S.; Cavalieri, A. L.; Komninos, Y.; Mercouris, T., Delay in photoemission. *Science* **2010,** *328* (5986), 1658-1662.
42. Zewail, A. H., Femtochemistry: Atomic-scale dynamics of the chemical bond. *J. Phys. Chem. A* **2000,** *104* (24), 5660-5694.
43. Santana, J. A. C., *Quantitative Core Level Photoelectron Spectroscopy*. Morgan & Claypool Publishers: 2016.
44. Hüfner, S., *Photoelectron spectroscopy: principles and applications*. Springer Science & Business Media: 1995.

45. Barthés-Labrousse, M.-G., The Auger Effect. *Microscopy Microanalysis Microstructures* **1995,** *6* (3), 253-262.
46. Rausch, R.; Potthoff, M., Pump-probe Auger-electron spectroscopy of Mott insulators. *Phys. Rev. B* **2019,** *99* (20), 205108.
47. Potthoff, M.; Braun, J.; Borstel, G.; Nolting, W., Theory of Auger electron and appearance-potential spectroscopy from solids with partially filled valence bands: Effects of valence-band–core interaction. *Phys. Rev. B* **1993,** *47* (19), 12480.
48. Carley, A. F., Surface Analysis: X-ray Photoelectron Spectroscopy. In *Encyclopedia of Materials: Science and Technology*, Buschow, K. H. J.; Cahn, R. W.; Flemings, M. C.; Ilschner, B.; Kramer, E. J.; Mahajan, S.; Veyssière, P., Eds. Elsevier: Oxford, 2001; pp 8991-8996.
49. Carlson, T., *Photoelectron and Auger spectroscopy*. Springer Science & Business Media: 2013.
50. Thürmer, S.; Seidel, R.; Eberhardt, W.; Bradforth, S. E.; Winter, B., Ultrafast hybridization screening in Fe^{3+} aqueous solution. *J. Am. Chem. Soc.* **2011,** *133* (32), 12528-12535.
51. Hergenhahn, U., Interatomic and intermolecular coulombic decay: The early years. *J. Electron Spectrosc. Relat. Phenom.* **2011,** *184* (3-6), 78-90.
52. Kirz, J.; Jacobsen, C.; Howells, M., Soft X-ray microscopes and their biological applications. *Q. Rev. Biophys.* **1995,** *28* (1), 33-130.
53. Guttmann, P.; Bittencourt, C., Overview of nanoscale NEXAFS performed with soft X-ray microscopes. *Beilstein journal of nanotechnology* **2015,** *6* (1), 595-604.
54. Jablonski, A.; Powell, C. J., Relationships between electron inelastic mean free paths, effective attenuation lengths, and mean escape depths. *J. Electron Spectrosc. Relat. Phenom.* **1999,** *100* (1-3), 137-160.
55. Ottosson, N.; Faubel, M.; Bradforth, S. E.; Jungwirth, P.; Winter, B., Photoelectron spectroscopy of liquid water and aqueous solution: Electron effective attenuation lengths and emission-angle anisotropy. *J. Electron Spectrosc. Relat. Phenom.* **2010,** *177* (2-3), 60-70.
56. Hofmann, S., *Auger-and X-ray photoelectron spectroscopy in materials science: a user-oriented guide*. Springer Science & Business Media: 2012; Vol. 49.
57. Thürmer, S., Inquiring photoelectrons about the dynamics in liquid water. **2013**.
58. Seah, M. P.; Dench, W., Quantitative electron spectroscopy of surfaces: A standard data base for electron inelastic mean free paths in solids. *Surf. Interface Anal.* **1979,** *1* (1), 2-11.
59. Thürmer, S.; Seidel, R.; Faubel, M.; Eberhardt, W.; Hemminger, J. C.; Bradforth, S. E.; Winter, B., Photoelectron angular distributions from liquid water: Effects of electron scattering. *Phys. Rev. Lett.* **2013,** *111* (17), 173005.
60. Suzuki, Y.-I.; Nishizawa, K.; Kurahashi, N.; Suzuki, T., Effective attenuation length of an electron in liquid water between 10 and 600 eV. *Physical Review E* **2014,** *90* (1), 010302.
61. Smith, J. W.; Saykally, R. J., Soft x-ray absorption spectroscopy of liquids and solutions. *Chem. Rev. (Washington, DC, U. S.)* **2017,** *117* (23), 13909-13934.

62. Seidel, R.; Pohl, M. N.; Ali, H.; Winter, B.; Aziz, E. F., Advances in liquid phase soft-x-ray photoemission spectroscopy: A new experimental setup at BESSY II. *Rev. Sci. Instrum.* **2017,** *88* (7), 073107.
63. Ekimova, M.; Quevedo, W.; Faubel, M.; Wernet, P.; Nibbering, E. T., A liquid flatjet system for solution phase soft-x-ray spectroscopy. *Structural Dynamics* **2015,** *2* (5), 054301.
64. Artiglia, L.; Edebeli, J.; Orlando, F.; Chen, S.; Lee, M.-T.; Arroyo, P. C.; Gilgen, A.; Bartels-Rausch, T.; Kleibert, A.; Vazdar, M., A surface-stabilized ozonide triggers bromide oxidation at the aqueous solution-vapour interface. *Nature Comm.* **2017,** *8* (1), 700.
65. Eriksson, S. K.; Hahlin, M.; Kahk, J. M.; Villar-Garcia, I. J.; Webb, M. J.; Grennberg, H.; Yakimova, R.; Rensmo, H.; Edström, K.; Hagfeldt, A., A versatile photoelectron spectrometer for pressures up to 30 mbar. *Rev. Sci. Instrum.* **2014,** *85* (7), 075119.
66. Scienta Omicron, Data sheet: HiPP-2 Electron Spectrometer
67. Gotz, M. Electronic Structure in Solution. Soft X-ray Absorption and Emission for Fe^{2+} in Water. Freie Universität Berlin, Germany, 2012.
68. Weber, R.; Winter, B.; Schmidt, P.; Widdra, W.; Hertel, I.; Dittmar, M.; Faubel, M., Photoemission from aqueous alkali-metal− iodide salt solutions using EUV synchrotron radiation. *J. Phys. Chem. B* **2004,** *108* (15), 4729-4736.
69. Faubel, M.; Steiner, B.; Toennies, J. P., Photoelectron spectroscopy of liquid water, some alcohols, and pure nonane in free micro jets. *J.Chem. Phys.* **1997,** *106* (22), 9013-9031.
70. Seidel, R. Electronic-Structure Interactions in Aqueous Solutions: A Liquid-Jet Photoelectron-Spectroscopy Study. Technische Universität Berlin, 2011.
71. Scharf, W., *Particle accelerators and their uses*. CRC Press: 1991.
72. Kunz, C., Synchrotron radiation. **1974**.
73. Brown, G.; Halbach, K.; Harris, J.; Winick, H., Wiggler and undulator magnets—A review. *Nuclear Instruments and Methods in Physics Research* **1983,** *208* (1-3), 65-77.
74. Chavanne, J.; Elleaume, P., Undulator and wiggler shimming. **1995**.
75. Winick, H.; Brown, G.; Halbach, K.; Harris, J., Wiggler and undulator magnets. *Physics Today* **1981,** *34* (5), 50-63.
76. Golnak, R. Investigation of the Electronic Structure of Transition Metal-Ions in Solution from Aqua-Complexes to Porphyrins. Freie Universität Berlin, 2015.
77. Unger, I. Relaxation Processes in Aqueous Solutions upon X-ray Exposure: Entanglement of Electronic and Nuclear Dynamics. Freie Universität Berlin, 2015.
78. Helmholtz-zentrum-Berlin BESSY II storage ring. https://www.helmholtz-berlin.de/mediathek/info/beschleunigerphysik-fuer-anfaenger/der-speicherring_en.html.
79. Kachel, T., The plane grating monochromator beamline U49-2 PGM-1 at BESSY II. *Journal of large-scale research facilities JLSRF* **2016,** *2*, 72.

80. Pohl, M. N.; Muchová, E.; Seidel, R.; Ali, H.; Sršeň, Š.; Wilkinson, I.; Winter, B.; Slavíček, P., Do water's electrons care about electrolytes? *Chem. Sci.* **2019,** *10* (3), 848-865.
81. Madelung, O., Landolt-Bornstein: Numerical Data and Functional Relationships in Science and Technology. *New series group III* **1987,** *22*, 63,117.
82. Thompson, A.; Vaughan, D., X-ray data booklet (center for X-ray optics and advanced light source). *Lawrence Berkeley National Laboratory* **2001**.
83. Banna, M.; McQuaide, B.; Malutzki, R.; Schmidt, V., The photoelectron spectrum of water in the 30 to 140 eV photon energy range. *J.Chem. Phys.* **1986,** *84* (9), 4739-4744.
84. Sankari, R.; Ehara, M.; Nakatsuji, H.; Senba, Y.; Hosokawa, K.; Yoshida, H.; De Fanis, A.; Tamenori, Y.; Aksela, S.; Ueda, K., Vibrationally resolved O 1s photoelectron spectrum of water. *Chem. Phys. Lett.* **2003,** *380* (5-6), 647-653.
85. Pohl, M. N. Intermolecular Electronic Decay in Aqueous Solutions: A Liquid-Phase Photoelectron Spectroscopy Study. 2018.
86. Winter, B., Liquid microjet for photoelectron spectroscopy. *Nucl. Instrum. Methods Phys. Res., Sect. A* **2009,** *601* (1), 139-150.
87. Winter, B.; Hergenhahn, U.; Faubel, M.; Björneholm, O.; Hertel, I. V., Hydrogen bonding in liquid water probed by resonant Auger-electron spectroscopy. *J.Chem. Phys.* **2007,** *127* (9), 094501.
88. Wang, M.-Y.; Shen, T.; Wang, M.; Zhang, D.-E.; Tong, Z.-w.; Chen, J., One-pot synthesis of α-Fe_2O_3 nanoparticles-decorated reduced graphene oxide for efficient nonenzymatic H_2O_2 biosensor. *Sensors and Actuators B: Chemical* **2014,** *190*, 645-650.
89. Reufer, M.; Dietsch, H.; Gasser, U.; Grobety, B.; Hirt, A.; Malik, V. K.; Schurtenberger, P., Magnetic properties of silica coated spindle-type hematite particles. *J. Phys.: Condens. Matter* **2011,** *23* (6), 065102.
90. Azevedo, J.; Seipp, T.; Burfeind, J.; Sousa, C.; Bentien, A.; Araújo, J. P.; Mendes, A., Unbiased solar energy storage: Photoelectrochemical redox flow battery. *Nano Energy* **2016,** *22*, 396-405.
91. Ramasami, A. K.; Ravishankar, T. N.; Sureshkumar, K.; Reddy, M. V.; Chowdari, B. V. R.; Ramakrishnappa, T.; Balakrishna, G. R., Synthesis, exploration of energy storage and electrochemical sensing properties of hematite nanoparticles. *J. Alloys Compd.* **2016,** *671*, 552-559.
92. Dias, P.; Vilanova, A.; Lopes, T.; Andrade, L.; Mendes, A., Extremely stable bare hematite photoanode for solar water splitting. *Nano Energy* **2016,** *23*, 70-79.
93. Ketteler, G.; Yamamoto, S.; Bluhm, H.; Andersson, K.; Starr, D. E.; Ogletree, D. F.; Ogasawara, H.; Nilsson, A.; Salmeron, M., The nature of water nucleation sites on TiO_2 (110) surfaces revealed by ambient pressure X-ray photoelectron spectroscopy. *J. Phys. Chem. C* **2007,** *111* (23), 8278-8282.

94. Crumlin, E. J.; Bluhm, H.; Liu, Z., In situ investigation of electrochemical devices using ambient pressure photoelectron spectroscopy. *J. Electron Spectrosc. Relat. Phenom.* **2013,** *190*, 84-92.
95. Karslıoğlu, O.; Nemšák, S.; Zegkinoglou, I.; Shavorskiy, A.; Hartl, M.; Salmassi, F.; Gullikson, E.; Ng, M.; Rameshan, C.; Rude, B., Aqueous solution/metal interfaces investigated in operando by photoelectron spectroscopy. *Faraday Discuss.* **2015,** *180*, 35-53.
96. Wu, C. H.; Weatherup, R. S.; Salmeron, M. B., Probing electrode/electrolyte interfaces in situ by X-ray spectroscopies: old methods, new tricks. *Phys. Chem. Chem. Phys.* **2015,** *17* (45), 30229-30239.
97. Axnanda, S.; Crumlin, E. J.; Mao, B.; Rani, S.; Chang, R.; Karlsson, P. G.; Edwards, M. O.; Lundqvist, M.; Moberg, R.; Ross, P., Using "Tender" X-ray ambient pressure X-Ray photoelectron spectroscopy as a direct probe of solid-liquid interface. *Sci. Rep.* **2015,** *5*, 9788.
98. Kolmakov, A.; Dikin, D. A.; Cote, L. J.; Huang, J.; Abyaneh, M. K.; Amati, M.; Gregoratti, L.; Günther, S.; Kiskinova, M., Graphene oxide windows for in situ environmental cell photoelectron spectroscopy. *Nat. Nanotechnol.* **2011,** *6* (10), 651-657.
99. Kraus, J.; Reichelt, R.; Günther, S.; Gregoratti, L.; Amati, M.; Kiskinova, M.; Yulaev, A.; Vlassiouk, I.; Kolmakov, A., Photoelectron spectroscopy of wet and gaseous samples through graphene membranes. *Nanoscale* **2014,** *6* (23), 14394-14403.
100. Seidel, R.; Thürmer, S.; Winter, B., Photoelectron spectroscopy meets aqueous solution: studies from a vacuum liquid microjet. *J. Phys. Chem. Lett.* **2011,** *2* (6), 633-641.
101. Faubel, M.; Steiner, B.; Toennies, J., Measurement of HeI photoelectron spectra of liquid water, formamide and ethylene glycol in fast-flowing microjets. *J. Electron Spectrosc. Relat. Phenom.* **1998,** *95* (2), 159-169.
102. Siefermann, K. R.; Liu, Y.; Lugovoy, E.; Link, O.; Faubel, M.; Buck, U.; Winter, B.; Abel, B., Binding energies, lifetimes and implications of bulk and interface solvated electrons in water. *Nature Chem.* **2010,** *2* (4), 274-279.
103. Tang, Y.; Shen, H.; Sekiguchi, K.; Kurahashi, N.; Mizuno, T.; Suzuki, Y.-I.; Suzuki, T., Direct measurement of vertical binding energy of a hydrated electron. *Phys. Chem. Chem. Phys.* **2010,** *12* (15), 3653-3655.
104. Shreve, A. T.; Yen, T. A.; Neumark, D. M., Photoelectron spectroscopy of hydrated electrons. *Chem. Phys. Lett.* **2010,** *493* (4), 216-219.
105. Lübcke, A.; Buchner, F.; Heine, N.; Hertel, I. V.; Schultz, T., Time-resolved photoelectron spectroscopy of solvated electrons in aqueous NaI solution. *Phys. Chem. Chem. Phys.* **2010,** *12* (43), 14629-14634.
106. Congiu, M.; De Marco, M. L.; Bonomo, M.; Nunes-Neto, O.; Dini, D.; Graeff, C. F., Pristine and Al-doped hematite printed films as photoanodes of p-type dye-sensitized solar cells. *Journal of Nanoparticle Research* **2017,** *19* (1), 7.

107. Corbellini, L.; Lacroix, C.; Harnagea, C.; Korinek, A.; Botton, G. A.; Ménard, D.; Pignolet, A., Epitaxially stabilized thin films of ε-Fe_2O_3 (001) grown on YSZ (100). *Sci. Rep.* **2017,** *7* (1), 3712.

108. Jubb, A. M.; Allen, H. C., Vibrational spectroscopic characterization of hematite, maghemite, and magnetite thin films produced by vapor deposition. *ACS Appl. Mater. Interfaces* **2010,** *2* (10), 2804-2812.

109. Liu, J.; Kim, Y.-T.; Kwon, Y.-U., Hematite Thin Films with Various Nanoscopic Morphologies Through Control of Self-Assembly Structures. *Nanoscale research letters* **2015,** *10* (1), 228.

110. Wang, W.; Liang, L.; Johs, A.; Gu, B., Thin films of uniform hematite nanoparticles: control of surface hydrophobicity and self-assembly. *J. Mater. Chem.* **2008,** *18* (47), 5770-5775.

111. Braun, A.; Sivula, K.; Bora, D. K.; Zhu, J.; Zhang, L.; Gratzel, M.; Guo, J.; Constable, E. C., Direct observation of two electron holes in a hematite photoanode during photoelectrochemical water splitting. *J. Phys. Chem. C* **2012,** *116* (32), 16870-16875.

112. Gajda-Schrantz, K.; Tymen, S.; Boudoire, F.; Toth, R.; Bora, D. K.; Calvet, W.; Grätzel, M.; Constable, E. C.; Braun, A., Formation of an electron hole doped film in the α-Fe_2O_3 photoanode upon electrochemical oxidation. *Phys. Chem. Chem. Phys.* **2013,** *15* (5), 1443-1451.

113. Sivula, K.; Le Formal, F.; Grätzel, M., Solar water splitting: progress using hematite (α-Fe_2O_3) photoelectrodes. *ChemSusChem* **2011,** *4* (4), 432-449.

114. Lemire, C.; Bertarione, S.; Zecchina, A.; Scarano, D.; Chaka, A.; Shaikhutdinov, S.; Freund, H.-J., Ferryl (Fe=O) Termination of the Hematite α−Fe_2O_3 (0001) Surface. *Phys. Rev. Lett.* **2005,** *94* (16), 166101.

115. Lad, R. J.; Henrich, V. E., Structure of α-Fe_2O_3 single crystal surfaces following Ar^+ ion bombardment and annealing in O_2. *Surf. Sci.* **1988,** *193* (1-2), 81-93.

116. Kurtz, R. L.; Henrich, V. E., Geometric structure of the α-Fe_2O_3 (001) surface: A LEED and XPS study. *Surf. Sci.* **1983,** *129* (2-3), 345-354.

117. Condon, N. G.; Murray, P. W.; Leibsle, F. M.; Thornton, G.; Lennie, A. R.; Vaughan, D. J., Fe_3O_4(111) termination of α-Fe_2O_3(0001). *Surf. Sci.* **1994,** *310* (1-3), L609-L613.

118. Condon, N.; Leibsle, F.; Lennie, A.; Murray, P.; Parker, T.; Vaughan, D.; Thornton, G., Scanning tunnelling microscopy studies of α-Fe_2O_3 (0001). *Surf. Sci.* **1998,** *397* (1-3), 278-287.

119. Tang, Y.; Qin, H.; Wu, K.; Guo, Q.; Guo, J., The reduction and oxidation of Fe_2O_3 (0001) surface investigated by scanning tunneling microscopy. *Surf. Sci.* **2013,** *609*, 67-72.

120. Lanier, C. H.; Chiaramonti, A. N.; Marks, L. D.; Poeppelmeier, K. R., The Fe_3O_4 origin of the "Biphase" reconstruction on α-Fe_2O_3 (0001). *Surf. Sci.* **2009,** *603* (16), 2574-2579.

121. Kiejna, A.; Pabisiak, T., Mixed termination of hematite (α-Fe_2O_3)(0001) surface. *J. Phys. Chem. C* **2013,** *117* (46), 24339-24344.

122. Kiejna, A.; Pabisiak, T., Surface properties of clean and Au or Pd covered hematite (α-Fe_2O_3)(0001). *J. Phys.: Condens. Matter* **2012,** *24* (9), 095003.

123. Alvarez-Ramırez, F.; Martınez-Magadán, J.; Gomes, J.; Illas, F., On the geometric structure of the (0001) hematite surface. *Surf. Sci.* **2004,** *558* (1), 4-14.
124. Wang, X.-G.; Weiss, W.; Shaikhutdinov, S. K.; Ritter, M.; Petersen, M.; Wagner, F.; Schlögl, R.; Scheffler, M., The hematite (α-Fe_2O_3)(0001) surface: evidence for domains of distinct chemistry. *Phys. Rev. Lett.* **1998,** *81* (5), 1038.
125. Barbier, A.; Stierle, A.; Kasper, N.; Guittet, M.-J.; Jupille, J., Surface termination of hematite at environmental oxygen pressures: Experimental surface phase diagram. *Phys. Rev. B* **2007,** *75* (23), 233406.
126. Parkinson, G. S., Iron oxide surfaces. *Surf. Sci. Rep.* **2016,** *71* (1), 272-365.
127. Kuhlenbeck, H.; Shaikhutdinov, S.; Freund, H.-J., Well-ordered transition metal oxide layers in model catalysis–a series of case studies. *Chem. Rev. (Washington, DC, U. S.)* **2013,** *113* (6), 3986-4034.
128. Hendewerk, M.; Salmeron, M.; Somorjai, G. A., Water adsorption on the (001) plane of Fe_2O_3: An XPS, UPS, Auger, and TPD study. *Surf. Sci.* **1986,** *172* (3), 544-556.
129. Morimoto, T.; Nagao, M.; Tokuda, F., Relation between the amounts of chemisorbed and physisorbed water on metal oxides. *J. Phys. Chem.* **1969,** *73* (1), 243-248.
130. McCafferty, E.; Zettlemoyer, A., Adsorption of water vapour on α-Fe_2O_3. *Discussions of the Faraday Society* **1971,** *52*, 239-254.
131. Nguyen, M.-T.; Seriani, N.; Gebauer, R., Water adsorption and dissociation on α-Fe_2O_3 (0001): PBE+ U calculations. *J.Chem. Phys.* **2013,** *138* (19), 194709.
132. Yin, S.; Ma, X.; Ellis, D., Initial stages of H_2O adsorption and hydroxylation of Fe-terminated α-Fe_2O_3 (0001) surface. *Surf. Sci.* **2007,** *601* (12), 2426-2437.
133. Pan, H.; Meng, X.; Qin, G., Hydrogen generation by water splitting on hematite (0001) surfaces: first-principles calculations. *Phys. Chem. Chem. Phys.* **2014,** *16* (46), 25442-25448.
134. von Rudorff, G. F.; Jakobsen, R.; Rosso, K. M.; Blumberger, J., Fast Interconversion of Hydrogen Bonding at the Hematite (001)–Liquid Water Interface. *J. Phys. Chem. Lett.* **2016,** *7* (7), 1155-1160.
135. Kerisit, S., Water structure at hematite–water interfaces. *Geochim. Cosmochim. Acta* **2011,** *75* (8), 2043-2061.
136. Yamamoto, S.; Kendelewicz, T.; Newberg, J. T.; Ketteler, G.; Starr, D. E.; Mysak, E. R.; Andersson, K. J.; Ogasawara, H.; Bluhm, H.; Salmeron, M., Water adsorption on α-Fe_2O_3 (0001) at near ambient conditions. *J. Phys. Chem. C* **2010,** *114* (5), 2256-2266.
137. Spagnoli, D.; Gilbert, B.; Waychunas, G. A.; Banfield, J. F., Prediction of the effects of size and morphology on the structure of water around hematite nanoparticles. *Geochim. Cosmochim. Acta* **2009,** *73* (14), 4023-4033.

138. Makowski, M. J.; Galhenage, R. P.; Langford, J.; Hemminger, J. C., Liquid-Jet X-ray Photoelectron Spectra of TiO_2 Nanoparticles in an Aqueous Electrolyte Solution. *J. Phys. Chem. Lett.* **2016,** *7* (9), 1732-1735.
139. Brown, M. A.; Seidel, R.; Thürmer, S.; Faubel, M.; Hemminger, J. C.; van Bokhoven, J. A.; Winter, B.; Sterrer, M., Electronic structure of sub-10 nm colloidal silica nanoparticles measured by in situ photoelectron spectroscopy at the aqueous-solid interface. *Phys. Chem. Chem. Phys.* **2011,** *13* (28), 12720-12723.
140. Lewis, T.; Winter, B.; Stern, A. C.; Baer, M. D.; Mundy, C. J.; Tobias, D. J.; Hemminger, J. C., Does nitric acid dissociate at the aqueous solution surface? *J. Phys. Chem. C* **2011,** *115* (43), 21183-21190.
141. Faubel, M.; Kisters, T., Non-equilibrium molecular evaporation of carboxylic acid dimers. *Nature* **1989,** *339* (6225), 527.
142. Jouaiti, A.; Mosser, A.; Romeo, M.; Shindo, S., Background calculation for X-ray photoelectron spectra analysis. *J. Electron Spectrosc. Relat. Phenom.* **1992,** *59* (4), 327-340.
143. Shirley, D. A., High-resolution X-ray photoemission spectrum of the valence bands of gold. *Phys. Rev. B* **1972,** *5* (12), 4709.
144. Seidel, R.; Atak, K.; Thürmer, S.; Aziz, E. F.; Winter, B., Ti^{3+} aqueous solution: hybridization and electronic relaxation probed by state-dependent electron spectroscopy. *J. Phys. Chem. B* **2015,** *119* (33), 10607-10615.
145. Lad, R. J.; Henrich, V. E., Photoemission study of the valence-band electronic structure in Fe_xO, Fe_3O_4, and α-Fe_2O_3 single crystals. *Phys. Rev. B* **1989,** *39* (18), 13478.
146. Fujimori, A.; Saeki, M.; Kimizuka, N.; Taniguchi, M.; Suga, S., Photoemission satellites and electronic structure of Fe_2O_3. *Phys. Rev. B* **1986,** *34* (10), 7318.
147. Sherman, D. M., The electronic structures of Fe^{3+} coordination sites in iron oxides: Applications to spectra, bonding, and magnetism. *Phys. Chem. Miner.* **1985,** *12* (3), 161-175.
148. Yepes, D.; Seidel, R.; Winter, B.; Blumberger, J.; Jaque, P., Photoemission Spectra and Density Functional Theory Calculations of 3d Transition Metal–Aqua Complexes (Ti–Cu) in Aqueous Solution. *J. Phys. Chem. B* **2014,** *118* (24), 6850-6863.
149. Radu, T.; Iacovita, C.; Benea, D.; Turcu, R., X-ray photoelectron spectroscopic characterization of iron oxide nanoparticles. *Appl. Surf. Sci.* **2017,** *405*, 337-343.
150. Fransson, T.; Harada, Y.; Kosugi, N.; Besley, N. A.; Winter, B.; Rehr, J. J.; Pettersson, L. G. M.; Nilsson, A., X-ray and Electron Spectroscopy of Water. *Chem. Rev. (Washington, DC, U. S.)* **2016,** *116* (13), 7551-7569.
151. Wernet, P.; Nordlund, D.; Bergmann, U.; Cavalleri, M.; Odelius, M.; Ogasawara, H.; Näslund, L.; Hirsch, T.; Ojamäe, L.; Glatzel, P., The structure of the first coordination shell in liquid water. *Science* **2004,** *304* (5673), 995-999.

152. Thürmer, S.; Unger, I.; Slavíček, P.; Winter, B., Relaxation of Electronically Excited Hydrogen Peroxide in Liquid Water: Insights from Auger-Electron Emission. *J. Phys. Chem. C* **2013,** *117* (43), 22268-22275.
153. Aziz, E. F.; Ottosson, N.; Faubel, M.; Hertel, I. V.; Winter, B., Interaction between liquid water and hydroxide revealed by core-hole de-excitation. *Nature* **2008,** *455* (7209), 89-91.
154. Cappa, C. D.; Smith, J. D.; Messer, B. M.; Cohen, R. C.; Saykally, R. J., Nature of the aqueous hydroxide ion probed by X-ray absorption spectroscopy. *J. Phys. Chem. A* **2007,** *111* (22), 4776-4785.
155. Poshusta, R.; Tseng, D.; Hess, A. C.; McCarthy, M. I., Periodic Hartree-Fock study of nitric acid monohydrate crystal: bulk and clean surface. *J. Phys. Chem.* **1993,** *97* (28), 7295-7303.
156. Cressey, G.; Henderson, C.; Van der Laan, G., Use of L-edge X-ray absorption spectroscopy to characterize multiple valence states of 3d transition metals; a new probe for mineralogical and geochemical research. *Phys. Chem. Miner.* **1993,** *20* (2), 111-119.
157. Bora, D. K.; Braun, A.; Erat, S.; Ariffin, A. K.; Löhnert, R.; Sivula, K.; Töpfer, J. r.; Grätzel, M.; Manzke, R.; Graule, T., Evolution of an oxygen near-edge X-ray absorption fine structure transition in the upper Hubbard band in α-Fe_2O_3 upon electrochemical oxidation. *J. Phys. Chem. C* **2011,** *115* (13), 5619-5625.
158. Wu, Z.; Gota, S.; Jollet, F.; Pollak, M.; Gautier-Soyer, M.; Natoli, C., Characterization of iron oxides by X-ray absorption at the oxygen K edge using a full multiple-scattering approach. *Phys. Rev. B* **1997,** *55* (4), 2570.
159. Pollak, M.; Gautier, M.; Thromat, N.; Gota, S.; Mackrodt, W.; Saunders, V., An in-situ study of the surface phase transitions of α-Fe_2O_3 by X-ray absorption spectroscopy at the oxygen K edge. *Nuclear Instruments and Methods in Physics Research Section B: Beam Interactions with Materials and Atoms* **1995,** *97* (1-4), 383-386.
160. Park, T.-J.; Sambasivan, S.; Fischer, D. A.; Yoon, W.-S.; Misewich, J. A.; Wong, S. S., Electronic structure and chemistry of iron-based metal oxide nanostructured materials: a NEXAFS investigation of $BiFeO_3$, $Bi_2Fe_4O_9$, α-Fe_2O_3, γ-Fe_2O_3, and Fe/Fe_3O_4. *J. Phys. Chem. C* **2008,** *112* (28), 10359-10369.
161. Colliex, C.; Manoubi, T.; Ortiz, C., Electron-energy-loss-spectroscopy near-edge fine structures in the iron-oxygen system. *Phys. Rev. B* **1991,** *44* (20), 11402-11411.
162. De Groot, F. M. F.; Grioni, M.; Fuggle, J. C.; Ghijsen, J.; Sawatzky, G. A.; Petersen, H., Oxygen 1s x-ray-absorption edges of transition-metal oxides. *Phys. Rev. B* **1989,** *40* (8), 5715-5723.
163. Gilbert, B.; Frandsen, C.; Maxey, E.; Sherman, D., Band-gap measurements of bulk and nanoscale hematite by soft X-ray spectroscopy. *Phys. Rev. B* **2009,** *79* (3), 035108.
164. Winter, B.; Aziz, E. F.; Hergenhahn, U.; Faubel, M.; Hertel, I. V., Hydrogen bonds in liquid water studied by photoelectron spectroscopy. *J.Chem. Phys.* **2007,** *126* (12), 124504.

165. Shchukarev, A.; Boily, J. F., XPS study of the hematite–aqueous solution interface. *Surf. Interface Anal.* **2008,** *40* (3-4), 349-353.
166. Brown, M. A.; Winter, B.; Faubel, M.; Hemminger, J. C., Spatial distribution of nitrate and nitrite anions at the liquid/vapor interface of aqueous solutions. *J. Am. Chem. Soc.* **2009,** *131* (24), 8354-8355.
167. Golnak, R.; Bokarev, S. I.; Seidel, R.; Xiao, J.; Grell, G.; Atak, K.; Unger, I.; Thürmer, S.; Aziz, S. G.; Kühn, O., Joint Analysis of Radiative and Non-Radiative Electronic Relaxation Upon X-ray Irradiation of Transition Metal Aqueous Solutions. *Sci. Rep.* **2016,** *6*, 2808-2814.
168. Golnak, R.; Xiao, J.; Atak, K.; Unger, I.; Seidel, R.; Winter, B.; Aziz, E. F., Undistorted X-ray Absorption Spectroscopy Using s-Core-Orbital Emissions. *J. Phys. Chem. A* **2016,** *120* (18), 2808-2814.
169. Björneholm, O.; Nilsson, A.; Sandell, A.; Hernnäs, B.; Mrtensson, N., Determination of time scales for charge-transfer screening in physisorbed molecules. *Phys. Rev. Lett.* **1992,** *68* (12), 1892.
170. Nordlund, D.; Ogasawara, H.; Bluhm, H.; Takahashi, O.; Odelius, M.; Nagasono, M.; Pettersson, L. G.; Nilsson, A., Probing the electron delocalization in liquid water and ice at attosecond time scales. *Phys. Rev. Lett.* **2007,** *99* (21), 217406.
171. Campbell, J.; Papp, T., Widths of the atomic K–N7 levels. *Atomic Data and Nuclear Data Tables* **2001,** *77* (1), 1-56.
172. Krause, M. O.; Oliver, J., Natural widths of atomic K and L levels, K α X-ray lines and several KLL Auger lines. *J. Phys. Chem. Ref. Data* **1979,** *8* (2), 329-338.
173. De Groot, F.; Kotani, A., *Core level spectroscopy of solids*. CRC press: 2008.
174. Slavicek, P.; Kryzhevoi, N. V.; Aziz, E. F.; Winter, B., Relaxation Processes in Aqueous Systems upon X-ray Ionization: Entanglement of Electronic and Nuclear Dynamics. *J. Phys. Chem. Lett.* **2016,** *7* (2), 234-243.
175. Hanaor, D. A.; Sorrell, C. C., Review of the anatase to rutile phase transformation. *J. Mater. Sci.* **2011,** *46* (4), 855-874.
176. Hamad, S.; Catlow, C.; Woodley, S.; Lago, S.; Mejias, J., Structure and stability of small TiO_2 nanoparticles. *J. Phys. Chem. B* **2005,** *109* (33), 15741-15748.
177. Diebold, U., The surface science of titanium dioxide. *Surf. Sci. Rep.* **2003,** *48* (5-8), 53-229.
178. Dette, C.; Pérez-Osorio, M. A.; Kley, C. S.; Punke, P.; Patrick, C. E.; Jacobson, P.; Giustino, F.; Jung, S. J.; Kern, K., TiO_2 anatase with a bandgap in the visible region. *Nano Lett.* **2014,** *14* (11), 6533-6538.
179. El-Sherbiny, S.; Morsy, F.; Samir, M.; Fouad, O. A., Synthesis, characterization and application of TiO_2 nanopowders as special paper coating pigment. *Appl. Nanosci.* **2014,** *4* (3), 305-313.
180. Nowotny, J.; Bak, T.; Nowotny, M.; Sheppard, L., TiO_2 surface active sites for water splitting. *J. Phys. Chem. B* **2006,** *110* (37), 18492-18495.

181. Nowotny, J.; Bak, T.; Nowotny, M.; Sheppard, L., Titanium dioxide for solar-hydrogen IV. Collective and local factors in photoreactivity. *Int. J. Hydrogen Energy* **2007,** *32* (14), 2651-2659.
182. Walter, M. G.; Warren, E. L.; McKone, J. R.; Boettcher, S. W.; Mi, Q.; Santori, E. A.; Lewis, N. S., Solar water splitting cells. *Chem. Rev. (Washington, DC, U. S.)* **2010,** *110* (11), 6446-6473.
183. Kazuhito, H.; Hiroshi, I.; Akira, F., TiO_2 Photocatalysis: A Historical Overview and Future Prospects. *Jpn. J. Appl. Phys.* **2005,** *44* (12R), 8269.
184. Asahi, R.; Morikawa, T.; Ohwaki, T.; Aoki, K.; Taga, Y., Visible-light photocatalysis in nitrogen-doped titanium oxides. *Science* **2001,** *293* (5528), 269-71.
185. Khan, S. U.; Al-Shahry, M.; Ingler, W. B., Efficient photochemical water splitting by a chemically modified n-TiO_2. *science* **2002,** *297* (5590), 2243-2245.
186. Nowotny, J.; Sorrell, C.; Bak, T.; Sheppard, L., Solar-hydrogen: Unresolved problems in solid-state science. *Solar Energy* **2005,** *78* (5), 593-602.
187. Grätzel, M., Photoelectrochemical cells. *nature* **2001,** *414* (6861), 338.
188. Young, J. L.; Steiner, M. A.; Döscher, H.; France, R. M.; Turner, J. A.; Deutsch, T. G., Direct solar-to-hydrogen conversion via inverted metamorphic multi-junction semiconductor architectures. *Nat. Energy* **2017,** *2* (4), 17028.
189. Ni, M.; Leung, M. K.; Leung, D. Y.; Sumathy, K., A review and recent developments in photocatalytic water-splitting using TiO_2 for hydrogen production. *Renewable Sustainable Energy Rev.* **2007,** *11* (3), 401-425.
190. Lu, X.; Xie, S.; Yang, H.; Tong, Y.; Ji, H., Photoelectrochemical hydrogen production from biomass derivatives and water. *Chem. Soc. Rev.* **2014,** *43* (22), 7581-7593.
191. Sun, C.; Liu, L.-M.; Selloni, A.; Lu, G. Q. M.; Smith, S. C., Titania-water interactions: a review of theoretical studies. *J. Mater. Chem.* **2010,** *20* (46), 10319-10334.
192. Walle, L.; Borg, A.; Johansson, E.; Plogmaker, S.; Rensmo, H.; Uvdal, P.; Sandell, A., Mixed dissociative and molecular water adsorption on anatase TiO_2 (101). *J. Phys. Chem. C* **2011,** *115* (19), 9545-9550.
193. Dette, C.; Pérez-Osorio, M. A.; Mangel, S.; Giustino, F.; Jung, S. J.; Kern, K., Atomic Structure of Water Monolayer on Anatase TiO_2 (101) Surface. *J. Phys. Chem. C* **2018**, 11954–11960.
194. Nadeem, I. M.; Treacy, J. P. W.; Selcuk, S.; Torrelles, X.; Hussain, H.; Wilson, A.; Grinter, D. C.; Cabailh, G.; Bikondoa, O.; Nicklin, C.; Selloni, A.; Zegenhagen, J.; Lindsay, R.; Thornton, G., Water Dissociates at the Aqueous Interface with Reduced Anatase TiO_2 (101). *J. Phys. Chem. Lett.* **2018,** *9* (11), 3131-3136.
195. Perron, H.; Vandenborre, J.; Domain, C.; Drot, R.; Roques, J.; Simoni, E.; Ehrhardt, J.-J.; Catalette, H., Combined investigation of water sorption on TiO_2 rutile (110) single crystal face: XPS vs. periodic DFT. *Surf. Sci.* **2007,** *601* (2), 518-527.

196. Hugenschmidt, M. B.; Gamble, L.; Campbell, C. T., The interaction of H_2O with a TiO_2 (110) surface. *Surf. Sci.* **1994,** *302* (3), 329-340.
197. Ali, H.; Seidel, R.; Pohl, M. N.; Winter, B., Molecular species forming at the α-Fe_2O_3 nanoparticle–aqueous solution interface. *Chem. Sci.* **2018,** *9* (19), 4511-4523.
198. Brown, M. A.; Beloqui Redondo, A.; Sterrer, M.; Winter, B.; Pacchioni, G.; Abbas, Z.; van Bokhoven, J. A., Measure of surface potential at the aqueous–oxide nanoparticle interface by XPS from a liquid microjet. *Nano Lett.* **2013,** *13* (11), 5403-5407.
199. Brown, M. A.; Jordan, I.; Redondo, A. B.; Kleibert, A.; Wörner, H. J.; van Bokhoven, J. A., In situ photoelectron spectroscopy at the liquid/nanoparticle interface. *Surf. Sci.* **2013,** *610*, 1-6.
200. Petit, T.; Ren, J.; Choudhury, S.; Golnak, R.; Lalithambika, S. S.; Tesch, M. F.; Xiao, J.; Aziz, E. F., X-Ray Absorption Spectroscopy of TiO_2 Nanoparticles in Water Using a Holey Membrane-Based Flow Cell. *Adv. Mater. Interfaces* **2017,** *4* (23), 1700755.
201. Luttrell, T.; Halpegamage, S.; Tao, J.; Kramer, A.; Sutter, E.; Batzill, M., Why is anatase a better photocatalyst than rutile?-Model studies on epitaxial TiO_2 films. *Sci. Rep.* **2014,** *4*, 4043.
202. Hadjiivanov, K. I.; Klissurski, D. G., Surface chemistry of titania (anatase) and titania-supported catalysts. *Chem. Soc. Rev.* **1996,** *25* (1), 61-69.
203. Kavan, L.; Grätzel, M.; Gilbert, S.; Klemenz, C.; Scheel, H., Electrochemical and photoelectrochemical investigation of single-crystal anatase. *J. Am. Chem. Soc*. **1996,** *118* (28), 6716-6723.
204. Barnard, A.; Curtiss, L., Prediction of TiO_2 nanoparticle phase and shape transitions controlled by surface chemistry. *Nano Lett.* **2005,** *5* (7), 1261-1266.
205. Vittadini, A.; Selloni, A.; Rotzinger, F.; Grätzel, M., Structure and energetics of water adsorbed at TiO_2 anatase (101) and (001) surfaces. *Phys. Rev. Lett.* **1998,** *81* (14), 2954.
206. Cui, Z.-H.; Wu, F.; Jiang, H., First-principles study of relative stability of rutile and anatase TiO_2 using the random phase approximation. *Phys. Chem. Chem. Phys.* **2016,** *18* (43), 29914-29922.
207. Sham, T.; Lazarus, M., X-ray photoelectron spectroscopy (XPS) studies of clean and hydrated TiO_2 (rutile) surfaces. *Chem. Phys. Lett.* **1979,** *68* (2-3), 426-432.
208. Wendt, S.; Matthiesen, J.; Schaub, R.; Vestergaard, E. K.; Lægsgaard, E.; Besenbacher, F.; Hammer, B., Formation and splitting of paired hydroxyl groups on reduced TiO_2 (110). *Phys. Rev. Lett.* **2006,** *96* (6), 066107.
209. Blomquist, J.; Walle, L. E.; Uvdal, P.; Borg, A.; Sandell, A., Water dissociation on single crystalline anatase TiO_2(001) studied by photoelectron spectroscopy. *J. Phys. Chem. C* **2008,** *112* (42), 16616-16621.
210. Walle, L.; Borg, A.; Uvdal, P.; Sandell, A., Experimental evidence for mixed dissociative and molecular adsorption of water on a rutile TiO_2 (110) surface without oxygen vacancies. *Phys. Rev. B* **2009,** *80* (23), 235436.

211. Balajka, J.; Hines, M. A.; DeBenedetti, W. J.; Komora, M.; Pavelec, J.; Schmid, M.; Diebold, U., High-affinity adsorption leads to molecularly ordered interfaces on TiO_2 in air and solution. *Science* **2018,** *361* (6404), 786-789.
212. Balajka, J.; Aschauer, U.; Mertens, S. F.; Selloni, A.; Schmid, M.; Diebold, U., Surface Structure of TiO_2 Rutile (011) Exposed to Liquid Water. *J. Phys. Chem. C* **2017,** *121* (47), 26424-26431.
213. Jackman, M. J.; Thomas, A. G.; Muryn, C., Photoelectron spectroscopy study of stoichiometric and reduced anatase TiO_2 (101) surfaces: the effect of subsurface defects on water adsorption at near-ambient pressures. *J. Phys. Chem. C* **2015,** *119* (24), 13682-13690.
214. Thompson, T. L.; Yates, J. T., TiO_2-based photocatalysis: surface defects, oxygen and charge transfer. *Top. Catal.* **2005,** *35* (3-4), 197-210.
215. Hossain, F.; Murch, G.; Sheppard, L.; Nowotny, J., Reactivity of ideal and defected rutile TiO_2 (110) surface with oxygen. *Adv. Appl. Ceram.* **2007,** *106* (1-2), 95-100.
216. Zhao, H.; Pan, F.; Li, Y., A review on the effects of TiO_2 surface point defects on CO_2 photoreduction with H_2O. *Journal of Materiomics* **2017,** *3* (1), 17-32.
217. Benkoula, S.; Sublemontier, O.; Patanen, M.; Nicolas, C.; Sirotti, F.; Naitabdi, A.; Gaie-Levrel, F.; Antonsson, E.; Aureau, D.; Ouf, F.-X., Water adsorption on TiO_2 surfaces probed by soft X-ray spectroscopies: bulk materials vs. isolated nanoparticles. *Sci. Rep.* **2015,** *5*, 15088.
218. Wang, Z.-T.; Wang, Y.-G.; Mu, R.; Yoon, Y.; Dahal, A.; Schenter, G. K.; Glezakou, V.-A.; Rousseau, R.; Lyubinetsky, I.; Dohnálek, Z., Probing equilibrium of molecular and deprotonated water on TiO_2 (110). *Proceedings of the National Academy of Sciences* **2017,** *114* (8), 1801-1805.
219. Diebold, U., Perspective: A controversial benchmark system for water-oxide interfaces: H_2O/TiO_2 (110). *J.Chem. Phys.* **2017,** *147* (4), 040901.
220. He, Y.; Tilocca, A.; Dulub, O.; Selloni, A.; Diebold, U., Local ordering and electronic signatures of submonolayer water on anatase TiO_2 (101). *Nat. Mater.* **2009,** *8* (7), 585.
221. Duncan, D.; Allegretti, F.; Woodruff, D., Water does partially dissociate on the perfect TiO_2 (110) surface: a quantitative structure determination. *Phys. Rev. B* **2012,** *86* (4), 045411.
222. Zheng, T.; Wu, C.; Chen, M.; Zhang, Y.; Cummings, P. T., A DFT study of water adsorption on rutile TiO_2 (110) surface: The effects of surface steps. *J.Chem. Phys.* **2016,** *145* (4), 044702.
223. Schindler, P.; Gamsjäger, H., Acid—base reactions of the TiO_2 (Anatase)—water interface and the point of zero charge of TiO_2 suspensions. *Kolloid-Zeitschrift und Zeitschrift für Polymere* **1972,** *250* (7), 759-763.
224. Cheng, J.; Sprik, M., Acidity of the aqueous rutile TiO_2 (110) surface from density functional theory based molecular dynamics. *J. Chem. Theory Comput.* **2010,** *6* (3), 880-889.
225. Vayssieres, L.; Persson, C.; Guo, J.-H., Size effect on the conduction band orbital character of anatase TiO_2 nanocrystals. *Appl. Phys. Lett.* **2011,** *99* (18), 183101.

226. Sentein, C.; Guizard, B.; Giraud, S.; Yé, C.; Ténégal, F., Dispersion and stability of TiO_2 nanoparticles synthesized by laser pyrolysis in aqueous suspensions. *J. Phys.: Conf. Ser.* **2009,** *170* (1), 012013.
227. Burns, R. G.; Burns, R. G., *Mineralogical applications of crystal field theory*. Cambridge University Press: 1993; Vol. 5.
228. Crocombette, J.; Jollet, F., Ti 2p X-ray absorption in titanium dioxides (TiO_2): the influence of the cation site environment. *J. Phys.: Condens. Matter* **1994,** *6* (49), 10811.
229. De Groot, F.; Figueiredo, M.; Basto, M.; Abbate, M.; Petersen, H.; Fuggle, J., 2p X-ray absorption of titanium in minerals. *Phys. Chem. Miner.* **1992,** *19* (3), 140-147.
230. Henderson, G. S.; De Groot, F. M.; Moulton, B. J., X-ray absorption near-edge structure (XANES) spectroscopy. *Rev. Mineral. Geochem.* **2014,** *78* (1), 75-138.
231. Henningsson, A.; Rensmo, H.; Sandell, A.; Siegbahn, H.; Södergren, S.; Lindström, H.; Hagfeldt, A., Electronic structure of electrochemically Li-inserted TiO_2 studied with synchrotron radiation electron spectroscopies. *J.Chem. Phys.* **2003,** *118* (12), 5607-5612.
232. Thomas, A.; Flavell, W.; Mallick, A.; Kumarasinghe, A.; Tsoutsou, D.; Khan, N.; Chatwin, C.; Rayner, S.; Smith, G.; Stockbauer, R., Comparison of the electronic structure of anatase and rutile TiO_2 single-crystal surfaces using resonant photoemission and X-ray absorption spectroscopy. *Phys. Rev. B* **2007,** *75* (3), 035105.
233. Mosquera, A. A.; Endrino, J. L.; Albella, J. M., XANES observations of the inhibition and promotion of anatase and rutile phases in silver containing films. *J. Anal. At. Spectrom.* **2014,** *29* (4), 736-742.
234. Ruus, R.; Kikas, A.; Saar, A.; Ausmees, A.; Nommiste, E.; Aarik, J.; Aidla, A.; Uustare, T.; Martinson, I., Ti 2p and O 1s X-ray absorption of TiO_2 polymorphs. *Solid State Commun.* **1997,** *104* (4), 199-203.
235. Tossell, J.; Vaughan, D.; Johnson, K., Electronic-Structure of Rutile, Wustite, and Hematite from Molecular-Orbital Calculations. *Am. Mineral.* **1974,** *59* (3-4), 319-334.
236. Debye, P.; Hückel, E., De la theorie des electrolytes. L'abaissement du point de congelation et phenomenes associes. *Physikalische Zeitschrift* **1923,** *24* (9), 185-206.
237. Kurahashi, N.; Karashima, S.; Tang, Y.; Horio, T.; Abulimiti, B.; Suzuki, Y.-I.; Ogi, Y.; Oura, M.; Suzuki, T., Photoelectron spectroscopy of aqueous solutions: Streaming potentials of NaX (X= Cl, Br, and I) solutions and electron binding energies of liquid water and X^-. *J.Chem. Phys.* **2014,** *140* (17), 174506.
238. Moustakas, N.; Kontos, A.; Likodimos, V.; Katsaros, F.; Boukos, N.; Tsoutsou, D.; Dimoulas, A.; Romanos, G. E.; Dionysiou, D.; Falaras, P., Inorganic–organic core–shell titania nanoparticles for efficient visible light activated photocatalysis. *Appl. Catal., B* **2013,** *130*, 14-24.

239. Sato, S.; White, J., Photodecomposition of water over Pt/TiO_2 catalysts. *Chem. Phys. Lett.* **1980,** *72* (1), 83-86.
240. Serpone, N.; Lawless, D.; Disdier, J.; Herrmann, J.-M., Spectroscopic, photoconductivity, and photocatalytic studies of TiO_2 colloids: naked and with the lattice doped with Cr^{3+}, Fe^{3+}, and V^{5+} cations. *Langmuir* **1994,** *10* (3), 643-652.
241. Di Paola, A.; Bellardita, M.; Palmisano, L., Brookite, the least known TiO_2 photocatalyst. *Catalysts* **2013,** *3* (1), 36-73.
242. Grätzel, M.; Rotzinger, F. P., The influence of the crystal lattice structure on the conduction band energy of oxides of titanium (IV). *Chem. Phys. Lett.* **1985,** *118* (5), 474-477.
243. Ola, O.; Maroto-Valer, M. M., Review of material design and reactor engineering on TiO_2 photocatalysis for CO_2 reduction. *Journal of Photochemistry and Photobiology C: Photochemistry Reviews* **2015,** *24*, 16-42.
244. Helmholtz, H. v., Ueber einige Gesetze der Vertheilung elektrischer Ströme in körperlichen Leitern, mit Anwendung auf die thierisch-elektrischen Versuche (Schluss.). *Annalen der Physik* **1853,** *165* (7), 353-377.
245. Chapman, D. L., LI. A contribution to the theory of electrocapillarity. *The London, Edinburgh, and Dublin philosophical magazine and journal of science* **1913,** *25* (148), 475-481.
246. Gouy, M., Sur la constitution de la charge électrique à la surface d'un électrolyte. *J. Phys. Theor. Appl.* **1910,** *9* (1), 457-468.
247. Stern, O., The theory of the electrolytic double-layer. *Z. Elektrochem* **1924,** *30* (508), 1014-1020.
248. Polte, J., Fundamental growth principles of colloidal metal nanoparticles–a new perspective. *CrystEngComm* **2015,** *17* (36), 6809-6830.
249. Guo, D.; Xie, G.; Luo, J., Mechanical properties of nanoparticles: basics and applications. *J. Phys. D: Appl. Phys.* **2013,** *47* (1), 013001.
250. Elimelech, M.; Gregory, J.; Jia, X., *Particle deposition and aggregation: measurement, modelling and simulation*. Butterworth-Heinemann: 2013.
251. Zhao, Z.; Li, Z.; Zou, Z., Structure and properties of water on the anatase TiO_2 (101) surface: from single-molecule adsorption to interface formation. *J. Phys. Chem. C* **2012,** *116* (20), 11054-11061.
252. Fenter, P.; Cheng, L.; Rihs, S.; Machesky, M.; Bedzyk, M. J.; Sturchio, N., Electrical double-layer structure at the rutile–water interface as observed in situ with small-period X-ray standing waves. *J. Colloid Interface Sci.* **2000,** *225* (1), 154-165.
253. Předota, M.; Bandura, A.; Cummings, P.; Kubicki, J.; Wesolowski, D.; Chialvo, A.; Machesky, M., Electric double layer at the rutile (110) surface. 1. Structure of surfaces and interfacial water from molecular dynamics by use of ab initio potentials. *J. Phys. Chem. B* **2004,** *108* (32), 12049-12060.

254. Cheng, J.; Sprik, M., The electric double layer at a rutile TiO_2 water interface modelled using density functional theory based molecular dynamics simulation. *J. Phys.: Condens. Matter* **2014,** *26* (24), 244108.
255. Favaro, M.; Jeong, B.; Ross, P. N.; Yano, J.; Hussain, Z.; Liu, Z.; Crumlin, E. J., Unravelling the electrochemical double layer by direct probing of the solid/liquid interface. *Nature Comm.* **2016,** *7*, 12695.
256. Rubasinghege, G.; Grassian, V. H., Role(s) of adsorbed water in the surface chemistry of environmental interfaces. *Chem. Commun. (Cambridge, U. K.)* **2013,** *49* (30), 3071-3094.
257. Ali, H.; Seidel, R.; Bergmann, A.; Winter, B., Electronic structure of aqueous-phase anatase titanium dioxide nanoparticles probed by liquid jet photoelectron spectroscopy. *Journal of Materials Chemistry A* **2019,** *7*, 6665-6675.
258. Helmholtz-zentrum-Berlin, LiXEdrom: High Energy Resolution RIXS Station dedicated to Liquid Investigation at BESSY II. *Journal of large-scale research facilities JLSRF* **2016,** *2*, 80.
259. Jordan, I.; Redondo, A. B.; Brown, M. A.; Fodor, D.; Staniuk, M.; Kleibert, A.; Wörner, H. J.; Giorgi, J. B.; van Bokhoven, J. A., Non-uniform spatial distribution of tin oxide (SnO_2) nanoparticles at the air–water interface. *Chem. Commun. (Cambridge, U. K.)* **2014,** *50* (32), 4242-4244.
260. Emerson, K.; Russo, R. C.; Lund, R. E.; Thurston, R. V., Aqueous ammonia equilibrium calculations: effect of pH and temperature. *Journal of the Fisheries Board of Canada* **1975,** *32* (12), 2379-2383.
261. Bates, R. G.; Pinching, G., Acidic dissociation constant of ammonium ion at 0 to 50 C, and the base strength of ammonia. *Journal of Research of the National Bureau of Standards* **1949,** *42*, 419-430.
262. Weinhardt, L.; Ertan, E.; Iannuzzi, M.; Weigand, M.; Fuchs, O.; Bär, M.; Blum, M.; Denlinger, J. D.; Yang, W.; Umbach, E., Probing hydrogen bonding orbitals: resonant inelastic soft X-ray scattering of aqueous NH_3. *Phys. Chem. Chem. Phys.* **2015,** *17* (40), 27145-27153.
263. Perry, R.; Chilton, C., Chemical Engineers' Handbook. Section 3. *McGraw Hill. New York* **1973,** *1*, 973.
264. Unger, I.; Hollas, D.; Seidel, R.; Thürmer, S.; Aziz, E. F.; Slavicek, P.; Winter, B., Control of X-ray induced electron and nuclear dynamics in ammonia and glycine aqueous solution via hydrogen bonding. *J. Phys. Chem. B* **2015,** *119* (33), 10750-10759.
265. Ogunremi, T.; Cutler, J.; Christensen, C.; Sparks, C. In *X-ray Absorption Spectroscopic analysis of raw and processed hog manure*, Soils and Crops Workshop, 2007.
266. Leinweber, P.; Kruse, J.; Walley, F. L.; Gillespie, A.; Eckhardt, K.-U.; Blyth, R. I.; Regier, T., Nitrogen K-edge XANES–an overview of reference compounds used to identify unknown'organic nitrogen in environmental samples. *Journal of synchrotron radiation* **2007,** *14* (6), 500-511.

267. Sidey, V., On the effective ionic radii for ammonium. *Acta Crystallographica Section B: Structural Science, Crystal Engineering and Materials* **2016,** *72* (4), 626-633.
268. Brown, M. A.; Faubel, M.; Winter, B., X-ray photo-and resonant Auger-electron spectroscopy studies of liquid water and aqueous solutions. *Annual Reports Section" C"(Physical Chemistry)* **2009,** *105*, 174-212.
269. Winter, B.; Faubel, M.; Vácha, R.; Jungwirth, P., Behavior of hydroxide at the water/vapor interface. *Chem. Phys. Lett.* **2009,** *474* (4-6), 241-247.
270. Tuckerman, M. E.; Chandra, A.; Marx, D., Structure and dynamics of OH^-(aq). *Acc. Chem. Res.* **2006,** *39* (2), 151-158.
271. Blum, M. Electronic and Chemical Properties of Liquids and Solutions. Universität Würzburg, 2009.
272. Tuckerman, M.; Laasonen, K.; Sprik, M.; Parrinello, M., Ab initio molecular dynamics simulation of the solvation and transport of hydronium and hydroxyl ions in water. *J.Chem. Phys.* **1995,** *103* (1), 150-161.
273. Asthagiri, D.; Pratt, L. R.; Kress, J. D.; Gomez, M. A., Hydration and mobility of HO^-(aq). *Proceedings of the National Academy of Sciences* **2004,** *101* (19), 7229-7233.
274. Chen, B.; Park, J. M.; Ivanov, I.; Tabacchi, G.; Klein, M. L.; Parrinello, M., First-principles study of aqueous hydroxide solutions. *J. Am. Chem. Soc.* **2002,** *124* (29), 8534-8535.
275. Zhu, L.; Gu, Q.; Sun, P.; Chen, W.; Wang, X.; Xue, G., Characterization of the mobility and reactivity of water molecules on TiO_2 nanoparticles by ^1H solid-state nuclear magnetic resonance. *ACS Appl. Mater. Interfaces* **2013,** *5* (20), 10352-10356.
276. Zaleska-Medynska, A., *Metal Oxide-based Photocatalysis: Fundamentals and Prospects for Application*. Elsevier: 2018.
277. Minggu, L. J.; Daud, W. R. W.; Kassim, M. B., An overview of photocells and photoreactors for photoelectrochemical water splitting. *Int. J. Hydrogen Energy* **2010,** *35* (11), 5233-5244.
278. Smith, A. M.; Lee, A. A.; Perkin, S., The electrostatic screening length in concentrated electrolytes increases with concentration. *J. Phys. Chem. Lett.* **2016,** *7* (12), 2157-2163.
279. Ali, H.; Golnak, R.; Seidel, R.; Winter, B.; Xiao, J., In-Situ X-ray Spectroscopy of the Electric Double Layer around TiO_2 Nanoparticles Dispersed in Aqueous Solution: Implications for H_2 Generation. *ACS Applied Nano Materials* **2020,** *3* (1), 264-273.
280. Wang, Q.; Jiao, L.; Du, H.; Wang, Y.; Yuan, H., Fe_3O_4 nanoparticles grown on graphene as advanced electrode materials for supercapacitors. *J. Power Sources* **2014,** *245*, 101-106.
281. Nithya, V.; Arul, N. S., Progress and development of Fe_3O_4 electrodes for supercapacitors. *Journal of Materials Chemistry A* **2016,** *4* (28), 10767-10778.
282. Barclay, J., Use of a ferrofluid as the heat-exchange fluid in a magnetic refrigerator. *J. Appl. Phys.* **1982,** *53* (4), 2887-2894.

283. Kim, E. H.; Lee, H. S.; Kwak, B. K.; Kim, B.-K., Synthesis of ferrofluid with magnetic nanoparticles by sonochemical method for MRI contrast agent. *J. Magn. Magn. Mater.* **2005,** *289*, 328-330.

284. Giustini, A. J.; Petryk, A. A.; Cassim, S. M.; Tate, J. A.; Baker, I.; Hoopes, P. J., Magnetic nanoparticle hyperthermia in cancer treatment. *Nano Life* **2010,** *1* (01n02), 17-32.

285. Dilnawaz, F.; Singh, A.; Mohanty, C.; Sahoo, S. K., Dual drug loaded superparamagnetic iron oxide nanoparticles for targeted cancer therapy. *Biomaterials* **2010,** *31* (13), 3694-3706.

286. Néel, M. L. In *Propriétés magnétiques des ferrites; ferrimagnétisme et antiferromagnétisme*, Annales de Physique, 1948; pp 137-198.

287. Alibeigi, S.; Vaezi, M. R., Phase transformation of iron oxide nanoparticles by varying the molar ratio of Fe^{2+}: Fe^{3+}. *Chemical Engineering & Technology: Industrial Chemistry-Plant Equipment-Process Engineering-Biotechnology* **2008,** *31* (11), 1591-1596.

288. Gorski, C. A.; Handler, R. M.; Beard, B. L.; Pasakarnis, T.; Johnson, C. M.; Scherer, M. M., Fe atom exchange between aqueous Fe^{2+} and magnetite. *Environ. Sci. Technol.* **2012,** *46* (22), 12399-12407.

289. Fock, J.; Bogart, L. K.; González-Alonso, D.; Espeso, J. I.; Hansen, M. F.; Varón, M.; Frandsen, C.; Pankhurst, Q. A., On the 'centre of gravity'method for measuring the composition of magnetite/maghemite mixtures, or the stoichiometry of magnetite-maghemite solid solutions, via ^{57}Fe Mössbauer spectroscopy. *J. Phys. D: Appl. Phys.* **2017,** *50* (26), 265005.

290. Sassi, M.; Pearce, C. I.; Bagus, P. S.; Arenholz, E.; Rosso, K. M., First-Principles Fe $L_{2,3}$-Edge and O K-Edge XANES and XMCD Spectra for Iron Oxides. *J. Phys. Chem. A* **2017,** *121* (40), 7613-7618.

291. Stookey, L. L., Ferrozinea—A new spectrophotometric reagent for iron. *Anal. Chem.* **1970,** *42* (7), 779-781.

292. Elsaidi, S. K.; Sinnwell, M. A.; Banerjee, D.; Devaraj, A.; Kukkadapu, R. K.; Droubay, T. C.; Nie, Z.; Kovarik, L.; Vijayakumar, M.; Manandhar, S.; Nandasiri, M.; McGrail, B. P.; Thallapally, P. K., Reduced Magnetism in Core–Shell Magnetite@MOF Composites. *Nano Lett.* **2017,** *17* (11), 6968-6973.

293. Abanades, S.; Legal, A.; Cordier, A.; Peraudeau, G.; Flamant, G.; Julbe, A., Investigation of reactive cerium-based oxides for H_2 production by thermochemical two-step water-splitting. *J. Mater. Sci.* **2010,** *45* (15), 4163-4173.

294. El Khalifi, M.; Picaud, F.; Bizi, M., Electronic and optical properties of CeO_2 from first principles calculations. *Analytical Methods* **2016,** *8* (25), 5045-5052.

295. Montini, T.; Melchionna, M.; Monai, M.; Fornasiero, P., Fundamentals and catalytic applications of CeO_2-based materials. *Chem. Rev. (Washington, DC, U. S.)* **2016,** *116* (10), 5987-6041.

296. Abanades, S.; Flamant, G., Thermochemical hydrogen production from a two-step solar-driven water-splitting cycle based on cerium oxides. *Solar energy* **2006,** *80* (12), 1611-1623.
297. Mullins, D. R., The surface chemistry of cerium oxide. *Surf. Sci. Rep.* **2015,** *70* (1), 42-85.
298. Fernández-Torre, D.; Kośmider, K.; Carrasco, J.; Ganduglia-Pirovano, M. V.; Pérez, R., Insight into the Adsorption of Water on the Clean CeO_2(111) Surface with van der Waals and Hybrid Density Functionals. *J. Phys. Chem. C* **2012,** *116* (25), 13584-13593.
299. Fronzi, M.; Piccinin, S.; Delley, B.; Traversa, E.; Stampfl, C., Water adsorption on the stoichiometric and reduced CeO_2 (111) surface: a first-principles investigation. *Phys. Chem. Chem. Phys.* **2009,** *11* (40), 9188-9199.
300. Han, Z. K.; Gao, Y., Water Adsorption and Dissociation on Ceria-Supported Single-Atom Catalysts: A First-Principles DFT+ U Investigation. *Chemistry–A European Journal* **2016,** *22* (6), 2092-2099.
301. Henderson, M. A.; Perkins, C.; Engelhard, M. H.; Thevuthasan, S.; Peden, C. H., Redox properties of water on the oxidized and reduced surfaces of CeO_2 (111). *Surf. Sci.* **2003,** *526* (1-2), 1-18.
302. Kropp, T.; Paier, J.; Sauer, J., Interactions of Water with the (111) and (100) Surfaces of Ceria. *J. Phys. Chem. C* **2017,** *121* (39), 21571-21578.
303. Maslakov, K. I.; Teterin, Y. A.; Ryzhkov, M. V.; Popel, A. J.; Teterin, A. Y.; Ivanov, K. E.; Kalmykov, S. N.; Petrov, V. G.; Petrov, P. K.; Farnan, I., The electronic structure and the nature of the chemical bond in CeO_2. *Phys. Chem. Chem. Phys.* **2018,** *20* (23), 16167-16175.
304. Ablett, J.; Prieur, D.; Céolin, D.; Lassalle-Kaiser, B.; Lebert, B.; Sauvage, M.; Moreno, T.; Bac, S.; Balédent, V.; Ovono, A., The GALAXIES inelastic hard X-ray scattering end-station at Synchrotron SOLEIL. *Journal of synchrotron radiation* **2019,** *26* (1).
305. Shinotsuka, H.; Da, B.; Tanuma, S.; Yoshikawa, H.; Powell, C.; Penn, D. R., Calculations of electron inelastic mean free paths. XI. Data for liquid water for energies from 50 eV to 30 keV. *Surf. Interface Anal.* **2017,** *49* (4), 238-252.
306. Wang, M.; Pyeon, M.; Gönüllü, Y.; Kaouk, A.; Shen, S.; Guo, L.; Mathur, S., Constructing Fe_2O_3/TiO_2 core–shell photoelectrodes for efficient photoelectrochemical water splitting. *Nanoscale* **2015,** *7* (22), 10094-10100.
307. Hsu, Y.-K.; Chen, Y.-C.; Lin, Y.-G., Novel ZnO/Fe_2O_3 core–shell nanowires for photoelectrochemical water splitting. *ACS Appl. Mater. Interfaces* **2015,** *7* (25), 14157-14162.

Acknowledgements

My PhD has been an amazing experience on both the scientific and social level. Many people have contributed to this experience, and I am very grateful to have met them in this period of my life and for their impact in this work. No words can express how much I am thankful to all of you.

First of all, Prof. Dr. Gerard J. M. Meijer, thank you for being my supervisor and allowing me to work in this awesome molecular physics department; I really like this place with its very motivated and friendly environment. You are always a strong supporter and advisor, who allowed me to individually conduct my projects and related research with large degree of freedom and trust. I learnt so much from you especially on the academic level. I also would like to thank Prof. Dr. John C. Hemminger, my second supervisor, for his kind support and motivation.

Foremost I thank Dr. Bernd Winter, my PhD mentor from day one, the expert in liquid-jet photoelectron spectroscopy. I still remember our first meeting to discuss the nanoparticles project and its challenges. Thank you for all your support, scientific knowledge, guidance and discussions. These are the main reasons I have become "The Queen of nanoparticles " as you usually call me. I could not have imagined having a better advisor and mentor for my PhD study.

My sincere thanks also go to Dr. Robert Seidel. You are always more than a mentor. I appreciate so much your continuous help and advice through the whole period of my PhD. You are an excellent teacher, who gave me my very first tour in the BESSY hall and all the support during my experiments and research. Thanks for your highly motivated, helpful and funny personality. "Correct! Life is boring when it is so serious". "One last thing", thanks for introducing me to all the chocolate kinds and brands around the world, even the Japanese green KitKat.

I would also like to express my special appreciation and thanks to Dr. Ronny Golnak for his support and for sharing with me many beamtime shifts on the Lixedrom as well as the SOL^3 PES setups. It was always trustworthy to talk to you and getting your advice. I am also very grateful to Dr. Jie Xiao for the long discussions about the photon-emission measurements, as well as for his patience and guidance. It was a pleasure to collaborate with you on the TiO_2 project.

Also, I would like to thank again Dr. Robert Seidel, Dr. Jie Xiao, Dr. Uwe Hergenhahn, Dr. Bernd Winter and Prof. Dr. Gerard Meijer for their corrections, comments and reviews of this dissertation.

I am very grateful for many colleagues who shared with me many fruitful beamtime shifts either during conducting my PhD project or other research projects: Marvin N. Pohl, Dr. Arno Bergmann, Dr. Anne Stephansen, Sebastian Malerz, Dr. Hanns Christian Schewe, Dr. Florian Trinter, Garlef Wartner and Dennis Hein. I am also thankful to many colleagues who became good friends:

Karen Mudryk, Dawei Cao, and Nicole Walter. Also to all my colleagues in the molecular physics department, FHI; I thank you for the very friendly working environment. I enjoyed a lot with all of you organizing and celebrating the “Sommer Fest 2018”, “Lange Nacht der Wissenschaft 2019” as well as many summer grills and ceremonies.

A big thank to my home university colleagues and friends especially, Haiam Adel and Nadia ElKady for all their support; also, the Egyptian Ministry of Higher Education and Scientific Research as well as Ain Shams University for my PhD grant.

Last, I am very grateful to the most precious people in my life, my family. Thanks for all the unconditional support.

Short Curriculum Vitae

Hebatallah Ali Assistant Lecturer of Spectroscopic Physics,
2009- Now Ain Shams University, Cairo, Egypt

Education

2004-2008 Ain Shams University, Cairo, Egypt
B.Sc. of Physics and Pure Mathematics
(with general grade "Very Good", in the 1st rank)
Honored by the excellence award for Bachelor graduate from the "Egyptian Association of Scientific Professions"

2008-2009 Ain Shams University, Cairo, Egypt
Preliminary year of Master Courses
(with general grade "Excellent", in the 1st rank)

2010-2013 Ain Shams University and Egyptian Atomic Energy Authority, Cairo, Egypt
M.Sc. of Spectroscopic Physics
Thesis title: "Elemental analysis inductively coupled plasma mass spectrometry and other spectroscopic methods of Beryl"
Honored by the excellence award for young scientists from "The Egyptian Society of Nuclear Sciences and Applications"

2016-2017 Freie Universität Berlin and Helmholtz-Zentrum Berlin, Germany
PhD Candidate: "Liquid-Jet Photoemission Studies of the Interface between Metal-Oxide Nanoparticles and Aqueous Solution"
Mentors: Dr. Bernd Winter and Dr. Robert Seidel,
in the institute of Methods for Material Development under the Supervision of Prof. Dr. Emad F. Aziz.
Funded by a Scholarship from the Egyptian Ministry of Higher Education and by Ain Shams University

2017-2019	Freie Universität Berlin and Fritz-Haber-Institut der Max-Planck-Gesellschaft, Berlin, Germany Continued PhD studies on: "Liquid-Jet Photoemission Studies of the Interface between Metal-Oxide Nanoparticles and Aqueous Solution" Mentors: Dr. Bernd Winter and Dr. Robert Seidel Supervisors: Prof. Dr. Gerard J. M. Meijer and Prof. Dr. John C. Hemminger. Funded by a Scholarship from the Egyptian Ministry of Higher Education and by Ain Shams University

Publications

Publications covered in this thesis:

- **Molecular species forming at the α-Fe_2O_3 nanoparticle–aqueous solution interface**
  Hebatallah Ali, Robert Seidel, Marvin N. Pohl and Bernd Winter
  Chemical Science 2018**, 9**, 4511-4523, **DOI:** 10.1039/C7SC05156E

- **Electronic Structure of Aqueous-Phase Anatase Titanium Dioxide Nanoparticles Probed by Liquid Jet Photoelectron Spectroscopy**
  Hebatallah Ali, Robert Seidel, Arno Bergmann and Bernd Winter
  Journal of Materials Chemistry A 2019, **7**, 6665-6675, **DOI:** 10.1039/C8TA09414D

- **In-situ probe of the electric double layer around the TiO_2 nanoparticles dispersed in aqueous solution**
  Hebatallah Ali, Ronny Golnak, Robert Seidel, Bernd Winter, and Jie Xiao
  ACS Applied Nano Materials 2020, **3** (1), 264-273, **DOI:** 10.1021/acsanm.9b01939

Publications not covered in this thesis:

- **Advances in Liquid Phase Soft-X-ray Photoemission Spectroscopy: A New Experimental Setup at BESSY II**
  Robert Seidel, Marvin N. Pohl, **Hebatallah Ali**, Bernd Winter, and Emad F. Aziz
  Review of Scientific Instruments 2017, **88** (7), 073107, **DOI:** 10.1063/1.4990797

- **Do water's electrons care about electrolytes?**
  Marvin N. Pohl, Eva Muchová, Robert Seidel, **Hebatallah Ali**, Štěpán Sršeň, Iain Wilkinson, Bernd Winter and Petr Slavíček
  Chemical Science 2019**, 10**, 848-865, **DOI:** 10.1039/C8SC03381A

- **Valence and Core-Level X-ray Photoelectron Spectroscopy of a Liquid Ammonia Microjet**
  Tillmann Buttersack, Philip E. Mason, Ryan S. McMullen, Tomas Martinek, Krystof Brezina, Dennis Hein, **Hebatallah Ali**, Claudia Kolbeck, Christian Schewe, Sebastian Malerz, Bernd Winter, Robert Seidel, Ondrej Marsalek, Pavel Jungwirth, and Stephen E. Bradforth
  Journal of the American Chemical Society 2019, **141** (5), 1838–1841, **DOI:**10.1021/jacs.8b10942

Selbstständigkeitserklärung

Hiermit erkläre ich, dass ich die vorliegende Dissertation selbstständig und nur mit Hilfe der angegebenen Quellen angefertigt habe. Ich versichere, dass diese Arbeit nicht in einem vorhergehenden Promotionsverfahren angenommen wurde oder als ungenugend beurteilt wurde.

Hebatallah Ali

Berlin, den 1.10.2019